ISSN 1590-8844
Vol. 17 No 01
2016

International Journal of Mechanics and Control

Editor: Andrea Manuello Bertetto

Scopus Indexed Journal

Reference Journal of IFToMM Italy
International Federation for the Promotion
of Mechanism and Machine Science

LIBRERIA EDITRICE UNIVERSITARIA
LEVROTTO & BELLA
TORINO

Official Torino Italy Court Registration
n.5390, 5th May 2000

Deposito presso il Tribunale di Torino
numero 5390 del 5 maggio 2000
Direttore responsabile:
Andrea Manuello Bertetto

International Journal of Mechanics and Control

The Journal is addressed to scientists and engineers who work in the fields of mechanics (mechanics, machines, systems, control, structures). It is edited in Turin (Northern Italy) by Levrotto&Bella Co., with an international board of editors. It will have not advertising.

Turin has a great and long tradition in mechanics and automation of mechanical systems. The journal would will to satisfy the needs of young research workers of having their work published on a qualified paper in a short time, and of the public need to read the results of researches as fast as possible.

Interested parties will be University Departments, Private or Public Research Centres, Innovative Industries.

Aims and scope

The *International Journal of Mechanics and Control* publishes as rapidly as possible manuscripts of high standards. It aims at providing a fast means of exchange of ideas among workers in Mechanics, at offering an effective method of bringing new results quickly to the public and at establishing an informal vehicle for the discussion of ideas that may still in the formative stages.

Language: English

International Journal of Mechanics and Control will publish both scientific and applied contributions. The scope of the journal includes theoretical and computational methods, their applications and experimental procedures used to validate the theoretical foundations. The research reported in the journal will address the issues of new formulations, solution, algorithms, computational efficiency, analytical and computational kinematics synthesis, system dynamics, structures, flexibility effects, control, optimisation, real-time simulation, reliability and durability. Fields such as vehicle dynamics, aerospace technology, robotics and mechatronics, machine dynamics, crashworthiness, biomechanics, computer graphics, or system identification are also covered by the journal.

Please address contributions to

Prof. Andrea Manuello Bertetto
PhD Eng. Elvio Bonisoli

Dept. of Mechanics
Technical University - Politecnico di Torino
C.so Duca degli Abruzzi, 24.
10129 - Torino - Italy - E.C.

www.jomac.it
e_mail: jomac@polito.it

Subscription information

Subscription order must be sent to
the publisher:

Libreria Editrice Universitaria
Levrotto&Bella
C.so Luigi Einaudi 57/c – 10129 Torino – Italy

www.levrotto-bella.net
e_mail: info@levrotto-bella.net
ph.: +39 011 4275423
mob.: +39 328 5369063
fax: +39 011 4275425

ISSN 1590-8844
International Journal of Mechanics and Control, Vol. 17, No. 01, 2016

Preface for the special issue of the International Journal of Mechanics and Control (JoMaC) dedicated to the 24th edition of the Workshop on Robotics in Alpe-Adria-Danube Region, RAAD 2015

In RAAD Conference, each year since 1992, take part researchers, professionals, academicians, students providing the opportunity to present and to exchange knowledge and experiences among researchers and institutions within all European countries and within world-wide robotic community too.

Last year the RAAD in 2015 was held in Bucharest and brought together academic and industry researchers in robotics from the Alpe-Adria-Danube Region affiliated countries and their worldwide partners in a collegial and stimulating environment.

As it is the tradition for several years, JoMaC, International Journal of Mechanics and Control provides for a special issue, dedicated to papers selected by the RAAD 2015 Organisers.

This editorial and scientific effort aims to keep alive the interest in this lively area of research.

Andrea Manuello Bertetto
JoMaC Editor

ISSN 1590-8844
International Journal of Mechanics and Control, Vol. 17, No. 01, 2016

3D PRINTING FOR FEASIBILITY CHECK OF MECHANISM DESIGN

D. Cafolla M. Ceccarelli M. F. Wang G. Carbone

LARM: Laboratory of Robotics and Mechatronics – DICEM – University of Cassino and South Latium,

ABSTRACT

In this paper 3D printing is presented as useful means for checking design feasibility of mechanism structures for robots. A procedure is outlined for rapid prototyping that can produce scaled prototypes for experimental validations since early stages of robot developments. An example from LARM activities for developing LARMbot humanoid is illustrated to show the soundness and practical implementation of the proposed procedure.

Keywords: Robot design, Prototyping, 3D Printing, Experimental Validation

1 INTRODUCTION

Prototype construction and validation testing is a fundamental activity in machine developments and particularly for robot designs. This activity is often time consuming and expensive, although necessary to achieve proper final design as pointed out in [1-3]. Thus, before a final production, it is required to work with prototypes that can be used for design checks and performance testing. Since early 1990s the technique of Rapid Prototyping has been developed by using scaled prototypes even with materials with fairly easy manufacturing. This has led to the development of 3D Printing whose practical feasibility has reached maturity only in the late 2000s. In recent years, new solutions have been proposed and are available in the market for fairly cheap printers and procedures. Thus, Rapid Prototyping with 3D print can be reconsidered even since early stages of the product designs. 3D printing as additive manufacturing is a process of making three dimensional solid objects from a digital file. A 3D printed object is created by laying down successive layers of material until the entire object is created. Each of these layers can be seen as a thinly sliced horizontal cross-section of the eventual object. Several different 3D printing processes have been invented since the late 1970s. The printers were original large, expensive, and highly limited in what they could produce [4]. Today a large number of additive processes are now available. The main differences among different processes are in the way that layers are deposited to create parts and in the materials that are used.

Contact author: Daniele Cafolla[1], Marco Ceccarelli[2]

[1]E-mail: cafolla@unicas.it.
[2]E-mail: ceccarelli@unicas.it.

Some methods melt or soften material to produce the layers, e.g. selective laser melting (SLM) or direct metal laser sintering (DMLS), selective laser sintering (SLS), fused deposition modeling (FDM), while others cure liquid materials using different sophisticated technologies, e.g. stereolithography (SLA).
In laminated object manufacturing (LOM), thin layers are cut and joined together (e.g. paper, polymer, metal). Each method has its own advantages and drawbacks, and this is why some companies consequently offer a choice between powder and polymer for the material to build the object, [5-9]. Other companies sometimes use standard, off-the-shelf business paper as the build material to produce a durable prototype. The main considerations in choosing a machine are generally speed, cost of the 3D printer, cost of the printed prototype, cost and choice of materials, and color capabilities, [10-11]. In this paper, the problem of using 3D printing with speedy low-cost procedure is proposed for a rapid prototyping of mechanism for robots that can be used since early stage of robot development to check the feasibility of the mechanism solution through its functionality and feasibility even in mechanical design.

2 RAPID PROTOTYPING VIA 3D PRINTING

Rapid Prototyping (RP) is a term used to describe a variety of processes, which are aimed at quickly creating three-dimensional physical parts from virtual 3D computer models using automated printing machines. The parts are built directly from a 3D CAD model and can match a model within the precision limits of the chosen process. All RP processes are additive since parts are built up by adding layer by layer, depositing, or solidifying one or more material in a horizontal layer process.

In addition to additive production processes, the possibilities of subtractive processes such as CNC (Computer Numerical Control) machining and laser cutting can be considered. These subtractive processes can help the optimization of the printed prototype improving its quality and the precision quitting burrs and errors due to chosen process and technology, [12]. 3D printable models can be created with a computer aided design (CAD) package or via a 3D scanner or via a plain digital camera and photogrammetry software. The manual modeling process of preparing geometric data for 3D computer graphics is similar to plastic arts such as sculpting. Regardless of the used 3D modeling software, a 3D model (often in .skp, .dae, .3ds or some other format) needs to be converted to either a .STL or a .OBJ format, in order to allow the printing software to be able to read it. Before printing, a 3D model must first be examined for "manifold errors".

This step is called the "fixup". Especially STLs that have been produced from a model obtained through 3D scanning, often have many manifold errors in them that need to be fixed. Examples of manifold errors are surfaces that do not connect, and gaps in the models. Examples of software that can be used to fix these errors are netfabb and Meshmixer, or even Cura, or Slic3r. Once created, the .STL file needs to be processed by a software called a "slicer" which converts the model into a series of thin layers and produces a G-code file containing instructions tailored to a specific type of 3D printer (FDM printers). This G-code file can then be printed with 3D printing client software,(which loads the G-code, and uses it to instruct the 3D printer during the 3D printing process. It should be noted that, the client software and slicer are often combined into one software program. Several open source slicer programs exist, such as Skeinforge, Slic3r, and Cura as well as closed source programs such as Simplify3D and KISSlicer.

Examples of 3D printing clients are Repetier-Host, ReplicatorG, Printrun/Pronterface. There is one other piece of software that is often used by people using 3D printing, namely a G-Code viewer. This software lets one examine the route of travel of the printer nozzle. By examining this, the user can decide to modify the G-Code to print the model in a different way (for example in a different position, e.g. standing versus lying down) so as to save plastic (depending on the position and nozzle travel, more or less support material may be needed). Examples of G-Code viewers are G-code Viewer for Blender and Pleasant3D.

A 3D printer follows the G-code instructions to lay down successive layers of liquid, powder, paper or sheet material to build the model from a series of cross sections. These layers, which correspond to the virtual cross sections in the CAD model, are joined or automatically fused to create the final shape. The primary advantage of this technique is its ability to create almost any shape or geometric feature. Printer resolution refers to layer thickness and X-Y resolution in dots per inch (dpi) or micrometres (µm).

Typical layer thickness is around 100 µm (250 DPI), although some machines such as the Objet Connex series and 3D Systems' ProJet series can print layers as thin as 16 µm (1,600 DPI), where X-Y resolution is comparable to that of laser printers with the particles (3D dots) around 50 to 100 µm (510 to 250 DPI) in diameter. Construction of a model can take from several hours to several days, depending on the used method, size and complexity of the model. Additive systems can typically reduce this time to few hours, although it varies widely depending on the type of machine, size and number of pieces being produced simultaneously.

Traditional techniques like injection molding can be less expensive for manufacturing polymer products in high quantities, but additive manufacturing can be faster, more flexible and less expensive when producing relatively small quantities of parts. 3D printers give designers and R&D teams the ability to produce parts and concept models by using a desktop size printer, [13- 15].

Some additive manufacturing techniques are capable of using multiple materials in the course of constructing parts. Some others are able to print in multiple colors and color combinations simultaneously. Supports are removable or dissolvable upon completion of the print and are used to support overhanging features during construction.

No matter which approach a 3-D printer uses, the overall printing process is generally the same. A procedure can be outlined for a suitable speedy efficient 3D printing of mechanism structures thorough a procedure that is summarized in Fig. 1:

Step 1: CAD Modeling - It is aimed to build a 3D model by using computer-aided design (CAD) software. The software may provide some hints related to the structural integrity that is expected in the finished product by using data of certain materials in virtual simulations and how the object will behave of certain conditions.

Step 2: Conversion to STL - The objective is to convert the CAD drawing to STL format. STL (Standard Tessellation Language) is a file format developed for 3D Systems in 1987 for use by stereolithography apparatus (SLA) machines.

Step 3: Transfer to AM (Automatic Machine) - A user copies the STL file to the computer that controls the 3D printer. There, the user can designate the size and orientation for printing choosing the best orientation.

Step 4: Parameter setup of the printer - Printer requirements include refilling the polymers, binders and other consumables the printer will use. It also covers adding a tray to serve as a foundation or adding the material to build temporary water-soluble supports. It is needed to check if the parameters of the printer such as the temperature of the extruder and the platform are compatible with the chosen material and the dimensions of the designed prototype are compatible with the printer characteristic and working space.

Step 5: 3D printing of elements - The build process is mostly automatic. Each layer is usually about 0.1 mm thick, though it can be much thinner or thicker. If quality of the printing is not satisfactory parameters should be changed or the CAD model should be changed to adapt the structure to the 3D printer capabilities.

Step 6: Polish and assembly - Safety precautions are necessary in removing the printed object from the printer platform in order to avoid injury by using wearing gloves to protect from hot surfaces or toxic chemical. Activities for polishing and assembly are required on printed object for brushing off any remaining powder and removing any support material.
Step 7: 3D Prototype – At the end, the prototype is ready for testing activity.

The above proposed procedure has been thought with sequential phases in order to have checks during the process permitting adjustments and optimizations even in the mechanical design of the parts.
The sequential steps of the 3D printing permits also a parallel activity in design optimization and numerical simulation of the adjustment during the prototype construction.

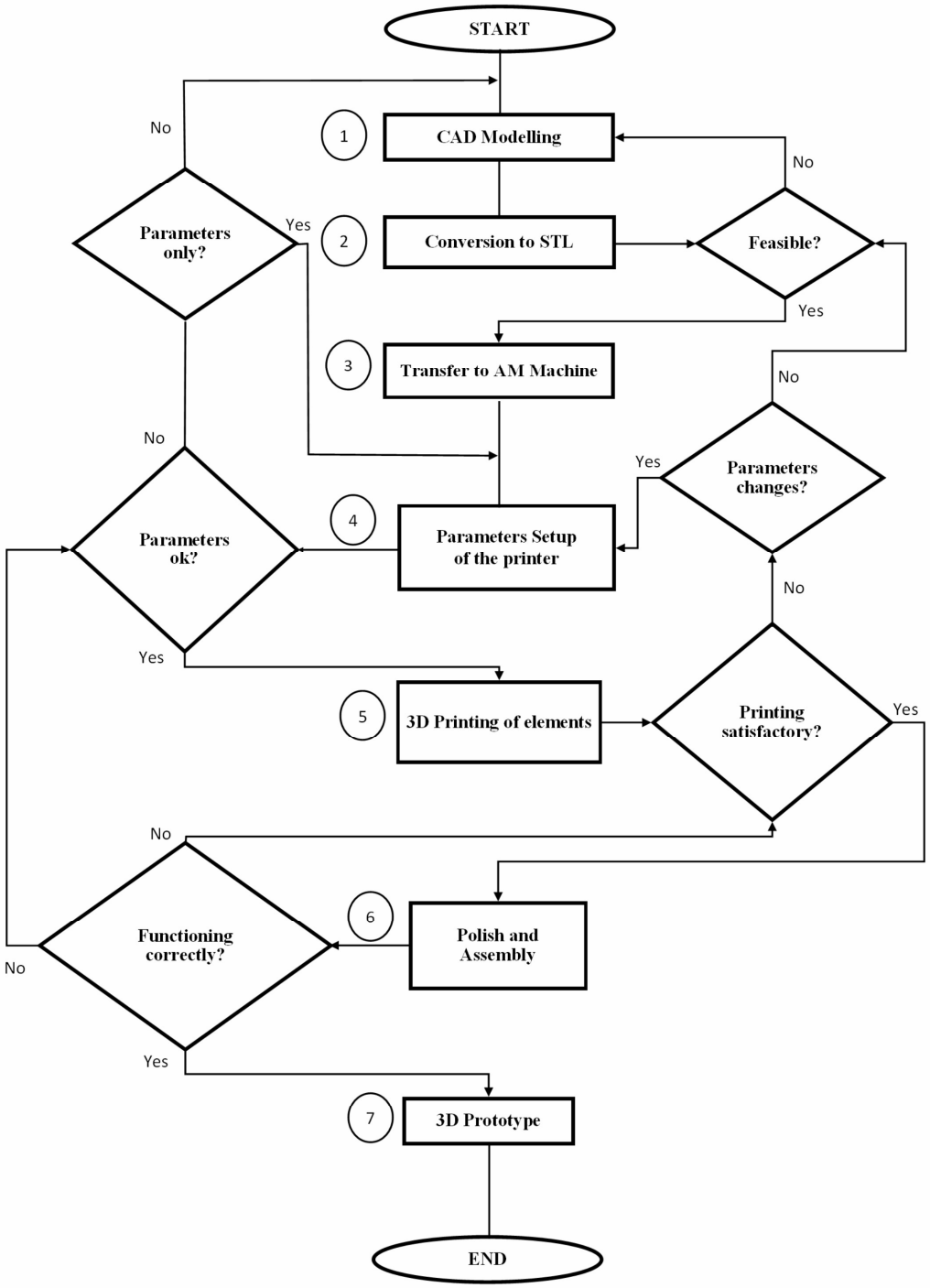

Figure 1 A scheme of a 3D printing procedure for rapid prototyping of robot mechanisms.

3 3D PRINTING ISSUES

Rapid prototyping via 3D printing is a very useful technique that can improve the developing of a new design. Nevertheless, its result is influenced by the equilibrium between several parameters. Thus, during the procedure several main issues can occur.

Figure 2 shows what happens if the plastic is not sticking to the bed. It is very important that the first layer of the print is strongly connected to the build platform so that the remainder of the part can be built on this foundation. This problem can happen for several reasons. The build platform can be not leveled since many printers include an adjustable bed with several screws or knobs that control the position of the bed. If the bed is not level, one side of the bed may be too close to the nozzle, while the other side is too far away. Achieving a perfect first layer requires a level print bed. Choosing a correct speed is very important. If the first layer is printed too fast, the plastic may not have time to bond to the build platform. For this reason, it is very useful to print the first layer at a slower speed so that the plastic has time to bond to the bed. Plastic tends to shrink as it cools from a warm temperature to a cool temperature. If the extruder prints ABS at 230 °C, but it is deposited onto a cold build platform, it is likely that the plastic would quickly cool down after leaving the hot nozzle. Some printers also include cooling fans that speed up this cooling process when they are being used. If this ABS part cooled down to a room temperature of 30 °C, a 100 mm wide part would shrink by almost 1.5 mm, so the plastic will tend to separate from the build platform as it cools. This is an important fact to keep in mind for the first layer. If the layer seems to stick initially, but later separates from the print bed as it cools, it is possible that the temperature and cooling settings are to be changed.

It is important to choose a good build platform surface since different plastics tend to adhere better to different materials. Several printers use a build task sheet on the top of their bed that tends to stick very well to PLA. Other manufacturers opt for a heat treated glass bed such as Borosilicate glass, which tends to work very well for ABS when heated. There are several types of tape that stick well to common 3D printing materials. Strips of tape can be applied to the build platform surface and easily removed or replaced with a different material. For example, ABS tends to stick better to Kapton tape known as Polyimide film. Sometimes when a very small part is being printed, it does not have enough surface area to stick to the build platform surface. Adding a Raft under the part provides a larger surface for bed adhesion.

Another important characteristic that a prototype should have is a good stiffness. To save plastic, most 3D printed parts are created to have a solid shell that surrounds a porous, partially hollow interior.

Figure 3 shows an overheating problem starting from a filament in normal condition on the left going through the overheating until burning it. Furthermore, the plastic that is under the extruder may be at any temperature between 190 °C and 240 °C.

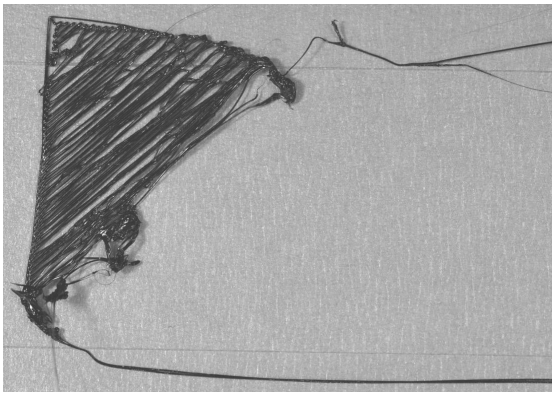

Figure 2 Example of plastic not sticking to the bed.

While the plastic is still hot, it is pliable and can easily be formed into different shapes. However, as it cools, it quickly becomes solid and retains its shape. A correct balance between temperature and cooling is needed so that the plastic can flow freely through the nozzle, but it can quickly solidify to maintain the exact dimensions of the 3D printed part. If this balance is not achieved, the exterior of the part is not as precise and defined as expected.

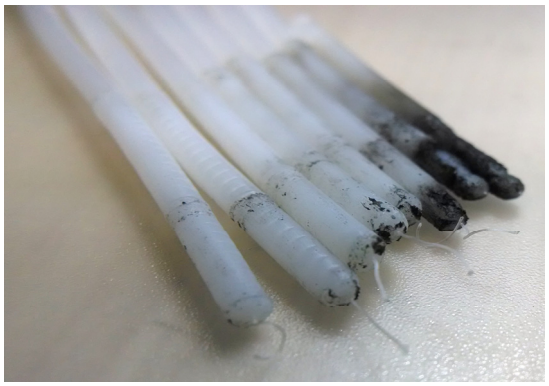

Figure 3 Example of overheating plastic filament.

The most common cause for overheating is that the plastic is not cooled fast enough. When this happens, the hot plastic is free to change shapes as it slowly cools. For many plastics, it is much better to quickly cool the layers to prevent them from changing shape after being printed. If the plastic is extruded at a lower temperature it will be able to solidify faster and retain its shape. 3D printing works by building the object one layer at a time. Each successive layer is printed on top of the previous layer. If the layers do not bond together well enough, the final part may split or separate, as shown in Figure 4. Warm plastic will always bond together much better than cold plastic. It may happen that the filament needs to be printed at a higher temperature to create a strong bond. For example, if ABS plastic is extruded at 185 °C, the layers of the part will easily break apart. This is because ABS typically needs to be printed around 220-240 °C to create a strong bond between the layers.

The success of the Rapid prototyping via 3D printing is straightly related not only to the output of the plastic filament but also to its input. Most 3D printers use a small drive gear that grabs the filament and sandwiches it against another bearing. The drive gear has sharp teeth that allow it to bite into the filament and push it forward or backward, depending on which direction the drive gear spins. The one of the most important component of the 3D printer is the extruder that can be clogged as mentioned above.

Figure 4. Example of layer separation.

The 3D printer must melt and extrude many kilograms of plastic over its lifetime. All of this plastic must exit the extruder through a tiny hole that is only as big as a single grain of sand. It may happen that jams or clogs are usually due to something inside the nozzle that is blocking the plastic from freely extruding. Figure 5 shows a clogged extruder. To solve this problem heating the extruder and manually pulling the filament out. If the process efficiency during printing is maintained, Rapid prototyping can be used as a satisfactory method for a feasibility check of a mechanism design.

The 3D Printing procedure can be used to check:

- Shape design;
- Joint design reliability;
- Assembly coherence and feasibility.

Shape design is a very important step during prototyping. Each shape has a different behavior depending on the field of use. With 3D printing it is possible to check if the design requirements are fulfilled. Furthermore, its stiffness can be tested and some modifications can be elaborated to improve the characteristics of the prototype. During the design of the prototype it is difficult to check if the desired joints will move as expected. Manufacture them may help to check their reliability and their behavior and possible undesired friction. Furthermore, this last step is useful to check if the assembly is feasible and its coherence. Assembling the prototype will help to have new ideas to improve its performance realizing its real behavior. All these details in combination with commercial components have been taken into account to build a mechanical structure for the LARMbot humanoid prototype.

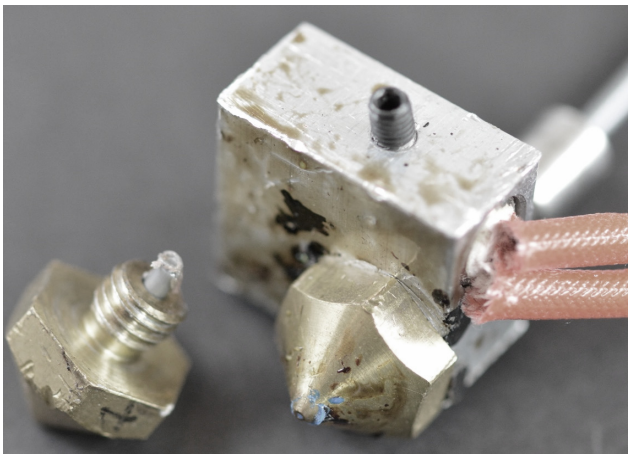

Figure 5. Example of clogged extruder.

4 A CASE STUDY: LARMBOT

The aim of the proposed novel humanoid is to mimic human anatomy and performance using mainly parallel architectures due to tjeir characteristics that permit a proper stiffness, payload capability and smoothness in movements. For a first configuration of the Humanoid robot the LARMbot in Cassino the CAUTO humanoid torso design has been assembled. The human-like behavior and shape of CAUTO (CAssino hUmanoid TOrso) [16] and its configurations had been an inspiration for the design and construction of a new humanoid. CAUTO is a hybrid cable-driven structure. The structure of the proposed humanoid torso for robots consists of 4 discs that replicate the function of the vertebrae in the human spine. The vertebrae are interconnected with each other by means of flexible couplings that behave as spherical joints allowing the rotation θ, Φ, and ψ around X-axis, Y-axis and Z-axis. The trunk is fixed on the spine through a vertebral disc. The spine is also connected to the abdomen using another vertebral disc. The pelvis is connected to the abdomen and houses 5 actuators 4 of which allows the 3 d.o.f.s of the humanoid spine. Four cables are fixed to the platform through the trunk, they pass through the holes of the other vertebral discs reaching the cables are pulled by the actuators. Moving the actuators antagonistically, the humanoid spine can bend right, left, forward and backward. When a cable is pulled, the corresponding is released. In addition, a circular motion can be performed thanks to the combination of the two above-mentioned movements.

LARM tripod Locomotor is a biped locomotor based on parallel leg mechanisms, [17]. The biped locomotor consists of two 3-DOF leg mechanisms and a waist. Two leg mechanisms are installed on the waist, and between the waist and feet there are two tripod mechanisms of six identical prismatic pairs with U-joints at each end.

Legged locomotion has a number of advantages as compared with conventional wheeled and crawler-type locomotion, such as higher mobility, better obstacle overcoming ability, active suspension and so on, especially when it operates in rough or unconstructed environment.

Table I - Specification parameters of the 3D Printer Creator, [18]

Extruder Model	*Printing Material*	*Software*	*Input File Format*	*Compatibility*
Dual-extruder	ABS&PLA 1.75-1.8 mm	Relicator G	STL/X3G	Linux, Mac and Windows
Machine Dimension	*Build Size*	*Print Precision*	*Positioning Precision*	
320× 467×381 mm	225× 145×150 mm	0.1-0.2 mm	0.0025 mm on Z axis; 0.011 mm on XY axes	
Flow Velocity	*Layer Thickness*	*Extruder Temperature*	*Heated Build Platform Temperatur*	
Approx. 24 cc/hr	0.1-0.5 mm	Maximum 230 ºC	Maximum 120 ºC	

The above prototypes have been built starting from a 3D model has been elaborated in SolidWorks® environment and the corresponding 3D prototype has been built by printing all the components and assembling them with commercial components. The 3D printer used in this case is FlashForge Creator [18], whose specification parameters are listed in Table I. Based on the built 3D model, the corresponding STL format file of each component can be directly generated in SolidWorks® environment.

By using the required RP program, Replicator G, and considering machine parameters like temperature, build size, printing precision, and printing speed, the proper G-code can be generated and then transferred to the 3D printer. G-Code is the name for the most widely used numerical control programming language; it is defined by instructions on where to move, how fast to move, and along which path to move. To allow the printer to print offline disconnecting it from the computer the G-code has been converted to X3g format and transferred to the SD Card of the printer. X3g is a binary file that the machine reads, and which contains all of the instructions for printing.

The interior of the pieces was filled with a rhomboidal grid with an infill of 80%, an infill perimeter overlap ratio of 0.3 and an infill solidity of 0.1. During parameter setting in Replicator G, the first two factors that should be considered are the build size of the 3D printer and the temperatures of extruder and build platform. In this case, each component is scaled down to 0.25 value by comparing with the original size of designed CAD model, and the temperatures of extruder and build platform are set as 208 °C and 63 °C, respectively as PLA has been chosen as printing material for the chest and the pelvis, while ABS for the spine and the locomotor setting the extruder and the platform respectively to 245 °C and 110 °C. Travel feed rate has been set to 55 mm/s and flow rate has been set equal to 40 mm/s.

Before choosing the final material of each part and the above parameters some preliminary prototype have been manufactured and tested with several printing configurations to improve the performances of the humanoid structure.

The key-parts of the novel torso CAUTO are the chest where pulling forces coming from the servomotors act and the humanoid spine that will transmit the motion though all the structure. A shape design check has been carried out starting from the chest. The first version of the torso have been built in 4 different shells assembled together using ABS plastic. Figure 6 shows the results of the printing. Figure 6a shows a torso shell part with its support structure. Figure 6b shows the defective part.

Layer separation due to an incorrect shape design can be noticed, this will affect the stiffness of the prototype under pulling forces. Thus, the structure has been improved going through a full redesign of the part. The novel chest has been designed using only one part to improve the stiffness and the inside of the structure have been filled with material. Figure 7 shows the new printed structure.

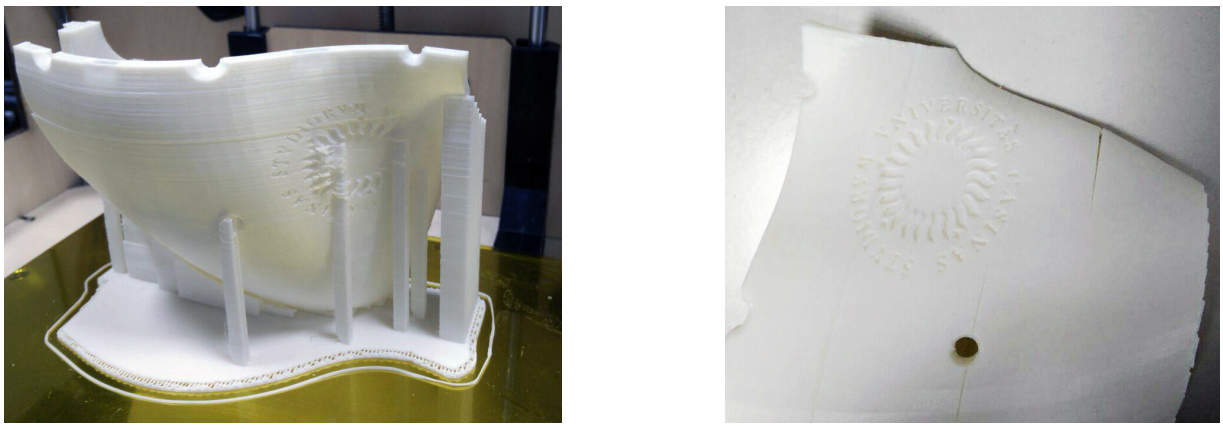

a) b)

Figure 6. CAUTO preliminary Chest Test: a) Printed chest shell part with support material, b) Printed chest shell part layer separation issue.

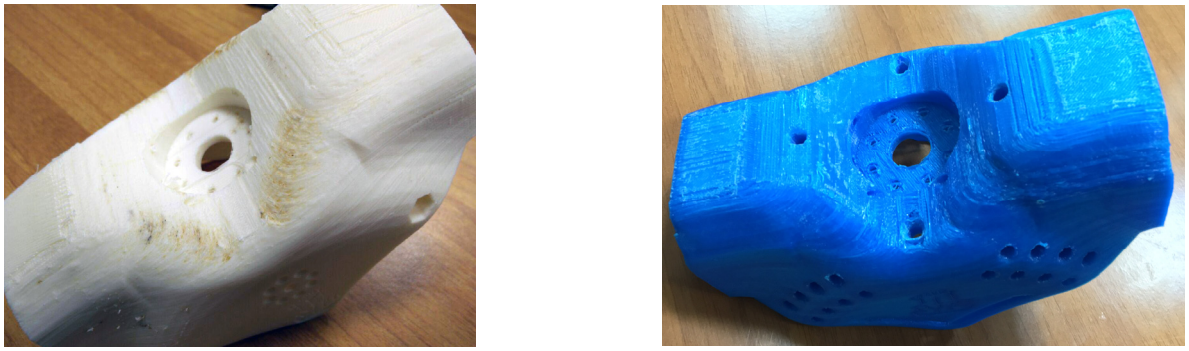

a) b)

Figure 7 CAUTO preliminary Chest Test: a) Printed chest using ABS with overheating issue, b) Printed chest using PLA.

The first attempt is shown in Figure 7a. The high temperature and the long time needed for the printer have produced an overheating issue. This can be seen in the upper part of the chest. Figure 7b shows another attemp, the material have been changed to PLA avoiding overheatig since the PLA needs lower printing temperature. Furthermore, PLA reacts to compression forces better then ABS. The second key-part of CAUTO is the spine so a joint design reliability and an assembly coherence and feasibility check have been worked out. Figure 8 shows the spine preliminary test layout. The 4 vertebrae have been printed in ABS and connected between each other using commercial multi-beam aluminium multi-helix flexible beam coupling. Four servo-motors have been stored on the base platform and hve been connected to the upper platform using nylon cables. The joint design reliability has been checked by controlling the servo-motor using Arduino, by presenting a satisfactory motion behavior assembly coherence. Considering the locomotor, several attempts for joint repeatability and assembly coherence have been made to improve its behavior and check its stiffness. These tests are fundamental since in the design requirements the locomotor is the part that will afford the major payload.

Printing parts with orientation based on the Z axis of the 3D printer has been identified as a key factor that affects printing quality. Generally, it is recommended to choose printing orientation as based on the principle that a relative large contact area provides more support material on the build platform. However, when there is coaxiality requirement of the components during the assembly, the axial direction should be considered as the printing orientation. For instance, each prismatic pair in this case consists of an upper tube part, a lower tube part, a ring connector and the rod part, as shown in Figure 9, where the tube part is divided into two parts by considering the verticality along axial direction as well as convenient assembly with the rod part. In order to choose the proper printing orientation, the lower tube part has been printed in two directions, as show in Figure 10. It can be noticed that the print precision and the stiffness of the tube along the axial is much higher than the other one along the radial direction.

When all the components are printed, the next step is to polish and assemble them. In order to achieve the aim of simple polishing and convenient assembly, the supporting material is planned as little as possible during the parameter setting, and the size of each pin is designed with 0.2 mm less than the corresponding hole by considering the print precision. Once all the parts have been ready and adjusted they have been assembled.

The preliminary prototype satisfactory fulfills the requirements so that the final one have been built. ABS has been chosen as the material for the final version for its characteristics to better absorb the impact forces compared to PLA. Having found suitable parameters, the final version of the prototypes has been manufactured.

Figure 11a shows the CAD Design of CAUTO and Figure 11b shows the production of the prototype using Rapid prototyping technology via 3D Printing.

Figure 11a shows the CAD Design of LARM tripod Locomotor and Figure 12b shows the 3D printed prototype of the locomotor. Analyzing the figures, it can be appreciated how the manufactured prototype satisfactory reproduce the CAD Design.

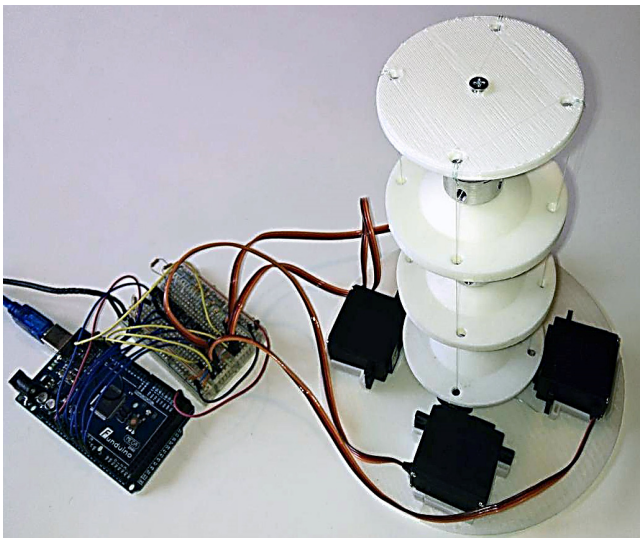

Figure 8 CAUTO spine preliminary test layout.

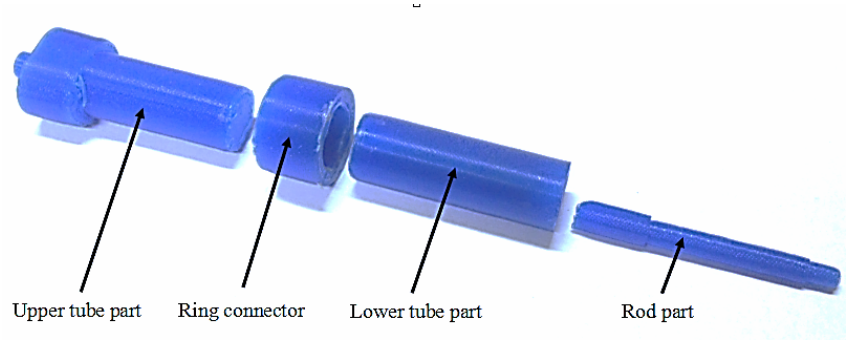

Figure 9 A preliminary printed prismatic pair for the LARM tripod Locomotor.

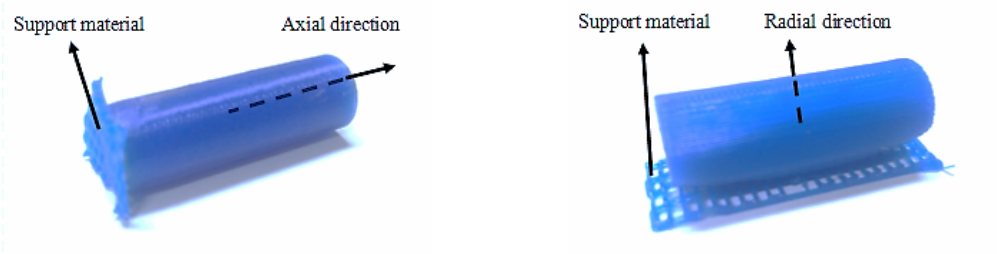

a) b)

Figure 10 A preliminary printed tube part of a prismatic pair when printed: a) axial direction; b) radial direction.

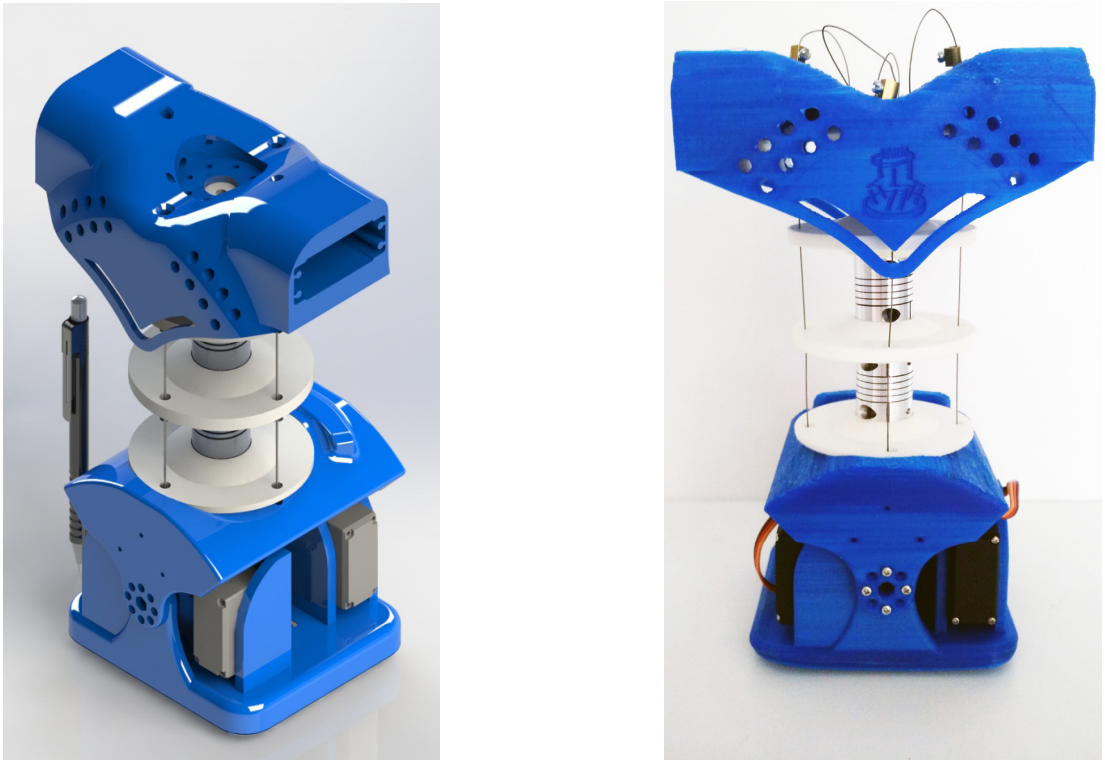

a) b)

Figure 11 CAUTO Prototype: a) CAD Design, b) 3D printed prototype.

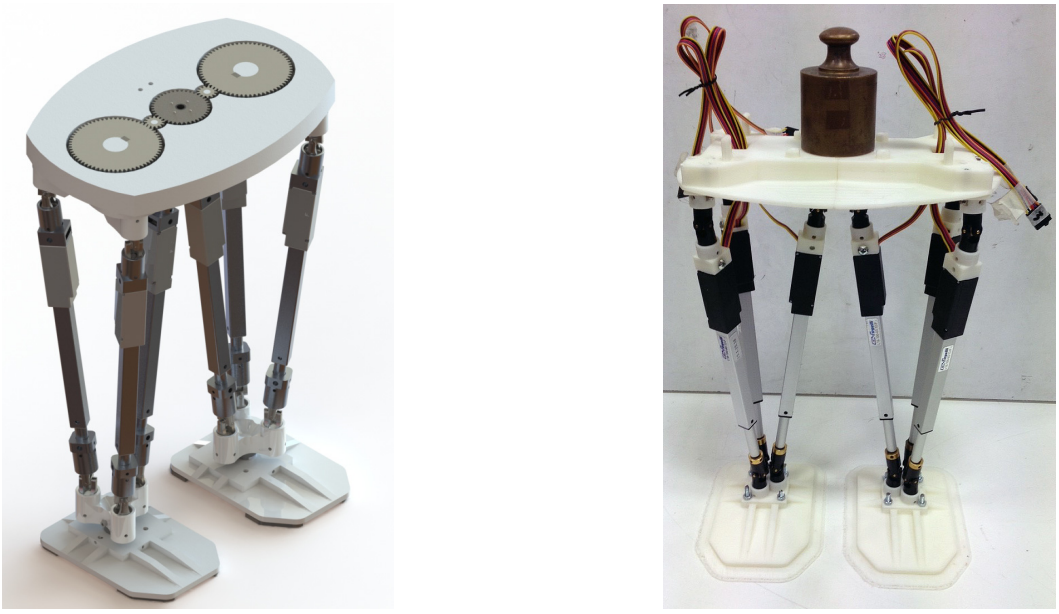

a) b)

Figure 12 LARM tripod Locomotor: a) CAD Design, b) 3D printed prototype.

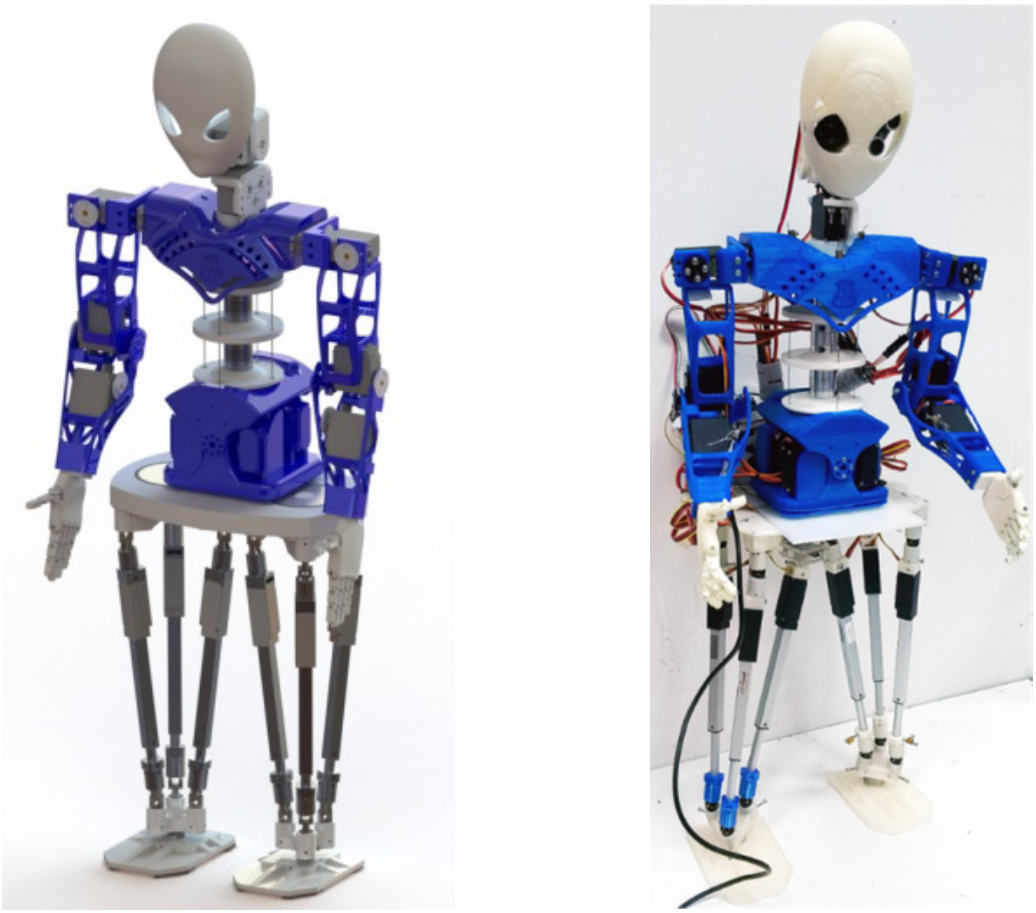

a) b)

Figure 13 LARMbot humanoid: a) CAD Design, b) 3D printed prototype.

The final assembly of the humanoid is shown in Figure 13. Figure 13a shows a CAD Design of the LARMbot, while Figure 13b shows the Final assembled prototype. This robot can be used in social fields helping people in daily operation or in industries to do dangerous tasks and among other applications. It is obstacle avoidance feature and Wi-Fi monitoring can be used to implement a software for remote operations.

5 CONCLUSIONS

In this paper 3D printing is recognized as a useful means in a design process with rapid prototyping of robot mechanisms through a procedure that permits a feasibility check of design solutions since early stages of robot developments. Specific experiences at LARM are presented as related to ongoing development of CAUTO and LARM tripod Locomotor. Finally, LARMbot humanoid is presented as an assembly of the two prototypes to show a practical convenience and soundness of using the proposed procedure of 3D printing prototyping for specific designs of mechanisms in humanoid robots.

REFERENCES

[1] Amon C.H., Beuth J.L., Weiss L.E., Merz R., Prinz, F.B., Shape Deposition Manufacturing With Microcasting: Processing, Thermal and Mechanical Issues. *Journal of Manufacturing Science and Engineering*, Vol. 120, No. 3, 2014.

[2] Beck J.E., Fritz B., Siewiorek D., Weiss L., Manufacturing Mechatronics Using Thermal Spray Shape Deposition. *Proceedings of the Solid Freeform Fabrication Symposium*, pp. 272-9, 1992.

[3] Ceccarelli M., Experimental Mechanics for Mechanism Design: An Illustrated Summary. *EUROMECH Colloquium 515 Advanced Applications and Perspectives of Multibody System Dynamics*, Blagoevgrad, paper EUM515-L1, 2010.

[4] Chua C.K.; Leong K.F., Lim C.S., *Rapid Prototyping*. World Scientific. pp. 124, 2003.

[5] Excell J., The rise of additive manufacturing. *The engineer, Retrieved*, 2013.

[6] Pham D.T., Dimov S.S., *Rapid manufacturing*. Springer-Verlag, London, pp. 6, 2001.

[7] Sherman L.M., 3D Printers Lead Growth of Rapid Prototyping. *Plastics Technology*, 2004.

[8] Wittbrodt B.T., Glover A.G., Laureto J., Anzalone G.C., Oppliger D., Irwin J.L., Pearce J.M., Life-cycle economic analysis of distributed manufacturing with open-source 3-D printers. *Mechatronics*, Vol. 23, No. 6, p. 713, 2013.

[9] Fumo M., Noorani R., Development of an Expert System for the Selection of Rapid Prototyping and 3D Printing Systems, In International Conference on Computer Science Education Innovation & Technology (CSEIT). *Proceedings, Global Science and Technology Forum*, p.14, 2015.

[10] Prinz F. B, Merz R., Weiss L., Ikawa N., Building Parts You Could Not Build Before, Proceedings of the 8th International Conference on Production Engineering., London, Chapman & Hall, pp. 40-44, 1997.

[11] Matias E., Rao B., 3D printing: On its historical evolution and the implications for business. *In Management of Engineering and Technology (PICMET)*, Portland International Conference IEEE, pp. 551-558, 2015.

[12] Freedman D.H., *Layer By Layer, Technology Review, 115.1*. Academic Search Premier, pp. 50-53, 2012.

[13] El-Sayed, M., El-Sayed, J., Additive Manufacturing Transition from Rapid Prototyping to Mass Production (No. 2016-01-0327). *SAE Technical Paper*, 2016.

[14] Rayna T. Striukova, L., From rapid prototyping to home fabrication: How 3D printing is changing business model innovation. *Technological Forecasting and Social Change*, Vol. 102, pp. 214-224, 2016.

[15] Chia H.N., Wu B.M., Recent advances in 3D printing of biomaterials. *Journal of biological engineering*, Vol. 9, No. 1, 2015.

[16] Cafolla D. Ceccarelli M., Design and simulation of a cable-driven vertebra-based humanoid torso, *International Journal of Humanoid Robotics*, 2015 (in printing).

[17] Wang M.F., Ceccarelli M., Design and Simulation of Walking Operation of a Cassino Biped Locomotor. *New Trend in Mechanism and Machine Science*. Vol. 24, pp. 613-621, 2015.

[18] Flashforge 3D Printer, 3D Printer Creator, http://www.ff3dp.com/#!creator/c1txh, 2016.

ISSN 1590-8844
International Journal of Mechanics and Control, Vol. 17, No. 01, 2016

BIOLOGICALLY INSPIRED DESIGN AND HYDRODYNAMIC ANALYSIS OF A REMOTELY OPERATED VEHICLE FOR RIVER UNDERWATER TASKS

Ilija Stevanović* Aleksandar Ćosić* Aleksandar Rodić* Boško Rašuo**

* University of Belgrade, Mihailo Pupin Institute
** University of Belgrade, Faculty of Mechanical Engineering

ABSTRACT

In this paper is presented comparison of two designs of the mechanical structure of river submarine robot dedicated to delicate and risky underwater tasks. The main factors that determine mechanical design of robots are hydrodynamic drags and good mobility in river flow. Robot body design of new robot is inspired by morphological characteristics fast-swimming animals by streamlining the shape of the body by optimising the fineness ratio as the natural geometry proportion that commonly appears with biological systems. Designed mechanical structure is evaluated by corresponding fluid dynamics simulation tests. In the paper is presented the simulation of underwater robots based on mathematical model of real submarine and simple PID controller. Trajectory tracking performance is presented under assumption that the disturbance occurs due to river flow.

Keywords: ROV, UUV, streamlining, PID controller, bionics

1 INTRODUCTION

The subject of research and development presented in this paper regards to prototype development of a remotely operated vehicle (ROV), i.e. unmanned underwater vehicle (UUV) for underwater river tasks. That regards to development of a river underwater robot-grebe intended for remotely operated underwater search, underwater camera shooting, monitoring and inspection of objects and infrastructure installation in the water, rescue missions, ecologic tasks of cleaning and waste disposal removing and sampling of river bottom material as well as assistance in extraction submerged objects from river. The prototype of the underwater robot-explorer is intended for use on big and smooth rivers (not trouble highland waters). That are mainly lowland rivers with large water potential (water flow), whose streaming speed neither overcomes 8 km/h nor depth 20 m. The ROV must be energy efficient and easy to control.

Contact author: Ilija Stevanović[1], Boško Rašuo[2]

[1]Volgina 15, 11060 Belgrade, Serbia.
[2]Kraljice Marije 16, 11060 Belgrade, Serbia.

Energy efficiency is achieved with design of body inspired by nature. Simplified control is achieved with proper position of thrusters for decoupled motion.
The current version of designed ROV is designed based on first version with some improvements.

2 ANALYSIS OF BODY MORPHOLOGY OF FAST-SWIMMING ANIMALS

Fast-swimming animals display morphological characteristics associated with enhanced thrust production, high propulsive efficiency, and reduced drag.
For cetaceans, these morphological characteristics include a streamlined body, tight skin, a strongly compressed caudal peduncle, and high aspect ratio flukes and flippers with sweepback. Drag is minimized primarily by streamlining the shape of the body and appendages (i.e., flukes, flippers, dorsal fin). Streamlining minimizes drag by reducing the magnitude of the pressure gradient over the body and allowing water to flow over the surface without separation.
The streamlined profile is characterized by a fusiform shape emulating an elongate teardrop with a rounded leading edge extending to a maximum thickness and a slowly tapering tail. This fusiform shape is displayed by all cetaceans (Figure 1) [1].

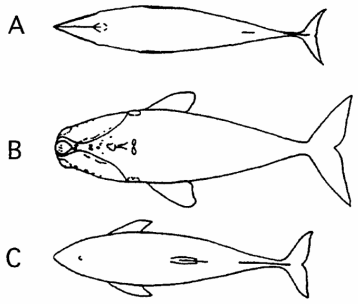

Figure 1 Body shape variation for:
a balaenopterid mysticete (A: *Balaenoptera acutorostrata),*
a balaenid mysticete (B: *Eubalaena glacialis),*
an odontocete (C: *Phocoena phocoena).*

2.1 STREAMLINING – REDUCING DRAG

Drag is minimized primarily by streamlining the shape of the body and appendages (i.e., flukes, flippers, dorsal fin). Streamlining minimizes drag by reducing the magnitude of the pressure gradient over the body and allowing water to flow over the surface without separation. The streamlined profile is characterized by a fusiform shape emulating an elongate teardrop with a rounded leading edge extending to a maximum thickness and a slowly tapering tail. This fusiform shape is displayed by all cetaceans (Figure 1), but is not axisymmetrical, as the caudal peduncle exhibits extreme narrow-necking in the plane of oscillation. Necking in the caudal region reduces virtual mass effects and unstable movements.

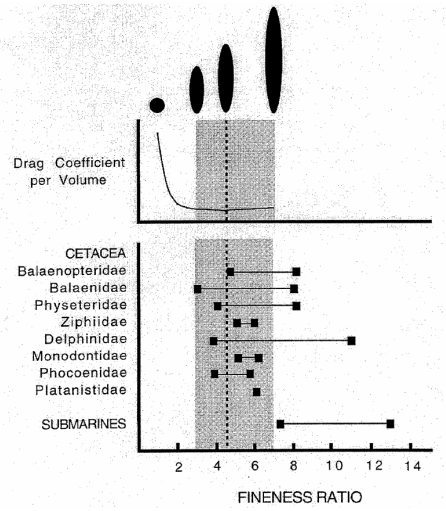

Figure 2. Fineness ratio (FR) in relation to drag per volume (adapted from von Mises, 1945) and FR for cetacean families (adapted from Fish, 1993a). Comparisons are made with modern submarine hulls. Silhouettes show the difference in shape in reference to FR from a circular shape (FR= 1) to an elongate form (FR = 7). The dashed line indicates the optimal FR of 4.5 whereby a body has the lowest drag for the maximum volume. The shaded area represents the FR range (3 through 7) in which drag increases by 10% above the minimum value. [1]

An indicator of the degree of streamlining is the fineness ratio *(FR* = body length/maximum diameter). The *FR* value of 4.5 gives the least drag and surface area for the maximum volume (Figure 2) although only a 10% increase in drag is realized in the *FR* range of 3 through 7. Since Gray (1936), there has been an active search for special mechanisms to reduce drag in dolphins. Despite the various mechanisms hypothesized, the body shape is the major determinant of drag (Figure 2). A stream- lined body with *FR* = 4.5 will have a 75% reduction in pressure drag coefficient from that for a sphere of equal volume.

The *FR* range for the various cetacean families spans a significant portion of optimal range for reduced drag (Figure 2). The greatest range of *FR* (4 through 11) is found in the cetacean family Delphinidae from Dall's porpoise *(Phocoenoides dalli)* to the northern right whale dolphin *(Lissodelphis borealis)*. The exaggerated length of the latter species has given it the name "snake porpoise". Despite the difference in body design as expressed by *FR,* these two species are considered among the fastest dolphins, with maximum speeds exceeding 8 m/s [1].

3 DESIGN OF ROV's

Two ROV's are designed and analysed in terms of hydrodynamics and control. The ROV's has a task to carry multi-segment, hyper-redundant flexible robot-arm with robot-gripper (Figure 3), different types of sensors (sonars, GPS, etc.), cameras and lights (Figure 5 b). Robot is requested to have fine mobility and manoeuvrability in the water to represents a dexterous underwater device capable to accomplish different underwater tasks. That assumes the robot can move in all directions: up and down, forward and backward, right and left, and twisting about the vertical axis of symmetry.

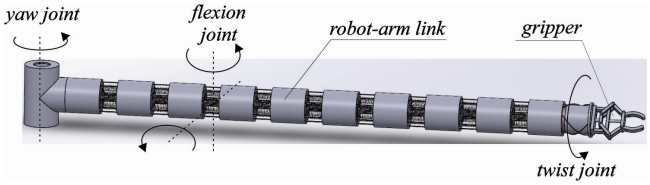

Figure 3 Multi-segment, hyper-redundant flexible robot-arm and robot-gripper

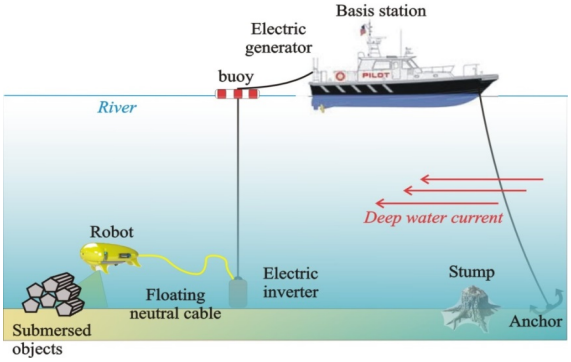

Figure 4 Principle of operation of the ROV – underwater robot.

Principe of operation of ROV – underwater robots are shown on (Figure 4). Robot is permanently in physical contact (connected) with basis station (Figure 4) due to the safety reasons (to prevent loosing), power supply and permanent communication keeping.

3.1 THE ROV 1

For the first ROV design are used streamline fusiform shape with fineness ratio equal to golden ratio (1.61803399) (745x1870x1200mm) and six thrusters.
Thrusters T1-T3 for forward motion and T4 - T6 for up and down motion. No thrusters for lateral motion in direction of X axe (Figure 4), in detail described in [3].

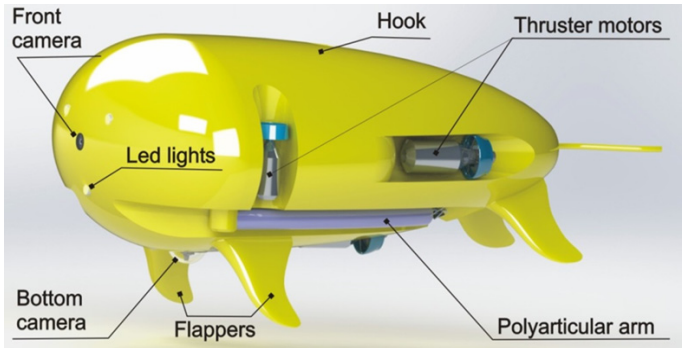

a)

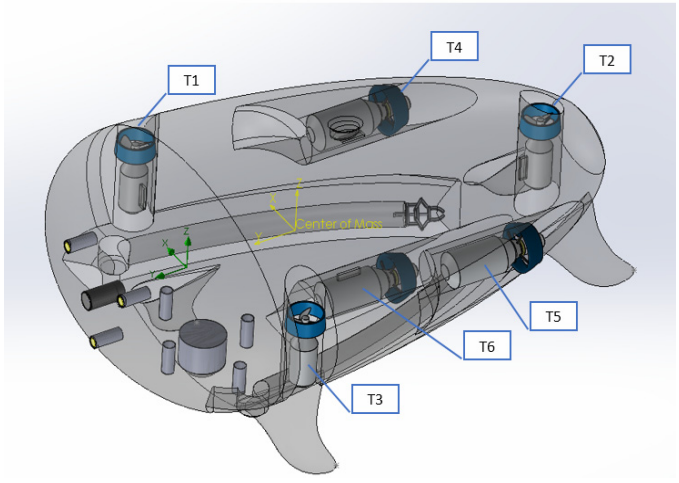

b)

Figure 5 Underwater robot with its components: a) side view; b) x-ray view.

3.2 THE ROV 2

The ROV 2 is designed after analysis of ROV 1. It has all the same requests as the ROV 1. ROV 1 had to be improved in terms of hydrodynamics, better mobility, and manoeuvrability in the water stream.

3.2.1 Streamlining ROV 2

For design of the body of the ROV 2 is used the fineness ratio (FR = body length/maximum diameter) of about 4.5 (240x1400x770 mm).

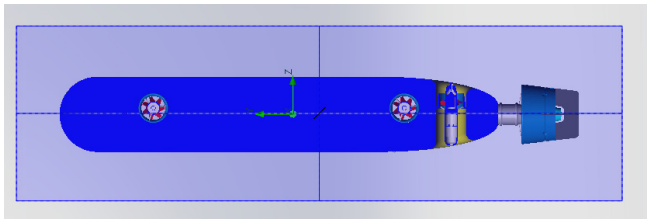

Figure 6 Cross section of ROV 2.

3.2.2 Manoeuvrability ROV 2

In section 6 simulations showed that ROV 1 cannot track spiral trajectory in water stream. Obviously it needs thrusters for lateral motion. However, for stationary water there is no problem for lacking of those thrusters. As a result of all this described ROV 2 is designed. It has 7 thrusters. T1-T3 for up-down motion, T4-T5 for forward-revers and T6-T7 lateral motion (Figure 7).

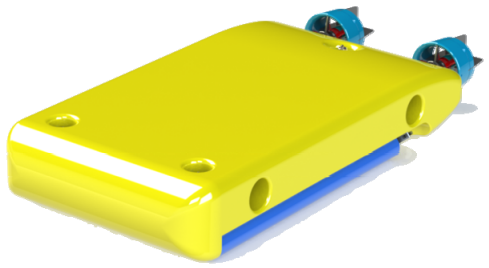

a)

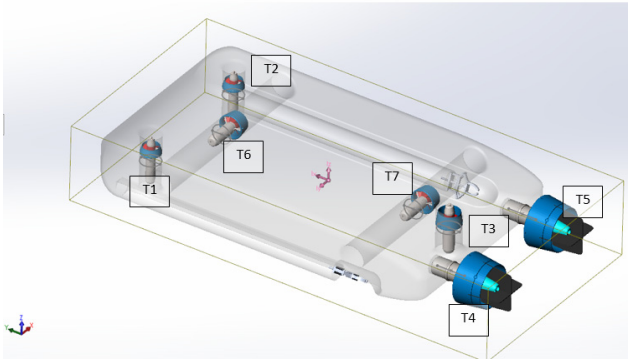

b)

Figure 7 ROV 2: a) side view; b) x-ray view.

The final shape and position of thrusters is logical and very similar as MARUM H-ROV [2]

4 HYDRODYNAMIC ANALYSIS OF ROV's

The hydro dynamically optimized underwater robot (Figure 8 a) and b) is tested up-on the drag forces by modelling in Solidworks. Solidworks Flow Simulation uses Computational Fluid Dynamics (CFD) analysis to enable simulation of fluid flow and to calculate fluid forces and understand the impact of a river stream on ROV performance.

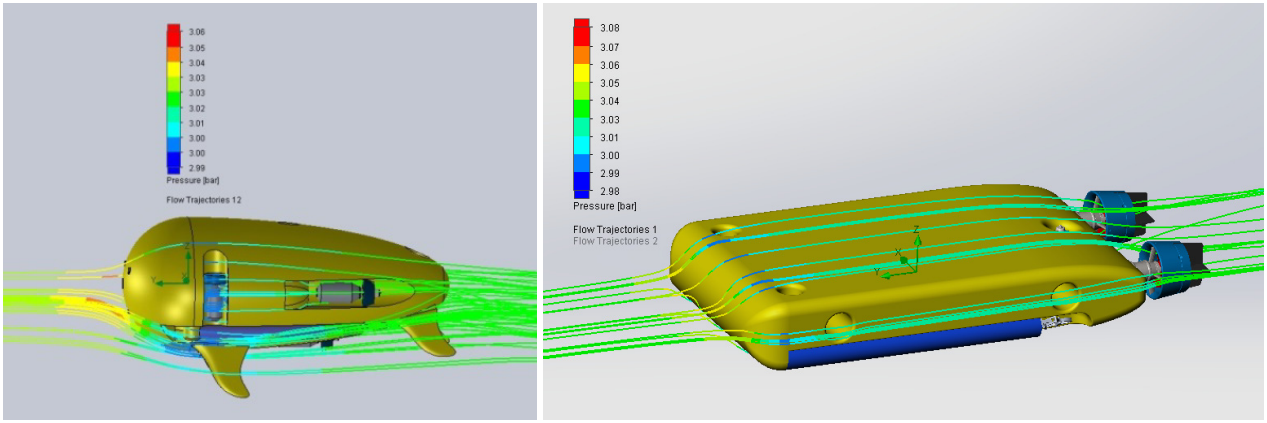

a) b)

Figure 8 Hydrodynamic analysis of the submarine body: a) ROV 1; b) ROV 2.

Tightly integrated with Solidworks CAD, CFD analysis uses Solidworks Simulation flow analysis and reduces the need for costly prototypes, eliminating rework and delays, and saves time and development costs. CFD is a branch of fluid mechanics that uses numerical analysis and algorithms to solve and analyse problems that involve fluid flows. Computers are used to perform the calculations required to simulate the interaction of liquids and gases with surfaces defined by boundary conditions.

The results of this simulation experiment and corresponding streamlines for ROV 1 and ROV 2 are presented in Figure 8 (case when the streaming speed is 10 km/h and the robot keeps position). The so obtained simulation results are systematized (as reported in table I and table II) and based on them thrusters are selected. Than it is analysed again and those results are transferred to Matlab simulation.

5 MODELLING AND CONTROL OF ROV

5.1 DYNAMIC MODEL OF ROV

Mathematical model of the designed underwater vehicle is based on the rigid body kinematics and dynamics. Derivation of the ROV's dynamic model is based on methodology taken from the modelling of serial robotic manipulators, what is comprehensively treated in the [4-6].

In this particular case, ROV can be considered as robot with 6 degrees of freedom (DOFs), i.e. 3 DOFs are prismatic (translation in *z*, *x*, and *y* direction, respectively), while the other 3 DOFs are rotational (yaw, roll and pitch rotations, respectively). Therefore, the robot can be represented by the kinematic chain, depicted in Fig. 9, where the prismatic DOFs are represented by cuboidal elements, whereas rotational DOFs are represented by cylindrical elements.

Table I - ROV 1 hydrodynamic drags obtained by simulation in Solid Works

		Resistance force during the robot movement [N]					
Speed of streaming [km/h]		1	2	3	5	7,5	10
Robot movement direction	Forward	8,355808128	-	75,90494183	210,4932276	461,4344195	804,9717383
	Backward	9,297515187	-	87,22105725	241,1581502	544,6749591	970,8956312
	Laterally	23,5458368	-	213,0559673	-	-	-
	Up	49,29869231	197,0768946	-	-	-	-
	Down	39,22048346	212,0448867	-	-	-	-

Table II - ROV 2 hydrodynamic drags obtained by simulation in Solid Works

		Resistance force during robot movement [N]					
Speed of streaming [km/h]		1	2	3	5	7,5	10
Robot movement direction	Forward	1,9	-	17,4	48,8	111,2	197,4
	Backward	2,6	-	23,9	66,4	150,8	268,0
	Laterally	8,8	-	79,3	-	-	-
	Up	31,1	124,4	-	-	-	-
	Down	39,9	159,7	-	-	-	-

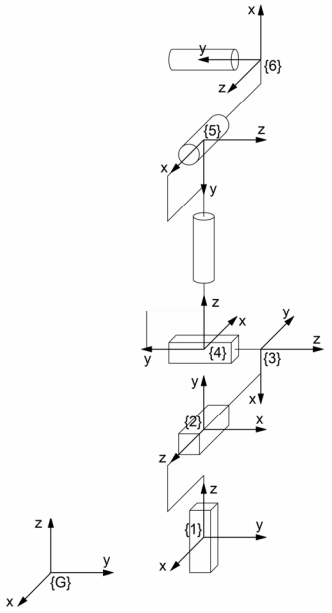

Figure 9 ROV DOFs represented by kinematic chain.

Homogeneous transformations between link frames can be further represented by Denavit-Hartenberg (DH) notation, given in Table III. The global reference frame is static (denoted by {G}), and one frame is assigned to every link according to DH notation. In total, there are 6 frames attached to the links, since there are 6 DOFs, and they are shown in Fig. 9. The pose of the robot corresponds to the pose of the last link frame. It can be noticed from the Table III that the kinematic chain is represented by zero length links, meaning that all the joints lies at a single point, which is the ROV's centre of mass (COM).

Table III – DH parameters

Link no.	DH parameters			
	a	α	d	θ
1	0	$+\pi/2$	q_1	$+\pi/2$
2	0	$-\pi/2$	q_2	$-\pi/2$
3	0	$-\pi/2$	q_3	$+\pi/2$
4	0	$+\pi/2$	0	$q_4-\pi/2$
5	0	$+\pi/2$	0	$q_5+\pi/2$
6	0	$+\pi/2$	0	$q_6+\pi/2$

The whole robot dynamics will be assigned to the last link. Moreover, if the joint coordinates are known, pose of the ROV can be easily determined by forward kinematics [4-6]. Also, if the joint velocities are known, velocity of the ROV can be determined using Jacobian matrix, given by Eq. (1).

$$v = J(q)\dot{q} \tag{1}$$

wherein q denotes vector of generalized coordinates, $\dot{q}$ denotes vector of generalized velocities, v denotes ROV's spatial velocity vector, while *J(q)* stands for Jacobian matrix.

Derivation of the dynamic model follows Lagrangian formulation yielding to a model represented in standard form [7]:

$$M(q)\ddot{q} + C(q,\dot{q})\dot{q} + G(q) - J^T(q)\left[B + W(\dot{q})\right] = \tau \tag{2}$$

wherein the following notation is used: $\ddot{q}$ - vector of generalized accelerations, $M(q)$ - inertial tensor, $C(q,\dot{q})$ - centrifugal and Coriolis matrix, $G(q)$ - gravitational term, $J(q)$ - Jacobian matrix, B - external force due to buoyancy and $W(\dot{q})$ - external force due to the viscous friction during the ROV motion through the fluid.

The Eq. (2) is well known in theory of robotic manipulators and it is comprehensively treated in [4-6]. Comparing the Eq. (2) to the equation of manipulator dynamics, it can be concluded that two external forces are presented, namely, upthrust force (buoyancy) and viscous friction as a result of vehicle motion in the fluid. Buoyancy represents force exerted by fluid and opposing the weight of the ROV submerged in the water. This force always acts in the vertical direction (global frame z direction) and it can be readily calculated using Archimedes' principle.

Unfortunately, it is not the case with the viscous friction, which is not easy to determine. The Eq. (2) denotes so-called inverse dynamics problem. Such a form stands for standardized formulation of robotic manipulators dynamics and it is comprehensively researched and developed.

Once the generalized forces are known, it is necessary to establish relation to the forces of the ROV's thrusters needed to achieve desired generalized forces vector. It can be easily accomplished by employing II Newton's law, therefore, sum of all forces exerted by thrusters must be equal to the force component of the generalized forces vector, and sum of all torques exerted by thrusters with respect to the ROV's COM must be equal to torque component of the generalized forces vector, that is:

$$\sum_i F_i = F_r, \sum_i r_i \times F_i = \tau_r \tag{3}$$

where terms F_i denote forces exerted by thrusters, F_r denotes force component of the generalized forces vector, while terms r_i denote radius vectors of thrusters with respect to ROV's COM and τ_r denotes torque component of the generalized forces vector. At the end, derived relation is linear and can be written in the matrix form:

$$\mathbf{A}\cdot\mathbf{F} = \boldsymbol{\tau}, \mathbf{F} = \begin{bmatrix} F_1 & \cdots & F_n \end{bmatrix}^T, \boldsymbol{\tau} = \begin{bmatrix} F_r \\ \tau_r \end{bmatrix} \tag{4}$$

where n denotes the total number of thrusters used for ROV actuation. Let us take a closer look at matrix **A**. In the first (ROV 1) case, the robot is not actuated along local x axis, and consequently *rank*(**A**)=5, yielding to underactuated system, since the first row of the matrix **A** contains all zeros. Therefore, due to nature of the actuating system, generalized force component along local x axis cannot be controlled and the robot is heavily affected by disturbances acting in that particular direction, which are always present in river flows. On the other hand, in the second design case (ROV 2), *rank*(**A**)=6, yielding to fully actuated system.

However, solving Eq. (4) in both design cases is not straight forward, since in the first design case we have 5 equations with 6 unknowns, while in the second design case we have 6 equations with 7 unknowns. Therefore, in both design cases, we can use the same solving technique. In both design cases, one unknown more provides additional degree of freedom which allows us to optimize control of thrusters with certain aim. The objective is to find the solution which minimizes energy consumption. Thus, the problem can be stated as minimization under linear constraint, that is:

$$\mathbf{F}^* = \arg\min_{\mathbf{F}} \|\mathbf{F}\|_W = \arg\min_{\mathbf{F}} \mathbf{F}^T W \mathbf{F}, \quad \text{constraint} : \mathbf{A}\cdot\mathbf{F} = \boldsymbol{\tau} \tag{5}$$

where W is diagonal weight matrix. Note that the minimization criterion is quadratic form with respect to $\mathbf{F}$, and the constraint is linear. Such a problem can be solved by using method of Lagrange multipliers. The first step involves creating Lagrangian L(F,λ) and solving system of generally nonlinear equations:

$$\mathrm{L}(\mathbf{F},\lambda) = \mathbf{F}^T W \mathbf{F} - \lambda(\mathbf{A}\cdot\mathbf{F} - \boldsymbol{\tau})$$
$$\frac{\partial \mathrm{L}(\mathbf{F},\lambda)}{\partial \mathbf{F}} = 0,\ \mathbf{A}\cdot\mathbf{F} = \boldsymbol{\tau} \tag{6}$$

The obtained solution minimizes weighted energy criterion, given by Eq. (5).

5.2 TRAJECTORY TRACKING CONTROLLER

In order to tackle trajectory tracking problem, simple decentralized proportional-integral-derivative (PID) controller has been designed. In order to control the pose of the underwater robots, various control laws can be introduced [7-8]. However, PID control is chosen due to its simplicity and wide variety of different applications in industry [9]. Moreover, if the model given by Eq. (2) is chosen, PD control with appropriately adjusted gains guarantee asymptotic stability of the closed loop system in the absence of viscous friction term. The basic block scheme of the closed loop control system is depicted in Fig. 10, where the following notation is adopted: K_p - proportional gain, K_d - differential gain, K_i - integral gain, q^* - desired joint coordinates, $\ddot{q}^*$ - desired joint accelerations, e - error vector and τ_c - control vector which represents generalized forces further transformed to the thruster forces by employing Eq. (6) and applied by the thruster motors.

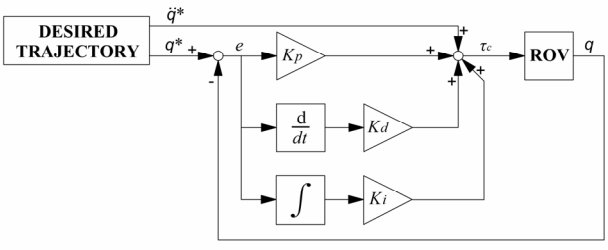

Figure 10 Block scheme of the closed loop control system.

Since the robot has 6 DOFs, PID controller has also 6 DOFs and the corresponding proportional, integral and differential gain matrices are 6x6 diagonal matrices. Therefore, control τ_c corresponds to the generalized forces vector, evaluated by the following expression:

$$\tau_c = \ddot{q}^* + K_p e + K_d \dot{e} + K_i \int e \cdot dt \tag{7}$$

Once the control is determined, the thruster forces can be easily obtained by employing Eq. (6).

As previously mentioned, for the ROV 1, gains corresponding to the generalized force component acting in the local x direction must be set to zero, since the robot is not actuated along that particular direction. This is not the case for the ROV 2, since the robot is fully actuated.

6 SIMULATION RESULTS

In this section, simulation results will be presented and compared for the ROVs 1 and 2. Simulation has been carried out in Mathworks MatLAB environment, using Robotics toolbox [5], [10]. In both cases, it is assumed that the ROV's motion has been carried out in the river, and the river flow course is constant with respect to the global frame of reference. It is further assumed that the speed of river flow is $0.42 m/s$ and directed at angle of 45° with respect to the x axis of the global reference frame. Modelling hydrodynamic drag is not trivial and it is conducted by the means of Dassault Systemes SolidWorks. Generally speaking, it is proportional to the squared speed of the vehicle, its cross sectional area and surrounding fluid density. It also depends on shape of the object and roughness of its surface. Trajectory tracking performance is assessed considering spiral desired trajectory, that is, ROV slowly dives following spiral trajectory, described by the following parametric equation:

$$x(t) = R_x \cos(\omega t + \phi_0) + x_0$$
$$y(t) = R_y \sin(\omega t + \phi_0) + y_0 \tag{8}$$
$$z(t) = ct + z_0$$

where $(R_x, R_y) = (5,4)m$ denotes the major and minor axes of the ellipse obtained by projecting spiral onto xy plane, $(x_0, y_0, z_0) = (0,0,0)$ denotes centre of the spiral in 3D space, $\omega = 0.0781 rad/s$ stands for angular velocity, whereas the $c = -0.02 m/s$ is the diving speed. Parameters are chosen such that the ROV's speed is approximately $0.5 m/s$. Eq. (8) defines only desired position of the ROV's COM in the 3D space, while the desired ROV's orientation is yet to be defined. However, careful examination of desired orientation is very important since the hydrodynamic drag is not equal in all directions during motion. Therefore, it is very important to determine desired orientation along trajectory in a way to decrease disturbance due to hydrodynamic drag, but bearing on mind that the ROV is designed in a way that it is the most hydrodynamic when it moves straight forward.

Taking that into account, we adopted that the y axis of the ROV's frame is tangent to the trajectory and that x axis lies in the xy plane of the global reference frame. Moreover, in order to assess tracking performance fairly, both ROVs start at the same initial point $X_0 = [5.5 \quad -0.5 \quad 0.2]^T \, m$ and the same initial orientation $\psi = [0 \quad 0 \quad 0]^T \, rad$ defining initial roll, pitch and yaw angles. Physical dimensions of the designed ROVs are given by Table IV, together with corresponding masses and volumes, and thruster limits. In both cases, PID tracking controllers are tuned manually, trying to make balance between trajectory tracking performance and disturbance rejection. In addition, diagonal weight matrices are chosen to be the same for ROV 1 and ROV 2 and equal to identity matrix, meaning that action of all the thrusters is equally penalized.

Table IV – ROVs physical parameters

parameter	ROV 1	ROV 2
mass	$88kg$	$58.3kg$
total volume	$0.768m^3$	$0.0589\ m^3$
dimensions (length x width x height)	$1.87x1.2x0.745m$	$1.4x0.77x0.24m$
number of thrusters	6	7
thruster limits	(25.5, 25.5, 25.5, 12.4, 12.4, 12.4)kg	(2.1, 2.1, 5.4, 25, 25, 10, 10) kg

6.1 TRACKING PERFORMANCE FOR ROV 1

Trajectory tracking performance for ROV 1 is given by Figs. 11-14. Fig. 11 shows tracking performance regarding x, y and z direction and roll (R), pitch (P) and yaw (Y) angles. Desired values are shown by dashed lines, whereas the achieved ones are shown by solid lines. Tracking errors along x, y and z axes and regarding roll (R), pitch (P) and yaw (Y) angles are presented in Fig. 12. Finally, thruster forces are given in Fig. 13, while the achieved trajectory in 3D space is shown in Fig. 14.

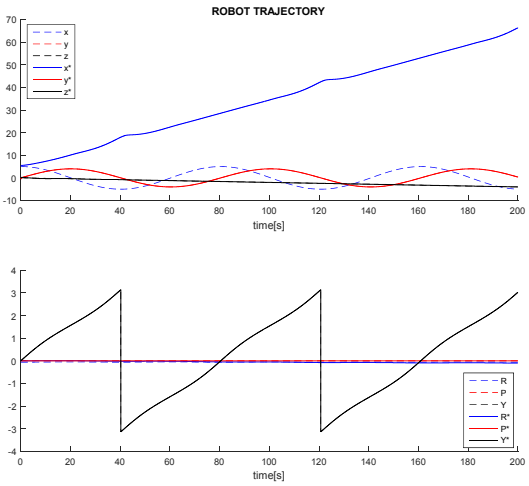

Figure 11 Trajectory tracking performance for ROV 1.

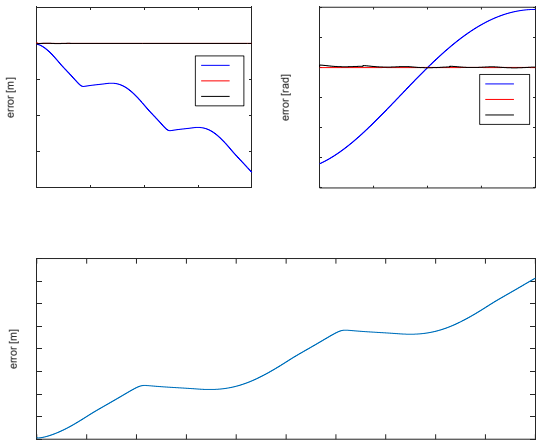

Figure 12 Tracking error for ROV 1.

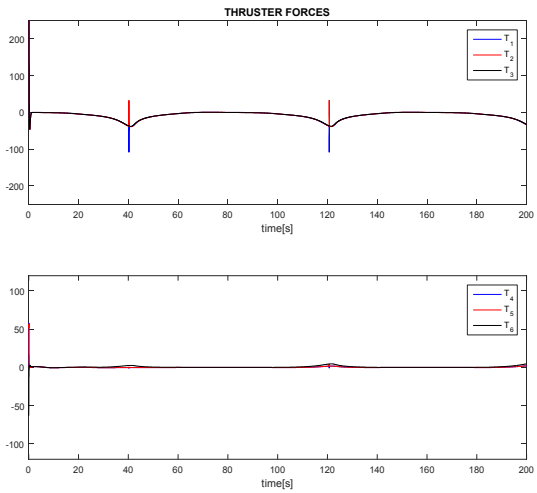

Figure 13 Thruster forces during tracking for ROV 1.

First of all, hydrodynamic drag can be considered as disturbance acting at the input of the system. If the vehicle is fully submerged, buoyancy is constant and known, and therefore, it is easy to compensate for it. Hence, control objective becomes ensuring trajectory tracking, together with disturbance rejection due to hydrodynamic drag.

It is evident that the error along x direction cannot be controlled if the disturbance is presented, since the ROV lacks actuation along that direction. Therefore, motion along y and z direction, and roll, pitch and yaw angles is stabilized, since those errors are kept small. However, error along x axis diverge, meaning that river carries ROV away from the desired position considering x direction. This statement can be clearly seen in Fig. 14. At the end, thruster forces are kept inside their limits, meaning that the motors are chosen appropriately. Peak in the control signal happens whenever ROV's yaw coordinate switches from 2π to 0 rad, and it is additionally increased by derivative action.

6.2 TRACKING PERFORMANCE FOR ROV 2

Trajectory tracking performance for ROV 2 is given by Figs. 15-18, which follow the same order and notation compared to the results for ROV 2. It is immediately noticed from Figs. 12 and 16, that the tracking performance is much better due to side thrusters which provide full actuation of the system. In the case of ROV 1 error diverge, oppositely to ROV 2 case where the error gradually vanishes as the motion evolves. Thruster forces remains inside their limits, therefore, the actuators are appropriately chosen. At the end, we conclude that the ROV 2 is better suited for tracking purposes, providing accurate trajectory tracking and disturbance rejection. However, ROV 1 can be used in calm waters, where the disturbance due to water motion is not considerable.

7 HYDRODYNAMIC ANALYSIS OF ROV's

Designing underwater river ROV by using analysis of bodies of fast-swimming animals and Solidworks CFD in cooperation of Matlab simulation of motion dynamics are resulted with improved performances of ROV 2. Behaviour of both ROVs has been examined in the simulations.

The performance of proposed designs is evaluated in trajectory tracking applications. ROV 2 outperforms ROV 1 in the river environments, where considerable disturbances occur.

Due to full actuation, ROV 2 is able to accurately track assigned trajectory and reject disturbances due to water flow. Oppositely, ROV 1 is underactuated system and tracking error diverges when significant disturbances occur along non-actuated DOF. Still, it is suitable for calm waters where the disturbances are not considerable.

ACKNOWLEDGEMENT

This work is supported by Ministry of Science Ministry of Education, Science and Technology Development of the Republic of Serbia under the grant TR-35003.

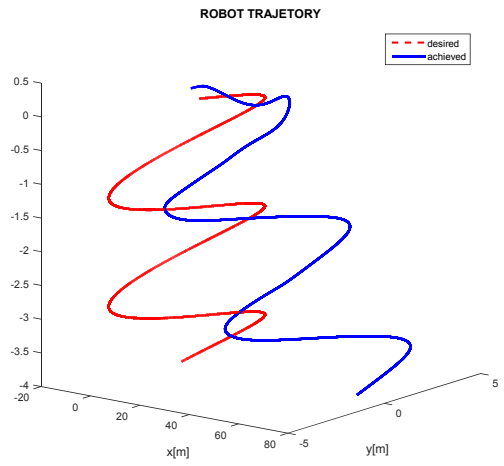

Figure 14 Trajectory achieved by ROV 1.

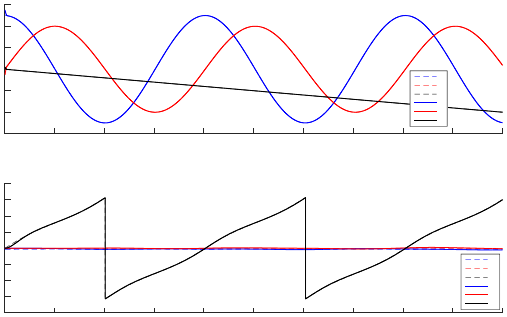

Figure 15 Trajectory tracking performance for ROV 2.

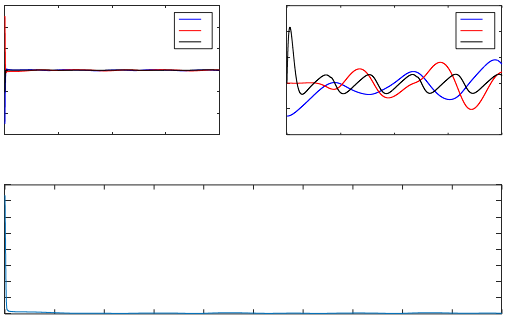

Figure 16 Tracking error for ROV 2.

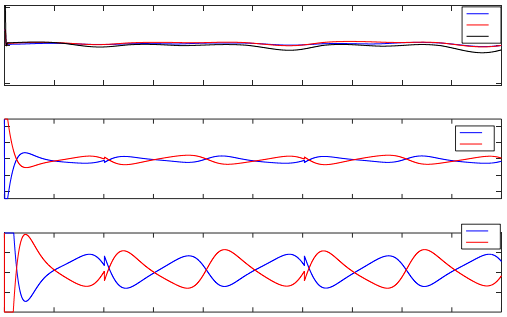

Figure 17 Thruster forces during tracking for ROV 2.

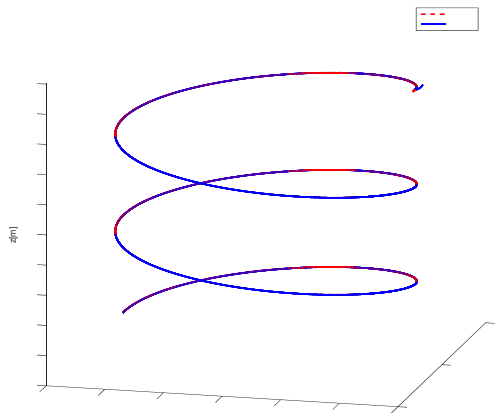

Figure 18 Trajectory achieved by ROV 2.

REFERENCES

[1] Fish F.E., Rohr J., *Review of Dolphin Hydrodynamics and Swimming Performance*. SSC San Diego, 1999.

[2] Meinecke G., Ratmeyer V., Renken J., HYBRID-ROV Development of a new underwater vehicle for high-risk areas. *Oceans'11mts/kona*, Vol. 1, No. 1, pp. 1-6, 2011.

[3] Rodić A., Stevanović I., Jovanović M., Urukalo Đ., On building remotely operated underwater robot-explorer with bi-manual poly-articular system*, Proceedings of Robotics in Alpe-Adria-DAnubae region (RAAD 2015),* Bucharest, pp. 1-8, 27-5, 2015.

[4] Paul R.B., *Robot Manipulators: Mathematics, Programming and Control*, 1st ed., MIT Press, Cambidge, MA, USA, 1982.

[5] Corke P., *Robotics, Vision and Control: Fundamental Algorithms in MATLAB*, Springer-Verlag Berlin Heidelberg, 2011.

[6] Siciliano B., Khatib O., *Springer Handbook of Robotics*, Springer-Verlag Berlin Heidelberg, 2008.

[7] Yuh J., Design and Control of Autonomous Underwater Robots: A Survey, *Autonomous Robots,* Vol. 8, No. 1, pp. 7-24, 2000.

[8] Valavanis K.P., Gracanin D., Matijasevic M., Kolluru R. and Demetriou G. A., Control architectures for autonomous underwater vehicles, *IEEE Control Systems*, Vol. 17, No. 6, pp. 48-64, 1997.

[9] Astrom K.J., Hagglund T., *PID Controllers – Theory, Design and Tuning,* 2nd edition, ISA, New York, USA, 1995.

[10] Corke P.I, MATLAB Toolboxes: Robotics and Vision for Students and Teachers, *IEEE Robotics and Automation Magazine,* Vol. 14, No. 4, pp. 16-17, 2007.

ISSN 1590-8844
International Journal of Mechanics and Control, Vol. 17, No. 01, 2016

ENERGY BALANCE AND MECHANICAL BEHAVIOUR OF A FLEXIBLE PNEUMATIC ACTUATOR FOR FISH-LIKE PROPULSION

Andrea Manuello Bertetto* Andrea Cadeddu** Luigi Antonio Besalduch**
Roberto Ricciu** Carlo Ferraresi***

* Department of Mechanical, chemical and material Engineering, University of Cagliari, Italy.

** Department of Civil - Environmental Engineering and Architecture, University of Cagliari, Italy.

*** Department of Mechanical and Aerospace Engineering, Politecnico di Torino, Italy.

ABSTRACT

The paper concerns an evaluation of a flexible actuator performances. The actuator is specially conceived for propulsion of biomorphic fish-like robots. Static and dynamic characteristics are presented, referring to the energy consumption and dynamic performances, evaluated by experimental activity performed by means of a hydraulic channel and by means of specially designed and realised experimental test rigs.

Keywords: Energy balance, bio-mimetic actuator, fish-like robot

1 INTRODUCTION

The robots represent the future in the hard work scenario in the new millennium. More power, precision, stability and repeatability when and where the human work is heavy or the human presence is impossible in hostile environment. The working robots use various types of energy, depending on the mission: electrical power [1], pneumatic [2] etc. for different type of actuators. Pneumatic actuators, in particular, are preferably used for unconventional applications, with customised architectures.

Among the non conventional actuators, the flexible pneumatic actuators are a very interesting proposal; in particular, a significant interest is evoked by the so-called pneumatic artificial muscles [2, 3]. The flexible pneumatic actuators were firstly conceived in 1930 by S. Garasiev, a Russian inventor [4]. One of the most interesting applications of these actuators is in medical field and they have been the input for some industrial and agricultural application. One of the most diffused flexible actuators is the McKibben artificial muscle.

Contact author: A. Manuello Bertetto

Department of Mechanical, chemical and material Engineering, University of Cagliari, Italy.
Via Marengo, 2. 09123 Cagliari, Italy.
Email: andrea.manuello@unica.it

It was designed to be used in an active orthosis for human motion recovery [5]. In any case the flexible actuators are very interesting for applications involving interaction with soft counterparties as in medical applications [6, 7]. The mobility recovery or the blood circulation retrieval by mechanical external actions on the patient [8, 9] are another application of flexible actuators. A very attractive solution for micro grippers for particular tasks as in micro manipulation is represented by flexible pneumatic actuators also in surgical environment.

Flexible pneumatic actuators are also an effective answer to challenging tasks as grasping of delicate objects in agricultural application (i.e. harvesting of agricultural products) or in pipes net inspection or pole climbing [10, 12]. Experimental and theoretical studies, also related to energy consumption, suggested that the flexible actuators may provide effective performances for fish-like propulsion. The classical Gray's studies [13-15], milestone for the research in this field, underlined the interesting advantages of the oscillating tail propulsion. For the tail actuation system, an interesting and innovative choice is represented by the flexible actuators [16-21]. This work is a study of a propulsion for an aquatic fish-like robot, equipped by a particular bending actuator. A specially designed test rig was realised to evaluate the energy consumption performances in the designed fish-like robot, during the operation. In the paper operating characteristic and the energy consumption was referred.

2 EXPERIMENTAL SET-UP AND METHODOLOGY

The actuator has a cylindrical geometry. The actuator body is a rubber made tube with two internal longitudinal chambers divided by a longitudinal wall, in Figure 1 the section of the actuator is presented, as well as the assembled actuator. Around the rubber made cylinder a sequence of aluminium made rings, to prevent radial deformation of the rubber cylinder, are assembled. Two heads, placed at the end of the cylinder, allow the compressed air supply to the two longitudinal chambers and the link to a frame and to the external load. The rubber is an elastomeric material with a 70 shore A hardness; it permits high deformations preserving an elastic behaviour, minimising the residual deformation depending on load velocity. The actuator is a two degrees of freedom device, its workspace is a surface: a two-dimensional plane region. A specially designed experimental set up was realised to trace the workspace of the actuator. This set up is shown in Figure 2.

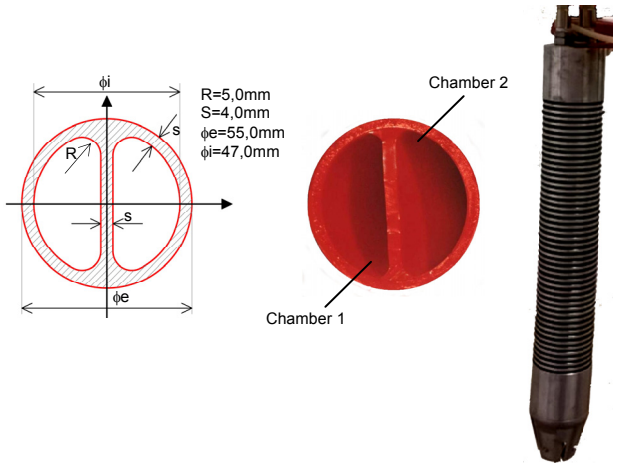

Figure 1 The actuator.

The actuator is vertically suspended to a rigid gantry, shown in Figure 2a, and measuring of the end effector position is performed in a three dimensional space, by means of trigonometric indirect measure. The end effector position, measured at given values of fluid pressures in the chambers, defines the workspace in relation to the chambers' supply pressures. The experimental apparatus, by means of wire position transducers, provides the length variation of the edges of a pyramid having the basis on a horizontal plane and the upper peak linked to the actuator end effector, as represented in Figure 2b. The pneumatic circuit to supply the actuator chambers is schematically drawn in Figure 2c: the two chambers are independently supplied in order to sweep the entire actuator workspace.
The energy consumption of the actuator during its movement was measured by a second test rig, schematically shown in Figure 3.

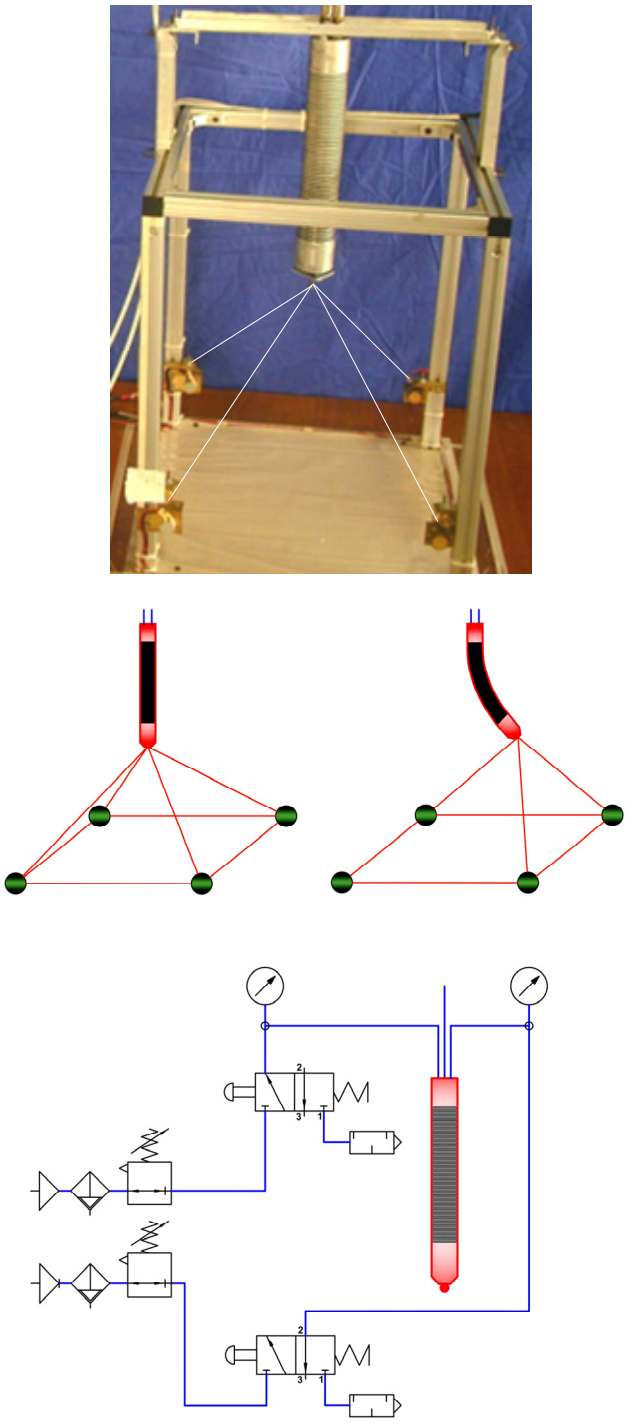

Figure 2 The test rig to trace the actuator workspace.

To control the air volume injected into the actuator a pneumatic cylinder was used (bore diameter 63 mm, stroke 750 mm), whose rod displacement was registered by means of a linear gauge (span 0 ÷ 1270 mm, static sensitivity 9,8455 V/m, repeatability ± 0.02% full stroke), and the pressure by means of two pressure gauges (span 689476 Pa, static sensitivity = 25.0 mV/100kPa).

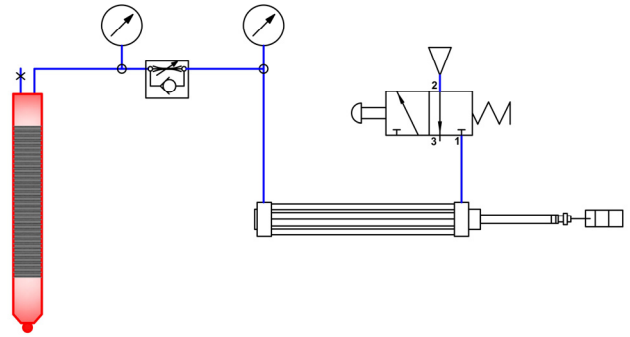

Figure 3 The test rig to evaluate energy consumption by volume and pressure detection.

The position of the flexible actuator was acquired by a digital photo camera. The Data Acquisition System used was: NI USB-6221. The data were acquired and processed by Matlab software.

3 THE WORKSPACE OF THE ACTUATOR

The actuator workspace, represented in Figure 4, is a plane surface perpendicular to the plane of the longitudinal undeformed internal wall dividing the actuator longitudinal chambers. The continuous line has been drawn with a maximum relative pressure of 4 bar. It was traced starting from the end effector (EF) in position A, with both chambers discharged; supplying only chamber 1, EF moves along the A-B curve reaching point B for 4 bar pressure in chamber 1 and ambient pressure in the other one. Maintaining 4 bar pressure in chamber 1 and increasing the pressure in chamber 2 from zero to 4 bar, EF reaches point C, where the fluid pressure is 4 bar in both chambers. By discharging chamber 1, maintaining a pressure of 4 bar relative in chamber 2, the curve C-D is traced. EF reaches again point A when both chambers are discharged. All points inside the edge can be reached by EF, combining the pressures in the chambers within the range 0-4bar relative.

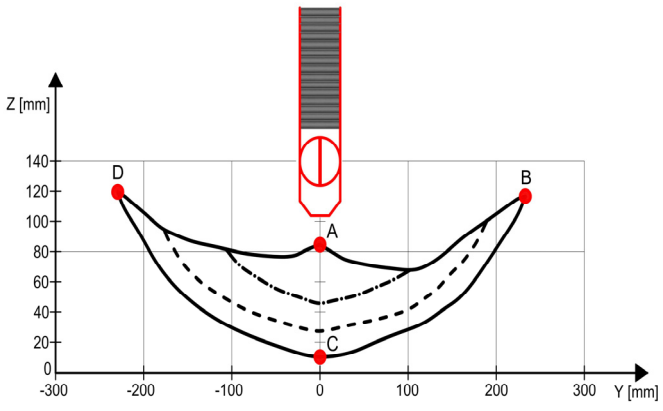

Figure 4 the actuator workspace.

In Figure 4, the bold line represents the workspace limit of the second test rig for a maximum relative pressure of 4 bar. With this set-up only the A-B curve can be drawn, but as it possible to notice, the two lines match quite well, so the behaviour is approximately the same. In Figure 5 the velocity and the acceleration of EF, measured by the second test rig, are shown. It is evident, from the velocity vectors, that the motion trend is very smooth, and also acceleration and deceleration are not so abrupt as in common hydraulic actuator, making this kind of actuator more suitable for the reproduction of fish fin motion.

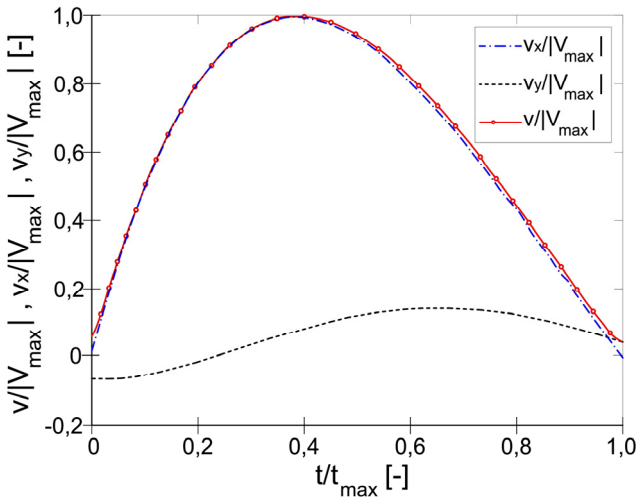

Figure 5 velocity and acceleration of the actuator EF measured by the second test rig.

In particular, the Figure 5 highlights that the velocity is mainly represented by the horizontal component Vx: the longitudinal motion of the EF is not so relevant. In Figure 6 the acceleration components are shown, the acceleration assumes significant values at the edges of the path.

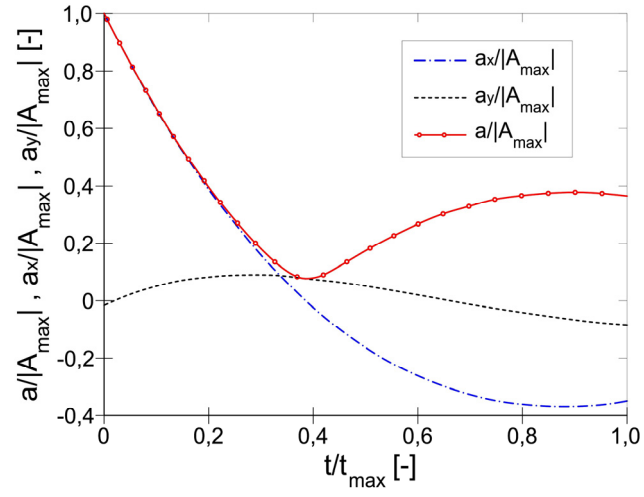

Figure 6 EF velocity components trend vs. time.

These kinematic evaluations can be justified by the Fig. 7, observing the different deformed geometries during the actuator motion. In the Figure 7 (a), without pressure, the actuator is in the rest position. Increasing the relative pressure in one chamber (b), it starts bending, and at approximately 4.5 bar (c) the actuator reaches its maximum curvature. From (a) to (b) the actuator is subjected to an initial stretching phase, whit light curvature, whereupon, from (b) to (c), the stretching stops and the bending behaviour predominate.

4 THERMODYNAMIC CONSIDERATIONS AND ENERGETIC PERFORMANCES

The actuator in the experimental set up (Fig. 3) has been thermodynamically characterized, by the air pressure and volume time recording during the operation.
The task was to know pressure and volume of air inside one actuator chamber during the displacement from initial to final position.
The pressure is measured by two pressure transducers described in the previous paragraph and inserted in the points of the circuit depicted in Figure 3.
The volume is obtained through the indirect measurement of the shift of the piston into the cylinder chamber, whose cross section area is known.
The temperature was measured during the movement of the actuator (sequence a, b, c of Figure 7) and was nearly constant, in the neighbourhood of the room temperature of 20° C.
Therefore the features of the air flow pushed by the piston in the actuator chamber are known.
In the set-up the energy was transferred from the cylinder to the actuator. In particular the energy transfer can be divided in two steps.
At the beginning, both actuator chambers are at atmospheric pressure, see Figure 7a, and the cylinder rod is completely extended.
In the second step the rod performs the complete stroke and the air, firstly in the cylinder posterior chamber, is completely transferred to the actuator that bends as in Figure 7b and finally reaching the configuration as in Figure 7c. The deformed actuator geometries shown in Figure 7 were acquired by digital photo camera.
During the experiment, all main physical quantities, i.e. pressures, volumes and temperatures of the air in cylinder and actuator chambers, were recorded. Figure 9 shows the trend versus the time of the air pressure and volume in the actuator chamber.
The pressure is detected at the inlet port of the actuator chamber and the volume is the indirectly measured by the cylinder rod position, detected by a linear position transducer.

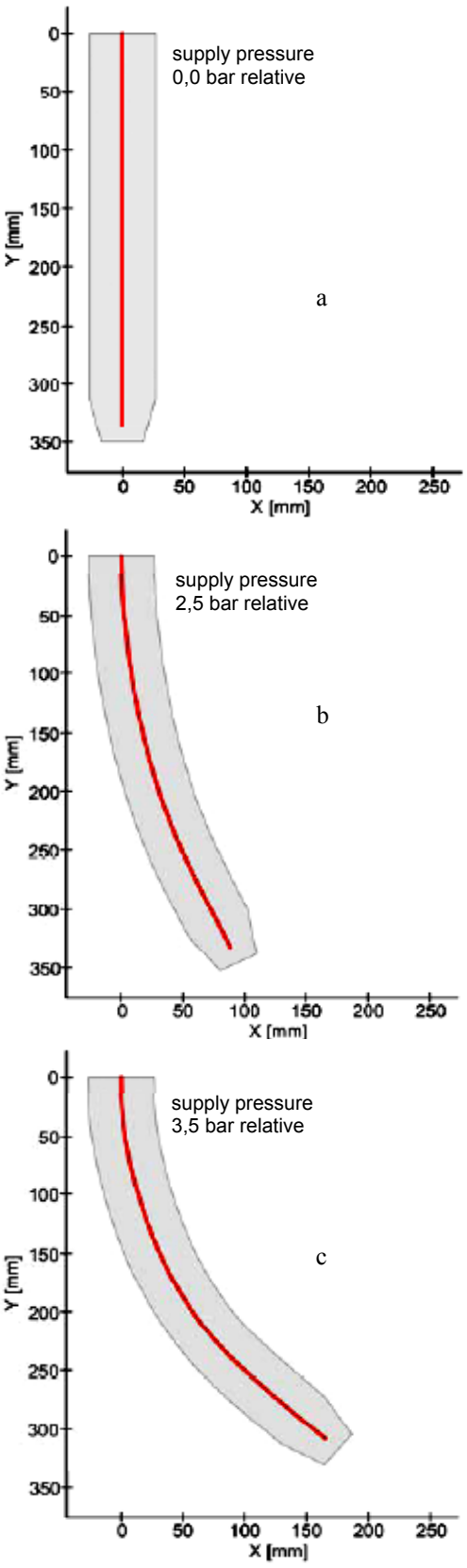

Figure 7 The actuator deformed geometry vs. supply pressure in chamber 1.

The system is considered as an irreversible and closed thermodynamic system. This assumption comes from that there is no temperature variation during the air transfer from cylinder to the actuator chamber: this is because the process is slow and the phenomenon is characterized by lost energy. Moreover no mass transfer exists with respect to the environment. Only heat and mechanical work are considered.
The work in term of infinitesimal variation is:

$$\delta E = P \times \delta V + V \times \delta P \quad (1)$$

where the work (E) is considered as negative if made by the surrounding. The total work (E) is calculated by integrating the equation (1). This can be done in approximated way considering the whole process as a sequence of small volume variations at constant pressure, therefore the total work was evaluated step by step with the following expression:

$$W = \Sigma Ei = \Sigma(Pi \times \delta Vi) \quad (2)$$

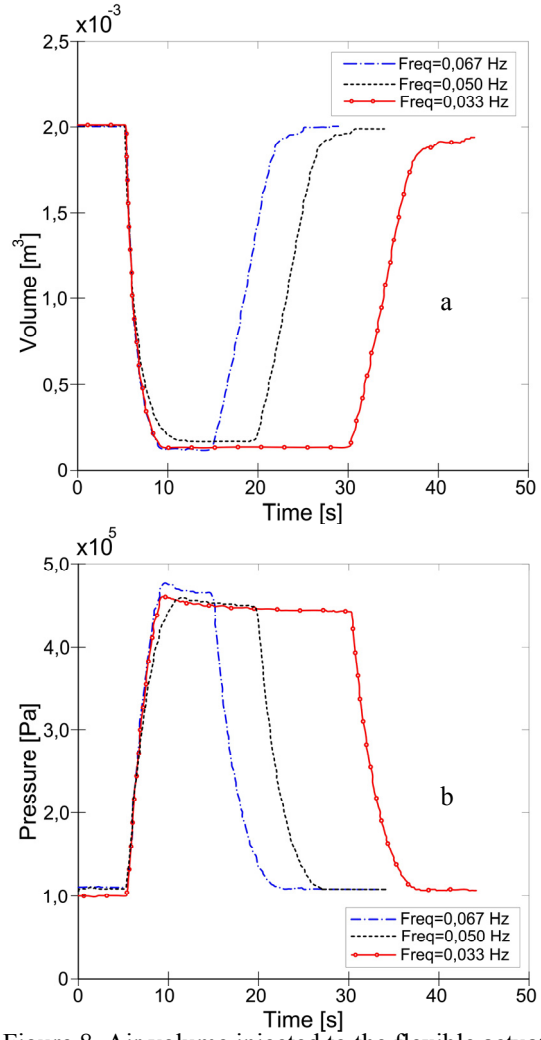

Figure 8 Air volume injected to the flexible actuator (a) and corresponding pressure in the actuator (b) for different oscillating frequencies.

The quantities Pi and δVi, where i = 1,…,N is the number of acquisitions, were measured by the set up described in Figure 2. The curves obtained are represented in Figure 8. Figures 8a and 8b show the trend of the volume V and of the pressure P vs. time t. Figure 9 shows the phenomenon in the Clapeyron plane (PV), for different frequencies of the compression/expansion cycles. The areas subtended by the curves in the Figure 9 represent the mechanical works: firstly the work is done on the system, subsequently the work is done by the system. The work balance is represented by the net area within the cycle which represents the lost work. The experiment indicates an energy loss of about 47 Joule for each cycle, while the energy retrieved in the return stroke was about 385 Joule. These values are approximately independent from the considered cycle, this suggests that the main losses should be due to the internal friction of the elastomeric actuator material, while the other effects (heat exchange and fluidic resistances) are negligible for slow functioning like in this case. Of course, for higher working frequencies, fluidic losses would have greater influence.

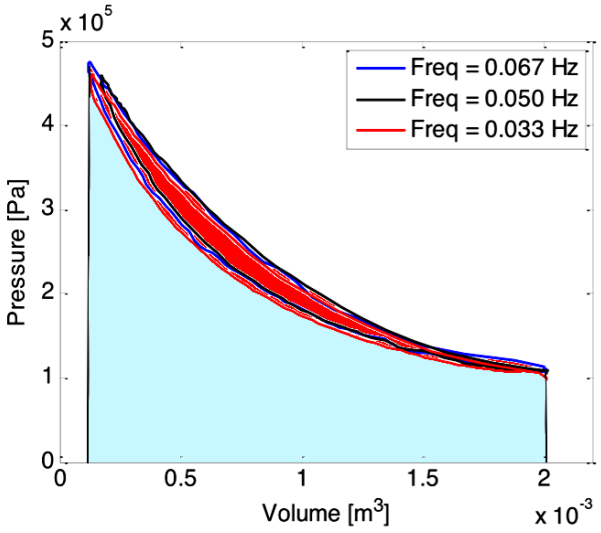

Figure 9 Curves of pressure vs. volume for different oscillating frequencies and in colour area the energy representation.

5 THE ACTUTOR FOR A FISH-LIKE ROBOT PROPULSION

The effectiveness of the actuator for propulsion of a fish-like robot was experimentally verified. The flexible actuator was linked to a tail having geometry referred to that of a carangiform real fish. The flexible actuator was then assembled inside a tapered body, linked to a strain gauges instrumented beam. The robot was then immersed into a hydraulic channel, to measure forces acting on the body in different working conditions.
In Figure 10a the actuator, linked to a carangiform fin, is presented in a bending condition coming from a chamber supply. In Figure 10b the whole robot body is shown.

Figure 10 The actuator and fin integrated system and the fish like robot.

Specific tests were performed in water, using the experimental apparatus schematically shown in Figure 11. Inside the channel, which is 16 m long and 1 m wide, it is possible to generate a water flow rate up to 500 l/s. On the top, a cart can be moved on a rail at a maximum speed of 2 m/s.

The cart is dragged by a wire driven by a controlled electrical motor. The cart carries the measuring system of the strain gauges of the instrumented beam and the PLC aimed at controlling the pneumatic valves to supply the chambers of the flexible actuator. The Figure 11 shows pictures of the channel and the fish-like robot suspended to an instrumented beam to detect the forces acting on the robot along the channel axis. During the actuator motion, for a given water velocity, the net force acting on the robot was measured. A drawing of the robot linked to the instrumented beam shows the device encumbrances. The robot body is 1100mm overall long and the transversal fin dimension is 360mm, the body has a diameter of 180mm.
In a separate test the resistance of the robot, for different fluid velocities and motionless actuator, was measured. The fin-actuator thrust is taken as the sum of resistance and net force. In the photographs of Figure 12 the channel and the experimental equipment are shown. The most relevant details are the channel transparent lateral side, the water free surface, the rail on the channel and the instrumented bar to detect the force acting on the immersed fish like robot.

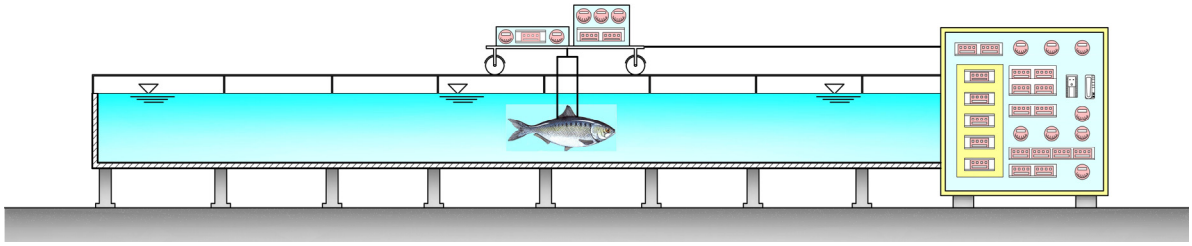

Figure 11 The hydraulic channel scheme.

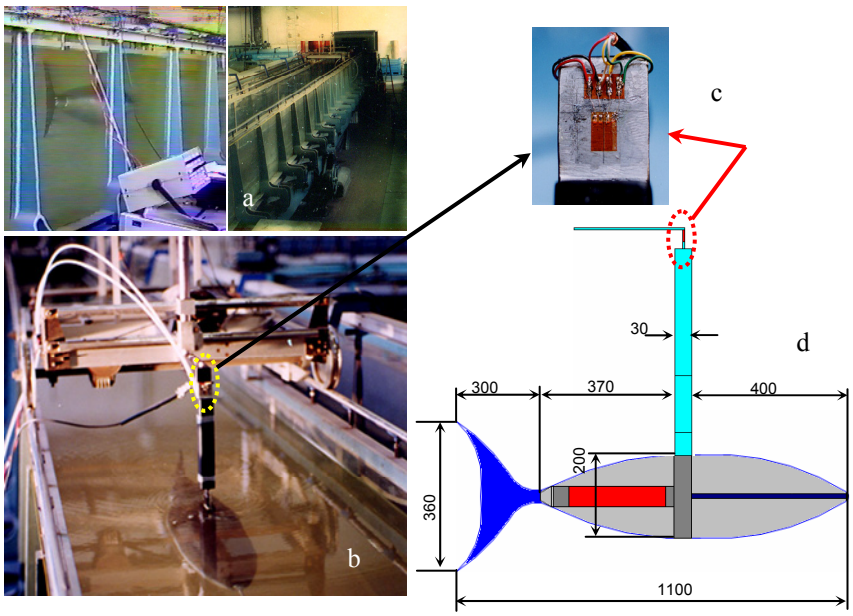

Figure 12 The hydraulic channel. It is possible to see the channel transparent lateral side (a), the water free surface and the immersed fish like robot, as the rail on the channel (b) and the instrumented bar to detect the force acting on the immersed fish like robot schematically represented in (d).

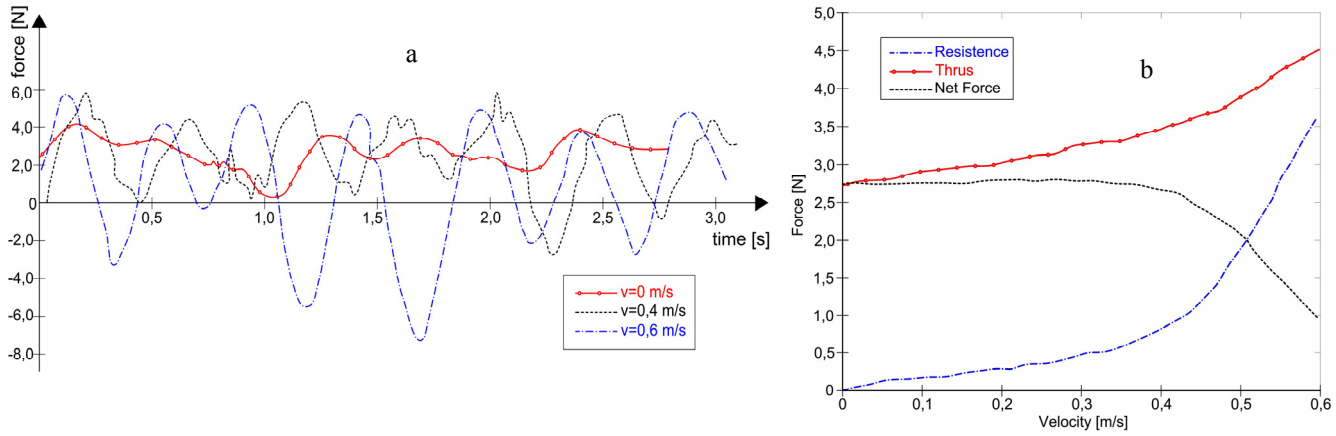

Figure 13 Force acting on the fish-like robot in the channel. (a): total measured force vs. time, at different water velocities; (b): mean values of resistance, thrust and net forces versus robot velocity in water.

The oscillating tail frequency, during in-channel tests, was 0.5 Hz, and a pneumatic supply pressure of 5 bar relative was given to perform an arc amplitude of the tail oscillating motion of 0.5m of the centre of the tail. The graphs of Figure 13a, at the left side, show the values of forces vs. time, during the oscillatory motion of the fin for three different water velocity values: 0, 0.4 and 0.6 m/s. The graphs of Figure 13b, at the right side, show the average force values in a fin oscillating period vs. robot velocity in water. The tree curves reported in Figure 13b represent: (i) the net force, obtained as a mean in time of the measured force values, dragging the robot at given velocity respect to the water; (ii) the resistance, measured directly dragging the fish, at different velocities, with non operating tail; (iii) the thrust of the tail, computed as the sum of the previously described force components. As it can be seen, the net force, acting on the immersed robot, is positive up to a robot velocity of about 0.6m/s relative to water.

6 CONCLUSIONS

This work investigated the performances of a flexible bending pneumatic actuator, designed for aquatic propulsion driving the oscillating motion of a fish-like fin. The experimental tests confirmed effective performances of the actuator as regards the propulsion capability, on the other hand, the experiment highlighted the performances from an energetic point of view. The study allowed to individuate the main problems that have to be faced and solved in future work, namely optimization of the fluid power transmission and the choice of materials with low internal friction for the actuator's body.

AKNOWLEDGEMENTS

This research was founded by the Italian Ministry of Research (MIUR).

REFERENCES

[1] Chaari M.Z., Applied to charge wirelessly the batteries of gas and petroleum pipes crawlers. *PowerWave: - 8th International Workshop of NDT Experts, Proceedings,* pp. 65-68, 2015.

[2] Ferraresi C., Franco W., Manuello Bertetto A., Flexible Pneumatic Actuators: a comparison between the McKibben and the straight fibres muscle. *J. of Robotics and Mechatronics*, 13-1, pp. 56-63, 2001.

[3] Ball E., Lin Y., Garcia E., Characterization and modeling of geometric variations in McKibben pneumatic artificial muscles, *Proceedings of SPIE - The International Society for Optical Engineering*; 8686, 868605, 2013.

[4] Palko A., Smrček J., The use of pneumatic artificial muscles in robot construction, *Industrial Robot: An International Journal*, Vol. 38 Iss: 1, pp.11–19, 2011.

[5] Schulte H. F., The characteristics of the McKibben artificial muscle. The Application of External Power in Prosthetics and Orthotics, Appendix H, , Publ. 874, *National Academy of Sciences, Washington, D.C.,* pp. 94-115, 1961.

[6] Watanabe Y., Maeda M., Yaji N., Nakamura R., Iseki H., Yamato M., et al., Small, soft, and safe microactuator for retinal pigment epithelium transplantation, *20th IEEE International Conference on Micro Electro Mechanical Systems (MEMS 2007)*, Kobe, Japan, pp. 494–497, 2007.

[7] Shimizu K., Mori Y., Hayashi K., Shunori A., Kawakami S., Hashida M., et al., Genedelivery in mice using an implanted pneumatically actuated microsystem. *Micro Electro Mechanical Systems (MEMS), in: 24th International Conferenceon IEEE*, pp. 181–184, 2011.

[8] Manuello Bertetto A., Meili S., Concu A., Crisafulli A. An Inflatable Pneumatic System For Blood Pressure Recovery, Mechanics Based Design of Structures and Machines, *Taylor and Francis* 40-4, pp. 506-518, 2012.

[9] Manuello Bertetto A., Meletti M., Mechatronic Device for Stimulating the Blood Circulation: Design and Implementation, *RAAD 2013 – 22nd International Workshop on Robotics in Alpe Adria Danube Region*, September, Portorose, Slovenia 11-13, 2013.

[10] Yu, L.Z.: Study on a pneumatic inspection micro robot, *Applied Mechanics and Materials* 519-520, pp. 1327-1330, 2014.

[11] Manuello Bertetto A., Ruggiu M., Pneumatic Robot for Pipe Inspection, International Journal of Mechanics and Control, Vol. 2 No. 2, 2001.

[12] Manuello Bertetto A., M. Ruggiu M., Pole Climbing Pneumatic Robot, Proceedings of the Fifth JFPS International Symposium on Fluid Power, pp. 43-48, 2002.

[13] Gray J., Studies in animal locomotion I. The movement of fish with special reference to the eel., *J. Exp. Biology*, 10, pp. 88-104, 1933.

[14] Gray J., Studies in animal locomotion II. The relationship between the waves of muscular contraction and the propulsive mechanism of the eel. *J. Exp. Biology*, 10, pp. 386-390, 1933.

[15] Gray J., Studies in animal locomotion III. The propulsive mechanism of whiting. *J. Exp. Biology*, 10, pp. 391-400, 1933.

[16] Shao J., Wang L., Yu J., Development of an artificial fish-like robot and its application in cooperative transportation, *Control Engineering Practice*. 16, pp 569–584, 2008.

[17] Cataudella C., Ferraresi C., Manuello Bertetto A., Flexible actuator for oscillating tail marine robot, Int. *Journal of Mechanics and Control*, Torino, 2, pp.13-21, 2001.

[18] Manuello Bertetto A., Ruggiu M.: Tail Actuator Propulsion Device for Aquatic Robot, *J. of Robotics and Mechatronics*, 18-1, pp. 80-90, 2006.

[19] Manuello Bertetto A. Underwater robots: a fascinating challenge. Chapter 4. *Mobile Robots for Dynamic Environments*, ed. Faruk Kececi and Marco Ceccarelli. New York, NY: ASME Press, pp. 1-21, 2015.

[20] Clark A.J., Tan X., McKinley P.K., Evolutionary multiobjective design of a flexible caudal fin for robotic fish, *Bioinspiration and Biomimetics* Volume 10, Issue 6, Article number 065006, doi:10.1088/1748-3190/10/6/065006, 2015.

[21] Bertetto A.M., Ferraresi C., Besalduch L.A., Ricciu R., Cadeddu A., Flexible actuator for biomorphic applications: Performances and energy consumption evaluation, *Advances in Intelligent Systems and Computing* Volume 371, pp. 115-123, 2016.

ISSN 1590-8844
International Journal of Mechanics and Control, Vol. 17, No. 01, 2016

PRECURSORS OF THE AUTOMATION IN THE HELLENISTIC AGE

Cesare Rossi

University of Naples "Federico II", Dept. of Industrial Engineering, Italy

ABSTRACT

Some devices conceived by scientists and engineers of the Hellenistic Age are presented. They be considered the precursors of the automation and clearly show how the concept of automation was present in the minds of ancient scientists and engineers since the II century B.C. or even earlier. The devices also clearly show the surprising modernity of the knowledge of the ancient scientists and engineers, both in conceiving the mechanical designs and the building of them. The chosen examples are presented by grouping them by inventor.

Keywords: Ancient automatic devices, Automata, History of Mechanism and Machine Science

1 INTRODUCTION

The word "automatic" comes from the ancient Greek αυτοματος, an adjective meaning literally self-moving or self-acting. So, also in ancient times, the term and the concept had practically the same meaning we use today.
Moreover, the oldest clues about these ideas are probably found in the Greek mythology. For instance, in the Iliad, it is told that the god Hephaestus (Iliad, XVIII, vv. 519-525) built some "automata" that helped him in his smith works.
Another legend tells that king Minos used a bronze mechanical giant, Talos, forged by Hephaestus, to patrol the isle of Krete.
As far as we can recognize of the past, automatic devices were first designed by the scientists/engineers of the Hellenistic Age; this is to say in the Mediterranean Area and in a period of time that strictly ranges between 323 B.C. and 31 B.C. but, from a cultural point of view ranges between the III Century B.C and the II Century A.D..
In this period of time, the human knowledge had a very considerable "jump" in almost any field of the culture and put the basis of the society in which we live today.
Concerning the scientific and technical knowledge, in particular, most of the inventions developed in this period of time were beaten not earlier than in the XVIII Century [1-15].

Contact author: Cesare Rossi

E-mail: cesare.rossi@unina.it

2 CTESIBIUS

Ctesibius (285–222 B.C.) was the director of the Library of Alexandria and is credited of a large number of inventions, several of them being automatic devices [1-5]. Among these, one of the most interesting can be considered the water clock, shown in figure 1; in the figure a virtual reconstruction and technical drawings showing the working principle are reported. To understand the reason why an automatic device was required for a water clock, we must remember that the length of a roman hour was not constant since it was defined as 1/12 of the time between sunrise and sunset during the day and 1/12 of the time between sunset and sunrise during the night. Thus, the time duration of one hour was different from day to night (except at the equinoxes) and from a given day to another one. The water clock designed by Ctesibius solved this problem [1].
A bottom tank is filled by a constant water flow from a top tank that is permanently maintained full. A yarn, wrapped in coil around the pointer axle, is connected to a floater and to a counter weight. The bottom tank is drained daily and the cycle starts again. The dial is fitted on an off-centre shaft on which a gear having 365 teeth is fitted; once a day the float passes through a certain position and moves a rod that pushes one tooth, hence the dial completes a revolution in one year.

3 DIONYSIUS OF ALEXANDRIA AND PHILON OF BYZANTIUM

The invention of the repeating catapult is tributed to Dionysius of Alexandria, (III Century B.C.) and was described by Philon of Byzantium (280 b.C. circa – 220 b.C. circa) [1, 15-19].

It can be considered as a concentration of the most advanced mechanical kinematic and automatic systems of the time, many of which are still widely used.

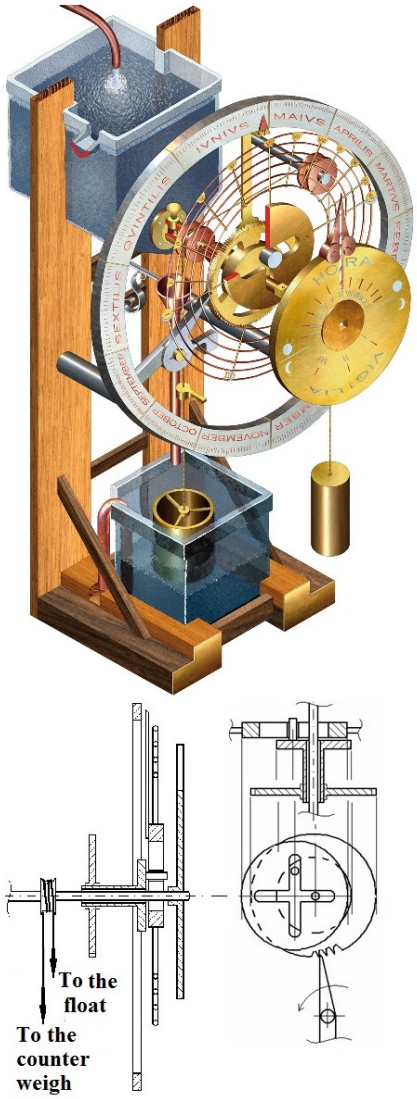

Figure 1 Ctesibius' automatic water clock. Adapted from [1].

According to the author's recent reconstruction, based on previous works and from Philon's description, the device is really automatic. Pictorial reconstruction and technical drawings of it are shown in Figures 2 and 3. The device essentially consisted in a container holding within it a number of arrows, a cylinder feeding device and movement chain. According to Philon, the arrows were located in a vertical feeder F and were transferred one at a time into the firing groove by means of a rotating cylinder C, activated alternatively by a guided cam, in turn activated by a slide. One of the longer interior teeth T of the chain pulls the slide S which in turn pulls the cord, loading the coils of the motor. In the same time, an attached cam caused a 180° rotation in the direction of the cylinder, drawing an arrow from the loader and placing it in the channel in front of the rope.

When the slide reached the rear of the weapon, the cog released it, while another opened the release mechanisms. An instant later, upon completion of sprocket rotation, the same cog coupled with the slide from underneath, pulling in the opposite direction. Near the top of the weapon, the second device closed the hook after it had retrieved the cord, while the feeder cylinder picked up another arrow from the feeder. A half rotation in the sprocket and the cycle was repeated.

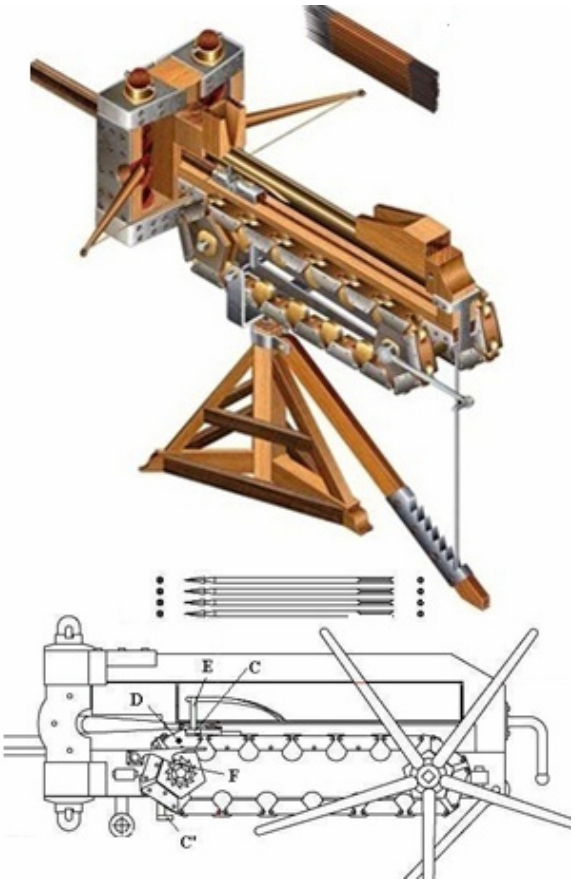

Figure 2 Pictorial reconstruction and technical drawing of the repeating catapult. Adapted from [15].

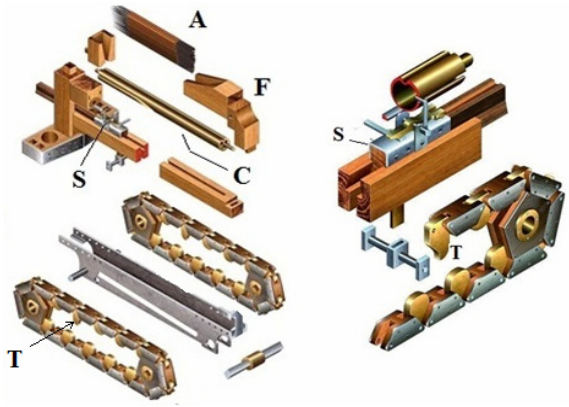

Figure 3 Mechanism of the repeating catapult. Adapted from [1].

It must be observed that our reconstruction, based on our translation of text by Philon, is really automatic; this because, differently from previous reconstructions, a simple rotation of the crank was sufficient to move the cylinder, the slide, the slide hooking mechanism and the trigger mechanism.

4 HERON OF ALEXANDRIA

Heron of Alexandria was probably the best known designer of automatic devices in ancient times. Although very few is known about his life, he is well-known for a wide number of his inventions in different fields; probably the widest fields of his inventions is the automation [1, 20, 21].
The main treatises by Heron about automatics (Pneumatica and Automata) were translated during the Italian Renaissance by Berardino Baldi, [22] (1553–1617), and by Giovan Battista Aleotti [23] (1546-1636); both describe a wide number of automatic devices. Some of the most interesting examples are reported in the following.
The most famous automatic device by Heron is probably the mechanism to open and close the doors of a temple shown in figure 4 with a virtual reconstruction.

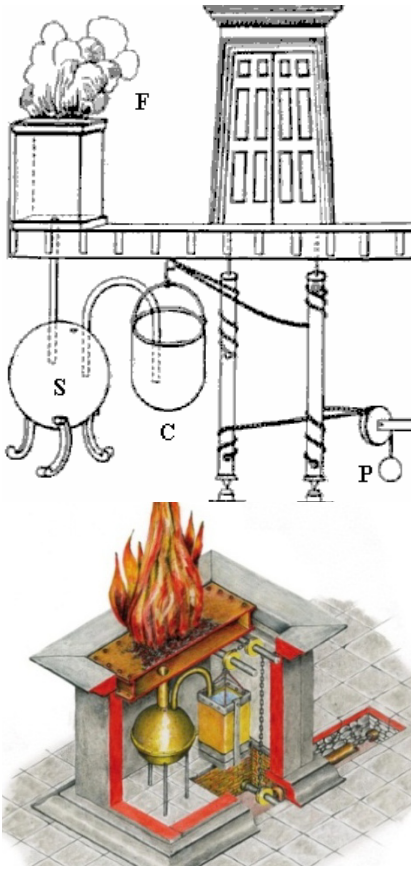

Figure 4 Heron's Mechanism for temple doors and virtual reconstruction, adapted from [20].

A fire was lit on the brazier F; so, the hot air heated the water in the pressure tank S. The pressure in this tank pushed the water in the mobile water container C through a U-shaped pipe. The mobile water container was connected to the temple doors by means of ropes or chains wrapped in coils on the door hinges. As the water container was filled with water, because of its weight the ropes were unrolled and the doors were opened. When the fire was extinguished, the steam in the pressure tank condensed, hence, the pressure in it decreased and the water was sucked up from the water container. As soon as the weight of the latter decreased enough, the counterweight P acted on the door hinges in the same way, but closing the doors.
Another interesting example of Heron's automata is reported in figure 5 where a reconstruction is shown made by G. B. Aleotti [23] of a famous Heron's automaton. This automaton was made up by two main characters: Heracles and a dragon. In few words: the dragon hisses, Hercules beats it with a club and the dragon spits on Hercules. The working principles can be deduced by Aleotti as it follows and is shown in the lower part of figure 5.

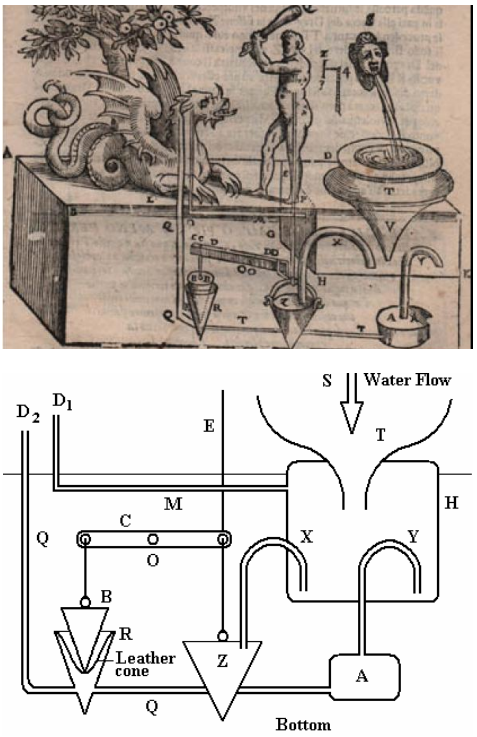

Figure 5 Aleotti's reconstruction of an Heron's automaton and working principle, adapted from [1].

A water flow from S fills a tank H through a funnel T. When the tank H is filled the air flows through a small pipe M that is linked to the dragon's mouth and this one hisses. A rocker C can rotate on a pin O; one of its arms is linked to a cone B and to a rope E, while the other arm is linked to a water container Z; the latter, if empty weighs less than cone B. As the water level in the tank goes up, the water fills the mobile water container Z through the U-shaped pipe X. When the mobile container Z is heavier than cone B, the rocker C rotates clockwise and rope E moves Hercules' arms through a simple T-shaped mechanism, not represented. In this way the club is lifted up.

At the same time, through pipe Y, tank A, pipe Q, and the cone R are filled. Since the mobile water container is conical, when it reaches the bottom, it turns upside down and the water in it is evacuated. Now cone B is heavier than container Z and the rocker rotates counter-clockwise. The rope R is tightened and the club beats the dragon's head. At the same time, cone B gets inside cone R that is full of water and so the pressure in the pipe Q rises. This pipe is linked to the dragon's mouth and so the latter spits a water jet onto Hercules. To Heron was also ascribed the water distributor that represent the ancestor of the modern drink vending machine. In figure 6 a scheme of this device is shown [23].

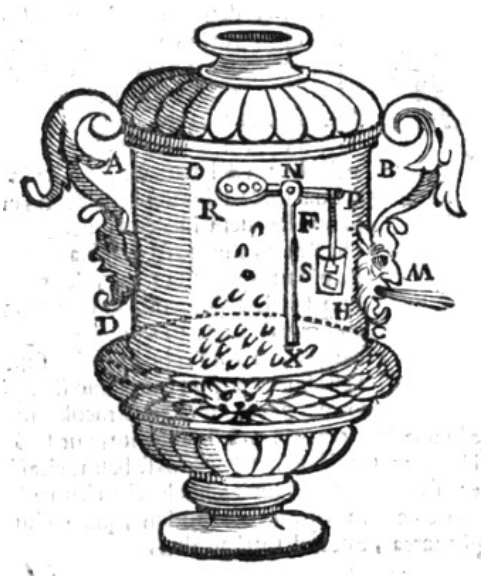

Figure 6 Aleotti's drawing of an Heron's vending machine.

The device provided an amount of water once a coin of 5 drachms was put in the slot. The weight of the coin, in fact acted on the plate R of the rocker arm N that, rotating, opened the valve S, permitting to an amount of water to flow outside from the hole M. Due to the rotation, the coin felt down and the rocker arm rotate in the opposite verse, closing the valve.

Another interesting device is the regulator for the distribution of the liquids; this device, in fact, represent a first example of feedback control.

In figure 7 a drawing by Aleotti [23] is shown. The vase on the left is the one from which the liquid is taken and the level of which must be always kept constant. The vase on the right is the one that is used for the feedback. Both the vases are connected by a pipe, so the level of the liquid inside them is the same.

Once some liquid is taken from the vase on the left, the level of the liquid tends to go down in the vase on the right also. Inside the latter a float is located that is connecter by a rod to the rocker arm H. So even a small a decrease of the level, causes the opening of the valve EF and the filling of both the vases; this until the balance is one more time reached.

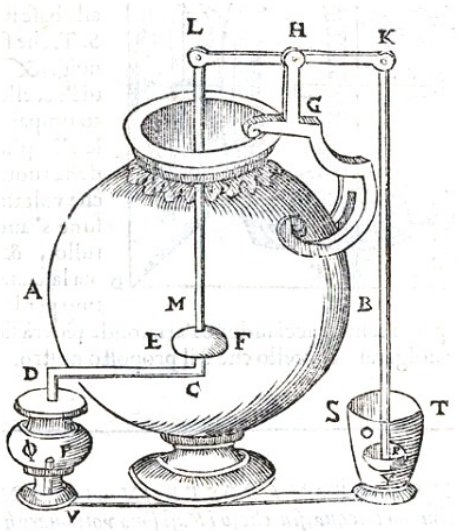

Figure 7 Aleotti's drawing of an Heron's regulator for the distribution of the liquids [23].

But Heron's most surprising automatic device is probably the programmable self-moving automata. These latter were described by B. Baldi [22] and were conceived as "actors" in a puppet theatre. On the theatre proscenium all the performance was played by those automata that were, hence, programmable. In figure 8 drawings from Baldi's work are reported, showing the working principle and the counterweight motor that moved those automata.

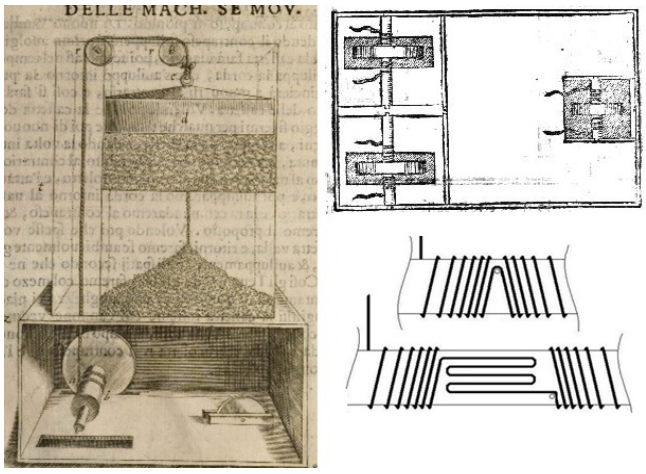

Figure 7 Heron's programmable self-moving robot

In the figure, on the left, one can observe the counterweight that is located in a tank filled with millet or mustard seeds in order to regulate the counterweight motion, hence the automaton speed. The same figure on the left shows the axle of the driving wheels divided in two axle shafts that are independent one from the other; on each one of the shaft a rope is rolled. If the rope is rolled on one of the axle shaft in a different way from the other, when the counterweight goes down pulling the rope, one of the two driving wheels will rotate in different way from the other one.

The programming of the motion was also obtained by putting some knobs on the axle shaft like shown on the bottom right of figure; by these knobs it was possible to modify the rolling of the rope, in order to obtain different laws of motion for each wheel [24-26].

4 CONCLUSIONS

Some examples of automatic devices were presented, all belonging to the Hellenistic Age. This historical period, in fact, represents a period of time during which the human thought and knowledge had a deep improvement especially concerning technology and engineering. The presented examples show how advanced were our predecessors about 2000 years ago. Most of their inventions, in fact, were beaten not earlier than in the XVIII Century [1-4]. So, we should give them a tribute for having "placed the foundation" of our knowledge and of our comfortable life nowadays. Moreover, it can be interesting (and may be also instructive) to observe how some devices represent solutions of problems that were obtained with a design showing a brilliant simplicity.

REFERENCES

[1] Rossi C., Russo F., Russo F., *Ancient Engineers' Inventions, Precursors of the present*. Springer, ISBN: 978-90-481-2252-3, 2009.

[2] Russo L., (reprint), *La rivoluzione dimenticata. Il pensiero scientifico greco e la scienza moderna*, Feltrinelli, Milano, ISBN 88-07-81644, 2003.

[3] Rossi C., On Designs by Ancient Engineers. *Journal of Mechanical Design*, Vol. 135, ISSN: 1050-0472, doi: 10.1115/1.4024362, pp. 1-2, 2013.

[4] Rossi C., Some Examples of the Hellenistic Surprising Knowledge: its Possible Origin from the East and its Influence on Later Arab and European Engineers. *Rivista Storica dell'Antichità*, XLIV, pp. 61-84, 2014.

[5] Russo F., Rossi C., Ceccarelli M., Russo F., Devices for Distance and Time Measurement at the time of the Roman Empire. *HMM Int. Symp. on History of Machines and Mechanisms*, Tainan, Taiwan, Nov. 10-14, pp. 101-114, 2008.

[6] Chondros T.G., The development of machine design as a science from classical times to modern era. *HMM Int. Symp. on History of Machines and Mechanisms*, Tainan, Taiwan, Nov. 11-14, Springer, NL, ISBN 987-1-4020-9484-2, 2008.

[7] Chondros T.G., Archimedes life works and machines. *Mechanism and Machine Theory*, Vol. 45, No. 11, pp. 1766-1775, 2010.

[8] Dimarogonas A.D., *Machine Design a CAD Approach*, John Wiley and Sons, Inc. N.Y. 2001 (Introduction - The machine: an istorical design, pp. 4-19)

[9] Rossi C., Unich A., A Study on Possible Archimede's Cannon. *Rivista Storica dell'Antichità*, Vol. 43, ISSN 0300-340X, 2013.

[10] Rossi C., Ancient Throwing Machines: a Method to Compute Their Performances. *Mechanism and Machine Theory*, Vol. 51, ISSN 0094-114X, pp. 1-13, 2012.

[11] Publius Flavius Vegezius Renatus - *Epitoma Rei Militaris*, Liber IV, cap. XVII.

[12] Penta F., Rossi C., Savino S., Mechanical Behavior of the Imperial Carroballista. *Mechanism and Machine Theory*, Vol. 80, ISSN: 0094-114X, pp.142-150, 2014.

[13] Vitruvius (I Cent. B.C - I A.D.), *De Architectura*, Liber X.

[14] Mays L., *Ancient Water Technologies*, Springer, 2010. ISBN 978-90-481-8631-0, e-ISBN 978-90-481-8632-7, doi: 10.1007/978-9

[15] Rossi C., Russo F., A Reconstruction of the Greek-Roman Repeating Catapult. *Mechanism and Machine Theory*, Vol. 45, No. 1, ISSN:0094-114X, pp. 36-45, 2010.

[16] Shramm E., *Die antiken Geshützen der Saalburg. Reprint, Bad Homburg*: Saalburg Museum, 1980.

[17] Marsden E.W., *Greek and Roman Artillery Historical Development*, Oxford University Press II, 1969.

[18] Soedel V., Foley V., Ancient Catapults. *Scientific American*, pp.101-114, March 1979.

[19] Russo F., Rossi C., Russo F., Automatic weapons of the Roman Empire. *EUCOMES 2008 2nd European Conf. on Mech. Science*, Sept. 17-20, Cassino, Italy, 2008.

[20] Russo F., Il miracolo di Erone (The miracle by Heron, in Italian). *Archeo*, n.201208, ISSN 1120-4559, Aug. 2012, pp. 96-101.

[21] Heron of Alexandria, "*Perì Automatopoietikès" Heronis opera quae supersunt omnia* ed. W. Schmidt/L. Nix/H. Schöne/J. L. Heiberg, Leipzig 1899.

[22] Baldi B., *Di Herone Alessandrino de gli avtomati ouero machine se moventi libri due. Tradotti dal greco da B. Baldi*. – Venezia, 1602.

[23] Aleotti G.B., *Gli artificiosi et curiosi moti spiritali di Erone. Bologna*. The Archimedes Project, Digital Research Library, 1589.

[24] Sharkey N. *The programmable robot of ancient Greece* - New Scientist #2611, July 4, 2007.

[25] Webb B., The first mobile Robot? *Proc. TIMR 99 Towards intelligent Mobile Robots*, 1999.

[26] Rossi C., Pagano S., A Study on Possible Motors for Siege Towers. *Journal of Mechanical Design*, Vol. 133, ISSN:1050-0472, pp.1-8, 2011.

ISSN 1590-8844
International Journal of Mechanics and Control, Vol. 17, No. 01, 2016

DESIGN AND TESTS OF TEXTILE PNEUMATIC MUSCLES FOR ACTIVE SUITS

G. Belforte* E. Bonisoli** G. Eula* A. Ivanov* S. Sirolli*

*Dept. of Mechanical and Aerospace Engineering

**Dept. of Management and Production Engineering

Politecnico di Torino – C.so Duca degli Abruzzi, 24 – 10129 Torino

ABSTRACT

This paper describes the design and test of some textile pneumatic muscles prototypes. Tests were carried out on materials, geometries and some numerical models constructed for a better characterization of these devices. The results are interesting and provide ideas for further research in applications such as active clothing where the pneumatic muscle, integrated in a T-shirt, allows the wearer to perform rehabilitation exercises.

Keywords: textile pneumatic muscles for active suits; active clothing with pneumatic muscles; textile pneumatic muscles numerical models.

1 INTRODUCTION

Pneumatic Artificial Muscles or PAMs are used as actuators which can simulate human muscle for rehabilitation purposes or to assist the movement of injured limbs [1, 2].
They simulates the behaviour of a human muscle, contracting thanks to the pressure of the fluid in its interior to generate a traction force at its ends.
The structure typically consists of a rubber or textile material, generally anisotropic, rigid in one direction and elastic in the orthogonal direction to permit axial deformation.
PMAs have been most commonly used in areas such as medical, industrial and entertainment robotics [3-10].
Soft materials are essential to the mechanical design of innovative actuators. The soft components provide numerous advantages. They conform to surfaces, distribute stress over a larger volume, and increase contact time, thereby lowering the maximum impact force [11].
If the fabric is not impermeable, or if the seams of the muscle assembly can leak, the outer fabric contains an interior latex tube which is impermeable to the supplied fluid [12-14].

Contact author: Gabriella Eula

Email: gabriella.eula@polito.it

The two concentric tubes are connected at their ends to fittings whereby the load is moved. Like human muscles, PAMs also operate in antagonistic pairs, since they can only generate traction forces and therefore movements in just one direction.
One innovative application for pneumatic muscles is active clothing, i.e. garments with integrated PAMs used for rehabilitation purposes or to assist the movement of the upper or lower limbs of the human body [23].
This article introduces textile pneumatic muscles entirely designed at the Politecnico di Torino Department of Mechanical and Aerospace Engineering (DIMEAS). The textile structure, with interior latex, was chosen because its light weight, low bulk, comfort, fit and biocompatibility make it suitable for biomedical applications in active suits.
Textile materials are characterized by a distinct hierarchy of structure, which should be represented by a model of textile geometry and mechanical behaviour [15-22].

2 DIMEAS TEXTILE PNEUMATIC MUSCLE PROTOTYPE

The muscle prototype consists of: two end fittings (Figure 1), one at the front which is perforated to allow air to be supplied to the muscle, and one at the rear which acts as a plug; one layer of fabric; and one layer of latex. Cone sealing couplings are used to secure the double fabric-latex

layer at the two ends. The fabric used is anisotropic and not airtight.
In particular the internal latex tube increase the size of structure but it avoids air loss from seam. The textile structure gives to the muscle stiffness and robustness. Furthermore it has a proper wearability for active suits. The tissue choice has to consider the maximum contraction obtainable and a proper load sustaining capacity.
In this paper cylindrical end-fitting of the muscle are used only for these preliminary experimental tests, while for an active suits a rectangular end-fitting of the muscle is preferable in order to improve wearability.
The wide study on various anisotropic fabrics carried on is useful for the choice of an anisotropic tissue with a proper radial elasticity and a good axial contraction. This study looks for a light and comfortable tissue, capable of working for a lot of cycles without any damage.
In particular Figure 2 shows an initial prototype of active suit fully developed and constructed in DIMEAS. It is made of a T-shirt with some DIMEAS textile pneumatic muscles prototypes put on the arm.
The initial experimentation on this prototype is still in progress and it is giving good results.

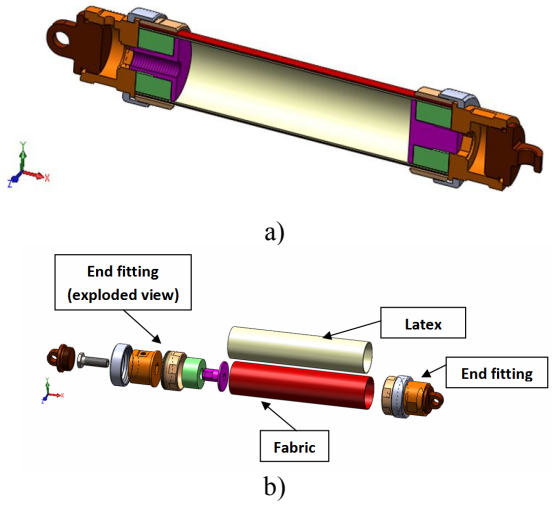

Figure 1 a) Pneumatic muscle with textile structure, b) Exploded view of muscle.

Figure 2 A preliminary DIMEAS prototype of active suits.

3 WORKING METHOD

Tests were conducted on a tensile testing machine to evaluate the mechanical properties of the fabric and the latex used.
Testing was performed in accordance with ISO 13934-1 - Part 1: "Textiles - Tensile properties of fabrics - Determination of maximum force and elongation at maximum force using the strip method" [24], and ISO 13934-2 - Part 2: "Textiles - Tensile properties of fabrics - Determination of maximum force using the grab method" [25].
Subsequently, pressure-contraction and pressure-force tests were conducted on a sensorised test bench built specifically for this purpose.
Lastly, preliminary models were developed to simulate the prototypes' operation and investigate their behaviour.
The numerical models realised are: isotropic, anisotropic with fabric only, anisotropic with separate layers of latex and fabric, anisotropic with a single equivalent latex-fabric layer, anisotropic single equivalent layer with modified joint, anisotropic single equivalent layer with imposed elongation (model 6). As the model 6 is the best of the all models realized, only this last one is here presented.

4 EXPERIMENTAL TESTS

The experimental tests here presented were carried on both using a standardized test material machine and an experimental muscle test bench. Referred to the experimental results here presented it is underlined that 1 bar = 10^5 Pa.

4.1 MATERIAL CHARACTERIZATION

To gain an understanding of certain characteristics of the materials, fabrics were tested in tension [14, 26, 27] according to the standards indicated above and using a standardized test machine.
In particular various kind of tests with various tissue were carried on in order to measure elastic modulus of the samples.
The fabric specimen is secured between a stationary lower clamp and a moving upper clamp. The total stroke of the crossbar is about 1.5 meters. A load cell is connected to the upper clamp and the crossbar to measure the forces acting on the specimen and transfer them to a special software program. Tests were carried out using a pull rate of 2 mm/s.
Using the standardized test machine, 102 experimental tests were carried on with specimens geometry in full agreement with standards [14, 26, 27] and made of various fabrics.
Base on the comparative analysis shown in Table I, where the various parameters are: El elastic direction; R rigid direction; the tensile strength σ_e (the upper limit of elastic deformation regime); the shear stress σ_r (the rupture stress); the elastic strain ε_e and the rupture strain ε_r, it is possible to conclude that:

- the Fabric A is a material in which the stress does not overcome 0.8 N/mm^2 and it has a transpiring membrane that does not give air impermeability criteria;

- the Fabric B has an elastic structure and an permeable to air membrane which is extremely sensitive to high stresses and for this reason is not suitable for this study;
- the Fabric C is a resistant material with an impermeable membrane. It detaches itself from the textile layer and so the material integrity is no longer preserved;
- the Fabric D is an optimum material but the membrane is transpiring that do not respect the air impermeability condition;
- the Fabric E has good mechanical property and air impermeability and for those reasons this material is suitable for manufacturing process of the textile PAM's here presented.

Tests were performed in two directions (elastic and rigid) to characterize the material anisotropic behaviour. Specimens measure 200 x 50 mm as required by the standard in all tests, carried out here referred in particular to Fabric D and Fabric E as the best fabrics examined.
Fabric D consists of woven warp and filling yarns, while Fabric E is a knit, i.e. continuous interlocking loops produced from a single yarn. Fabrics have various layers: an inner transparent polyurethane membrane and outer polyester layers.
For each type of material, the test was repeated several times using three different specimens.

Table I - The comparative analyse of laminated fabric tested.

Material /Direction		σ_e [N/mm^2]	ε_e [%]	σ_r [N/mm^2]	ε_r [%]	E [N/mm^2]	Notes
FABRIC A Bi-laminate	-	1	40	6.4	81	4	- Fatigue resistance to external loads between 40 – 80 N; - Transpiring membrane and sensible to gripping device; - Permanent plastic deformations;
FABRIC B Bi-laminate	El	2	60	8.3	120	2.5	- Fatigue resistance to external loads between 50 – 100 N; - Membrane that detaches from the textile layer; - Permanent plastic deformations - Are proposed further investigations for lower external loading.
	R	16	31	17	33	50	- Fatigue resistance to external loads between 300 – 400 N; - Membrane that detaches from the textile layer ; - Permanent plastic deformations.
FABRIC C Tri-laminate	-	2.5	5	27	25	-	- Fatigue resistance to external loads between 400 – 600 N; - Transpiring membrane; - Permanent plastic deformations.
FABRIC D bi-laminate	El	0.8	35	6.8	71	1.2	- Fatigue resistance to external loads between 100 – 150 N; - Transpiring membrane and sensible to gripping device; - Permanent plastic deformations.
	R	1	3	21	25	-	- Fatigue resistance to external loads between 100 – 250 N; - Transpiring membrane and sensible to gripping device; - Permanent plastic deformations.
FABRIC E Tri-laminate	El	1	80	2.5	117	0.6	- Fatigue resistance to external loads between 20 – 40 N; - Permanent plastic deformations.
	R	2	30	18	68	5	- Fatigue resistance to external loads between 100 – 300 N; - Permanent plastic deformations.

Selected tensile test results for Fabric D are shown in Figure 3, where elongation is plotted on the abscissa and the force on the specimen during the tensile test is plotted on the ordinate. In this graph the specimens tested are both in textile material (in its rigid and elastic direction respectively) and in tissue and latex rubber linked together, in order to measure the elastic modulus of a sample made of two different materials. This is important as the pneumatic muscle structure here considered is made of textile material and latex rubber internal tube.
For each case, consecutive tests were performed, with results showing good repeatability.
For clarity, only the average curves from the various tests are given in the figure.
The tests start with the specimen in the initial unreformed condition (200 x 50 mm).
The initial cross sectional area of the fabric layer is 15 mm^2.
As can be seen from the graph in Figure 3 (Fabric D), only the latex and fabric specimen tested in the tissue elastic direction shows good linear behaviour, while the other cases show nonlinearities related to the materials employed.
The curves for the elastic fabric with latex sample and the rigid fabric with latex sample were used to calculate the elastic modulus according to ISO 527-1/2, 2012 [28, 29]; ISO 527-3, 1995 [30]; ISO 527-4, 1997 [31]; ISO 527-5, 2009 [32], given a specimen section of 15 mm^2.
Two values were obtained: 14106 Pa for latex rubber + tissue in elastic direction, and 122106 Pa for latex rubber + tissue in rigid direction.
These values were then used to model the muscles under examination.

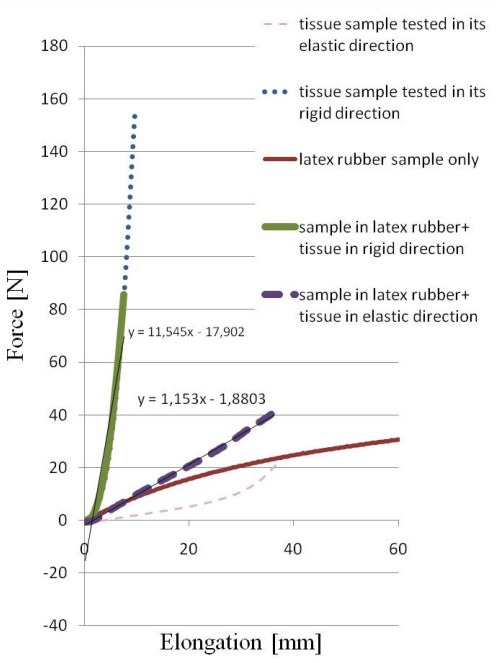

Figure 3 Tensile force versus longitudinal elongation (Fabric D).

Figures 4a and b show the Fabric E with latex behaviour during the tests in the elastic direction and in the rigid direction, showing here the only interpolation curves. From these tests the elastic module E is obtained both in the elastic direction (E_y = 3544426 N/m^2) and in the rigid direction (E_x = 14146596 N/m^2).
Given that the pneumatic muscle is a cylindrical structure with a sewn seam in the fabric, specimens featuring different types of seam were constructed in order to gain a better understanding of the fabric tensile behaviour.
Another possibility for joining the fabric could be hot welding. This type of method was studied in earlier stage of the research project of pneumatic muscles and turned out not to be successful. A problem was the increase of rigidity in the joining points, which is a result of melted fabric. To maintain elasticity in one direction is vital for the pneumatic muscles. Joining the fabrics with glue has also been tested, that turned out not to be successful.
The seam shall preferably have characteristics so that it rather supports the essential fabric properties, for the muscles performance, than impair them.
The seam shall have rigid properties, preferably as similar as possible to the ones of the fabric. Likewise shall the seam support the elasticity in the seam direction of the elongations muscles. Therefore the knowledge of the seam behaviour in the fabric is necessary.
Tests were performed accordingly on the fabric with seam/seams to determine the seams impact in the fabric regarding the rigidity verses elasticity.
Three samples were performed in the same way on the same machine, the MTS-machine.

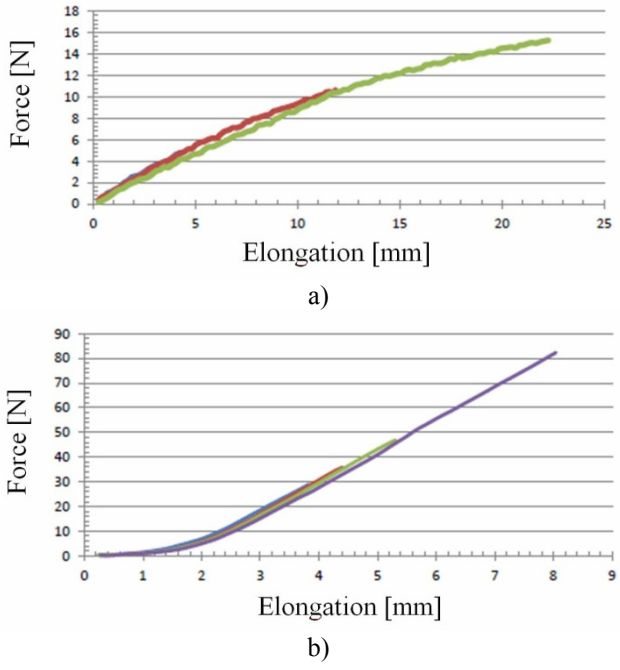

Figure 4 a) Fabric E, elastic direction: Load-Elongation tensile test curve; b) Fabric E, rigid direction: Load-Elongation tensile test curve.

Because of unidirectionality of the MTS-machine was the behaviour of muscle in each direction, longitudinal and radial, studied separately. Each direction was studied for both types of muscles that are elastic and rigid direction. This analysis was focused on the effect of the seam in the longitudinal direction of the muscle. Some of the results obtained on Fabric D and Fabric E are shown in Table II.
The first column indicates whether or not the specimen features a seam, the second column shows the maximum force allowable for a proper use of the material, the third indicates the corresponding elongation, the fourth indicates the contribution of a single seam in the case of specimens with four seams to evaluate their effect on the specimen elongation under a maximum allowable force value.
In addition, the table summarizes the force and elongation values recorded during tests along the elastic and rigid directions. Comparing the two tissues it can be noticed a similar behaviour on both fabrics.
To work in the elastic area of the fabric is important in order to avoid a damage of the muscle structure during its functioning. Furthermore several other fabrics were tested with and without seams of various kinds, in order to carry out a detailed analysis of the characteristics of possible materials useful for in the construction of pneumatic muscles.

Table II – Tensile tests on Fabrics D and E.

FABRIC D		MAXIMUM FORCE RANGE [N]	ELONGATION RANGE [mm]
Elastic direction (El)		10-15	9-28
Rigid direction (R)		35-60	4.0-4.8
FABRIC D	Average maximum allowable force [N]	Elongation [mm]	Contribution of one seam [mm]
Without seams (El)	14	28	-
With seams (El)	16	9-15	15-20
Without seams (R)	50	4.2	-
With seams (R)	60	4.3	4.2
FABRIC E		MAXIMUM FORCE RANGE [N]	ELONGATION RANGE [mm]
Elastic direction (El)		4-15	4-15
Rigid direction (R)		40-60	3.3-4.5
FABRIC E	Average maximum allowable force [N]	Elongation [mm]	Contribution of one seam [mm]
Without seams (El)	13	15	-
With seams (El)	20	4-9	12-14
Without seams (R)	50	3.7	-
With seams (R)	50	1.5-4.5	3.4-4.4

4.2 TESTS ON PNEUMATIC MUSCLE PROTOTYPES

The experimental muscle test bench constructed at the Politecnico di Torino DIMEAS laboratory to validate prototype pneumatic muscles is pictured in Figure 5.

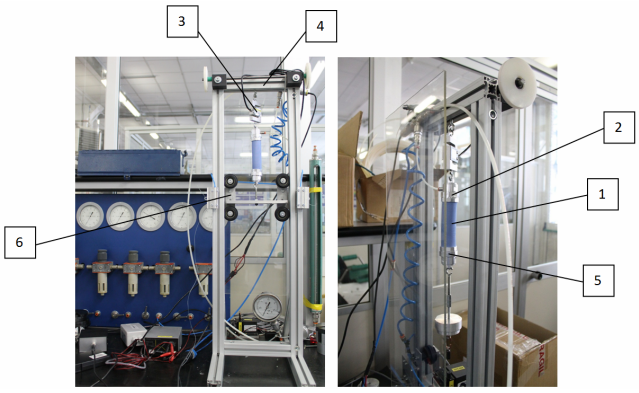

Figure 5 Muscle test bench.

The muscle (1) is mounted vertically with the rigid fabric direction along the muscle axis and its front end fitting (2) is attached to a load cell (3) connected directly to the fixed frame (4). The muscle's rear end fitting (5) has a threaded hole to receive the end of a flush position transducer and a lower crossbar (6) which slides vertically and can be attached to weights.
To minimise friction, the mobile crossbar is mounted on rollers with a guide that facilitates vertical motion.
Using the muscle prototypes test bench here presented various kinds of cylindrical muscles were tested, with diameters variable from 13 mm to 30 mm and length at rest 100 mm, built with Fabric D and E.
Muscle supply pressure is adjusted manually via a pressure reducer from 0 to 1.5 relative bar. To measure the force that the prototype is able to exert at a certain set length, the mobile crossbar can be locked on the frame.
The software records muscle pressure, stroke and pulling force. Data are acquired at a sampling frequency of 5 Hz, i.e. one sample every 200 ms.

The initial length of the pneumatic muscle under test is 100 mm.
For the sake of brevity, only certain selected muscle pressure-contraction and hysteresis tests are shown, as these are the tests that are most useful for comparison with the next model that was developed.
Furthermore in some fabrics here tested an initial assessment of material was noticed.
Anyway after this phenomenon all of materials work without any plastic deformation or damage.
In the Figures 6a and 7 some experimental graphs obtained using Fabric D and Fabric E are illustrated.
It is possible to notice that Fabric D shows a lower load capacity and less contraction, due to its different anisotropic textile structure, as radial deformation and axial contraction.
In Figure 6a, muscle M_1 contraction is plotted versus supply pressure, with a load consisting of the mobile crossbar alone (1 kg) and, for a closer examination of the muscle behaviour, with an additional 5 kg external load.
The muscle M_1 has the structure shown in Figure 1.
The percentage contraction shown in the graph in Figure 6a was calculated with the formula:

$$Contraction\% = 100\frac{L_0 - L_f}{L_0} \quad (1)$$

where L_0 = initial length, L_f = final length of the muscle tested.

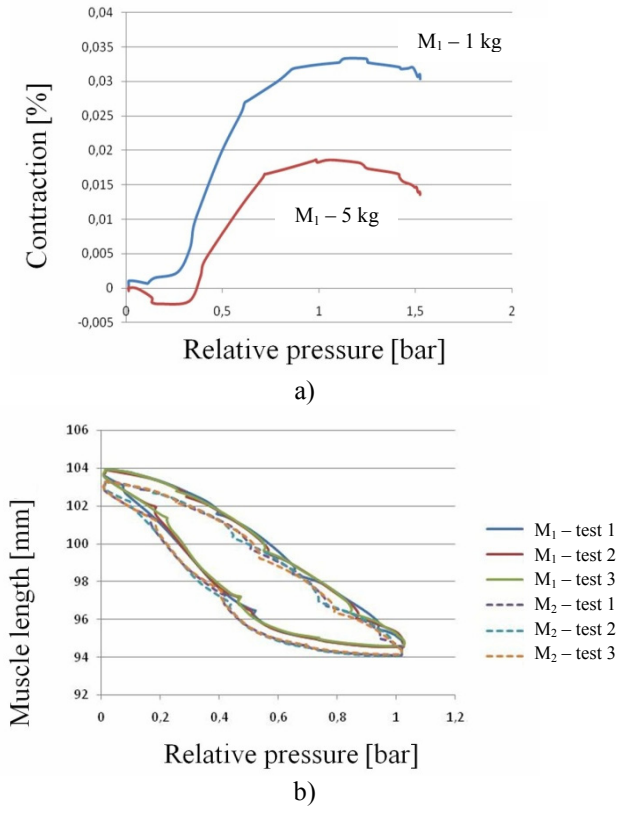

Figure 6 a) Examples of experimental tests on muscles with Fabric D and inner latex tube; b) Hysteresis tests on the materials used (p_{max} = bar; load 5 kg – Fabric D).

Given their structure, the muscles also present hysteresis.
Their active and passive strokes do not coincide, and this hysteresis is due to friction phenomena both between the inner latex layer and the outer fabric, and between the fabric's weft and filling yarns.
In particular, Figure 6b illustrates the hysteresis cycle in two pneumatic muscles (M_1 and M_2) of the same geometry subjected to an external load of 5 kg. The muscles M_1 and M_2 have the structure shown in Figure 1.
A hysteresis cycle is clearly present for both prototypes m1 and m2 in three consecutive trials.
As can be seen from the graph, results show good repeatability for both muscles.
Using Fabric E also a different muscle structure was experimented, as shown in Figure 7 where the prototypes behaviour of new different muscles (called M_a-M_b-M_c-M_d) are shown.
In fact with Fabric E only the Ma muscle prototype (Figure 7) was constructed with the same structure used for Fabric D here shown in Figure 1.
The other prototypes presented in Figure 7 instead were built with some axial wires connected between the two muscle end-fittings in order to increase the textile load capacity.
In Figure 7 experimental tests with fabric E are shown, using the formula (1) for the percentage contraction calculation. These tests were carried out on pneumatic muscles with 30 mm nominal diameter and 100 mm length, varying supply pressure from 0.5 bar to 1.5 bar without any external load applied to the muscle.
In particular the best performance was obtained with the prototype M_a, comparable with the structure of the muscle above described with fabric D.
This demonstrate that the addition of axial wires does not improve the characteristics of the muscle that also with Fabric E works better with design illustrated in Figure 1.

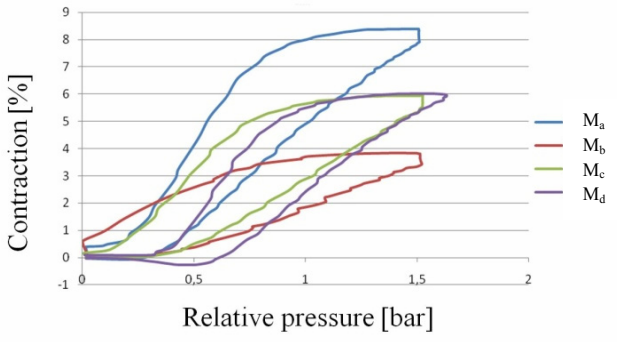

Figure 7 Examples of experimental tests on muscles with Fabric E and inner latex tube.

5 MUSCLE NUMERICAL MODELS

Several initial models were constructed which can be useful in developing a rapid and reliable method for designing and validating these pneumatic muscles and for modelling their application in an active suit in order to study in the future

the optimal linkage and geometry muscle configuration for this purpose.

In particular, model 6 refers to simulations of an entire muscle assembly consisting of an outer fabric sheath and an inner latex tube.

The assumption of a linear elastic material made here is compatible with the fact that the muscle's contraction is here very limited (about 3 mm out of a length at rest of 100 mm), as was determined in the experimental tests.

For the present purposes, the nonlinearity of the material used can thus be neglected.

The hysteresis shown by the tested prototypes does not affect the initial models presented as they simulate a unidirectional, non-cyclic movement.

The elastic modulus and Poisson's ratio used initially for the models were those provided directly by the MTS tensile testing machine on hybrid fabric + latex samples.

As regards the orthogonal reference system, the x axis is along the muscle axis, while axes y and z are radial.

In the present case, the muscle model is constrained at the rear end fitting, while the front end fitting is free to move axially. All simulations presented refer to muscles of 100 mm length and 30 mm outside diameter, with different models constructed as seamless cylinders. No external load was applied to the muscle at this stage of the investigation.

The air pressure used in the models is 0.2-0.5-1.0 relative bar.

The software calculates stresses, elongations and strains.

For each point, there are three mutually orthogonal planes, called the principal stress planes, with normal vectors (σ_1, σ_2, σ_3) as the principal stress directions. The main stresses here used are σ_x, σ_y, σ_z located according to the [x, y, z] reference system used in the models, as are the three tangential components τ_{xy}, τ_{xz}, τ_{yz}.

The optimal model that was developed (model 6) is presented below.

As the material is anisotropic material, it was not possible to use the Von Mises yield criterion. According, the Hashin failure criterion [33, 34] was considered, as it is suitable for anisotropic composite materials. This criterion defines an interaction between the normal stress and the shear stress.

5.1 ANISOTROPIC MODEL WITH A SINGLE EQUIVALENT LAYER AND INTERLOCKING MODIFIED AS IMPOSED ELONGATION

The substantial limit of the simulations carried out with the first models lies in the areas of maximum fabric strain near the end fittings. In those areas, the radial preload to which the fabric is subjected when the muscle is attached to the cone sealing couplings was neglected.

In model 6, a 0.7 mm fictitious radial elongation is imposed in the two end sections of the tube in order to simulate the fabric prestress resulting from the actual assembly method.

In these conditions, a circumferential tensile stress state is generated which initially decreases when the internal pressure increases. The assumptions made are: linear elastic materials; only one equivalent material, homogeneous and anisotropic (equivalent elastic modulus E obtained from experimental tests on the hybrid specimens); elongation imposed on the ends to simulate the assembly prestress; one of the two ends of the muscle constrained, as otherwise the structure would be unstable; none external load applied to the muscle during simulation. The Hashin criterion is used to verify yield strength.

5.2 ANALYSIS OF RESULTS

The actual geometry of the end fitting is shown in Figure 8a, where the prestressed area of the fabric is circled in blue. Prestressing is obtained by imposing a 0.7 mm radial elongation over an axial length of 17 mm on both ends of the cylinder that simulates the pneumatic muscle under examination. Figures 8b and 8c illustrate the Von Mises equivalent stress along the muscle x axis, simulated with this model supplied at 0.5 relative bar. The strain is now consistent with the experimental results, and the contraction along the x axis is 3.2 mm (Fabric D). Figure 8c shows a detail of the Von Mises stresses calculated in the area of the elongation (supply pressure = 0.5 relative bar). Figures 8d and 8e show the axial contraction of the muscle modelled here, again with a supply pressure of 0.5 relative bar. A modelled muscle contraction detail along the x axis is plotted in Figure 8e.

Also in this case, yield strength checks on the data obtained from the model were made using Hashin's formula with a supply pressure of 0.5 relative bar and 1 relative bar.

The calculations made with Hashin's formula indicate that the muscle will not fail when subjected to a supply pressure of 0.5 relative bar, but that failure will take place at 1 relative bar.

In particular, in analyzing the actual samples, the fabric remains unchanged and adheres to the inner latex tube with the 0.5 relative bar supply pressure.

During experimental tests at 1 relative bar, the fabric is altered and a residual strain persists.

The contraction obtained with numerical model 6 in these conditions is 3.2 mm, while the experimental contraction is 3 mm at a relative supply pressure of 0.5 relative bar.

The error between the model and the experimental result is therefore 6.7 % with 0.5 relative bar supply pressure.

Given the assumptions made and the parameters included in the model, it can be concluded the model provides good results in this case.

At a supply pressure of 1 relative bar, by contrast, failure occurs when numerical model 6 is used with Hashin's formula. Alterations in the pneumatic muscles' outer fabric sheath also occurred at this pressure in the experimental tests. In this case, the error between the model and the experimental result is -36.4 %.

Since the discrepancies between the theoretical model and the data measured on the prototypes may also be due to the experimental values of Young's modulus, a sensitivity analysis of the two Young's moduli used in model 6 was performed, starting from the data provided by the standardized test machine software.

This analysis consists in varying one parameter at a time, moving in the plane illustrated in Figure 9.

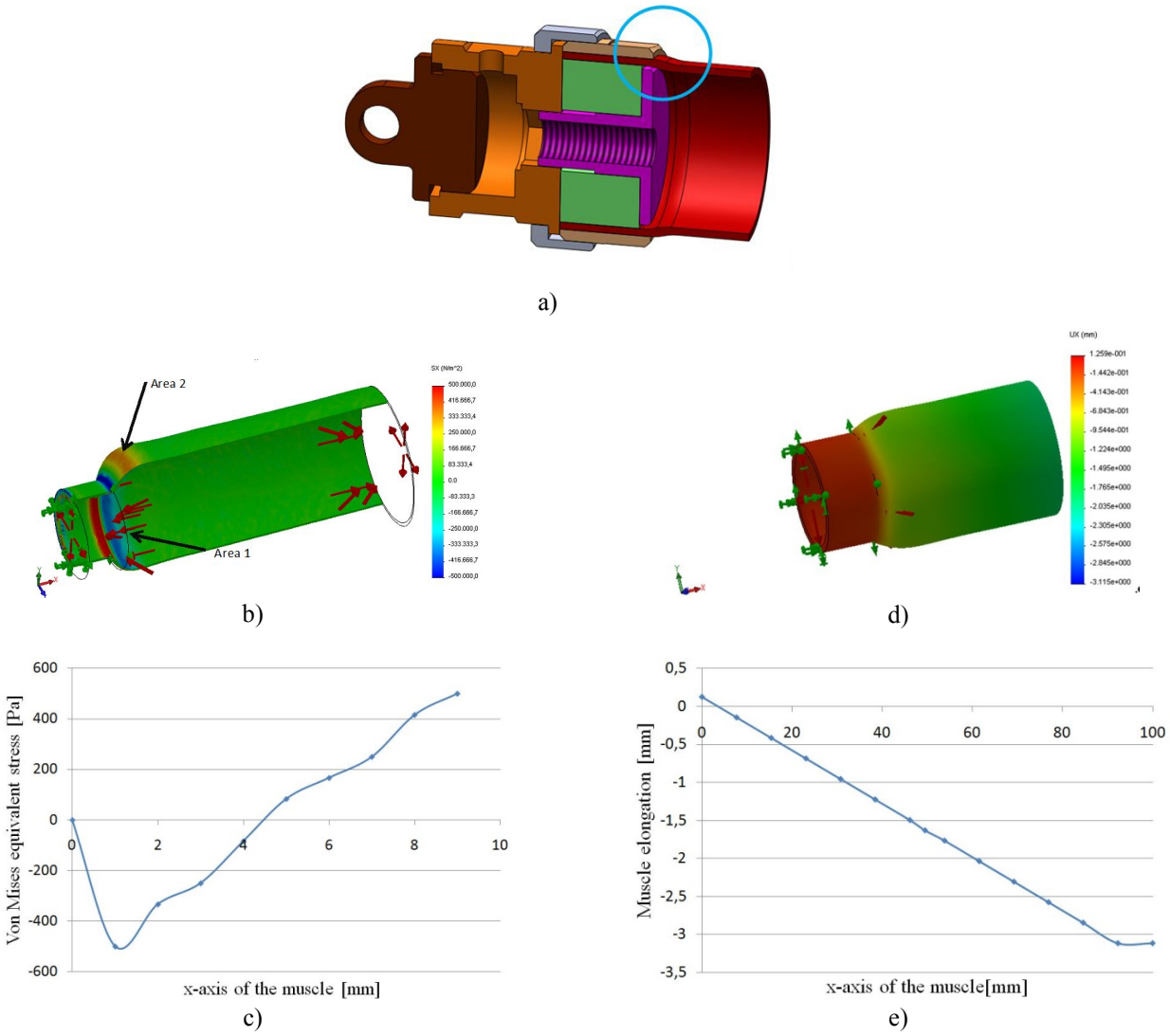

Figure 8 a) Details of the actual muscle end fitting
b) c) Normal stress σ_x in the cone sealing attachment area
d) Detail of the area with sharp edge
e) Axial strains (x) of the muscle over the entire length (100 mm).

Each point, designated with a letter, represents the increments to the initial values of the moduli with a variation of 10 %.
In all analysis presented here, the supply pressure was considered to be 1 relative bar and the load was 1 kg.
This is useful in order to evaluate the muscle's performance at supply pressures sufficient to move the human upper limb correctly when the muscle prototype is integrated in active clothing used for rehabilitation exercises or as an aid for the disabled.
Twelve simulations were then performed on the basis of the twelve points represented above.
The contraction values and the percentage error for model 6 are shown in Table III and compared with the experimental results.

The error between the contraction values obtained with the model and with the experimental tests was also calculated using the formula:

$$Err_{\%} = 100\frac{Contraction\%_{Exp} - Contraction\%_{Mod}}{Contraction\%_{Exp}} \quad (2)$$

The negative percentage errors indicate that pneumatic muscle model 6 overestimates the experimental results, while positive percentage errors indicate that model 6 underestimates the experimental results.
As can be seen from Table III, the best pair of increments in Young's modulus is provided by point L, at which there is a 15 % increase in Young's modulus along the x direction

and 10 % along the *y* axis.
This also helps balance out any approximations related to the use of Hashin's criterion for knitted fabrics.
A comparison of the results of this sensitivity analysis with the elastic modulus E calculated according to (ISO 527-1/2, 2012; ISO 527-3, 1995; ISO 527-4, 1997; ISO 527-5, 2009) [30-34] from the experimental data shown in Figure 3, i.e. 14106 Pa for the latex + elastic specimen, shows good agreement.
In particular, it should be noted that the sensitivity analysis presented here was very useful, inasmuch as the elastic modulus data provided by the tensile testing machine software show uncertainties related to the hybrid structure of the specimens.
In fact, the tested materials consist of two parts (latex rubber + tissue sample), and the fabric consists of woven yarns, and is thus more complex than a homogeneous material.

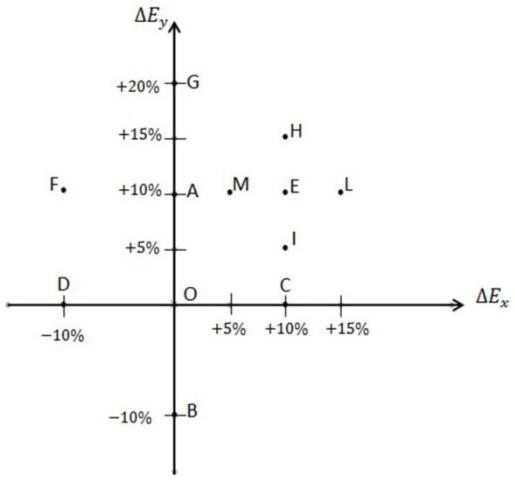

Figure 9 Sensitivity analysis.

Table III – Contraction analysis with Fabric D.

Point	$E_x + \Delta E_y$ [Pa]	$E_y + \Delta E_x$ [Pa]	Simulation contraction [mm]	Experimental contraction [mm]	Percentage error [%]
O	11873108	1806514	3	2.2	-36.4
A	11873108	1987165	2.8	2.2	-27.3
B	11873108	1625863	3	2.2	-36.4
C	13060419	1806514	2.8	2.2	-27.3
D	10685797	1806514	3.2	2.2	-45.4
E	13060419	1987165	2.6	2.2	-18.2
F	10685797	1987165	3	2.2	-36.4
G	11873108	2167817	3.4	2.2	-54.5
H	13060419	2077491	2.9	2.2	-31.8
I	13060419	1896840	2.7	2.2	-22.7
L	**13654074**	**1987165**	**2.5**	**2.2**	**-13.6**
M	12466763	1987165	2.7	2.2	-22.7

In Figure 10 results obtained with model 6 and Fabric E are shown, referred to the experimental results shown in Figure 7.
In the model the muscle (length 100 mm, diameter 30 mm) has an extremity fully fixed and the other one capable of moving axially, with a contraction equal to 6.6 mm.
With Fabric E the calculation of E modulus was been carried on as here explained.
To calculate stress σ_s and Young's modulus E, yielding force F_s and sample elongation were measured, in order to use the formula $\sigma_s = F_s / A$ with A = wide*thickness of the sample.
In this way, using the formula

$$p_{\lim} = \frac{2\,F_s}{d\,L} \tag{3}$$

it is possible to calculate the maximum supply pressure ($p_{\lim}$) for the fabric without any damage in its structure.

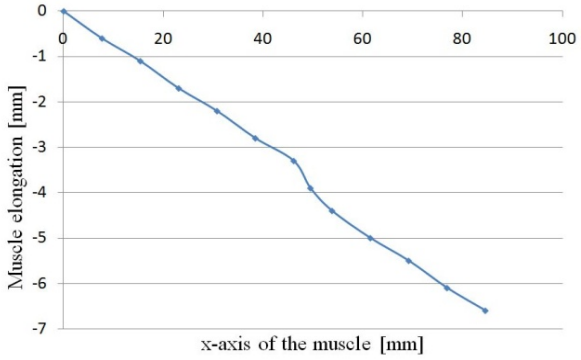

Figure 10 Axial strains (x) of the muscle over the entire length (100 mm – Fabric E).

In the formula d is the latex tube internal diameter and L is the sample wide. Fabric E has a higher contraction than Fabric D both in the simulation and in the experimental

tests. In Table IV the results obtained from simulation and the percentage error between experimental and numerical results are shown using Fabric E and various supply pressure. In particular: in the first simulation an anisotropic material was imposed with $E_x = 6845153$ N/m^2, $E_y = 3544426$ N/m^2, Poisson's ratio $\nu_{xy} = 0.35$, $\nu_{yz} = 0.32$, $\nu_{xz} = 0.32$; in the second simulation an anisotropic material was created with $E_x = 6845153$ N/m^2; E_y variable with the supply pressure applied, $E_z = 14146596$ N/m^2, Poisson's ratio variable; in the third simulation an anisotropic material equal to the second simulation was imposed with Poisson's ratio equal to $\nu_{xy} = 0.31$, $\nu_{yz} = 0.28$, $\nu_{xz} = 0.28$; in the forth simulation $E_x = 6845153$ N/m^2, $E_y = 3544426$ N/m^2, E_z and Poisson's ratio variable with the supply pressure applied were used. Overall the best correspondence between experimental and numerical model results is obtained with the first-second-third simulation.

Table IV – Contraction analysis with Fabric E.

Pressure [bar]	Contraction [mm] and percentage error					
	Experimental	Simulation1	Simulation2	Simulation3	Simulation4	Simulation5
0,5	**1,3**	2,3	2,3	1,9	3,1	3,0
		-76,92 %	-76,92 %	-46,15 %	-138,46 %	-130,77 %
0,8	**3,4**	3,6	3,8	3,4	5,0	5,4
		-5,88 %	-11,76 %	0,00 %	-47,06 %	-58,82 %
1	**5,0**	4,5	5,4	4,9	6,2	7,8
		10,00 %	-8,00 %	2,00 %	-24,00 %	-56,00 %
1,3	**7,1**	5,9	8,6	8,3	7,9	11,9
		16,90 %	-21,13 %	-16,90 %	-11,27 %	-67,61 %
1,5	**8,4**	6,9	10,9	10,9	8,8	14,3
		17,86 %	-29,76 %	-29,76 %	-4,76 %	-70,24 %

6 CONCLUSIONS

This article presents a preliminary study of several prototype pneumatic artificial muscles that can develop tensile forces when supply pressure is varied, and which consist of a textile structure. Their applications, in this case, are in the biomedical field, i.e. in rehabilitation and in assisting upper limb movement. Experimental tests were carried out to characterize the materials used and to gain an understanding of each prototype performance. These tests were followed by a theoretical study. The theoretical models of muscles presented here are reliable, as they relate to a muscle contraction which is small enough to be regarded as within the range of linear behaviour. The results obtained are good and provide interesting ideas for further work on these prototypes. In the next stage of the study presented here, the performance of the preliminary prototypes will be optimised in terms of achievable axial contraction. Now new experimental tests are carried on using a stronger textile material, directly produced on the market with a cylindrical geometry. This avoid the seam presence in the muscle prototype. Anyway the latex internal tube is required in order to guarantee the system air tightness.

ACKNOWLEDGEMENTS

Authors thanks Eng. A.L. Visan, Eng. F. Ekholm, Eng. C. Keipert, Eng. E. Rulfi, Eng. D. Contigiani for their help in this research.

REFERENCES

[1] Ranjan R., Upadhyay P. K., Kumar A. and Dhyani P., Theoretical and experimental modeling of air muscle. *International Journal of Emerging Technology and Advanced Engineering*, Vol. 2, No. 4, pp. 112-119, 2012.

[2] Wickramatunge K. C. and Leephakpreeda T., Empirical modeling of pneumatic artificial muscle. *Proceedings of the International MultiConference of Engineers and Computer Scientists*, Hong Kong, II, 2009.

[3] Pilch Z. and Bieniek T., Pneumatic muscle – measurement results and simulation models. *Proceedings of Electrotechnical Institute*, Issue 240, pp. 179-193, 2009.

[4] Belforte G., Quaglia G., Testore F., Eula G. and Appendino S., Wearable textiles for rehabilitation of disabled patients. *Smart Textiles for Medicine and Healthcare The Textile Institute*, Cambridge, UK In: L. Van Langenhove (Ed.), Chapter 12, pp. 221-251, 2007.

[5] Belforte G., Eula G. and Appendino S., Design and development of innovative textile pneumatic muscles. *The Journal of the Textile Institute*, doi: 10.1080/00405000.2011.603508, iFirst, pp. 1-11, 2011.

[6] Belforte G., Eula G., Ivanov A. and Visan A.L., Bellows textile muscle. *The Journal of the Textile Institute*, doi: 10.1080/00405000.2013.840414, Vol. 105, No. 3, pp. 1-9, 2014.

[7] Belforte G., Eula G., Ivanov A., Grassi R., Askri H. and Appendino S., Comparison of assembly techniques for textiles used in pneumatic devices. *The Journal of the Textile Institute*, doi: 10.1080/00405000.2013.846494, Vol. 105, No. 7, pp. 717-728, 2014.

[8] Belforte G., Eula G., Ivanov A. and Sirolli S., Soft pneumatic actuators for rehabilitation. *Special Issue "Soft Actuators" - Actuators*, doi: 10.3390/act3020084, Vol. 3, pp. 84-106, 2014.

[9] Ching-Ping C. and Blake H., Measurement and modeling of McKibben pneumatic artificial muscles. *IEEE Transactions on Robotics and Automation*, Vol. 12, No. 1, pp. 90-102, 1996.

[10] Klute G.K., Czerniecki J.M. and Hannaford B., McKibben Artificial Muscles: Pneumatic Actuators with Biomechanical Intelligence, IEEE/ASME 1999 Int. Conference on Advanced Intelligent Mechatronics (AIM '99), Atlanta (GA), 1999.

[11] Lomov S.V., Huysmans G., Luo Y., Parnas R.S., Prodromou A., Verpoest I. and Phelan F.R., Textile composites: modelling strategies. *Composites*, *Part A*, Vol. 32, No. 10, pp. 1379-1394, 2001.

[12] Caldwell D.G., Medrano-Cerda G.A. and Bowler C. J., Investigation of bipedal robot locomotion using pneumatic muscle actuators. *Proceedings of the 1997 IEEE International Conference on Robotics and Automation*, Albuquerque, New Mexico, 1997.

[13] Kobayashi H. and Hiramatsu K., Development of muscle suit for upper limb. *Proceedings of the 2004 IEEE International Conference on Robotics and Automation*, New Orleans, LA. 2004.

[14] Pan N. and Yoon M.Y., Structural anisotropy, failure criterion, and shear strength of woven fabrics. *Textile Res. J.*, doi: 10.1177/004051759606600409, Vol. 66, No. 4, pp. 238-244, 1996.

[15] Visan A., Alexandrescu N., Belforte G., Eula G. and Ivanov A., Experimental researches on textile laminate materials, *Industria Textila*, Vol. 63, No. 6, pp. 315-321, 2012.

[16] Boržíková J., Balara M. and Pitel J., The mathematical model of contraction characteristic k = (F,p) of the pneumatic artificial muscle. *Proceedings of XXXII. Seminar ASR'2007 - Instruments and Control*. pp. 21-25, 2007.

[17] Doumit M., Fahim A. and Munro M., Analytical modelling and experimental validation of the braided pneumatic muscle. *IEEE Transactions on Robotics*, doi: 10.1109/TRO.2009.2032959, Vol. 25, No. 6, pp. 1282-1293, 2009.

[18] Manuello Bertetto A. and Ruggiu M., Characterization and modeling of air muscles. *Mechanics Research Communications*, doi: 10.1016/S0093-6413(03)00088-0, Vol. 31, No. 2, pp. 185-194, 2004.

[19] Sui L. and Xie S., Modelling of pneumatic muscle actuator and antagonistic joint using linearised parameters. *Int. J. Biomechatronics and Biomedical Robotics*, pp. 67-74, 2013.

[20] Wang G., Wereley N.M. and Pillsbury P., Non-linear quasi-static model of pneumatic artificial muscle actuators. *Journal of Intelligent Material Systems and Structures*, doi: 10.1177/1045389X14533430, Vol. 26, No. 5, 2014.

[21] Kobayashi H., Hasegawa S. and Nozaki H., Development of muscle suit for supporting manual worker. *SICE Annual Conference 2007*, Kagawa University, Japan, 2007.

[22] Prior S.D. and White A.S., Measurements and simulation of a pneumatic muscle actuator for a rehabilitation robot. *Simulation Practice and Theory*, doi: 10.1016/0928-4869(95)00010-Q., Vol. 3, pp. 81-117, 1995.

[23] Sasaki D., Noritsugu T. and Takaiwa M., Development of wearable master-slave training device for upper limb constructed with pneumatic artificial muscles. *Proceedings of the 8th JFPS International Symposium on Fluid Power*, Okinawa, 2011.

[24] International Standard ISO 13934-1 (1999). *Textiles – Tensile properties of fabrics – Part 1: Determination of maximum force and elongation at maximum force using the strip method*.

[25] International Standard ISO 13934-2 (1999). *Textiles – Tensile properties of fabrics – Part 2: Determination of maximum force using the grab method*.

[26] Ekholm F., Textile pneumatic muscles design and testing for integration in textile active suits. E-team master's thesis, Politecnico di Torino, Torino, Italy 2012.

[27] Keipert C., Design and testing of textile pneumatic muscles for rehabilitation devices. E-team master's thesis, Politecnico di Torino, Torino, Italy 2012.

[28] Chen Q. and Pugno N.M., Modeling the elastic anisotropy of woven hierarchical tissues. *Composites*, doi: 10.1016/j.compositesb, Part B No. 42, pp. 2030-2037, 2011.

[29] Peng X.Q. and Cao J., A continuum mechanics-based non-orthogonal constitutive model for woven composite fabrics. *Composites*, Part A: Applied Science and Manufacturing, doi: 10.1016/j. compositesa.2004.08.008.2005; Vol. 36, No. 6, pp. 859-874, 2005.

[30] International Standard ISO 527-1:2012. *Plastics – Determination of tensile properties – Part 1: General principles*.

[31] International Standard ISO 527-2:2012 *Plastics – Determination of tensile properties – Part 2: Test conditions for moulding and extrusion plastics*.

[32] International Standard ISO 527-3:1995 *Plastics – Determination of tensile properties – Part 3: Test conditions for films and sheets*.

[33] International Standard ISO 527-4:1997 *Plastics – Determination of tensile properties – Part 4: Test conditions for isotropic and orthotropic fibre-reinforced plastic composites*.

[34] International Standard ISO 527-5:2009. *Plastics – Determination of tensile properties – Part 5: Test conditions for unidirectional fibre-reinforced plastic composites*.

ISSN 1590-8844
International Journal of Mechanics and Control, Vol. 17, No. 01, 2016

A NEW PARALLEL MANIPULATOR HYDRAULICALLY ACTUATED

K.S. Sholanov* K.A. Abzhaparov* Zh.T. Zhumasheva* M. Ceccarelli**

* Kazakh National Research Technical University after K.I Satpaev, Republic of Kazakhstan,

** LARM: Laboratory of Robotics and Mechatronics, University of Cassino, South Latium, Italy

ABSTRACT

The paper describes a new 6 DOF parallel manipulator named as SHOLKOR. The main properties of the new design are presented in terms of an analytical solution for direct kinematics and efficient force control of platform actions. Due to its properties, the proposed manipulator design can be used as an active support for protecting machines, buildings and other structures from disproportionate impacts. This application has been tested with a prototype by using controllable hydraulic actuator and results are reported to show the feasibility of the new design and its successful potentiality.

Keywords: Design, Parallel Manipulators, Active support, Hydraulic actuator

1 INTRODUCTION

Several parallel manipulator architectures are currently used in various fields. These manipulators have a structural topology that is similar to one of the Gough-Stewart platform [1-2]. However, most of the parallel manipulators with more than 3 degrees of freedom, show variable coordinates of the movable platform that are coupled to each other so that a movement of a drive requires simultaneous coordination with the other drives. There is not a general solution of the direct kinematic problem for parallel manipulators [3-5] and specific investigations are required for particular structures. Parallel manipulators are well understood for greater payload capability, stiffness, accuracy and dynamic performance as compared to traditional serial manipulators. Thus, parallel manipulators have attracted research interests for design and applications that can be achieved with less than 6 degrees of freedom (DOF). As shown in [6] parallel manipulator with three up to six degrees of mobility are used for guidance of the platform though three, four, five, and six points.

Contact author: Kuanysh Abzhaparov[1], Marco Ceccarelli[2]

[1] Kazakh National Research Technical University
22 Satpayev Str., Almaty 05040, Republic of Kazakhstan
Email: koli-87@mail.ru

[2] University di Cassino, Via di Biasio 43
03043 Cassino, Fr, Italy
Email: ceccarelli @unicas.it

The parallel structure was initially employed in the Gough machine for testing the tires of the airplane [7] and in Stewart Machine as a flight simulator [8]. CaPaMan (Cassino Parallel Manipulator) is a 3-DOF of spatial parallel manipulator, which has been conceived and built at Laboratory of Robotics and Mechatronics (LARM) in Cassino Italy [9] and [10]. Results of experimental tests have successfully proved a novel application of CaPaMan a 3-DOF spatial parallel manipulator, as a test bed earthquake simulator [11-14].

In [15] a parallel manipulator with pneumatic actuation is presented as the active controller supports, installed between the protected object and the source of sudden mechanical impacts. Thus, the idea to use parallel manipulators as active supports is substantially new.

In this paper a new parallel manipulator functionality is examined for the purpose of the substantiation of the use of parallel manipulators as an active support with six axes.

2 THE PROPOSED NEW DESIGN

The new parallel manipulator is based on a structure that has been introduced in [16]. This manipulator consists of two platforms that are connected with six connecting links (CL).

Figure 1 a) shows the structure of the proposed design of parallel manipulator whose main parts are: 1, which is the stationary platform, 2, which is the movable platform, and 3-8, which are six connecting links with a linear actuator.

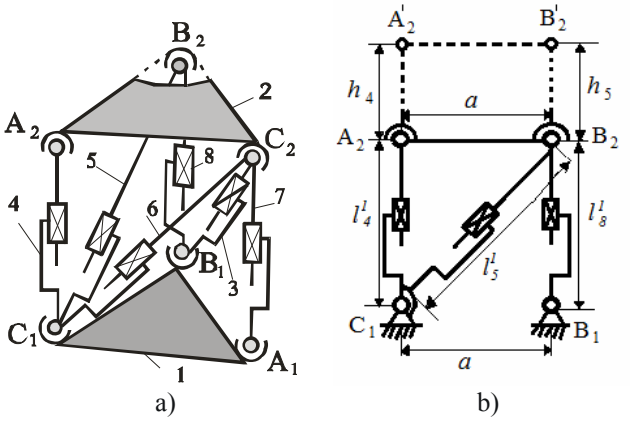

Figure 1 The proposed new parallel manipulator: a) a scheme of the structure; b) kinematic scheme with the variables l_i.

In order to show principle of link's lengths change on figure 1 b) it is shown the part of manipulator's kinematic scheme with links l_4, l_5, l_8. Variable lengths of links are expressed as $l_i = l_i^1 + h_i$ $(i = 3,\ldots,8)$ that are the input data. Where, l_i^1 – initial length of connecting links, h_i – change in length CL due to movement which is done by actuator mechanism. It is assumed that the points of the movable and stationary platforms form regular triangles $A_1B_1C_1$ and $A_2B_2C_2$ with sides$a$. The lengths of the other connecting links initially are selected to obtain a platform configuration in the form of the prism. Also, accept that the lengths of the ribs $l_4^1 = l_7^1 = l_8^1 = ka$; the diagonal of the rectangles faces of the prism is also equal, therefore $l_3^1 = l_5^1 = l_6^1 = a\sqrt{1+k^2}$. Here, k – is a coefficient selected for practical reasons.

Then using the introduced initial data for the considered parallel manipulator in analytical form, it is solved the direct problem of kinematics. This uses the method of converting the coordinate system, according to the eight parameters, as reported in [17]. Mathcad is used in the formation of the matrix transformation and in operations with them.

To determine the position of C_2 movable platform firstly we consider a pyramid $C_2A_1B_1C_1$ (Figure 2). Origin of coordinates $C_1X_1Y_1Z_1$, linked to the platform 1 is selected in the point C_1.C_1X_1 axis is directed along the A_1C_1 side of the $A_1B_1C_1$ triangle from C_1 to A_1.C_1Z_1 axis is directed perpendicular to the plane of the $A_1B_1C_1$ triangle. The position of C_2 depends on lengths l_3, l_6, l_7 of the 3, 6,7connecting links. To get the dependencies for determining the coordinates of the C_2 point in the considered pyramid, we perform a subsequent transformation of coordinate systems by three chains C_1-C_2, C_1-B_1-C_2, C_1-A_1-C_2 to match the basic coordinate system. The solution of the problem begins with the change of moving coordinate system $C_1X_6Y_6Z_6$, connected with the link 6, into the base coordinate system $C_1X_1Y_1Z_1$ by the chain C_1-C_2. Further, in this work, in order to exclude repeat of the geometric calculations the final calculations and some unique features are outlined. The transformation in (Figure 2) is worked out by a series of progressive movements of $C_1X_1Y_1Z_1$ system till complete matching with the coordinate system $C_1X_6Y_6Z_6$. The first movement is a turn of the system $O_1X_1Y_1Z_1$ at the angle θ_6 around axis C_1Z_1 until the axis $C_1X_1$is located in the base plane perpendicular to the axis C_1Z_6 ($\beta = \pi/2$).

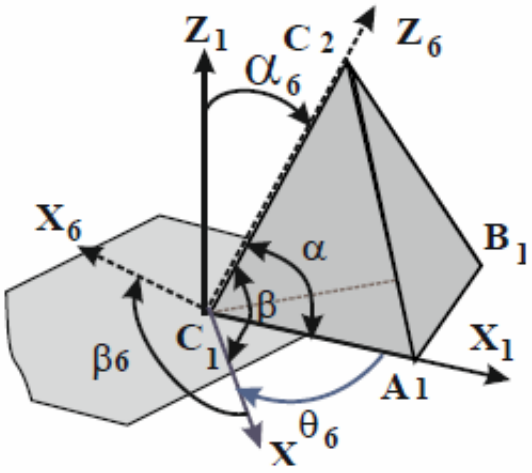

Figure 2 Main pyramid is determined by links 6, 7 and 3.

The pyramid geometry of figure 2 can be described by using the vectors as

$$\mathbf{r}_{C2}^0 = \mathbf{A}_6^0\mathbf{r}_6\,,\ \mathbf{r}_{C2}^0 = (x_{C2}\,y_{C2}\,z_{C2}\,1)^T\,,\ \boldsymbol{r_6} = (0\ 0\ l_6\ 1)^T,$$

$$\mathbf{r}_{C2}^0 = \mathbf{A}_{03}^0\mathbf{A}_3^{03}\mathbf{r}_3\,,\ \boldsymbol{r_3}=(0\ 0\ l_3\ 1)^T, \qquad (1)$$

$$\mathbf{r}_{C2}^0 = \mathbf{A}_{07}^0\mathbf{A}_7^{07}\mathbf{r}_7\,,\ \boldsymbol{r_7} = (0\ 0\ l_7\ 1).$$

Manipulating equations (1) gives the coordinates of the point C_2 and angles α_3, α_6, α_7 in the form

$$\alpha_7 = Sin^{-1}\left(\frac{B\cdot a}{F\cdot B - G\cdot A}\right)$$

$$y_{C2} = -G\cdot\frac{B\cdot a}{F\cdot B - G\cdot A},\ z_{C2} = l_7\cdot Cos(\alpha_7) \qquad (2)$$

$$\alpha_6 = Sin^{-1}\left(\frac{x_{C2}}{A}\right),\ \alpha_3 = Cos^{-1}\left(\frac{z_{C2}}{l_3}\right)$$

Here we introduce the auxiliary variables

$A = l_6\cdot Sin(\theta_6)$, $B = l_6\cdot Cos(\theta_6)$

$F = l_7\cdot Sin(\theta_7)$, $G = l_7\cdot Cos(\theta_7)$

The position of the B_2 can be determined from the geometry of tetrahedron Figure 3 *a* with the condition that it B_2 is situated on the surface of the sphere with the radius C_2B_2. Thus, the position of B_2can be determined by a

matrix equation, from $\mathbf{A}_5^0, \mathbf{A}_{08}^0, \mathbf{A}_8^{08}$ matrixes that are expressed with eight parameters from

$$\mathbf{r}_{B2}^0 = \mathbf{A}_5^0 \mathbf{r}_5 \,,\ \boldsymbol{r_5} = (0\ 0\ l_5\ 1)^T,$$
$$\mathbf{r}_{B2}^0 = \mathbf{A}_{08}^0 \mathbf{A}_8^{08} \mathbf{r}_8 \,,\ \boldsymbol{r_8} = (0\ 0\ l_8\ 1)^T \quad (3)$$

When the condition is considered as

$$(x_{C2} - x_{B2})^2 + (y_{C2} - y_{B2})^2 + (z_{C2} - z_{B2})^2 - a^2 = 0 \quad (4)$$

Solving of equations (3) and (4) gives

$$\alpha_8 = Sin^{-1}\left[\frac{a(A1\sqrt{3} - B1)}{A1 \cdot D1 + B1 \cdot C1}\right],\ z_{B2} = (h_8 + l_8)Cos(\alpha_8)$$
$$(x_{B2})_{1,2} = \frac{-P \pm \sqrt{P^2 - U1(1+k^2)}}{1+k^2} \quad (5)$$
$$y_{B2} = \frac{B1 \cdot x_{B2}}{A1},\quad \alpha_5 = Sin^{-1}(\frac{x_{B2}}{A1})$$

Here auxiliary variables used: A_1, B_1, C_1, D_1, k, U, P.

$$A1 = \sin(\theta_5) \cdot l_5,\ \ B1 = -\cos(\theta_5) \cdot l_5,\ \ C1 = [\sin(\theta_8 + \sqrt{3}\cos(\theta_8)] \cdot l_8,$$
$$D1 = [\cos(\theta_8) - \sqrt{3}\sin(\theta_8] \cdot l_8,$$
$$U = \{z_{C2} - l_8 \cdot \cos\left[\frac{a(A1\sqrt{3} - B1)}{A1 \cdot D1 + B1 \cdot C1}\right]\}^2 - a^2$$

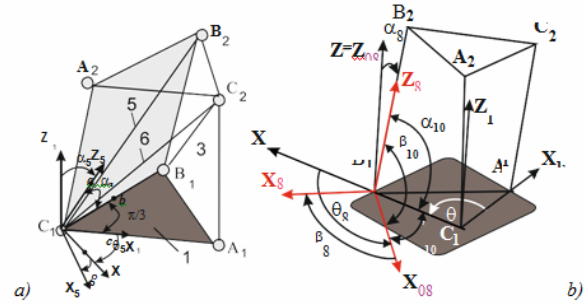

Figure 3 Geometry of tetrahedron with kinematic variables: (a) by the chain C_1-B_2; (b) by the chain C_1-B_1-B_2

Therefore coordinates of A_2 must satisfy the following three equations

$$(x_{A2} - x_{B2})^2 + (y_{A2} - y_{B2})^2 + (z_{A2} - z_{B2})^2 - a^2 = 0\,,$$
$$x_{A2}^2 + y_{A2}^2 + z_{A2}^2 - (l_4 + h_4)^2 = 0, \quad (6)$$
$$(x_{C2} - x_{A2})^2 + (y_{C2} - y_{A2})^2 + (z_{C2} - z_{A2})^2 - a^2 = 0$$

Solving equations (6) it is obtained

$$(z_{A2})_{1,2} = \frac{-\nu \pm \sqrt{\nu^2 - 4 \cdot \mu \cdot \tau}}{2\mu}$$
$$x_{A2} = \frac{\frac{1}{2}(\varepsilon \cdot y_{C2} - \eta \cdot y_{B2}) + (z_{C2} \cdot y_{B2} - z_{B2} \cdot y_{C2}) \cdot z_{A2}}{x_{B2}y_{C2} - x_{C2}y_{B2}} \quad (7)$$
$$y_{A2} = \frac{\frac{1}{2}(\eta \cdot x_{B2} - \varepsilon \cdot x_{C2}) + (z_{B2} \cdot x_{C2} - z_{C2} \cdot x_{B2}) \cdot z_{A2}}{x_{B2}y_{C2} - x_{C2}y_{B2}}$$

In (7) variables used are given by

$$\varepsilon = (l_5)^2 - a^2 + (l_4)^2,\quad \eta = (l_6)^2 - a^2 + (l_4)^2,$$
$$Q = y_{C2}^2 + x_{C2}^2,\quad R = y_{B2}^2 + x_{B2}^2,$$
$$S = y_{C2}y_{B2} + x_{C2}x_{B2},\quad T = y_{C2}x_{B2} - x_{C2}y_{B2},$$
$$\mu = Qz_{B2}^2 + Rz_{C2}^2 - 2Sz_{B2}z_{C2} + T,$$
$$\nu = -\varepsilon Q z_{B2} - \eta R z_{C2} + \eta S z_{B2} + \varepsilon S z_{B2}$$
$$\tau = Q\varepsilon^2/4 + R\eta^2/4 - S\varepsilon \cdot \eta/2 - (x_{B2}y_{C2} - x_{C2}y_{B2})^2 (l_4)^2$$

Position point C_2 is determined by the variable lengths l_3, l_6, $l_7$of links 3,6,7; the position of the B_2 is determined by links l_5, l_8,and also depends on the position of the C_2; the position of the A_2 is determined by length l_4 and depends on the positions of C_2 and B_2. Thus, using egs (1) to (7) the configuration of the platform can be computed. As an example, on the basis of obtained algorithm using Matlab made calculations and diagrams were constructed for translational (fig. 4,a), spherical (fig. 4,b) motion.

In the calculations were taken: a=580 mm; k=1.2 ; for translational motion h_4= h_7= h_8=8 mm, h_3= h_5= h_6=6 mm; for spherical motion h_3= h_6= h_7=0., h_4= h_5= h_8=8 mm; number of cycles N=5.

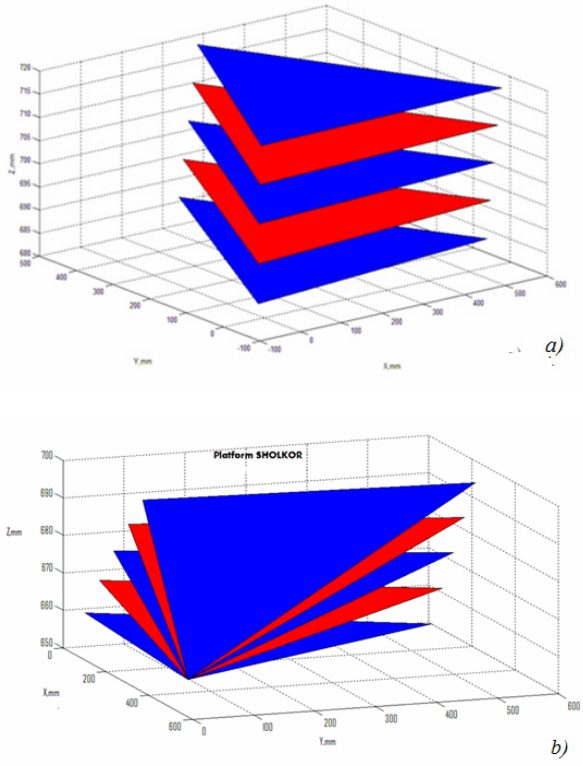

Figure 4 Computed platform position by using Eqs (1) to (7) a) translational motion; b) spherical motion.

3 KINESTOTATIC ANALYSIS

These pressures for each hydraulic drive are determined by power analysis of adaptive support's bearing platform.
In Fig. 5 it is shown a diagram of the application as an active parallel manipulator support SHOLKOR. An active support is located between the object 0 and base 9. The manipulator has two platforms 1 and 2 that are connected by six connecting links 3-8 (Fig. 5, b). The lengths of the connecting links are changed by a controlled electrohydraulic drive (Fig. 8).

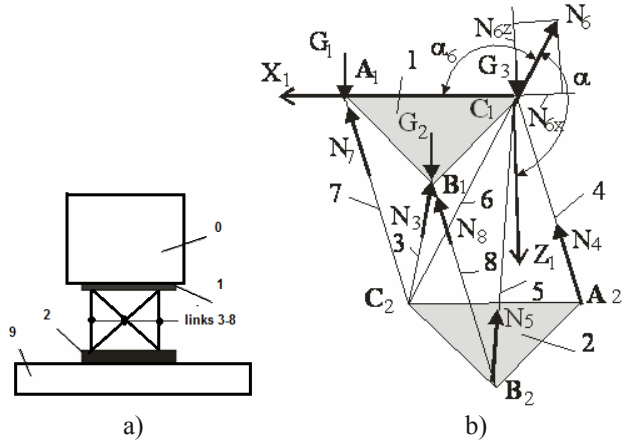

a) b)

Figure 5 A model for kinestatic analysis: a) the system structure; b) a scheme with acting forces.

When a mechanical action acts on the base 9, platform 2 is moved together with the base. If the support is represented by a rigid structure, then at moving to the lower platform 2 it would move together with the upper platform 1and protected object. However, the length of the connecting links 3-8 of the active support can be varied and they compensate the movement of the lower platform. The main purpose is to provide the state of rest of the protected object. The kinestatic analysis can be as in the following.
On the platform 1 the forces of gravity G_1, G_2, G_3 of the object and platform will act at the three nodal points A_1, B_1, C_1 . On the other hand the reaction forces N_3, N_4, N_5, N_6, N_7, N_8 from the six hydraulic actuators of connectors 3-8 are directed along the corresponding links. It can be noted that these reactions depend on the inertia forces applied to the platform 2 and mechanical impact forces. Thus kinetostatics equations can be expressed as:

$$\begin{aligned}
&\sum_{i=3}^{i=8} N_{ix} = 0; \ \sum_{i=3}^{i=8} N_{iy} = 0;\\
&\sum_{i=3}^{i=8} N_{iz} + G_1 + G_2 + G_3 = 0;\\
&\sum_{i=3}^{i=8} M_x(\mathbf{N}_i) + y_{A1}G_1 + y_{B1}G_2 = 0;\\
&\sum_{i=3}^{i=8} M_y(\mathbf{N}_i) - x_{A1}G_1 - x_{B1}G_2 = 0;\\
&\sum_{i=3}^{i=8} M_z(\mathbf{N}_i) = 0.
\end{aligned} \qquad (8)$$

Here the coordinates (x_{A1},x_{B1},y_{A1},y_{B1})) of A_1, B_1 points of application of vector forces $\mathbf{N_i}$ are known since they are determined from the kinematic calculations. For example, Fig. 5 *b)* shows the reaction force N_6 applied to a point C_1, which coincides with the origin of the $C_1X_1Y_1Z_1$ coordinate system. In Fig. 5 *b)* the projection force N_6 on axis C_1Z_1 and C_1X_1 are determined by

$$N_{6z} = N_6 Cos\alpha_6 , \ N_{6x} = N_6 Cos\alpha \qquad (9)$$

In these equations angle α6 and α are determined according to Fig. 2 from equation (2). Thus in the six equations (8), the unknown variables are the quantities of the six hydraulic drives' reaction forces N_i *(*i = 3,…,8*)*. Each N_i force depends on the liquid pressure in the cavity i - of the hydraulic cylinder' rod P_{Ni} and the piston area S_i and is defined by the equation N_i=$P_{Ni}S_i$. Therefore by solving the equations (8) the fluid pressure P_{Ni} is determined in the hydraulic cylinder's rod cavities of six connectors. Thus, the static state of the protected object is achieved by maintaining the desired pressure P_{Ni} in hydraulic cylinder's rod cavities of six connectors.
If the forces of gravity G_1, G_2, G_3 are identified by a force sensor in 3-nodal points A_1, B_1, C_1, then the pressure in the cavities of hydraulic cylinders P_{Si} can be determined by a pressure sensor installed in each hydraulic cylinder of the pressure chamber.

4 DESIGNS AND CONSTRUCTION OF A PROTOTYPE WITH MANUAL CONTROL

A prototype which is shown in Fig. 6 is built in order to demonstrate the possibilities of the parallel manipulator positioning. Prototype consists of the lower (stationary) platform 1, the movable platform 2. Platforms of the manipulator are connected using six connecting links, the lengths of which are changed with hydraulic actuators 3 with manually operated spill valves 4.
Figure 7 shows the specific mechanical designs of the spherical joints that are used for the construction of a prototype of the parallel manipulator with the topology of the structure shown in figure 1 *a*. In spherical three link joint (Figure 7, a) link 1 has a hollow spherical head, which its outer surface forms a spherical connection with a spherical head of link 2 and its inner surface forms a spherical relation to the round head element 3. Four link spherical joint (Figure 7,b) composed of a cardan connection with the universal-joint fork 6 and 7, in which the crossbar is made in the form of a spherical race 8, which forms a spherical connection with the links 4 and 5 is similar to spherical three link connection is shown in (Figure 7,a).
Research conducted on the prototype had helped to persuade the parallel manipulator's features, namely:
Each of the six actuators (Figure 6) can move independently. For example, it is possible to change the length of a one connecting links using the drive without changing lengths of the other connecting links, with corresponding motion.

Figure 6 The prototype of the parallel manipulator Sholkor
1-stationary platform; 2- movable platform;
3- actuators; 4- regulating valve.

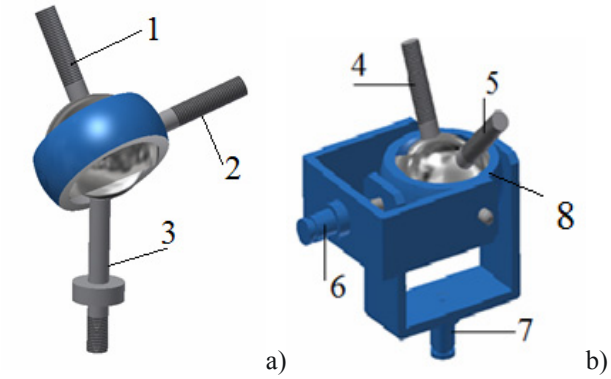

Figure 7 Multilink spherical joints: a) three link spherical joint; b) four link spherical joint.

By varying lengths of a certain set of CL in a pre-specified way, it is possible to obtain any spatial position of the movable platform or simple movements.
Each spatial position of the movable platform meets certain length of CL. From this it follows that it is possible to move the movable platform as a leading element, thus, as a consequence the length of CL will vary. Namely, due to these peculiarities, the manipulator under consideration can be used as active support, where in under the action of mechanical impact's a source, the lower platform as guide link can perform the spatial movement, relative to the upper platform, which related to the protected object.

5 THE PROTOTYPE CONSTRUCTION OF THE ACTIVE SIX AXLE SUPPORT

In order to respond to the action of source of sudden mechanical impacts and to avoid the disturbance action on the protected object between the protected object and the source of mechanical impacts, it is installed the active support. In this operation, as an active control support for large mass objects will be proposed a parallel manipulator. Therefore, the parallel manipulator must be equipped with hydraulic actuators with automatic control, operating in the mode of controlled dampers.

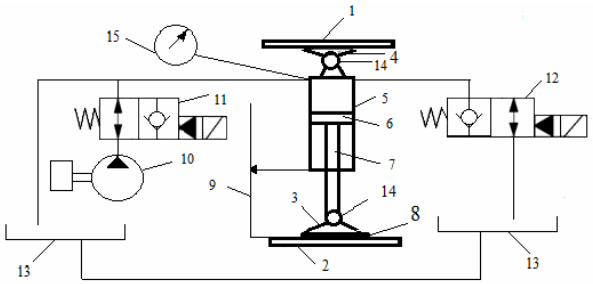

Figure 8 A scheme of an hydraulic actuator for active support.

Figure 8 shows the system of one automatically operated hydraulic actuator of the parallel manipulator. The actuator of an active support installed between the protected object 1 and the source of impact 2 and consists of the lower (movable) 3, the upper (stationary) platform 4. Actuating motor is in the form a hydraulic cylinder of unilateral actions 5, with the piston 6 and a rod 7. The force sensor (FS) 8 determines the load on the lower movable platform. The motion sensor (MS) 9 measures the movement of a rod of a hydraulic cylinder. The hydraulic system consists of pump station 10, normally open delivery solenoid valve (NO) 11 and normally closed electromagnetic drain (bleeding) valve (NC) 12, the tank 13. The sensor (PS) 15 measures the pressure in the piston chamber. The movable and lower platforms are connected to the hydraulic cylinder by ball joints 14. Work of a controlled hydraulic actuator is to provide automatically the required pressure in the piston cavity of a hydraulic cylinder.
Dissipation mechanism of sudden mechanical impacts based on the fact, that at any given time, by controlling the pressure in the upper enclosure of six hydro cylinders can be achieved the equilibration forces, acting on the upper platform, i.e. stationary upper platform, while when the lower platform can perform unwanted movements, together with the source of mechanical impacts. In this connection the control system of each hydraulic drive should automatically provide the necessary pressure in the cylinder above the piston enclosure of hydraulic actuator. Figure 8 shows an algorithm flowchart of hydraulic actuator's control an active support.
According to the algorithm, the active support in the form of parallel manipulator is set to the initial position. At each position, nominal values at step 1 are set by scanning the sensors. Upon detection of impact the controller will consider the sensor data, step 1. With the known position of the platform (by position sensor) the value of pressure is determined at step 2. At step 3 the calculated pressures in enclosure of the hydraulic cylinders are compared with the sensed pressure and are fed to give a binary signal on one of the valves to proceed to step 4. When the pressures are equal, then the state of valves is not changed. At step 4, as depending of the condition PH>PD a signal will be give to open or close the valve in order to keep controlled the object position.

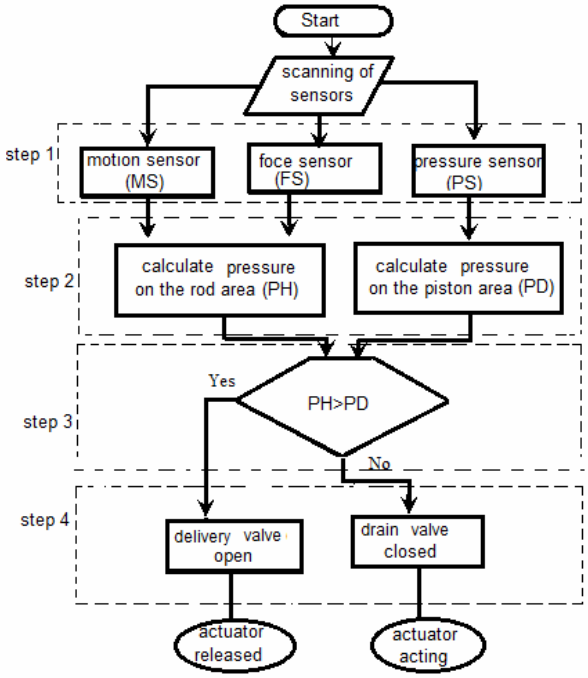

Figure 9 A flowchart of the control algorithm for the generation of active support at each position.

In order to investigate the possibility of using parallel manipulator as a six axle active support in the work created a prototype active controlled support (Figure 10).
Each hydraulic actuator in this parallel manipulator has a hydraulic circuit diagram shown in figure 7. Each hydraulic drive is equipped with pressure sensors 3, movement sensors 2, force sensors 1 between the movable platform and three connecting points. Actuators are six delivery valves 4 and six drain solenoid valves 5. The hydraulic system of actuators an active support is powered by a hydraulic pump 6.
To perform the operation of the parallel manipulator as active support, the control system (CS) shown in Figure 11 was designed. The Figure 10 displays the same notation as in Figure 7, except for number 16 that indicates Mitsubishi FX3U - 16MR/ES industrial controller.
The controller 16 (Figure 11) processes the signals from the pressure sensors 15, motion sensors 5 and the force sensor 8. The algorithm is implemented as a program for controller FX3U - SCADA visualization system displays 16mr / ES in algorithmic language C. Current system parameters and modes of valves operation on the computer screen (Figure 12).

6 AN EXPERIMENTAL CHARACTERIZATION

An active control support must react promptly to the action of contingencies action's sources and prevent the effects on the protected object by harmful disturbances. In this way the effectiveness of the active support's functioning in a large extent is determined by its motor reaction.

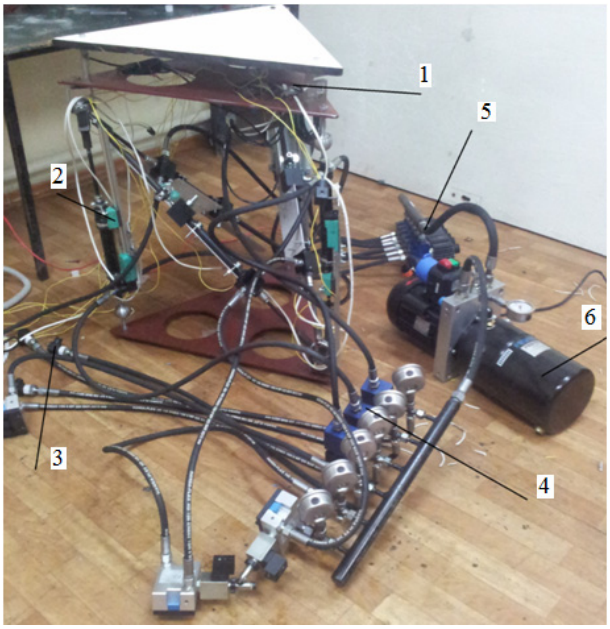

Figure 10 A prototype of active support of the parallel manipulator: 1-force sensor; 2- movement sensor; 3- pressure sensor; 4- delivery valve; 5-drain solenoid valve; 6- hydraulic pump.

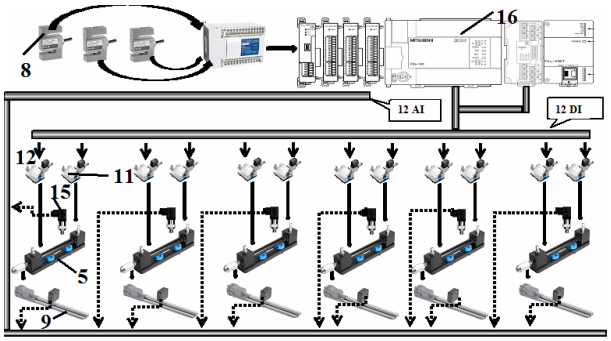

Figure 11 Components of the active support control system for prototype in Figure 10
8- force sensor; 9- piston sensor; 11, 12- valves of cylinders; 15- pressure sensor; 16- controller.

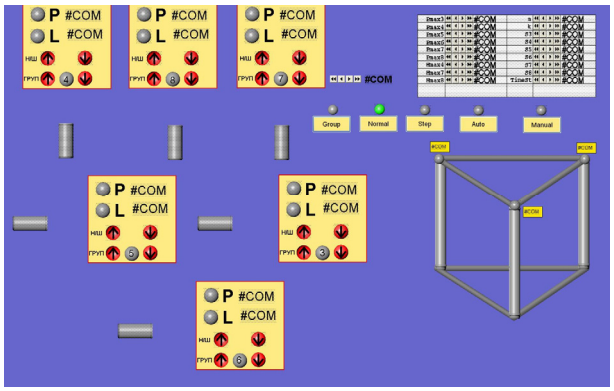

Figure 12 Screen programs in SCADA system

It is known that under consideration motor reaction we understand the time of the quickest answer, done by simple and well known in advance movement to the signal, which appears suddenly, but which is well known. The motor response of active support depends on the motor reactions of controlled hydraulic actuators. In this connection, it is given an experimental investigation of the motor reactions of controlled actuators by applying the prototype of the active support (Fig. 10).

For carrying out experiments on the movement platform of the parallel manipulator freight of the set weight of 15 kg settled down. Sensors of the movement were installed in the initial situation when rods are in a starting position. Using force sensors and sensors of pressure values of the efforts operating on a rod and pressure in working cavities of hydraulic cylinders were defined. The controller processed these values and used by the program of the managing director of the parallel manipulator. Then, according to the set sequence, the control unit exercised to control the movement of a platform of the parallel manipulator. The controller processed the received data from the information and measuring system according to the set program, and the graphs of the dependence of movement of a rod and pressure in a hydraulic cylinder of the drain valve were displayed on the SCADA monitor. It should be noted that in the prototype of active support generally is available on three hydraulic actuators of a look 7 and 3 which differ in that in a hydraulic actuator 7 diameter of the d1 piston = 20 mm., and in a hydraulic actuator 3 diameter of the piston of a hydraulic cylinder of d2 = 16 mm., also in a hydraulic actuator 7 the piston has choking openings, and a hydraulic actuator 3 – there are no choking openings. However, all hydraulic actuators are unilateral with a returnable spring.

On the graphs (Figure 13) received for a hydraulic actuator 3 as a result of measurements during t=4s. Experimental data give the chance to measure a time interval of delays of which motive reaction of a concrete hydraulic actuator is formed. Indeed, the schedules constructed for a hydraulic actuator 3 that after the command for closing off the drain valve forcing of working fluid in a hydraulic cylinder cavity begins. The pressure in a cavity of a hydraulic cylinder starts changing through Δ_1=0.37s time and after Δ_2=0.37s the movement of a rod of a hydraulic cylinder starts. Thus, movement reaction of a hydraulic actuator to the team of promotion of a rod by closing off the drain valve makes up Δ_{ON}=074s. The same schedules allow determining time intervals of a delay on team lowering of a rod. The team of lowering of a bar is realized by the opening of the drain valve. Thus, working fluid pressure in a cavity of a hydraulic cylinder falls, and the rod under the influence of a returnable spring descends. As it can be seen from the results of the experiment (Figure 13), after opening the drain valve before reduction of pressure in a cavity is observed a temporary delay of Δ_3=0.25s. Then from the moment of reduction of pressure before the movement of a rod passes Δ_4=0.25s time interval. Thus, motor reaction to the return trip of a rod makes Δ_{Off}=0.5s.

Similar test studies were conducted with the hydraulic actuator 7 with choking channels. These data were captured during the time frame t=4s (Fig. 14) and carried out with the purpose to determine movement reaction of the drive with a choking on the execution of the command of promotion of a rod.

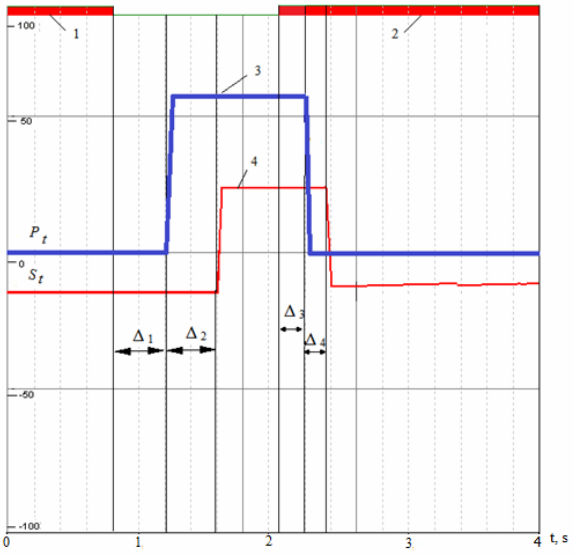

Figure 13 An experimental curve of hydraulic actuator 3 on the pressure and displacement with time
1,2 – schedules for a phase of opening of the drain valve;
3 – schedule of change of pressure in a rod plenum;
4– schedules of change of movement of a rod

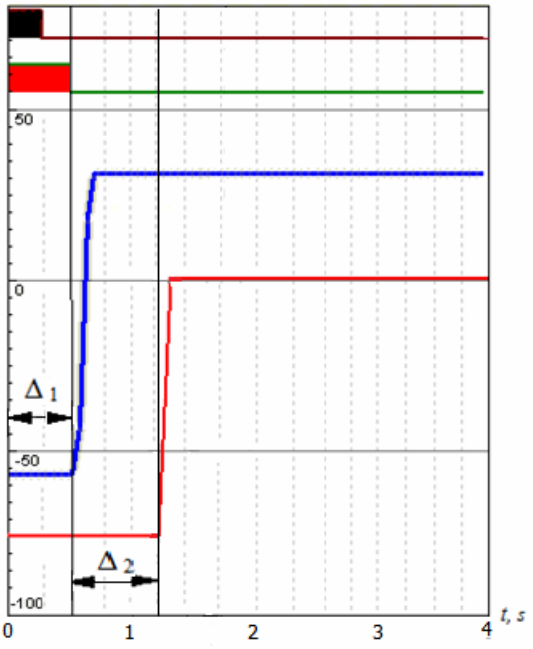

Figure 14 An experimental curve of hydraulic actuator 7 on the pressure and displacement with time.

As appears from these experiments after closing the drain valve before the pressure increases time frame of Δ_1=0.5s passes in a cavity of a hydraulic cylinder and further after the beginning of the rise in pressure before the movement of a rod Δ_2 time frame = 0.82s. passes. Thus, motor reaction of the given hydraulic actuator to the command of a rod movement makes Δ_{ON}=1.32 s.

Thus, the technique for definition the motor reactions of drives on experimental samples are obtained. The received results characterizing components of motor reactions of two types of hydraulic actuators allow us to make the following conclusions: the working fluid ways are the reason of delays of Δ_1; motor reaction of Δ_{ON} of a hydraulic actuator with choking channels is more than in a hydraulic actuator without choking. It means that improvement of motor reaction of the drive requires joint execution in a hydraulic actuator of actuation mechanisms and control equipment's, i.e. application of the mechatronic hydraulic actuators is necessary to exclude the impact of the working fluid ways. On the other hand, experiments showed that application of the choking elements in hydraulic actuators in the parallel manipulator used as active supports decreases their motor reaction.

Results of the test studies showed that it is possible to achieve the required figures of motor reactions so that the parallel manipulator hydraulically actuated could be used as an active controlled support.

7 EXAMPLE OF THE ACTIVE SUPPORT APPLICATION AS A SEISMIC ISOLATION SYSTEM

As an example we shall consider the implementation of combined technology of seismic protection consisting (Figure 15) of active and passive seismic systems, between the ground part of the building 1 and foundation 2 with the bottom part of base 3 are to be installed passive seismic isolation devices, for example, such as kinematic foundations 4. On the sides of the base of the building for liquidating horizontal inertial forces are installed systems of active seismic protection, composed of eight parallel manipulators 5 [18].

Some parallel manipulators depends on the construction area. Calculations for the first option of the combined system, as per bearing capacity, by average values in the hydraulic system of 35 bars and piston diameter of 250 mm show that one parallel manipulators installed for every 220 sq.m. of the building area. The practice shows that approximate weight of 1 sq.m. of the building is ten kN. There are a lot of areas in which the use of active supports is of vital necessity.

CONCLUSION

In this article in the analytical form is solved the direct problem of parallel kinematic's manipulator with a new topology structure. The solution of the direct problem of kinematics, and also the prototype of the parallel manipulator had shown that the parallel manipulator has got the functional possibilities which enable to use it as the active control support.

To substantiate the possibilities of using the parallel manipulator as active support is created the prototype of the active six axle support. The scheme of automatically controlled hydraulic drive is developed. The algorithm of drive's control in the mode of active support is created.

From the results of experimental investigations of the motor reactions value in hydraulic actuators follows, that for improving the drive's motor reaction it is necessary to use the mechatronic hydraulic actuators without the throttling elements.

The value of the motor reaction, equal to 0.74 c., which is derived for hydraulic drive without throttling apertures which indicates that the parallel manipulator can be used as an active controlled support.

A diagram of a seismic protection system shows the possibility of application in the future the parallel manipulators as active controlled support.

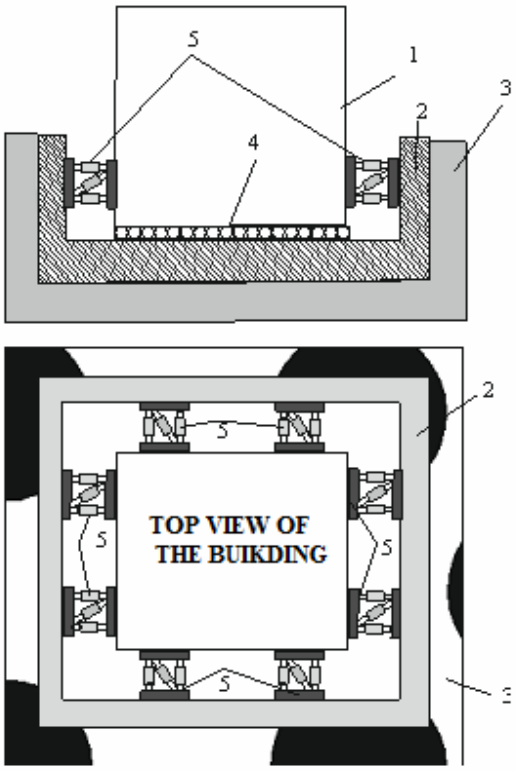

Figure15 An example of active isolation seismic systems with parallel manipulator
1-the ground part of the building; 2-foundation; 3-the bottom part of the base; 4-kinematic foundations; 5-parallel manipulator isolation units.

REFERENCES

[1] Stewart D.A., Platform with six degrees of freedom, *Proceedings of the Institution of Mechanical Engineers*, London. Vol. 180, No 15, pp. 371-385, 1965.

[2] Dasgupta B., Mruthyunjaya T.S., The Stewart platform manipulator: a review. *Mechanism and Machine Theory*, Vol. 35, pp. 15-40, 2000.

[3] Merlet J.P., *Parallel Robots*. Springer Publishers, Dordrecht, 2006.

[4] Angeles J., *Fundamentals of robotic mechanical systems: theory, methods and algorithms*. 2nd Ed., Springer, pp. 520, 2002.

[5] Nanua P., Waldron K.J., Murthy V., Direct kinematic solution of a Stewart platform. *IEEE Trans. On Robotics and Automation*, Vol. 6, pp. 438-444, 1990.

[6] Gao F., Li W., Zhao X., Jin Z., Zhao H., New kinematic structures for 2-,3-,4-, and 5-DOF parallel manipulator designs. *Int. J. Robot*, Res 21, pp. 799-810, 2002.

[7] Wang Y., A direct numerical solution to the forward kinematics of general Stewart-Gough platforms. *Robotic*, Vol. 25(01), pp. 121-128, 2006.

[8] Cao Y., Singularity kinematics principle and position singularity analyzes of the 6-3 Stewart-Gough parallel manipulators. *Journal of Mechanical Science and Technology*, Vol. 25(2), pp. 513-522, 2011.

[9] Ceccarelli M., A new 3 d.o.f. parallel spatial mechanism", *IFToMM Journal Mechanism and Machine Theory*, Vol. 32, No. 8, pp. 895-902, 1997.

[10] Ceccarelli M., Historical development of CaPaMan, Cassino Parallel Manipulator, *New Trends in Mechanisms and Machine Science*, Springer Dordrecht, pp. 749-747, 2012.

[11] Ottaviano E., Ceccarelli M., An application of a 3-dof parallel manipulator for earthquake simulations. *IEEE Transactions on Mechatronics*, Vol. 11, No. 2, pp. 140-146, 2006.

[12] Ceccarelli M., Ottaviano E., Galvagno M., A 3-dof parallel manipulator as earthquake motion simulator. *7th International Conference on Control, Automation, Robotics and Vision ICARCV 2002*, Singapore, paper P1534, 2002.

[13] Ottaviano E., Ceccarelli M., Castelli G., Experimental results of a 3-dof parallel manipulator an earthquake motion simulator. *ASME Design Engineering Technical Conference and Computers in Engineering Conference*, Salt Lake City, Paper DETC2004-57075, 2004.

[14] Selvi O., Ceccarelli M., An experimental evaluation of earthquake effects on mechanism operation. *Proceedings of the Int. Symposium of Mechanism and Machine Science AzCIFToMM*, Izmir,Turkey, pp. 408-416, 5-8 October 2010.

[15] ThanhLeю, KyoungDanh, Kwan Ahn., Active pneumatic vibration isolation system using negative stiffness structures for a vehicle. *Journal of Sound and Vibration*, Vol. 333, No. 5, pp. 1245-1268, 2014.

[16] Sholanov K.S., *Platform robot manipulator*. WO/2015/016692/5.02.2015.

[17] Sholanov K.S., Manipulator of a platform type robot Sholkor. *Advanced Materials Research*, Vol. 930 pp. 321-326, 2014.

[18] Sholanov K.S., *Combined earthquake protection system (variants)*. WIPO WO2015/099519A1, 02.07.2015.

ISSN 1590-8844
International Journal of Mechanics and Control, Vol. 17, No. 01, 2016

MAGNETIC AND STRUCTURAL CO-DESIGN OF SYNCHRONOUS RELUCTANCE ELECTRIC MACHINES IN AN OPEN-SOURCE FRAMEWORK

Simone Ferrari Gianmario Pellegrino Elvio Bonisoli

Politecnico di Torino, corso Duca degli Abruzzi, 24 – 10129 Torino Italy

ABSTRACT

Synchronous reluctance motors (SyRM) produce torque thanks to the rotor magnetic anisotropy, without use of permanent magnets (PMs) or windings on their rotor. Consequently, SyRMs are cost-competitive against costly PM synchronous machines and more efficient than asynchronous motors, because of the absence of the squirrel cage and related Joule loss in the rotor. The SyR motor's rotor laminations have air cavities called flux barriers carved in each pole to maximize anisotropy and torque. The rotor iron parts, called flux carriers, are kept together by tiny pieces of steel called the structural ribs, which withstand significant centrifugal stress at high operating speed. If the ribs size is increased, more flux bypasses the flux barriers are bypassed and the reluctance torque diminishes. Altogether, magnetic anisotropy and structural integrity need a proper co-design strategy to be formulated. Since magnetic design relies on non-negotiable 2D finite element model (FEM) analysis, using 2D-FEM also for centrifugal stress evaluation would lead the computational burden to unacceptable levels. The paper develops a comprehensive co-design methodology based 2D magnetic FEM and beam structural analysis (1D-FEM), that limits the size of the structural problem and make extra time dedicated to structural computation negligible.

Keywords: synchronous reluctance machine, design of electrical machines, magnetic and structural co-design, high speed rotors, high speed electrical machines

1 INTRODUCTION

Synchronous Reluctance machines (SyRMs) are a class of AC electrical machines renowned for their high-efficiency and convenient manufacturing cost [1-3]. They are more efficient than asynchronous machines and less expensive than permanent magnet synchronous machines, because of the absence of magnets. Recently, they have been considered for high-speed applications [4-5]. The stator of a SyRM resembles the one of a standard induction motor (IM). Design wise, the most important part of a SyRM is the rotor. Synchronous reluctance torque (1) is maximised by maximization of the difference between the *d*- and *q*-axis inductances:

$$T = \frac{3}{2} p \cdot (L_d - L_q) \cdot I_s \cdot \frac{\sin(2\gamma)}{2} - \Delta T_{ribs} \quad (1)$$

where *d* and *q* are the rotor directions defined in Fig. 1, I_s is the amplitude of the stator phase current and γ is the phase angle of the current vector in the *dq* reference frame, synchronous to the rotor. The two inductances L_d and L_q summarize the properties of the two rotor axes: *d* is the direction of maximum permeability (Fig. 1a), whereas *q* is the direction of maximum reluctance (Fig. 1b).

The reluctance comes from the presence of the rotor cavities, called the flux barriers. The difference (L_d - L_q) determines the reluctance torque of the machine (1). A subtractive torque component comes from the rotor ribs flux linkage λ_{ribs} [Vs], that is the flux that bypasses the flux barriers in the *q* direction via the structural ribs. Such ribs, defined in Fig. 2, keep together the rotor parts. Their negative impact on torque is roughly proportional to the sum of their widths (w_{rib}):

$$\Delta T_{ribs} = \lambda_{ribs} \cdot I_s \cdot \cos(\gamma) \propto \sum_{j=1}^{nribs} w_{rib,j} \quad (2)$$

Contact author: Simone Ferrari

Email: simone.ferrari@polito.it

The design of high-speed SyRM rotors requires that (2) is minimized while structural integrity at maximum speed is retained. The key point of such tradeoff is the design of the structural ribs.

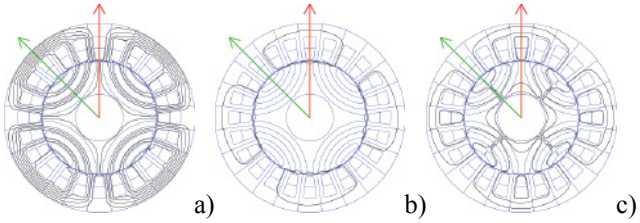

Figure 1 Flux lines when the two main rotor directions (d = red, q = green) are magnetized with the same peak current. a) d-axis; b) q-axis, with tangential ribs; c) q-axis, with tangential and radial ribs.

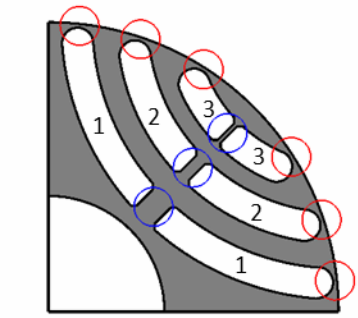

Figure 2 Red: tangential ribs. Blue: radial ribs.

Fig. 2 illustrates the two types of structural ribs investigated in this paper: tangential (red) and radial (blue). Tangential ribs cannot be omitted and their minimum size is normally dictated by the thickness of the lamination and the cutting process. For low speed applications they can guarantee the structural integrity of the rotor without additional radial ribs. Conversely, in high-speed applications the centrifugal force becomes too high and radial ribs (blue) are included. The insertion of the radial ribs further reduces the reluctance torque of the SyR machine, according to (1) and (2).

The design tool adopted in this paper is SyR-e [6], an open-source design platform written in Matlab and based on the 2D magnetic simulation engine FEMM [7]. SyR-e uses multi-objective differential evolution (MODE) and FEMM to optimize the shape and size of the SyRM rotor barriers. A simple ribs stress formulation is adopted, to design the radial ribs thickness according to speed. The tangential ribs are set to a constant thickness, according to the cutting process, as said. The design approach of SyR-e becomes more and more imprecise at higher rotational speeds. A better way to include structural co-design of the ribs into SyR-e would be to use a 2D-FEM (shell) also for the structural design. In this case, the integration between magnetic and structural FEM would not be trivial and computing time could become very long.

This paper studies the feasibility of using 1D-FEM analysis for the structural design part, based on beam elements [8, 9]. The 1D-FEM requires a limited computing time, so that the total computational time of one machine design in SyR-e remains nearly the same. Moreover, the 1D-FEM mesh creation is much easier to integrate into the magnetic design pipeline.

The paper is organized as follows. First, the automatic construction of the 1D mesh of the SyRM rotor is addressed. Then, the accuracy of the 1D-FEM model is assessed against linear and nonlinear 2D-FEM. Finally, a magnetic and structural co-design strategy is defined and implemented in SyR-e.

2 1D-FEM MODEL

The 1D-FEM model, objective of this work, will be validated against the results of the more accurate and time consuming 2D structural FEM, using triangular mesh elements of the second order in SolidWorks (CTRIA6).

2.1 LINEAR VS NON-LINEAR 2D MODEL

Linear and nonlinear 2D-FEM results are compared in this section. Two simulations of the same rotor are carried out, with the same mesh (6217 nodes, 2689 elements, curvature based mesh), and the same rotational speed (50000 rpm, tip speed 157 m/s), one in the linear case and the other one considering the non-linear strain-stress curve of the M530-65A electrical steel. The computing time was about 10 seconds for the linear case and 15 minutes for the nonlinear one.

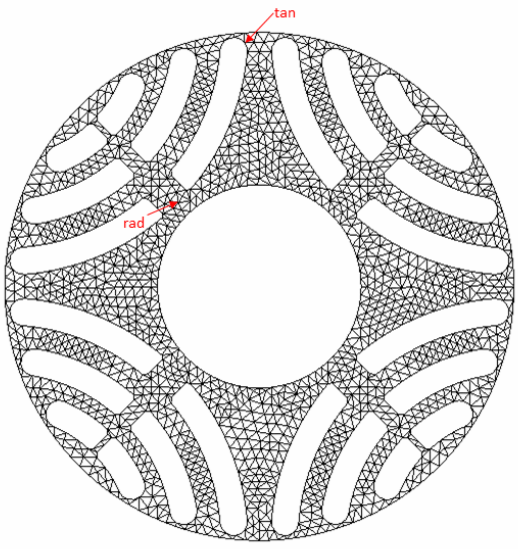

Figure 3 Mesh of the 2D-FEM used for the comparison between linear and non-linear model (6217 nodes, 2689 elements, curvature based mesh).

The Von Mises equivalent stress in the most loaded tangential e radial ribs are reported in Fig. 4. In both cases the tangential ribs exceeds the yield strength, but the

nonlinear model tells that the ultimate tensile strength is not exceeded. Indeed, the linear model overestimates stress by far, in case the yield limit is trespassed. Dealing with the radial ribs results, stress is far from the yield limit according to both models. The conclusion is that if the radial rib is strong enough, then the rotor can survive from the plasticisation of the tangential ribs [10]. Plus, under this assumption, the stress in the radial rib is modelled fairly well also by the linear model. Therefore, for simplicity, the 1D-FEM model will use a linear steel model and non-linear simulation will be used for validation with 2D-FEM.

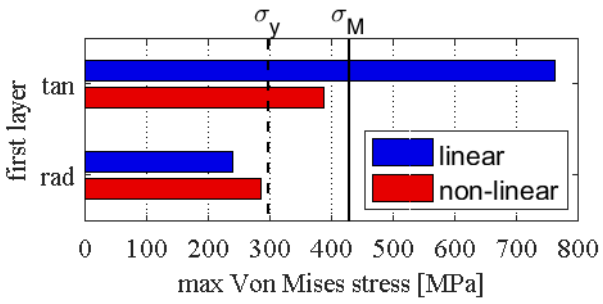

Figure 4 Results from 2D linear and non-linear simulations.

2.2 AUTOMATIC BEAM CONSTRUCTION

One pole of rotor lamination is modelled with a beam structure. An automatic procedure is implemented for integrating the beam model construction into SyR-e. First of all, a set of nodes is automatically placed in key positions of the structure, as represented in Fig. 5a. After the nodes, the beams are defined, as show in Figure 5b. The ribs are modelled as single beams. The width of the beam connected to the tangential ribs is calculated from the radius of the end-arc of the flux barrier and the width of the tangential rib. The width of the terminal beam of the inner flux carrier is calculated from the distance between the ends of the end-arc of the nearby flux barriers.

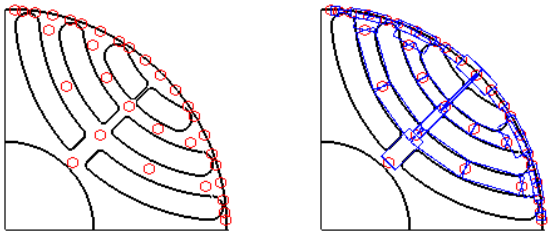

a) b)

Figure 5 a) nodes and b) beam of the 1D-FEM.

2.3 CENTRIFUGAL FORCES

One radial force is associated to each beam, applied to its centre of mass, taking into account the centrifugal load:

$$F = A \cdot h \cdot \rho \cdot r \cdot \omega^2 \quad (3)$$

where A [m^2] is the cross section of the rectangular beam, h [m] the axial thickness, ρ [kg/m^3] the material density, r [m] the distance between the centre of mass and the rotation axis and ω [rad/s] is the rotational speed.

Figure 6 shows the areas presenting some exceptionality in the construction process of beam and forces. The green area around tangential ribs consists of three beams, with only one force associated, applied to the node in common to the three beams. The area highlighted in yellow in Figure 6 is considered in place of the entire beam area, for the radial ribs. Finally, the beams in the external flux carrier use the polygonal areas highlighted in cyan and magenta.

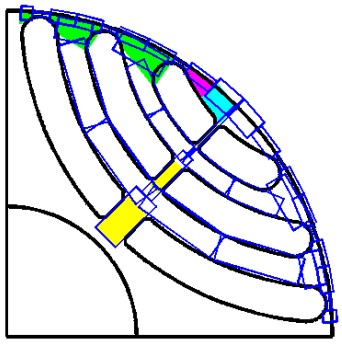

Figure 6 Beam structure and areas with exceptions in the evaluation of centrifugal forces.

2.4 VALIDATION

The 1D-FEM approach is validated using linear 2D-FEM, as said. The reference rotor geometry is shown in Figure 7 and summarized in Table I. At first, only the tangential ribs are considered, at 15000 rpm. Later, simulations at higher speed levels are carried out, with insertion of radial ribs of progressive size. The layers are numbered from the innermost to the outermost as indicated in Figure 2. The equivalent Von Mises stress of the beams representing the ribs is considered.

Table I - Dimensions of the design example.

Rotor diameter	mm	30
Maximum speed	rpm	15000
Tangential ribs thickness (nominal)	mm	0.4

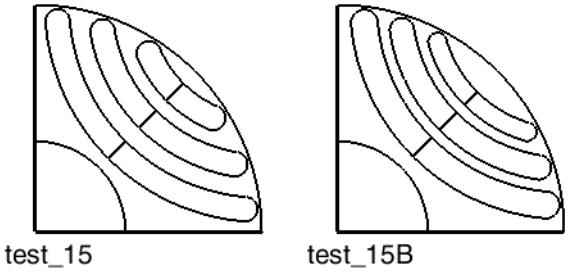

Figure 7 Test geometry for the comparison between 1D-FEM and 2D-FEM.

2.2.1 Test with nominal tangential ribs

The simulations are performed at 15000 rpm. The dimension of the tangential ribs is the nominal one, equal to 0.4 mm. This corresponds to the lower limit of the manufacturing process. The computing time of the 1D-FEM is lower than 1 second.

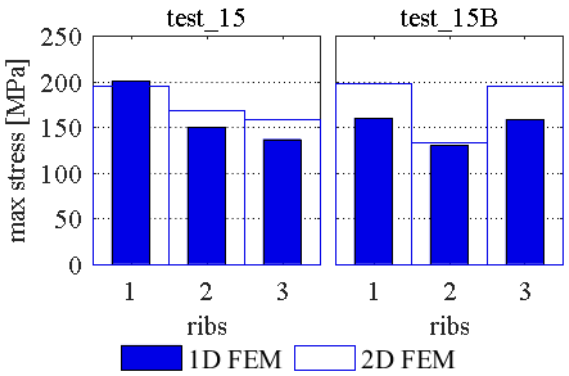

Figure 8 Maximum Von Mises stress of the laminations without radial ribs evaluated with 1D-FEM and 2D-FEM.

2.2.2 Tests with radial ribs

These laminations are obtained starting from the same basic geometry of test_15 (fig. 7a) and setting a higher levels of maximum speed in SyR-e. SyR-e can design the radial ribs according to speed, using a simplified structural model, as said. The three cases are summarised in Table II. At 25000 rpm the machine has one radial rib in layer one, at 30000 rpm two radial ribs (layers 1 and 2), and at 50000 rpm three ribs. The ribs thicknesses are reported in Table II. The dimension of the tangential ribs is 0.4 mm for all the rotors. Figure 9 reports the maximum Von Mises stresses of the laminations with radial ribs evaluated with 1D and 2D-FEM. Overall, the proposed 1D-FEM approach represents the centrifugal stress quite accurately. Errors are in the range of 20%, considering the most significant point of each lamination.

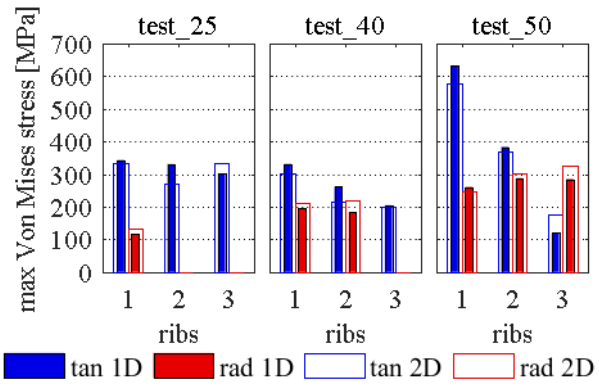

Figure 9 Maximum Von Mises stress of the laminations with radial ribs evaluated with 1D-FEM and 2D-FEM.

Table II - Dimension of the radial ribs.

Name	Speed (rpm)	Radial rib 1 (mm)	Radial rib 2 (mm)	Radial rib 3 (mm)
test_25	25000	0.7	/	/
test_30	30000	1.0	0.5	/
test_50	50000	2.6	1.3	0.4

3 MAGNETIC AND STRUCTURAL CO-DESIGN

This section analyses the magnetic and structural effect of ribs widths, to help defining a correct method to design the tangential and radial ribs. Two sets of rotor lamination are considered, derived from the geometry of test_15 (see Fig. 7a). A first set of laminations have all tangential ribs progressively increased by 0.2 mm, 0.5 mm, 1 mm and 1.5 mm, respectively, leading to a total ribs width increase of 0.4 mm, 1.0 mm, 2.0 mm and 3.0 mm per each layer. In the second set of rotors, the tangential ribs are all at 0.4 mm, as in the baseline geometry, and radial ribs are progressively inserted, using the same reference quantities (0.4, 1.0, 2.0, 3.0 mm). Table III reports the dimensions of the ribs for of the rotor laminations used for these tests.

Table III – Designs with augmented ribs dimensions.

Name	Width of tang. ribs (mm)	Width of rad. ribs (mm)	Total increase (mm)
base	0.4	/	/
R04	0.4	0.4	0.4
T04	0.6	/	0.4
R10	0.4	1.0	1.0
T10	0.9	/	1.0
R20	0.4	2.0	2.0
T20	1.4	/	2.0
R30	0.4	3.0	3.0
T30	1.9	/	3.0

3.1 EFFECT OF RIBS SIZE ON TORQUE AND SPEED LIMITS

Torque is computed with 2D magnetic FEM through SyR-e for all the considered rotors. All simulations refer to the same current loading conditions (90 A/mm), in amplitude and phase. According to (2), with the same current, torque will decrease in inverse proportion of the ribs size. Figure 10 shows the output torque as a function the total ribs increase in [mm]. The bars at 0 mm represent the baseline rotor (test_15 of Fig. 7), which is intuitively the one giving the highest torque. For the same width increase (e.g. 3 mm), radial ribs have a stronger impact on torque.

2D-FEM linear analysis is used to compare the same set of rotors in terms of maximum stress at constant speed (Fig. 11a). Consequently, the maximum speed capability of each machine is evaluated, imposing that the ribs stress equals the yield limit (Fig. 11b). Given the results of the simulation at n_0 = 15.000 rpm, speed can be increased as far

as the yield point is touched. In the linear case, stress is proportional to the square of the speed, leading to:

$$n_{\max} = n_0 \cdot \sqrt{\frac{\sigma_{yield}}{\sigma_0}} \tag{4}$$

where n_{max} [rpm] is the mechanical speed limit, n_0 = 15000 rpm is the test speed, σ_{yield} [MPa] is the yield strength of the steel and σ_0 [MPa] is the stress evaluated in the test simulations. The two figures put in evidence that radial ribs have a way stronger impact on structural strength than tangential ribs, although they penalize torque production slightly more.

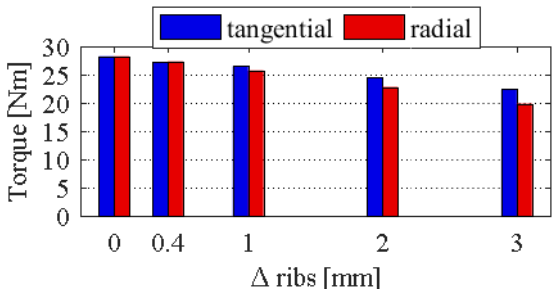

Figure 10 Torque versus increase on ribs, at given current conditions.

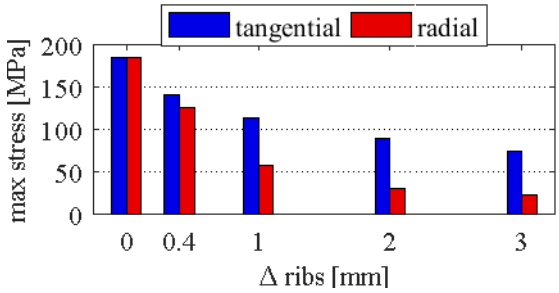

a)

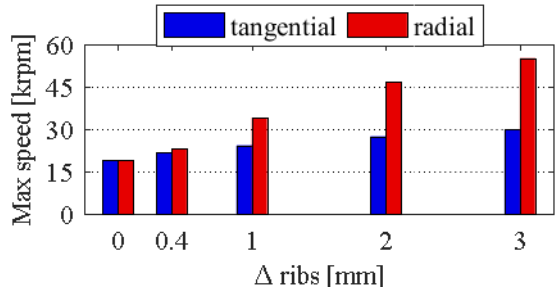

b)

Figure 11 a) Max Von Mises stress versus ribs growth at 15000 rpm. b) Maximum speed limit of the geometries with augmented ribs.

3.3 CO-DESIGN STRATEGY

The co-design strategy must be developed from the magnetic and structural analysis. The maximum torque and speed is not the real maximum characteristics of the machine, because they depend also from the power supply. The values obtained from these analyses are the upper limits, due to the rotor geometry. To join the two analysis, all the test machines are plotted in the torque-speed plane (Figure 12). Near the dots who represent the machine, it is shown the name of the machine (see Table III for the dimension of the ribs). The chart shows that the best solution to improve the mechanical characteristic of the rotor lamination is using the radial ribs, indeed they allow to provide a higher torque than increasing the tangential ribs, at the same speed. Moreover, they allow reaching higher power than increasing only the tangential ribs. The only disadvantage of the radial ribs is the minimum dimension (0.4 mm for this example): The red characteristic from base to T04 does not exist because of the small width of the radial ribs. The co-design algorithm will follow the green line: before the tangential ribs will be increased, until 50% plus than the base width; than the radial rib will be inserted and the tangential ribs will revert to the base width. This method will be applied for each layer.

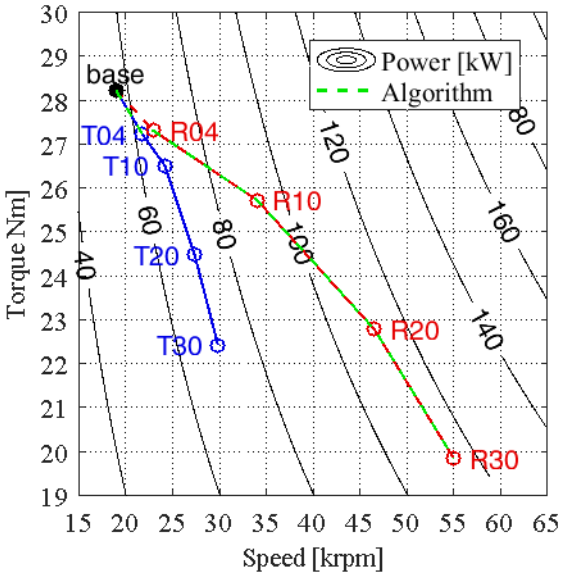

Figure 12 Magnetic and structural analysis on the torque-speed plane.

The algorithm is based on a loop. Before the loop, some block build the 1D-FEM automatically and do a preliminary design of the ribs. This preliminary design check the stress in the tangential ribs and, if the maximum stress is higher than the yield strength, the procedure calculate the new width of the tangential ribs which allows to have the maximum stress equal to the yield strength. The evaluation formula is the (5), where w [mm] is the width of the ribs, σ [MPa] is the stress, with *old* is shown the previous value and with *new* is showed the new value. This formula is not exact, but it gives an easy way to change the dimension of the ribs, using the stress. The loop will correct the errors.

$$w_{new} = w_{old} \cdot \frac{\sigma_{old}}{\sigma_{\max}} \tag{5}$$

If the new width of the tangential ribs is higher than 1.5 times the minimum width of the ribs, then the radial rib will be added, with a dimension calculated from the (6). In this formula w [m] is the width of the radial rib, M [kg] the mass supported from the rib, r [m] is the distance between the centre of mass and the rotation axis, σ_{max} [Pa] is the yield strength and h [m] is the axial width of the rib. This equation ignore the structural effect of the tangential ribs, but all the errors will be correct after some iteration of the loop.

$$w = \frac{M \cdot r \cdot \omega^2}{\sigma_{\max} \cdot h} \tag{6}$$

In the loop, first of all the 1D-FEM is simulated, and then all the layers are checked. If exist the radial rib, the stress of the tangential ribs is ignored. For each layer, the algorithm check if the significant stress is into a defined range (the range used for the evaluation is 95%÷100% of yield strength). If the stress is out of the bounds of the range, the (5) is used to correct the width of the ribs. The width of the tangential ribs is limited in the range 1÷1.5 of the minimum width. If at the maximum width, the stress of the tangential ribs is over the yield strength, then the radial rib is added. The width of the radial ribs is only bounded below at the minimum width of the ribs. The principle of the algorithm is sketch in a simpler and compact form in Figure 13.

4 COMPARISON BETWEEN OLD AND NEW CO-DESIGN PROCEDURES

Starting from the rotor geometry test_15 (Figure 7) it is designed two sets of rotor lamination, the first set is designed with the old algorithm of SyR-e, and the second is designed using the method proposed in this paper. The input of the design is the maximum speed of the motor, and no safe coefficient is applied in the mechanical design: the stress target for the radial ribs is the yield strength.

4.1 RIBS WIDTH VERSUS SPEED

The Figure 14 shows the dimension of the ribs versus the design speed. The machines designed with the proposed method are shown in green, while the machines designed with the actual method (SyR-e) are shown in blue. The old method acts only over the radial ribs, keeping constant the tangential ribs width, while the new algorithm changes also the tangential ribs. The new algorithm insert the radial ribs at lower speed than the old method, this fact points out a lack in the old method. Plus, the new method allows to insert a smaller rib for the first layer, for mid-high speed. You can also see that the layers depend on each other, indeed the insertion of the third radial rib (39000 rpm), causes an increase of the width of the others radial ribs.

4.2 TORQUE VERSUS SPEED COMPARISON

Another relevant comparison between the old method and the new algorithm can be performed in the torque-speed plane, as show in Figure 15. The blue plot show the motor designed with the old method of design and the green plot show the motor designed with the new method. You can see that the new method allows to design, for a mid-high speed (from 20000 to 60000 rpm), more performing machine, with an higher torque (and then an higher power). This is caused from the smaller width of the first radial rib of the machines designed with the new method. At high speed (over 60000 rpm) the new method design worst machine than the old way to design, but performing a first fast structural test (with the 1D-FEM), it turns out that most of the machine designed with the old method (15 of 24) have some mechanical problem, while the machines designed with the new algorithm haven't structural problem.

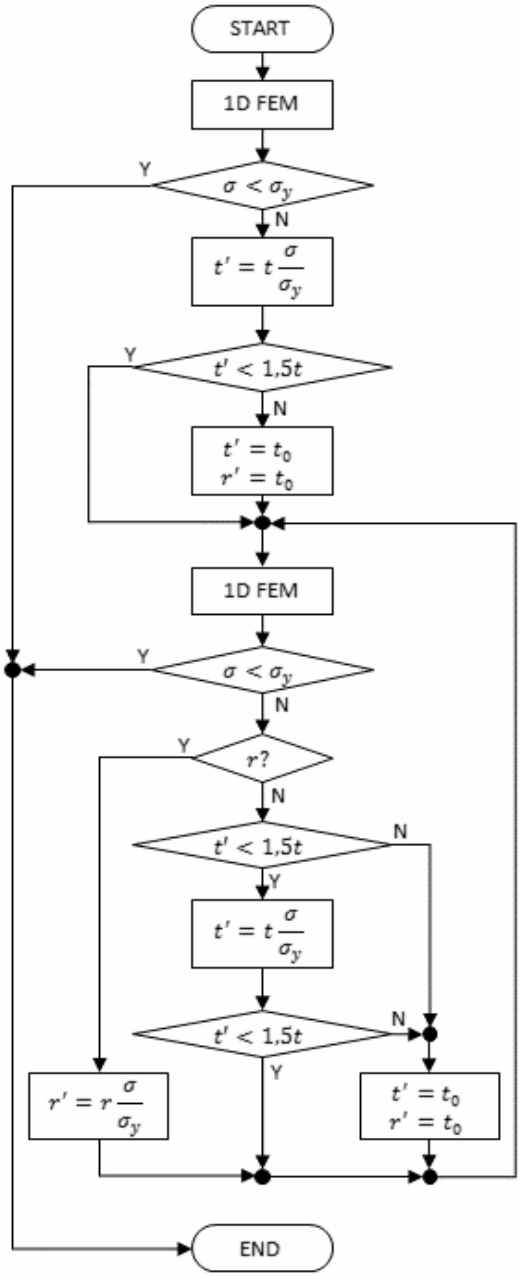

Figure 13 Principle of the proposed co-design algorithm.

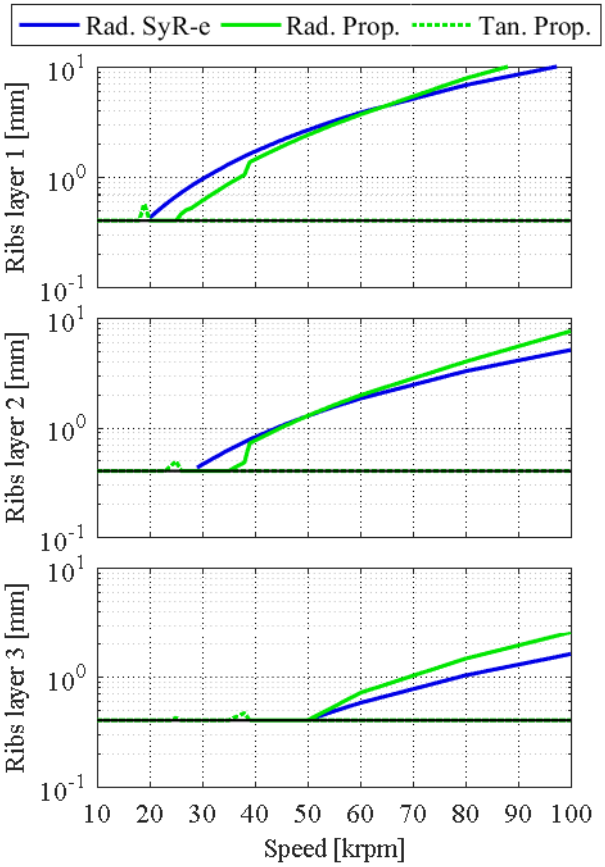

Figure 14 Ribs width comparison for each layer between the machine designed with the proposed algorithm (green) and the machine designed with the old SyR-e (blue).

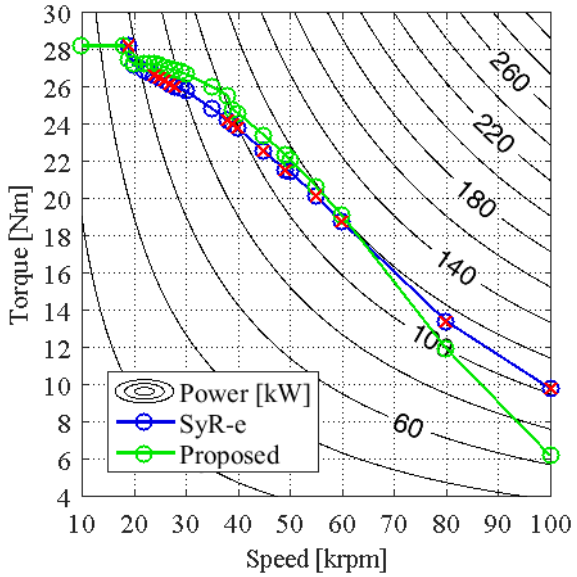

Figure 15 Comparison between the old method and the new algorithm of design on the torque-speed plane.

4.3 STRESS VERIFICATION WITH NON-LINEAR 2D-FEM

In order to check the correct structural design, all the designed machines are simulated with 2D-FEM and a non-linear model of the material. The results are sum up in Figure 17, Figure 18 and Figure 19. You can note that in the first layer (Figure 17), the old algorithm designs oversized machines (the stress in the radial ribs is much lower than the yield strength), but the new algorithm make some errors because some machines have the maximum stress equal or little higher than the yield strength. In the other layers, the behaviour is the same, with less range of speed where the new algorithm make mistakes. Anyway, the stress never reach the ultimate tensile strength, so, all the motor do not break because of the maximum speed. Some problem can be caused from fatigue, but it is not the intent of this paper.

In Figure 16 all the machines designed are shown. The orange crosses mark the machines that have the maximum stress over the yield strength and under the break strength. No one machine reach the ultimate tensile strength, but the very high-speed machines (over 80000 rpm) have a maximum stress closer to the ultimate tensile strength. For the new method 18/24 machines reach the yield strength, while for the old method, only 16/24 machines reach this limit. This is easily avoidable using a safe coefficient in the design method.

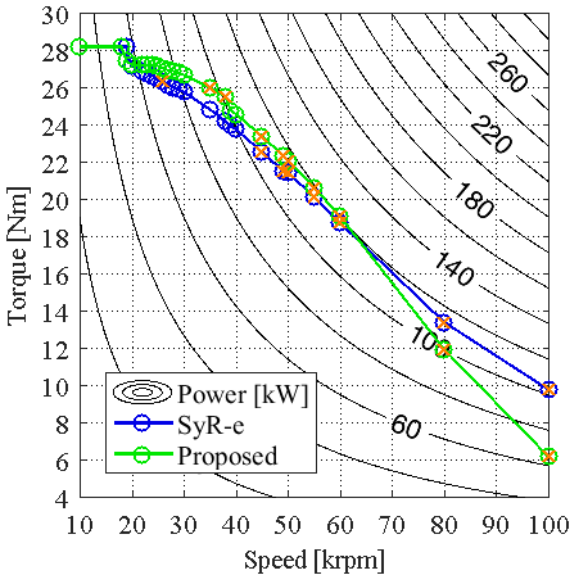

Figure 16 Comparison between the old method and the new algorithm of design on the torque-speed plane and tested with 2D-FEM.

5 CONCLUSIONS

This paper presents a new method of design for SyR machines. The innovations introduced are: the definition of a generalized method to create a 1D-FEM of the SyR

machine's rotor; and the chance to use the 1D-FEM in the design pipeline of SyR motors. It is also investigates the magnetic and structural differences between tangential ribs and radial ribs, and the importance in the choice of the material model for the structural analysis.
Finally, the new method of design, using the 1D-FEM is applied and compared to the old method, showing the advantages in the design, avoiding the high oversizing applied by the old method. The disadvantage is the approximation of the 1D-FEM, which can cause an undersize of the radial ribs and then too high stresses, which can exceed the set limit.

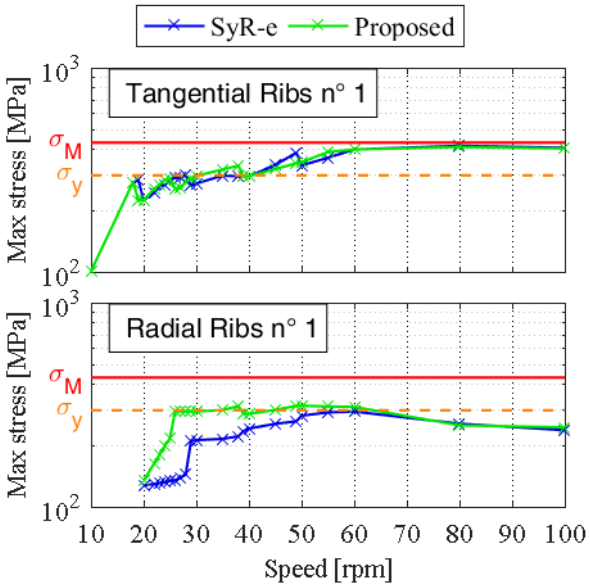

Figure 17 Stress in the first layer evaluated with 2D non-linear FEM.

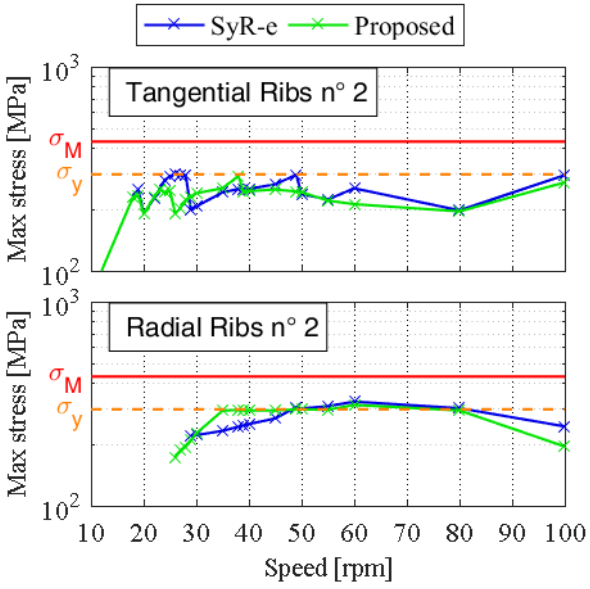

Figure 18 Stress in the second layer evaluated with 2D non-linear FEM.

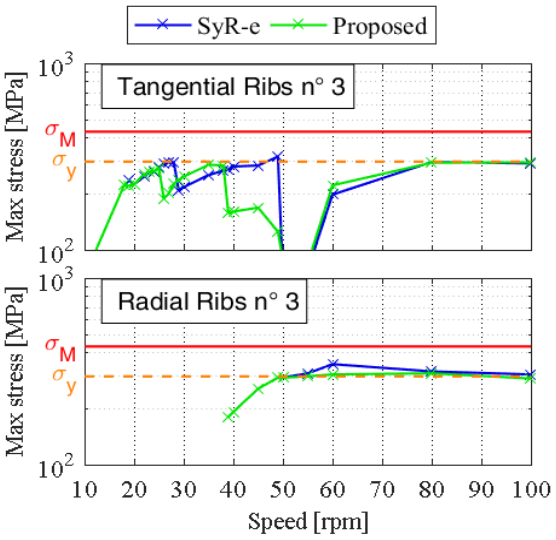

Figure 19 Stress in the third layer evaluated with 2D non-linear FEM.

REFERENCES

[1] *Rotating Electrical Machines—Part 30-1: Efficiency classes of line operated AC motors*. (IE-Code), Ed. 1, IEC 60034-30-1, Dec. 2014.

[2] Vagati A., Fratta A., Franceschini G., Rosso P., AC motors for high-performance drives: a design-based comparison. *IEEE Transactions on Industry Applications*, Vol. 32, No. 5, pp. 1211-1219, Sep/Oct 1996.

[3] Moghaddam R.R., Magnussen F., Sadarangani C., Theoretical and experimental re-evaluation of synchronous reluctance machine. *IEEE Transactions on Industrial Electronics*, Vol. 57, No. 1, pp. 6-13, Jan. 2010.

[4] Di Nardo M., Galea M., Gerada C., Palmieri M., Cupertino F., Multi-physics optimization strategies for high speed synchronous reluctance machines. *2015 IEEE Energy Conversion Congress and Exposition (ECCE)*, Montreal, QC, pp. 2813-2820, 2015.

[5] Ikäheimo J., Kolehmainen J., Känsäkangas T., Kivelä V., Moghaddam R.R., Synchronous high-speed reluctance machine with novel rotor construction. *IEEE Transactions on Industrial Electronics*, Vol. 61, No. 6, pp. 2969-2975, June 2014.

[6] Pellegrino G., Cupertino F., *SyR-e User's Manual ver 1.0*. available online at www.sourceforge.net.

[7] Meeker D., *FEMM Reference Manual*. available online at www.femm.info/wiki/HomePage.

[8] Bathe K.J., F*inite element procedures*. Prentice-Hall, New Jersey, 1996.

[9] Hughes T.J.R., *The finite element method*. Prentice-Hall, New Jersey, 1987.

[10] Juvinall R.C., Marshek K.M., *Fundamentals of machine design*. 5th Ed., Wiley & Sons, 2011.

ISSN 1590-8844
International Journal of Mechanics and Control, Vol. 17, No. 01, 2016

UNDERACTUATED MECHANICAL HAND CONTROL BY EMG SENSORS

Sergio Savino

University of Naples "Federico II", Department of Industrial Engineering - Naples - Italy

ABSTRACT

The control of the human hand uses several neural impulses to control muscles and tendons, which allow an almost limitless range of gestures and movements. If we want to consider only the most common gestures - greet, indicate, open palm, shake hands - use should be made of monitoring and acquisition of at least four pairs of muscle impulses. To acquire this large quantity of pulses in a patient fitted with a prosthesis, it would require a large number of electrodes, placed on different areas of the arm and forearm. However, this is not always possible due to the different degrees of impairment to which the patient may be subject. In addition, the yield of the movement to be faithful to that of a human hand, would require the use of at least 15 motors. The studies carried out at the Department of Industrial Engineering of the University of Naples, allowed the realization of an prosthetic hand prototype equipped with a single pair of electrodes and a single motor.
In this paper different types of control developed for the above prototype, are described. By means of such control techniques, making use of a finite state language, the user is able to control the hand with on-off and proportional techniques, that provide a wide range of situations in which the prosthesis is effective and responsive.

Keywords: undercatuated mechanism, control, hand prostheses, EMG sensor.

1 INTRODUCTION

The hand can be considered the first instrument of the humanity. In the last years there has been a more careful research regarding the development of projects related to creating prostheses, artificial limbs or simply machinery for motor rehabilitation [1].
Some of the most significant developed projects have led to the realization of artificial hand control systems based on sensors that interface with the user even at the neurosensorial level [2-4]. The main aim of these studies is to manage different types of grip without being a cognitive challenge for the user.
The basic idea behind this type of control is that the user needs to store only one type of switch signal - "Trigger". The trigger in this case may be represented by a signal or by a signal sequence.

Contact author: Sergio Savino[1]

[1]Email: sergio.savino@fastwebnet.it

The purpose of this paper is the development of a electromyographic control system that makes use of a simple and effective language, capable of interpreting the signal acquired by a single pair of electrodes, in order to control the hand prosthesis developed by the Department of Industrial Engineering of University of Naples "Federico II" [5-8].

2 MECHANICAL HAND

Generally, to grasp an object with an irregular shape a mechanical hand would need at least 4 motors: one to move the thumb, one for the index, one for the medium and one for the ring finger and the little finger. An alternative to the use of four motors could be represented by the use of elastic tendons connected to a single motor. In such a case, the motor transmits the same force on each tendon, causing each finger performs the same movement. However, during the grasp of an irregularly shaped object, when the first fingers touch it, they meet an obstacle and they stop their movement, while the other fingers continue to close, because they have not any obstacle. This implies that the

fingers which first touched the object and remained more open, exert a minor force on it than the others, because they have lost force in stretching the tendons.
To avoid the above described behaviour a mechanical hand characterized by a series of differential mechanisms was conceived, that is shown in Figure 1 [5-8]. Unlike the mechanical hand with elastic tendons, in this one the difference among the elongations of the tendons is compensated by the rotation and the translation of the pulleys. The prototype object of this paper, results to be very inexpensive, as it is realized by means of a simple kinematic pairs. In addition, the force exerted by each finger is constant, whatever the configuration to be achieved is. This property enables the prototype to grasp very different objects and permits to adjust the closing force, by acting on the only motor.

Figure 1 Prototype of mechanical hand.

2.1 PROSTHESES PROTOTYPE

The mechanical hand has been used to assemble a prototype of the prosthesis.

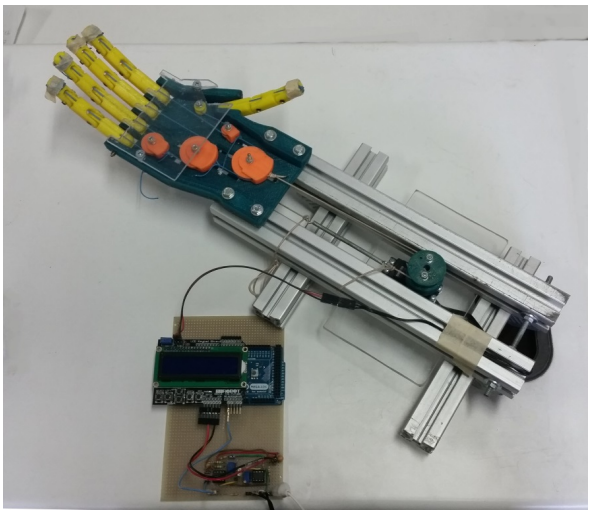

Figure 2 Prostheses prototype.

The main elements of the prototype are:

- Electronic board for the acquisition of EMG signal;
- Microcontroller Arduino Mega ADK;
- Servomotor Hitec HS-5990TG;
- Shield LCD Keypad SKU: DFR0009;
- Mechanical hand above described.

The prototype of the prosthesis is shown in Figure 2.

2.1.1 Electronic board for the acquisition of EMG signals

An electronic board prototype has been made to interpret, capture and filter an electrical signal from a muscle impulse, using three electrodes placed on the muscle that is being monitored.
In order to have a correct acquisition, it is necessary to place a pair of electrodes on the muscular band of which you want to capture the pulse and a third electrode on an area without sensorial relevance, to provide to the board a reference threshold for the correct interpretation of the signal.
An example of connection is shown in Figure 3.

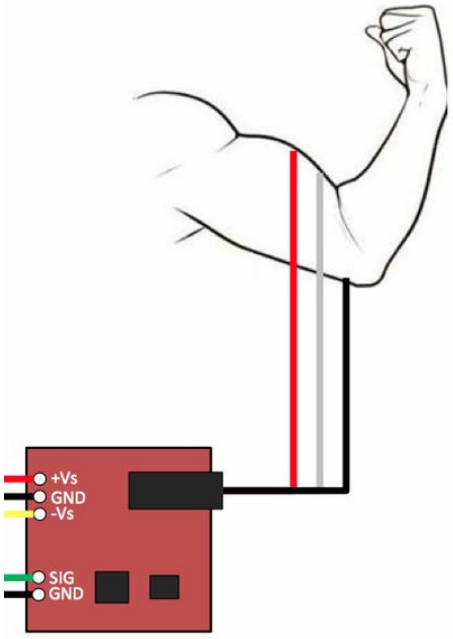

Figure 3 Connection scheme of EMG sensors to the biceps.

Once the raw EMG signal has been acquired, this is rectified and subsequently filtered by means of a low-pass filter. The control logic, implemented on the microprocessor that is connected to acquisition board of the EMG signal, integrates the signal itself with variable window. In this way, it becomes possible to increase the number of states available from the superficial acquisition of the electromyographic signal [9].
This expedient, although providing a wide range of parameters for the discernment of the amplitude of the EMG signal, allows the distinction of not more than two classes of movement. To obtain a control based on the recognition of multiple classes of gestures, more pairs of

electrodes are needed, associated with a type of control based on transient states rather than on the static levels of threshold [10].

2.1.2 Microcontroller

Arduino Mega ADK is a microcontroller board based on protocol ATmega2560 [11].

It has a USB interface protocol based on standard MAX3421eIC. Each of the 50 digital pins of the Mega ADK can be used as input or output, using the function pinMode(), digitalWrite(), and digitalRead().They operate at 5 V and each pin can provide or receive a maximum of 40 mA and has an internal resistance of pull-up (disconnected by default) of 20-50 kOhms.

Arduino Mega ADK has 16 analog inputs, each of which provides 10 bits of resolution.

The serial communication with Arduino Mega can be administered by means of an auxiliary software, called "Processing". It is also possible, using this software, manage the acquired data with the board to display the values on the screen, show them on a graphic, or write them to a file for postprocessing.

2.1.3 Servomotor

The prosthesis has been equipped with a digital servomotor HSR-5990TG.

This servo motor has digital systems to control the positioning and provides, therefore, a quick and accurate response.

The motor is, therefore, driven by means of a PWM signal at the frequency of 250 Hz, with a duty cycle between 10% and 60%:

- with a duycycle of 10%, the servo rotated 90° clockwise;
- with a duty cycle of 60%, the servo rotated 90° counterclockwise;
- with a duty cycle of 35%, the servo is stabilized in the central position.

3 CALIBRATION OF EMG SIGNAL

In order for a prosthesis proves responsive and efficient in a large number of environments, it is necessary to provide control laws that can adapt to the context in which it is used, as well as to the individual who uses it. In this regard, the "user training" is accompanied by what that IEEE defines "system training" [12]: a set of calibration techniques, pre-processing and interpretation of intent, that give flexibility in the control of prostheses.

Below the choices employed for the calibration of the prosthetic system in question, will be discussed; in particular, it will exhibit the techniques implemented to achieve the following purposes:

- setting the minimum threshold of EMG signal;
- recognition of mean threshold of the EMG signal noise;
- setting of maximum threshold of EMG signal;
- estimate of the trend of the response of the EMG signal to a progressive contraction of the muscle.

3.1 MINIMUM THRESHOLD OF THE EMG SIGNAL

Having no a constant reference of mass, due to the variable position of the ground electrode, the signal value at rest is highly variable and it differs of significant quantities for each positioning of the electrodes on the user.

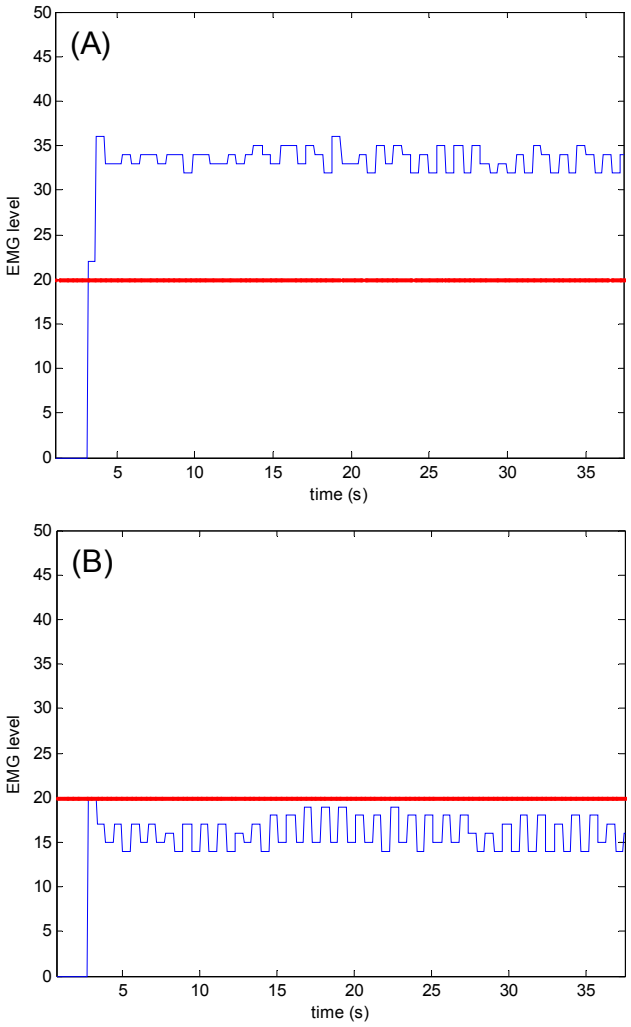

Figure 4 EMG signal minimum threshold connecting the electrodes to the forearm (A) and to the biceps (B).

In Figure 4 it is possible to see the different minimum threshold obtained by connecting the electrodes to the forearm (a) and to the biceps (b).

To make possible the use of a larger number of muscular bands it was thought to rescale the EMG signal by a value equal to the first reading of the signal itself, in this way it is possible to assign a reference of mass very close to zero, on which to calculate the signal differences.

This is done using an appropriate function, loaded on board microcontroller, which initializes the EMG signal five seconds after the power.

The result obtained can be appreciated in Fig. 5.

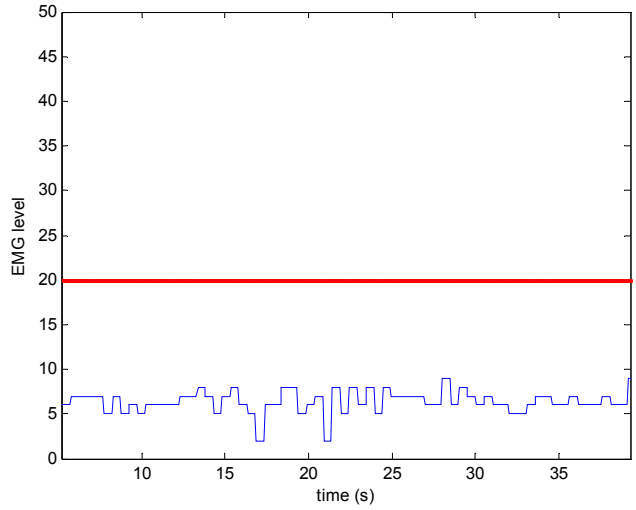

Figure 5 Minimum threshold setting of EMG signal.

3.2 MEAN THRESHOLD OF THE EMG SIGNAL NOISE

An important data to provide an estimate of the quality of the control system is the mean threshold of the EMG signal noise. By studying this parameter it is possible to evaluate the accuracy attainable with the control laws. So it was conducted a qualitative analysis of the nature of the disturbances to provide some indications on the main defects of the acquisition board of the EMG signal, on which to act in the construction of a prototype future.

A first test was carried out by shorting the terminals of the electrodes of acquisition with the purpose of highlighting the noise captured by the individual connectors, Figure 6.

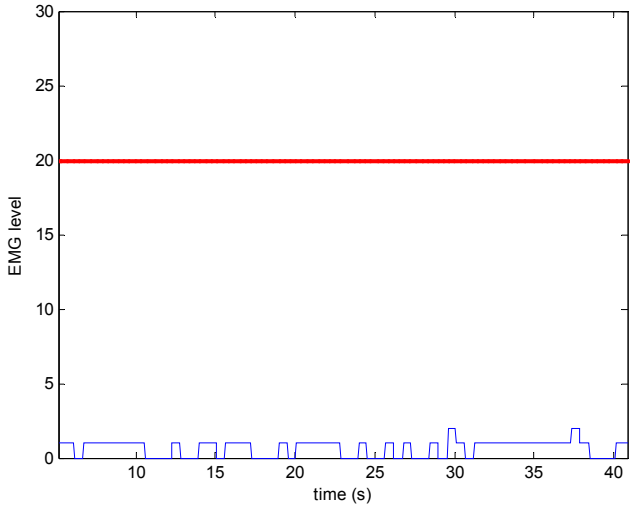

Figure 6 EMG signal noise by shorting the electrodes

A second test was conducted by placing the electrodes on the user and observing the output signal in the absence of voluntary contractions, in this way it can be appreciated the quality of the "filtering" of the EMG board towards other electrical signals of the human body differ from those associated with muscle contraction, Figure 7.

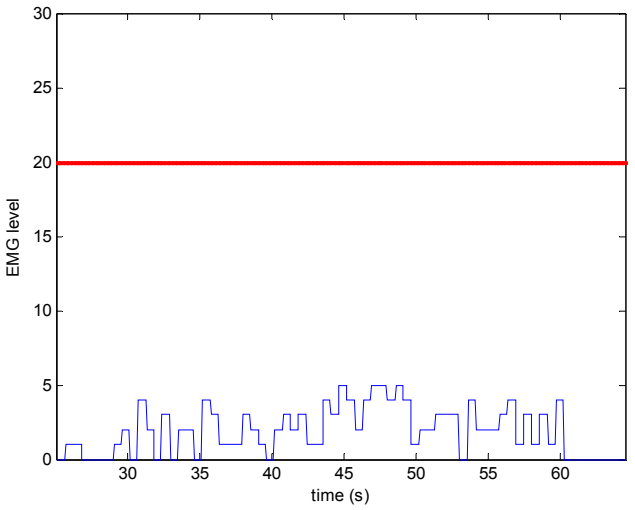

Figure 7 EMG signal noise in absence of voluntary contractions.

As can be seen in Figure 7, the EMG signal has a mean oscillation amplitude equal to 5 units. This parameter will be useful for the implementation of a proportional control, specifically in the dimensioning of the amplitude of the floating window of recognition of the intent.

3.3 MAXIMUM THRESHOLD OF THE EMG SIGNAL

To make the prosthesis usable by many users, is necessary to determine and set a maximum threshold of the EMG signal, to which is mapped a complete closure of the hand.

Since the EMG signal is directly proportional to electric impulse of the muscle to which the electrodes are connected, it is intuitive to understand that the user's physical prowess has a decisive role in generating the maximum amplitude of the pulse that he is able to produce.

For this purpose, several acquisitions were conducted on several volunteers, in order to find a method which gives a satisfactory result in the determination of the pulse necessary to act a tight and to maintain closed the hand.

The test was conducted by asking users to maintain a constant contraction corresponding to the total closure of the hand, followed by a contraction at maximum effort.

The data obtained for three users are shown in Table I.

Table I - Experimental values.

User	Mean value (mv)	Maximum value (Mv)	Ratio (Mv/mv)
1	70.52	230	3.26
2	60.26	234	3.88
3	97.85	352	3.59

From the analysis of the experimental data, a calibration procedure at startup of the control software has been implemented. This procedure, following the acquisition of a pulse under maximum stress, sets the threshold of closing of the hand in the ratio 1: 3.5 with such peak value.

3.4 EMG SIGNAL IN A PROGRESSIVE MUSCOLAR CONTRACTION

From the analysis of the acquired response signals, it was found that an attempt to progressive contraction of control muscle, corresponds to a non-linear increase of the value acquired by the EMG board. On the basis of this consideration, many tests were carried out in which users have performed a single continuous contraction and progressively greater in amplitude. The study of these data, allowed to search for a function that approximates the response of the EMG signal.
The approximation function with mean square error less is the sum of exponential terms:

$$f(x) = a\, e^{b \cdot x} + c\, e^{d \cdot x} \qquad (1)$$

An example of approximation of the EMG signal relating to a progressive muscle contraction, with a function of type (1), is shown in Figure 8.

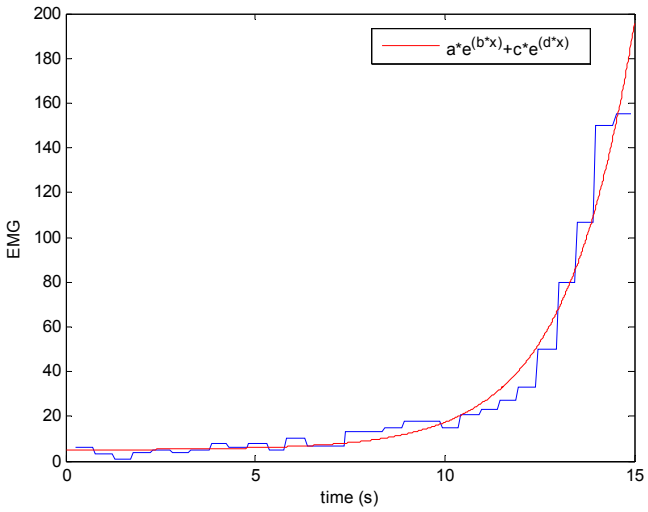

Figure 8 Approximation function for EMG signal in a progressive muscular contraction.

This result may be relevant in order to improve the proportional control of the prosthesis, because the control signal can be scaled with a function of type (1) rather than linear.

4 PROSTHESIS CONTROL

On the basis of the common classification of prosthetic control, [13], as a first step, operating logics based on on-off control and proportional control, has been implemented. The following step has been to create a hybrid logic, more elaborate, which makes use of both the simple controls.
For each type of control, different algorithms were developed and tested.

4.1 ON-OFF CONTROL

4.1.1 Single rising edge

The most banal operating logic implementable is based on the detection of a rising edge to a preset minimum threshold.
When this threshold is exceeded, a trigger starts the function that activates the closure of the hand (or the opening, if this had already closed). This function controls the servomotor in position, by providing a command of maximum - or minimum - motor angular position that matches the configuration of the opening or closing of the hand.
The results obtained by means of this operating logic are shown in Figure 9, in terms of the EMG signal and motor angular position.

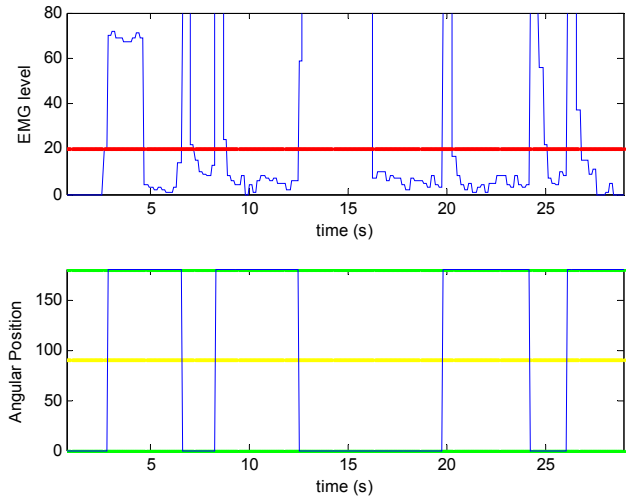

Figure 9 Single rising edge ON-OFF control.

As can be seen, each passage for the rising edge associated with the value 20 (in red in Figure 9), corresponds to a variation of the angular position of the motor from 0° to 180° and viceversa. This change results in a total closing movement - or opening - of the hand.
This type of control is convenient in the management of the prosthesis in situations where the response need for short processing times. On the basis of tests carried out in the laboratory, this kind of control is the most effective in tests in which users must grasp an object in motion. This efficiency is primarily due to the reduction of the length of the processing window guaranteed by the simplicity of the control type.

4.1.2 Double rising edge

To make the On-Off control more robust from a point of view of interferences of the external noise or the user control, it is possible to implement a control that takes account of the recurrence of two consecutive rising edges - separated by a time interval fixed inside the observation window - to control the total closing and opening of the hand. The sizing of the observation window is proportional

to the duration of the acquisition cycle. In the case shown in Figure 10, the time needed for the execution of each cycle is about 390 ms. Four cycles (opening and closing of the hand), therefore, correspond to a time window of just over 1.5 seconds.
In Figure 10 two different cases that may occur with this operating logic are shown. In the case (A) the two pairs of pulses are both performed in the established time window and the hand is closed with the first pair and is opened again with the second. In the case (B) only the second pair of pulses is performed in the established interval and the hand only closes.

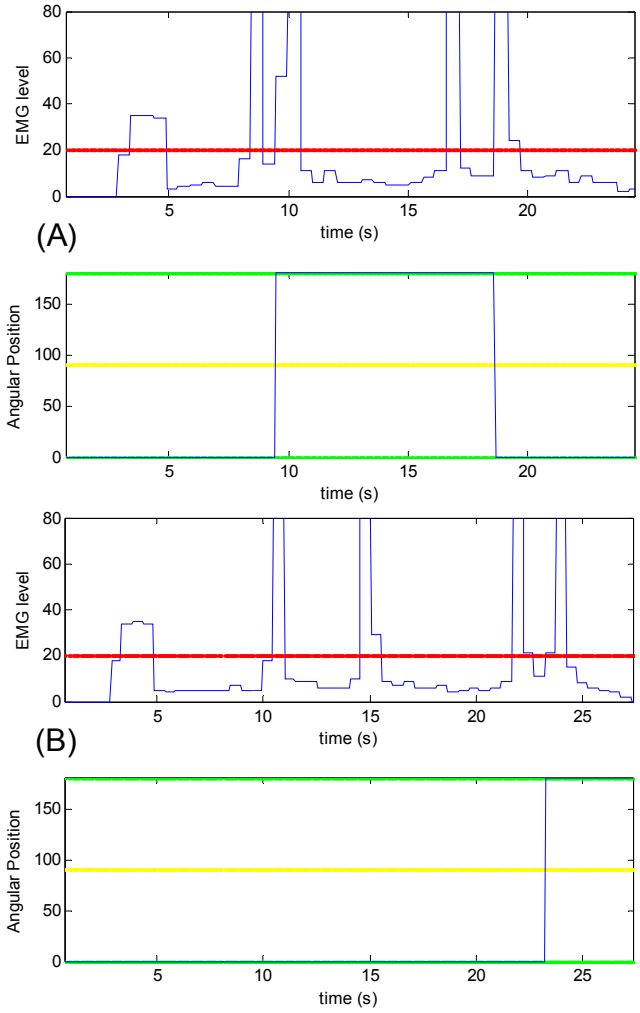

Figure 10 Double rising edge ON-OFF control

A logic based on double rising edge may become necessary in the case in which the monitored muscle can contract in situations not dependent on the user control (eg. weight lifting, moving an object). In such situations the double consecutive contraction in a given interval, provides greater security of voluntariness.

4.1.3 Consecutive rising edge

To avoid the necessity of waiting for the signal falls below the minimum threshold, an operating logic has been implemented that, always in a fixed time interval, after a first rising edge, recognizes a second pulse only when it is a signal increase following a peak of descent of established amplitude. In this way, a more responsive recognition of the two pulses is possible, making more reactive the elaboration of the intent.
The time interval dimension, in which the second pulse must be recognized, sets the elaboration speed of the control.
In figure 11 an example of the signals associated with the control just described is shown. It is possible to see that all four consecutive rising edge, even if are different, are recognized like user's intent.

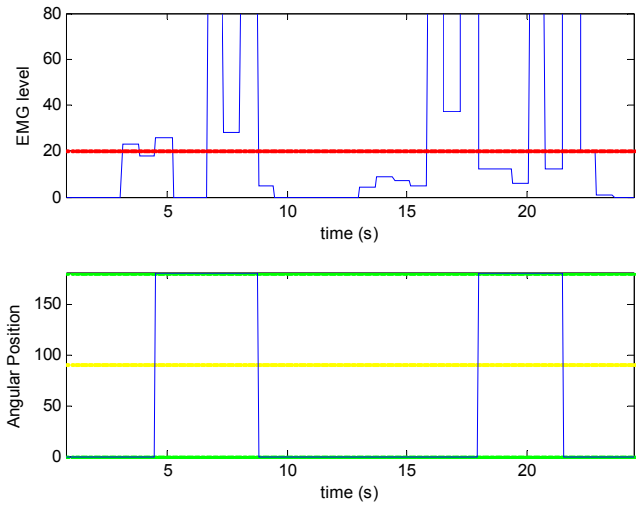

Figure 11 Consecutive rising edge ON-OFF control

4.2 PROPORTIONAL CONTROL

4.2.1 Without filtering

The control logic proposed below, provides the ability to control the closure of the hand with an accuracy equal to the angular resolution of the motor which activates the hand itself. The proportional control is implemented by means of a scaling of the electromyographic signal so that that the minimum threshold, corresponds to the position of the motor that generates the opening of the hand, and the maximum threshold to the position of total closure.
This type of control offers the possibility to control the hand in a very wide range of values but is very susceptible to noise acting on the EMG signal and to the inability of the user to generate a perfectly constant pulse if he wants to keep a given configuration hand.
The results of this type of control are shown in Figure 12.
As can be seen, a variation of the EMG signal corresponds to a flickering on the control signal which results in a hand-

shake. This undesired phenomenon, can, in the long term, be stressful for both the mechanical components of the prosthesis, both the electrical ones due to a not negligible current consumption.

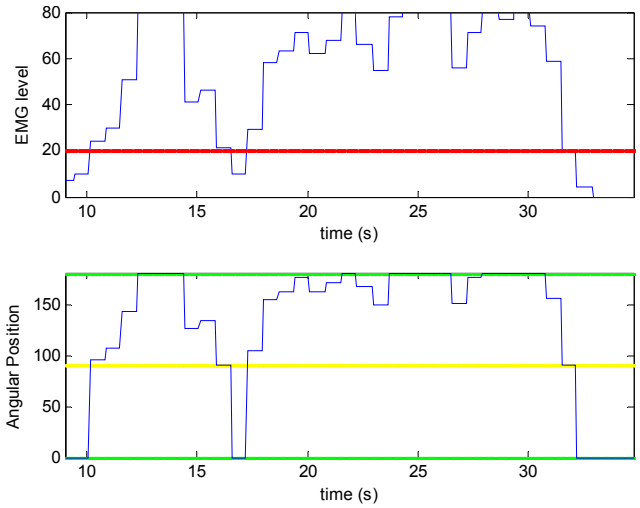

Figure 12 Without filtering proportional control.

4.2.2 Floating control window

Below a variant of the simple proportional control is discussed. The advantages of this variant are the absence of flickering on the control signal and the consequent reduction the current consumption by the motor.

To achieve this result is applied a mobile windowing on the EMG signal that changes the position of the actuator only if it differs, in absolute value, of 15 ° from the previous one.

The results obtained are shown in Figure 13, where it is possible to note the trend constant piecewise of the angular position of the motor and the reduction of its oscillations.

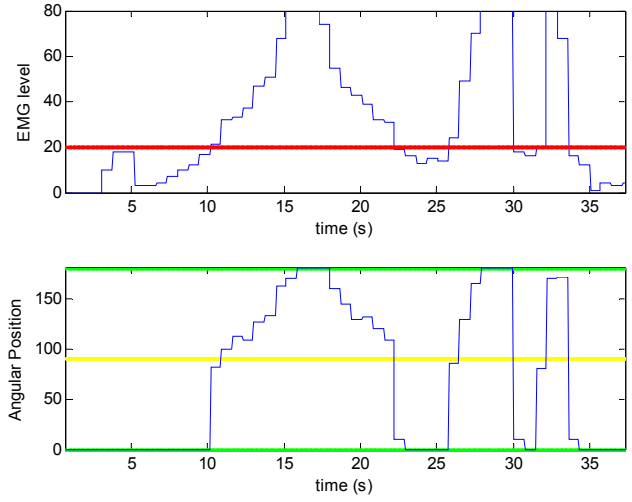

Figure 13 Floating control window in proportional control

4.3 HYBRID CONTROL LOGIC

4.3.1 Proportional control with on-off closing

In order to obtain a control that was usable in more situations, a hybrid operating logic was implemented: proportional type, but with the possibility to switch to a on-off control in consequence of a double contraction of the user.

The function that was developed for this type of control, provides a total closure of the hand when a double rising edge on a calibrated minimum threshold, of the EMG signal is received. The closure is then maintained until a further double pulse which resets the type of control in proportional logic.

The result that can be obtained with this type of control is shown in Figure 14.

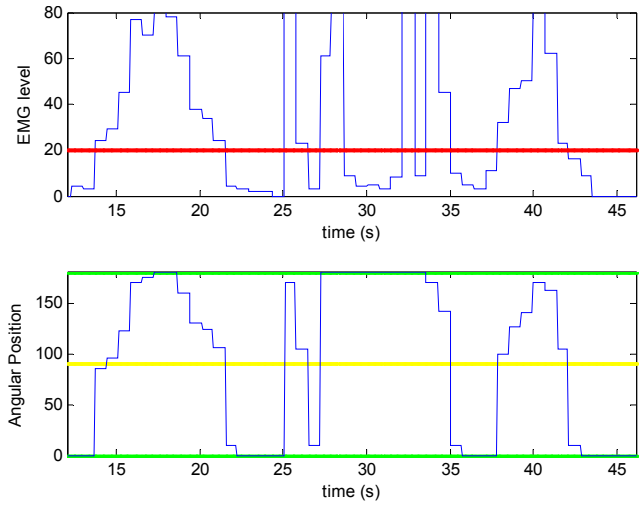

Figure 14 Proportional control with on-off closing.

The limit of this logic is that the first impulse necessary for the transition to the on-off control is processed by the controller and causes a partial closing and opening of the hand.

4.3.2 Proportional control with continued closure

A partial solution to the problems described above, can be supplied by a proportional control logic with continued closure. The logic allows the user to control the prosthesis in a proportional manner and to keep the hand closed even in the absence of muscle contraction.

To achieve this result, the user, after a full grasp by means of proportional control, shall perform an fast contraction that is recognized when a threshold of maximum is crossed rapidly downhill and then uphill. In this way is possible to grasp an object also gradually and keep a secure grip without having to hold a constant muscle contraction.

Once activated the continued closure, the sending of a new pulse which exceeds the maximum threshold, returns the proportional control logic.

An inconvenience of this control logic consists in the

permanence of the hand in the closed configuration even in presence of an opening intention; this occurs during the time ł set for detection of the second pulse edge.
In Figure 15 it is possible to recognize a first section with a simply proportional control, a second section with a proportional control that reaches the maximum without holding it, a third section in which after reaching the maximum a pulse is sent to perform the continued closure, and a fourth section where, as a result of a further pulse, the control returns purely proportional.

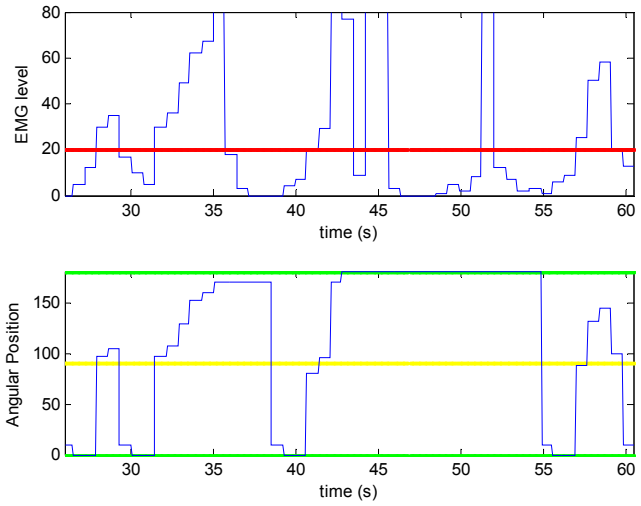

Figure 15 Proportional control with continued closure.

5 CONCLUSION

The control tests by the users who have experienced the prosthesis showed that it is intuitive and effective, as seen in Figure 16.
The results, therefore, are considered satisfactory as for the goals were set in this preliminary stage of the study of the prosthesis.
The development of many operating logics permitted to the mechanical hand to be usable in a wide range of environments; nevertheless there is a clear need to test the prosthesis on a greater number of users.
The few limits that the prosthesis currently shows, are largely due to its hardware components.
At this point of the investigations, the following improvements seem to be recommended.
To improve the control law, the detection of the thresholds of contraction and the elaboration of the intent of the user, a better noise rejection by the EMG acquisition board is needed.
To provide the user a more complex "language", reducing processing errors and providing the possibility to change the type of control logic, it is necessary to increase the number of sensors.
To guarantee users a more natural experience, it is possible to implement a feedback network by which provide the user with an indicator about the active type of control. A possibility would consist in installing pressure sensors on the fingertips of the mechanical hand and electric vibrators installed on the forearm of the user; in this way it would be possible to generate a vibration which amplitude is proportional to the force detected by the sensors.
To optimize actuator's law of motion, it is possible introduce a previously proposed algorithm, [14,15] in the motor control.

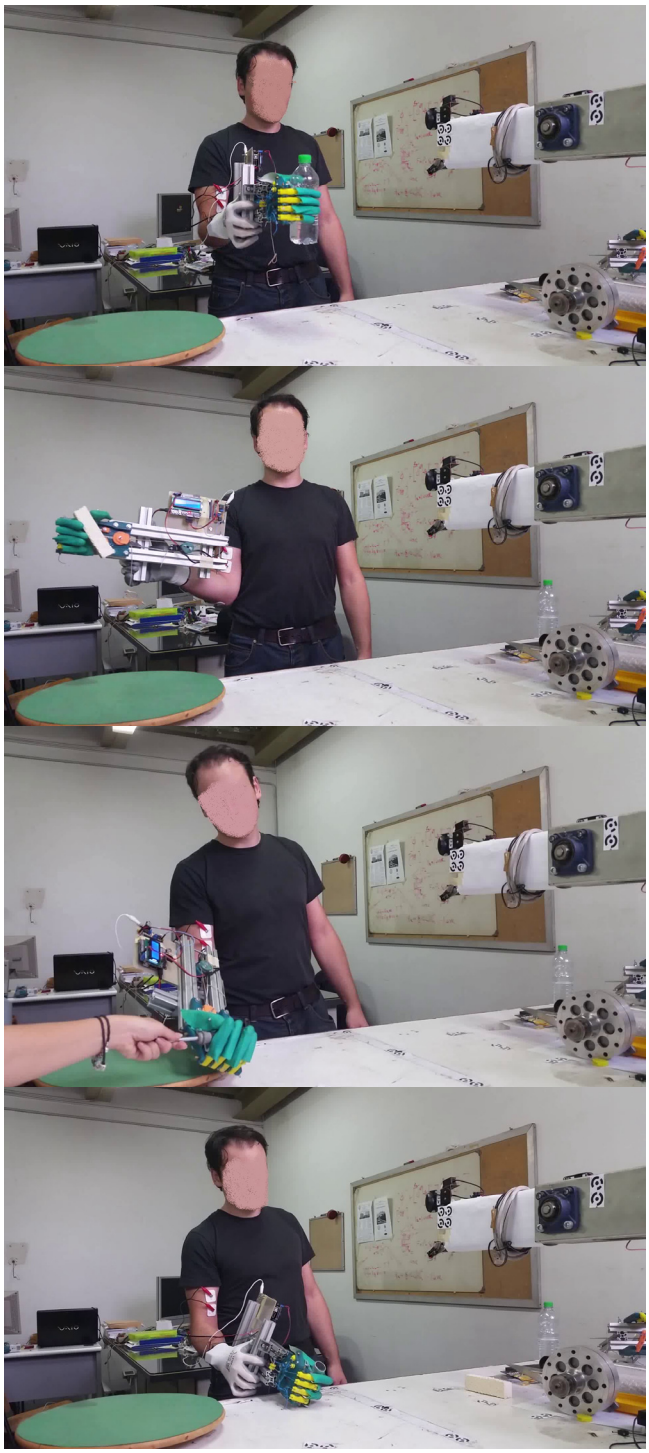

Figure 16 Laboratory tests of prosthetic hands.

ACKNOWLEDGEMENT

During this research a valuable help was provided by Mr. Stefano Nardella who was working for the bachelor's degree. The author thanks him for his diligence and his help.

REFERENCES

[1] Belter J.T., Segil J.L., Dollar A.M. and Weir R.F., Mechanical design and performances specifications of anthropomorphic prosthetic hands: a review. *J. Rehabil. Res. Dev.*, Vol. 50, doi: 10.1682/jrrd.2011. 10.0188, pp. 599-618, 2013.

[2] Atzori M. and Müller H., Control Capabilities of Myoelectric Robotic Prostheses by Hand Amputees: a scientific research and market overview. *Frontiers in Systems Neuroscience*. Vol. 9, paper 162, doi: 10.3389/fnsys.2015.00162, 2015.

[3] Cipriani C., Antfolk C., Controzzi M., Lundborg G., Rosen B., Carrozza M.C., et al. Online myoelectric control of a dexterous hand prosthesis by transradial amputees. *IEEE Trans. Neural Syst. Rehabil. Eng.*, Vol. 19, pp. 260-270, doi: 10.1109/TNSRE.2011. 2108667, 2011.

[4] Atzori M., Gijsberts A., Castellini C., Caputo B., Hager A.G.M., Elsig S., et al. Electromyography data for non-invasive naturally-controlled Robotic hand prostheses. *Sci. Data*, 1:140053, doi:10.1038/sdata. 2014.53, 2014.

[5] Niola V., Rossi C., Savino S., A new mechanical hand: Theoretical studies and first prototyping. *International Review of Mechanical Engineering*, Vol. 8, No. 5, pp. 835-844, ISSN: 19708734, 2014.

[6] Rossi C., Savino S, An underactuated multi-finger grasping device. *International Journal of Advanced Robotic Systems*, Vol. 11, No. 1, 17 February 2014, Article number 20.

[7] Rossi C., Savino S., Niola V., Troncone S., A study of a robotic hand with tendon driven fingers. *Robotica*, ISSN: 0263-5747, doi: 10.1017/S0263574714001179, 2014.

[8] Penta F., Rossi C., Savino S., An underactuated finger for a robotic hand. *International Journal of Mechanics and Control*, Vol. 15, No. 2, ISSN: 1590-8844, 2014.

[9] Giorgetti G., Una mano tutta italiana. *Robotica Magazine*, Vol. 2, No. 2, pp. 10-17, 2011.

[10] Alley R.D. and Sears H.H., Powered upper-limb prosthetics in adults. *Powered Upper Limb Prostheses: Control, Implementation and Clinical Application*, A. Muzumdar, Ed. New York, Springer-Verlag, 2004, ch. 7, pp. 117-145.

[11] Kobrinski A.E., Bolkhovitin S.V., Voskoboinikova L.M., Ioffe D.M., Polyan E.P., Slavutski Y.L., Sysin A.Y. and Yakobson Y.S., Problems of bioelectric control. *Proc. IFAC Int. Congr. of Autom. Rem. Contr.*, Vol. 1, pp. 619-623, 1960.

[12] Fougner A., Stavdahl Ø., Kyberd P.J., Losier Y.G., Parker P.A., Control of upper limb prostheses: terminology and proportional myoelectric control. *IEEE Transactions on neural systems and rehabilitation engineering*, pp. 2-5, 2012.

[13] Losier Y., Shoulder complex motion based input strategies for prosthetic limb control. *Ph.D. dissertation*, Univ. New Brunswick, Fredericton, NB, Canada, 2009.

[14] Niola V., Rossi C., Savino S., Strano S., Robot trajectory planning by points and tangents, *Proc. 10th WSEAS Int. Conference on Robotics, Control and Manufacturing Technology*, Hangzhou, China, April 11-13, ISSN: 1790-5117 91, ISBN: 978-960-474-175-5, pp. 91-96, 2010.

[15] Rossi C. and Savino S., Robot trajectory planning by assigning positions and Tangential Velocities, *Robotics and Computer Integrated Manufacturing*. Vol. 29, No. 1, doi: 10.1016/j.rcim.2012.04.003, pp. 139-156, 2012.

ISSN 1590-8844
International Journal of Mechanics and Control, Vol. 17, No. 01, 2016

NEURAL NETWORK DESIGN FOR INCIPIENT FAILURE DETECTION ON AIRCRAFT EM ACTUATOR

Matteo D. L. Dalla Vedova Davide De Fano Paolo Maggiore

Politecnico di Torino, Department of Aerospace Engineering, Corso Duca degli Abruzzi, 24 - 10129 Torino, Italy

ABSTRACT

Electro-Mechanic actuators are usually driven by Brushless-DC motors. Those ones can be affected by damages caused by fatigue and usage. At incipient stage, failures like partial short-circuit and rotor static eccentricity do not influences overall actuator performance, causing however oscillations in speed and command signals. Focusing on these oscillations, which presents periodic behaviour over the rotor revolution, neural networks are designed and trained to detect and quantify the damage entity. A different approach to this problem is performed, ignoring electrical measures of phase currents and potential drops, which are usually noisy and hardly available as actuator output. Classification results shows good performance in every speed-torque combination, reducing undetected failures and being capable to distinguish between the two kids of failures implemented.

Keywords: ANN, Prognostic, EMA, Short-circuit, Rotor Eccentricity

1 INTRODUCTION

Electro-Mechanic-Actuators(EMA) are one of the most common types of augmented flight control systems in fly-by-wire architectures. Especially for primary FCS, duty cycles are very difficult to predict, standing to the mission-user combination. This difficulty leads the research on components reliability and maintainability, in order to optimise procedures, reducing MTBF and MDT. In this scenario, prognostic studies results fundamental in order to reduce maintenance costs for preserving safety. Differently from mechanical fatigue, which can be predicted with a certain confidence level, electrical failures related to actuators, like partial short-circuit and rotor unbalancing, are hard to detect by the means of an external analysis. Those are mostly caused by extraordinary causes like current peaks or unexpected stresses, and consequences are undetectable in a large scale, as system performance and response could remain almost constant, while the initial incipient damage could rapidly degrades into a severe damage which compromise the system correct working, causing the actuator failure. Considering approximated models for incipient partial phase short circuit and static rotor unbalance damages, a mathematical model of an EMA in failure conditions is simulated, with the purpose of capturing damage-caused dynamics in the actuator output.

Contact author: Matteo D. L. Dalla Vedova

E-mail: matteo.dallavedova@polito.it

As the nature of the problem itself results highly nonlinear and non-fully deterministic, the adoption of Artificial Neural Networks is considered. Designing an appropriate architecture, ANN permits to detect also incipient failures with a good uncertainty level, also with a limited set of inputs, coming directly from noisy sensors. Therefore, the purpose of this work so is to develop a network architecture which takes as input typical system outputs and classifies them in order to detect failures and classifies them, reducing data size and data pre-processing phase, in order to perform a real-time classification.

2 EMA NUMERICAL MODEL

As previously mentioned, the goal of this research is the proposal of a new technique able to identify precocious symptoms (usually defined as failure precursors) of EMA degradations.

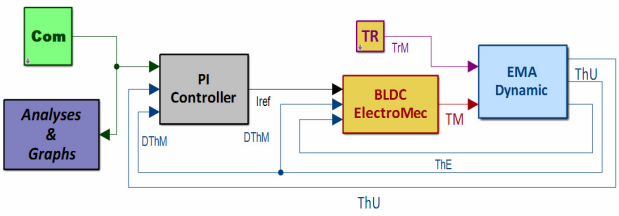

Figure 1 EMA Reference Model.

In order to assess the feasibility, the performance and the robustness of the aforesaid technique, a suitable simulation test bench has been developed in MATLAB/Simulink®. This numerical model, that is widely described in [1], is coherent with the considered EMA architecture shown in Fig. 1:

1. *Com*: generates input position commands.
2. *PI Controller*: simulates the actuator control electronics, closing position and speed feedback loops in and computing as output the reference current *Iref*.
3. *BLDC EM Model*: simulates the power drive electronics trough a SimScape model and the trapezoidal BLDC electromagnetic behaviour, evaluating torque developed as a function of three-phase current generated by an ideal H-bridge regulator.
4. *EMA Dynamic Model*: resolves the dynamic equation of mechanical behaviour by means of a 2 degree-of-freedom (d.o.f.) dynamic system.
5. *TR*: input block simulating the aerodynamic torques acting on the moving surface controlled by the actuator.
6. *Analyses & Graphs*: subsystem containing the EMA monitoring system.

It is useful to remark that this numerical model is able to simulate the dynamic behaviour of the considered EMA servomechanism taking also into account the effects of BLDC motor non-linearities [2-6], end-of-travels, compliance and backlashes acting on the mechanical transmission [7], analogic to digital conversion of the feedback signals, electrical noise acting on the signal lines and electrical offset of the position transducers [8] and dry friction (e.g. acting on bearings, gears, hinges and screw actuators) [9].

2.1 FAILURES IMPLEMENTATION

The present work is focused on two typical BLDC motor failures: the coil short-circuits (SC) and the bearing wear generating rotor static eccentricity (RE). Those are notable examples of progressive failures. At initial stage, those kinds of failures do not influence overall actuator performance substantially and the characteristics of the mechanical transmission, in terms of inertia, dry and viscous frictions, backlashes, noises, etc., could disguise or mitigate the failure effects. In these cases the analysis of electrical harmonics (e.g. phase currents) usually provides a better understanding of the failure progression and its estimation. One hidden aim of this work is to neglect electrical measures and harmonics analyses, focusing on speed and control signal oscillation over an entire rotor revolution. Short-circuit fault can actually occur within a coil, between two coils of the same phase, and two different phases: given that the first case is the most common and is the only one which permits the motor to continue working in degraded conditions. It also generally occurs first and will be the only case considered in this paper. According to [1], for simplicity is assumed that each phase winding consists of turns connected in series and the three-phase windings are wye-connected with a floating neutral point.

Three-phase windings with inter-turn fault in the *a*-phase winding is shown in Figure 3, where *as1* and *as2* represent the healthy and the damaged turns respectively, *ia* is the *a*-phase current, *if* is the circulating current in the shorted turns and *Zf* represents the possible external impedance between the shorted turns [10]. Short-circuits usually start between a few turns.

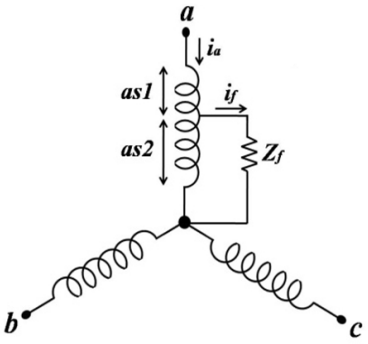

Figure 2 Schematic of turn-to-turn coil short circuit [11].

As in short-circuited resistance decreases, the resulting current increases, generating a localized temperature rising in the conductor which degrades the insulating paint, favours the extension of the failure to adjacent coils.
Considering previous hypothesis, this damage is implemented through an *integrity factor*, computed as follow:

$$N_{ph} = \frac{as2}{(as1+as2)} \qquad 0{,}75 \leq N_{ph} \leq 1 \tag{1}$$

This factor is bounded downward to 0.75, in order to guarantee hypothesis validity and incipient failure stage.
The modification of electrical impedance is so implemented through the following:

$$R_{ph} = R_0 \cdot N_{ph} \tag{2}$$

$$L_{ph} = \frac{L_0}{2 \cdot {N_{ph}}^2} \tag{3}$$

Rotor static eccentricity consists in a misalignment between its rotation axis and the stator axis of symmetry. It occurs usually due to tolerances and imperfections introduced during motor construction or to gradual increase of wear of the rotor shaft bearings. Whenever it occurs, the motor, supposed to have more than one polar couple, generates a periodically variable magnetic flux, as the air gap varies during rotation (Fig. 3) as a function of the rotor position θ:

$$g(\theta) = g_0(1 + \zeta \cos(\theta)) \quad \textit{where} \quad \zeta = \frac{x_0}{g_0} \tag{4}$$

In (4) RE is normalised to the nominal air-gap value g_0.
Considering performances, as reported in [12], output torque is lowered at same phase current condition respect to nominal, whereas, spectral analysis reveals the presence of sub-harmonics increasing with eccentricity.

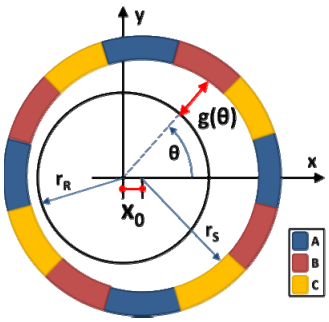

Figure 3 Schematic static RE.

RE and SC effects is by means of a simplified numerical algorithm, as both change the magnetic coupling between stator and rotor, in fact, failures can be modelled by proper static gains and angular modulations of the back-EMF coefficients:

$$\theta_e = 2\theta mod(360) \quad where \quad \varphi_{ph} = \begin{cases} 0° \\ 120° \\ 240° \end{cases} \tag{5}$$

$$K_{ph} = K(\theta_e) \cdot N_{ph} \cdot \left(1 + \zeta cos\left(\theta_e + \varphi_{ph}\right)\right) \tag{6}$$

The effects that these progressive failures produce on the dynamic behaviours of the considered actuation system are discussed in [1].

3 NEURAL NETWORK INPUT BUILDING

Three simulation campaigns were performed, to analyse single failure behaviour for RE and SC, then a multiple failures combination. Every simulation presents a constant speed command with fixed values of resistant torque and damage entity. Initial condition for every simulation is actuator settled in neutral position.
The principal hypothesis for simulations is that phase currents would not reach the maximum value of 22.5A, so that *PI controller* is not saturated. In order to assure this, a characterisation of the actuator were performed, finding the extreme working line at maximum current conditions.

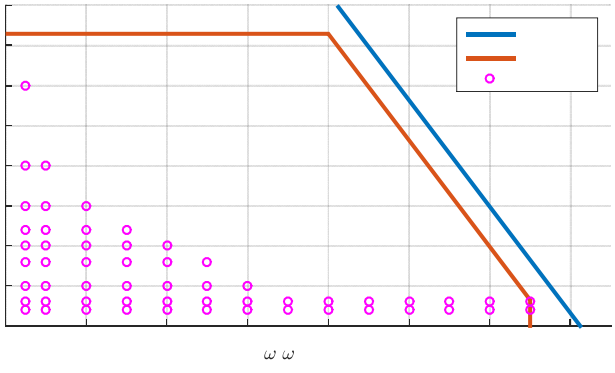

Figure 4 Simulation grid & boundaries.

Simulation grid is shaped to cover typical actuator working conditions, featured by low torque and high speeds. The considered output were the rotor speed and the reference signal coming from the controller.

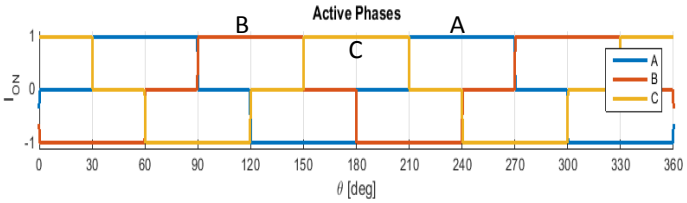

Figure 5 H-bridge switching sequence.

4 SHORT CIRCUIT OUTPUT ANALYSES

For the output analyses, a rotated reference system is introduced to match the x axis with the boundary point between two A and B phases windings. Doing so, it is possible to divide an entire revolution in twelve sectors corresponding to the stator windings.

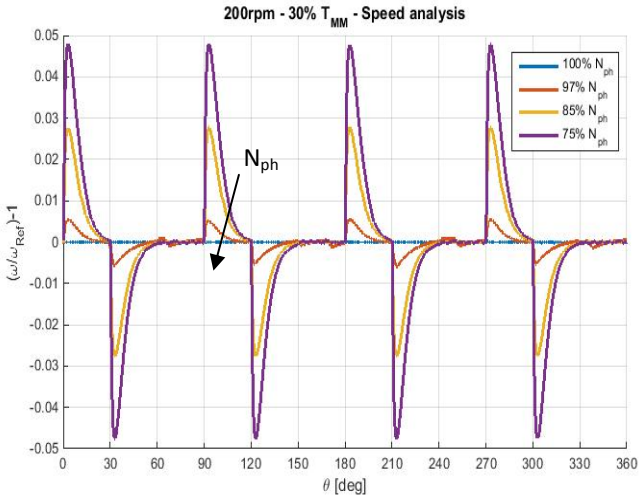

Figure 6 Speed response at various SC conditions.

To emphasise oscillations, as in Figure 6, signals are normalised to the average value for the entire rotation.

$$\hat{X}(\theta) = \frac{X(\theta)}{X_{360}} - 1 \tag{7}$$

Considering damaged phase A windings, it is possible to observe speed oscillations caused by its switching transition between three possible states. These oscillation are caused by two factors. First one is the electrical modification described by (2) and (3). Then the back-EMF modification described in (6). Considering the electrical and controller dynamics, circulating current tend to remain constant for a short transition phase, with a resultant torque respectively higher if the A winding is turned OFF and lower if it is turned ON from idle.

5 ROTOR ECCENTRICITY OUTPUT ANALYSES

The main hypothesis for static rotor eccentricity (RE) simulations is the unbalance direction, fixed in the middle of one A-phase winding (as shown in Fig. 3). This assumption reduces the number of variables to considerate to the measure described in (4). The same computation described in (7) is performed in this case, leading to analogous results. In this case, speed oscillations are caused only by back-EMF modification, and presents more discontinuities around the revolution. Moreover, back-EMF is proportional to rotor speed, causing a rise in total load applied to the stator circuit. Differently from the aforesaid turn-to-turn coil short circuit (SC) case, this damage involves all phases in different manner, determined by the eccentricity direction fixed previously.

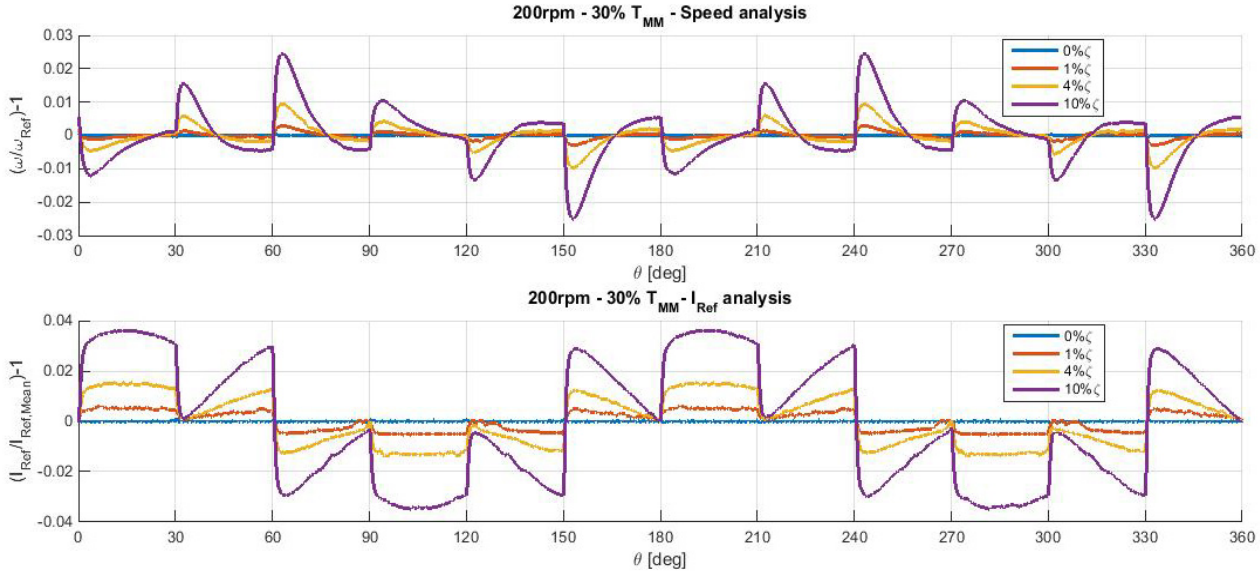

Figure 7 Speed and reference signal response at various RE conditions.

6 DATA PRE-PROCESSING

In order to reduce input data size without losing main signal features, the average value over a 30° interval, corresponding to a single winding coverage, is computed for speed and reference signal:

$$X_{30,i} = \frac{\int_{\theta_i}^{\theta_i+30} X(\theta)\, d\theta}{30} \qquad 1 \le i \le 12 \tag{8}$$

Recalling (7), signals are then normalised, and an entire revolution can be represented by twelve significant points corresponding to the windings. One further step is the computation of RMS value over the twelve normalised:

$$X_{RMS} = \sqrt{\frac{\sum_{i=1}^{12}\left(\hat{X}_i\right)^2}{12}} \tag{9}$$

At this point is possible to build the neural network input vector, composed by the working condition by the mean of speed and reference current average values over a revolution and the RMS values representative of the oscillation magnitude:

$$X_{NN} = \begin{bmatrix} \omega_{360} \\ I_{360} \\ \omega_{RMS} \\ I_{RMS} \end{bmatrix} \tag{10}$$

7 NEURAL NETWORK ARCHITECTURE

Characteristic periodic behaviour of speed and reference current can lead to a damage classification by the mean of a *Pattern recognition* network [13]. By the means of one *tansig* hidden layer followed by a *competitive* layer permits to classify input vectors in user-defined classes.

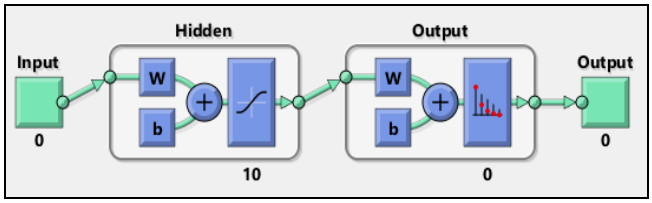

Figure 8 Pattern recognition network.

The *Pattern-recognition* output vectors as per their nature, resolves a nominal classification problem. Considering the fault effects on rotor speed and reference current signal, at different speed and torque conditions, it is not possible to develop a deterministic model, due to the underlying mechanical and electro-magnetic effects. *Tansig* layer is a continuous function, limited between -1 and +1. Its main features is to mitigate values far from origin, highlighting differences between values lying around zero. This fits well the normalisation process performed ahead the network

input. Hence damage classification becomes a stochastic problem, which can be modelled as a *Multinomial Logistic Regression*, performed by a *softmax* layer:

$$\sigma(z)_i = \frac{e^{z_i}}{\sum_{k=1}^{N} e^{z_k}} \tag{11}$$

$$\sum_{i=1}^{N} \sigma_i = 1 \tag{12}$$

This function normalises an input real values-composed vector into a same-size vector which elements sum results one. Under the hypotheses of input data statistic independence, which is satisfied by (10), it is possible to discretize the damage entity in numbered classes.
The output of this layer represents so a probability distribution, where the emerging class is considered for final classification.

7.1 TRAINING PHASE

For every point in Figure 4 several simulations with different failures are performed. The considered damage entity are represented by the following vectors:

$$N_{ph} = [100 \quad 99 \quad 97 \quad 95 \quad 90 \quad 85 \quad 80 \quad 75]_8\% \tag{13}$$

$$\zeta = [0 \quad 1 \quad \dots \quad 10]_{11}\% \tag{14}$$

As eight SC and eleven RE cases are simulated, target sequences are represented by identity matrices respectively of 8 and 11 dimension. Back propagation algorithm is used to train all networks developed.. The scaled conjugate gradient algorithm is used to calculate derivatives of performance with respect to the weight and bias variables. It is based on conjugate directions, and does not perform a line search at each iteration [14]. To assure network generalisation input / target sequence is presented randomly to the training algorithm, as weights and biases initialization.

8 CLASSIFICATION ACCURACY

To evaluate the resultant classification accuracy, confusion matrices is considered. These presents target classes coming from its relative matrix on the x-axis and the related network output, after training phase is conducted. Well classified samples lays on the main diagonal, where target and output corresponds.
In Figure 9, the first row represents normal condition output class (*undamaged*). Every sample out from the first box represents an undetected damage. Considering the #2 and #3 classes (99% and 97% N_{ph} respectively), in which undetected failures occurs, it is possible to states the network sensitivity to SC. Maintaining the input matrix, it is possible to build several target matrices to perform different kinds of classifications. One trivial solution tried is to divide samples into two main categories: normal and damaged condition.

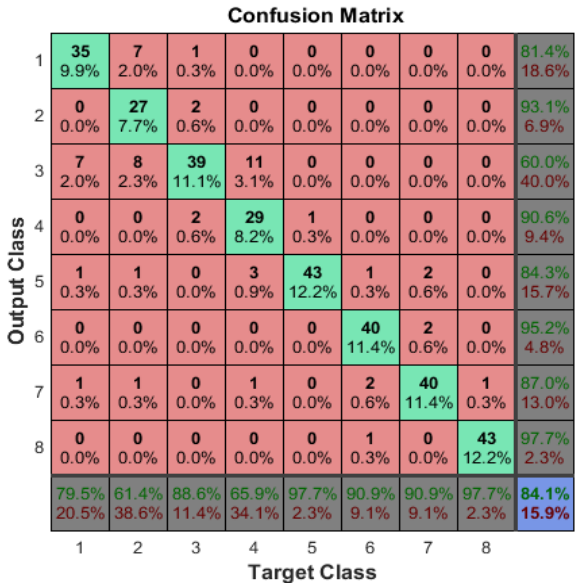

Figure 9 SC confusion matrix.

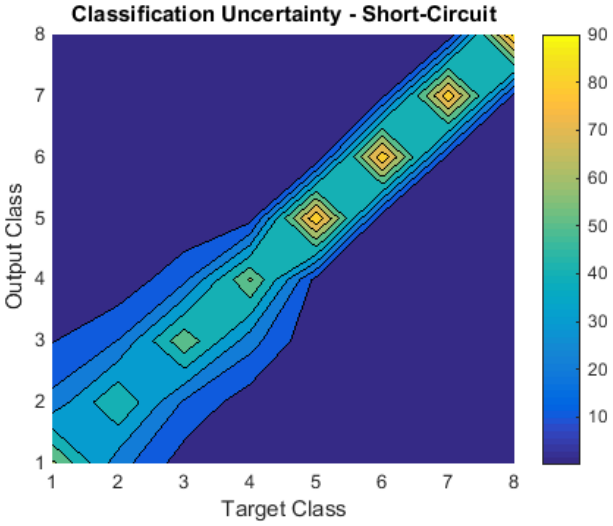

Figure 10 SC Accuracy map.

As the number of considered classes decreases, the classification performance generally rises, as demonstrated in [15]. Analogous results are reached in RE case, proving the method reliability. Taking advantage of the stochastic nature of *softmax* output, it is possible to transform the discrete classification results into a continuous map. By the processing of every network output it is possible to evaluate an overall accuracy as showed in Figure 10. As per the confusion matrix, the main diagonal indicates the well classified elements. Considering the simulated failures vector (13), the higher accuracy occurs for major damages, which are also well distinguished from the adjacent classes, due to the major damage entity gap (1% between classes #1 and #2 – 15% between #7 and #8).

9 MULTIPLE FAILURES

To test the robustness of the designed networks, a multiple failures simulation campaign is performed. Considering the increasing size of the problem, a fixed value of 5%T_{MM} output torque is demanded, with the following *unbalance-short-circuit* combinations considered:

$$\zeta_{\%} = [0 \quad 5 \quad 15]\% \tag{15}$$

$$SC_{\%} = [0 \quad 10 \quad 25]\% \tag{16}$$

As per the architecture and training samples, which considers RMS and averaged values, most of the damage combinations could lead to false positives detection for both damages[15].

9.1 MULTIPLE FAILURES NETWORK

A different approach is followed to develop an additional ANN, which is capable to distinguish the type of failure. *Pattern recognition* networks results the most suitable architecture also in this case. Despite taking advantage of RMS values, which is a scalar measure of oscillation entity, the oscillation shape around an entire revolution is considered. It must be noted that the normalisation process remains the same previously described in (7).

Differently from previous networks, the input vector is composed by the revolution-average values and the sorted vectors of $\hat{X}_{30,i}$ values of speed and *Iref*:

$$X_{rev} = \begin{bmatrix} \hat{X}_{30.1} \\ \vdots \\ \hat{X}_{30.12} \end{bmatrix}_{12\times 1} \tag{17}$$

$$X_{NN} = \begin{bmatrix} \omega_{rev12\times 1} \\ I_{rev12\times 1} \\ \omega_{360} \\ I_{360} \end{bmatrix} \tag{18}$$

The purpose of this network is to recognize oscillation features of different failures combinations trough the analyses of twelve significant points representative of the entire rotation. Also target building has got different purpose. In fact, three classes compose the target vector. Two over three represents the SC and RE failure. The third class is called *interference* class (INT): its purpose is to mitigate the inactive failure probability in the output vector and distinguish also the normal working condition:

$$T_i = \begin{bmatrix} SC \\ INT \\ RE \end{bmatrix} \tag{19}$$

When just one kind of failure is active, relative target vector will contain both the relative failure class and the interference class with a value limited to 0.5 in order to lead the network output and weight modification toward the right class during training phase. The considered target vector and resultant classification lead to a different analysis of results. For this network the confusion matrix cannot highlights the classification performance.

As nine damage combinations are simulated for every speed condition, it is possible to observe the classification results for every combination by pie charts.

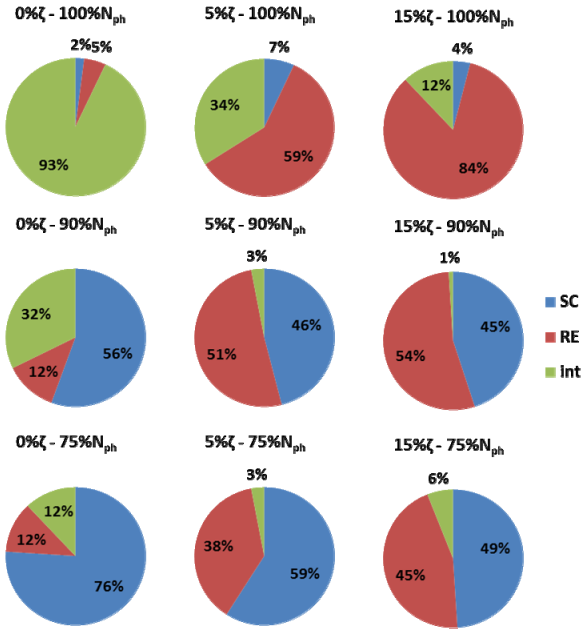

Figure 11 Multiple-failures network accuracy map.

10 CONCLUSIONS

Considering the reduced number and size of inputs, the limited data pre-processing and simple network architecture, the overall classification performance results satisfactory. Fault design is an approximation, not considering the complete electro-magnetic interactions between stator and rotor. Considering the limited failure entity and the low torques and currents involved, hypotheses results acceptable. In fact, the major result is the detection through mechanical and logical signals (shaft speed and Controller Reference current), neglecting electrical signals as phase currents or voltages. Advantages of this approach consists in a limited sensor data demand (i.e. shaft position and Brushless DC motor controller output), which are also cleaner in noise more available respect to electrical measures (e.g. phase voltages and currents). The need of Controller output signal binds the network training to the overall actuation system. This means that the solution shall be characterized for further applications. Interesting developments can be found investigating network suitability in other kinds of actuators. In fact, primary FCS can be considered as speed-position drives where components are not subject to constant stresses and usually works in transitory rather than steady conditions. Other applications like torque motors or pumps concerns significant torques and currents and can work in steady conditions, simplifying the actuator characterization and prognostic work.

REFERENCES

[1] Maggiore P., Dalla Vedova M.D.L., Pace L., Desando A., Proposal of fault analysis parametric method applied to an electro mechanical servomechanisms affected by failures. *International Journal of Prognostics and Health Management*, Vol. 6, No. 1, 2015. ISSN: 2153-2648

[2] Çunkas M., Aydoğdu O., Realization of Fuzzy Logic Controlled Brushless DC Motor Drives using Matlab/Simulink. *Mathematical and Computational Applications*, Vol. 15, pp. 218-229, 2010.

[3] Halvaei Niasar A., Moghbelli H., Vahedi A., Modelling, Simulation and Implementation of Four-Switch Brushless DC Motor Drive Based On Switching Functions. *IEEE EUROCON 2009*, St. Petersburg, pp. 682 -687, 2009.

[4] Lee B.K., Ehsani M., Advanced Simulation Model for Brushless DC Motor Drives. *Electric Power Components and Systems*, Vol. 31, No. 9, pp. 841-868, 2003. ISSN: 1532-5008

[5] Hemanand T., Rajesh T., Speed Control of Brushless DC Motor Drive Employing Hard Chopping PWM Technique Using DSP. *Proceedings of India Intern. Conference on Power Electronics (IICPE 2006),* 2006.

[6] Haskew T.A., Schinstock D.E., Waldrep E., Two-Phase On' Drive Operation in a Permanent Magnet Synchronous Machine Electromechanical Actuator. *IEEE Trans. on Energy Conversion*, Vol. 14, No. 2, 1999.

[7] Borello L., Villero G., Dalla Vedova M.D.L., New asymmetry monitoring techniques: effects on attitude control. *Aerospace Science and Technology*, Vol. 13, No. 8, pp. 475-487, 2009.

[8] Borello L., Dalla Vedova M.D.L., Jacazio G., Sorli M., A Prognostic Model for Electrohydraulic Servovalves. *Annual Conference of the Prognostics and Health Management Society*, San Diego, CA, 2009.

[9] Borello L., Dalla Vedova M.D.L., A dry friction model and robust computational algorithm for reversible or irreversible motion transmission. *International Journal of Mechanics and Control*, Vol. 13, No. 2, pp. 37-4, 2012.

[10] Farooq J.A., Djerdir A., Miraoui A., Modelling and simulation of stator winding inter-turn faults in permanent magnet synchronous motors. *COMPEL - The International Journal for Computation and Mathematics in Electrical and Electronic Engineering*, Vol. 27, No. 4, pp. 887–896, 2008. ISSN: 0332-1649

[11] Kim B.W., Kim K.T., Hur J., Simplified impedance modeling and analysis for inter-turn fault of IPM-type BLDC motor. *Journal of Power Electronics*, Vol. 12, pp. 10-18, 2012. ISSN: 1598-2092

[12] Dalla Vedova M.D.L., Maggiore P., Pace L., Romeo S., Proposal of a model based fault identification neural technique for more-electric aircraft flight control EM actuators. *WSEAS Transactions on Systems*, Vol. 15, Art. #3, pp. 19-27, 2016.

[13] Chopra I., Ganguli R., Haas D.J, Detection of Helicopter Rotor System Simulated Faults Using Neural Networks. *Proceedings of the 37th Structures, Structural Dynamics and Materials Conference (AIAA-96-1646-CP)*, Salt Lake City, UT, pp. 1246-1263, 1996.

[14] Møller M.F., A scaled conjugate gradient algorithm for fast supervised learning. *Neural networks*, Vol. 6, No. 4, pp. 525-533, 1993.

[15] De Fano D., *Artificial Neural Network design for BLDC Motor short circuit and rotor unbalance early detection*. MSc Thesis, Politecnico di Torino, 2016.

ISSN 1590-8844
International Journal of Mechanics and Control, Vol. 17, No. 01, 2016

CLOSING SEQUENCE OF AN UNDERACTUATED ANTHROPOMORPHIC MECHANICAL FINGER

Francesco Penta

Università degli Studi di Napoli Federico II, Dipartimento di Ingegneria Industriale

ABSTRACT

The mechanical behavior of an under-actuated finger device equipped with only one flexural tendon and only one extensor tendon is studied. The finger equilibrium is analyzed by an energetic approach; this permitted to identify some preliminary design criteria useful to obtain both the regularity of the finger motion and a human like closure sequence. Furthermore, a sufficient condition for the stability of the finger equilibrium is also derived. In the paper some numerical data to be used as starting point for any finger design purpose are also reported. To substantiate the proposed criteria, numerical results obtained from a finger case study are finally presented and discussed.

Keywords: Mechanical finger, finger design criteria, finger buckling, anthropomorphic closing sequence

1 INTRODUCTION

Since long time for the construction of robotic grasping devices and human hand prosthesis, the principles of under-actuation are adopted. This because by this approach, the number of servomotors or servo-actuators are greatly reduced and the control architectures are also simplified [1-13]. However, under-actuation make crucial the analysis and design of the main components of these devices, i.e. the fingers. If, actually, in the finger equilibrium paths unstable configurations are present, device control become impossible and, consequently, the grasping forces may reduce to unsatisfying levels. A second feature that also has to be examined with particular care is the sequence of relative rotations between the phalanxes by which the finger encloses the object to be grasped [14-19]. It is quite evident that if the closing sequence is incorrect the grasping action may become precarious or unstable or even the finger may close on itself without grasping. At present, the design of an under-actuated finger is carried out by trial and error on the base of results obtained by numerical models or direct experimentation on finger prototypes.

Contact author: Francesco Penta

Address: P.le V. Tecchio n° 80 – 80125 Naples – Italy
Phone: +39 – (0)81 7682451
E-mail: penta@unina.it

The high number of geometrical parameters on which the mechanical behaviour of an under-actuated finger depends and the analytical difficulties that are encountered when the stiffness matrix of the device is analysed make practically impossible the use of a direct method to identify the optimal geometry of its joints. In the present paper for the special case of an under-actuated finger equipped with double tendon (one for the flexion, the other for the finger extension) an approximated method is presented to optimize the geometry of the tendon guides of both the tendons. The study is based on some theoretical and experimental results obtained in previous works [7, 20-21]. Firstly, a sufficient condition for the stability of the finger equilibrium is given. Then, preliminary design criteria for the regularity of the finger motion and an anthropomorphic closure sequence are also obtained. Finally, to substantiate the proposed methods, some numerical examples are presented and discussed.

2 THE FINGER MECHANICAL MODEL

A schematic sketch of the finger device analysed in the present study is given in fig. 1. The finger is composed of four rigid links jointed by means of three hinges free of friction. Of these four links, one is fixed since it acts as metacarpal phalanx; the remaining three are movable and function as proximal, medial and distal phalanxes. The flexor and extensor moments are applied to each phalanx thanks to a couple of tendons having an end fixed to the distal phalanx.

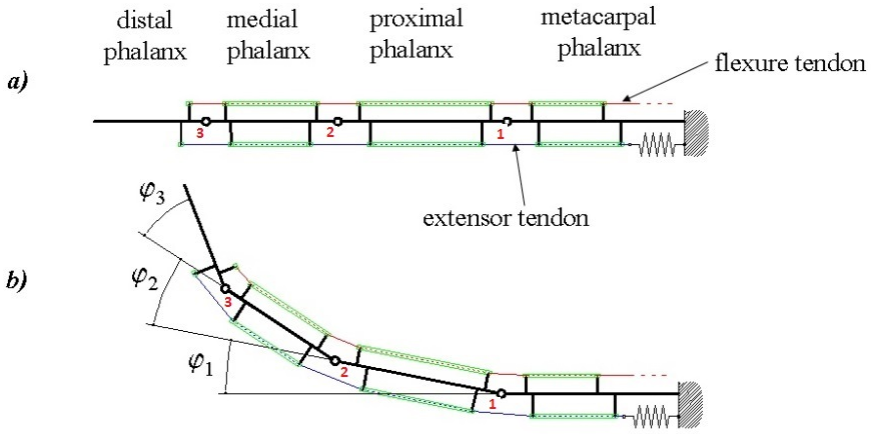

Figure 1 Scheme of the finger; initial or extended configuration (a) and deformed or bent configuration (b). Adapted from [21].

The extensor tendon is also elastically constrained to the metacarpal phalanx by a spring which stiffness is *k*. To the free end of the flexural tendon, instead an actuator applies the traction force causing the finger deformation. All the phalanxes, furthermore, are provided with a couple of cylindrical guides where the tendons can freely slide when the finger phalanxes rotate. We assume that both tendons are inextensible, have negligible thickness and negligible bending stiffness.

As lagrangian coordinates of the finger the absolute rotation φ_1 of its proximal phalanx, the relative rotation φ_2 between the proximal and the medial phalanx and, finally, the relative rotation φ_3 between the medial and the distal phalanx were considered (Fig. 2b). Hence, a finger configuration is univocally defined by the vector column $\boldsymbol{\varphi} = \left[\varphi_1, \varphi_2, \varphi_3\right]^T$.

In the present study the initial or reference configuration of the finger is the one with all the phalanxes totally extended (see Fig. 2-a)), that is with all the rotations $\varphi_i = 0,$ with $i = 1,2,3$. For sake of simplicity, the hinges of the finger are numbered consistently with the notation adopted for the lagrangian coordinates: *i* will denote the hinge where the rotation φ_i occurs.

Moreover, a movable phalanx is also identified by the same number of the hinge that is on its right side in the reference configuration.

The parameters that define the geometry of the tendons close to the *i*-th joint or hinge are shown in the enlarged view of fig. 2. The length z_i of the free-path P_iQ_i followed by the flexural tendon and the length l_i of the free path R_iS_i of the extensor tendon can be expressed as:

$$\begin{aligned} z_i &= \sqrt{s_i^2 + d_i^2 - 2 s_i d_i \cos\left(\Phi_i - \varphi_i\right)} = s_i \cdot \zeta_i\left(\varphi_i\right) \\ l_i &= \sqrt{\bar{s}_i^2 + \bar{d}_i^2 - 2 \bar{s}_i \bar{d}_i \cos\left(\bar{\Phi}_i + \varphi_i\right)} = \bar{s}_i \cdot \lambda_i\left(\varphi_i\right), \end{aligned} \tag{1}$$

$\zeta_i = \sqrt{1 + \varepsilon_i^2 - 2\varepsilon_i \cos\left(\Phi_i - \varphi_i\right)}$ and $\lambda_i = \sqrt{1 + \bar{\varepsilon}_i^2 - 2\bar{\varepsilon}_i \cos\left(\bar{\Phi}_i - \varphi_i\right)}$ are non-dimensional functions of the relative rotation φ_i, that depend respectively also on the non-dimensional ratios $\varepsilon_i = \dfrac{d_i}{s_i}$ and $\bar{\varepsilon}_i = \dfrac{\bar{d}_i}{\bar{s}_i}$ defining the initial shape of the joint.

The distances b_i and $\bar{b}_i$ of fig. 2, that separate the free-paths respectively of the flexor and extensor tendons from the hinge center O_i, are given by:

$$\begin{aligned} b_i &= -\frac{dz_i}{d\varphi_i} = s_i \cdot \beta_i\left(\varphi_i\right), \\ \bar{b}_i &= \frac{dl_i}{d\varphi_i} = \bar{s}_i \cdot \bar{\beta}_i\left(\varphi_i\right), \end{aligned} \tag{2}$$

where:

$$\begin{aligned} \beta_i &:= \frac{\varepsilon_i \sin\left(\Phi_i - \varphi_i\right)}{\sqrt{1 + \varepsilon_i^2 - 2\varepsilon_i \cos\left(\Phi_i - \varphi_i\right)}}, \\ \bar{\beta}_i &:= \frac{\bar{\varepsilon}_i \sin\left(\bar{\Phi}_i + \varphi_i\right)}{\sqrt{1 + \bar{\varepsilon}_i^2 - 2\bar{\varepsilon}_i \cos\left(\bar{\Phi} + \varphi_i\right)}}. \end{aligned} \tag{3}$$

When the finger, starting from its reference configuration reaches the configuration $\boldsymbol{\varphi}$, the flexor tendon free paths $P_i\bar{Q}_i$ experience the shortenings

$$\Delta z_i = z_{0i} - z_i, \; i = 1,2,3; \tag{4}$$

with z_{0i} initial value of z_i (Fig. 2-a). Consequently, the free end of the flexor tendon performs the displacement u given by:

$$u = \sum_{i=1}^{3} \Delta z_i \tag{5}$$

Similarly, the elongation Δl of the spring constraining the extensor tendon to the metacarpal phalanx is:

$$\Delta l = \sum_{i=1}^{3} \bar{s}_i \left[\lambda_i\left(\varphi_i\right) - \lambda_{i0}\right] \tag{6}$$

with $\lambda_{i0} = \lambda_i(0) = \sqrt{1 + \bar{\varepsilon}_i^2 + 2\bar{\varepsilon}_i \cos\left(\bar{\Phi}\right)}$ initial value of λ.

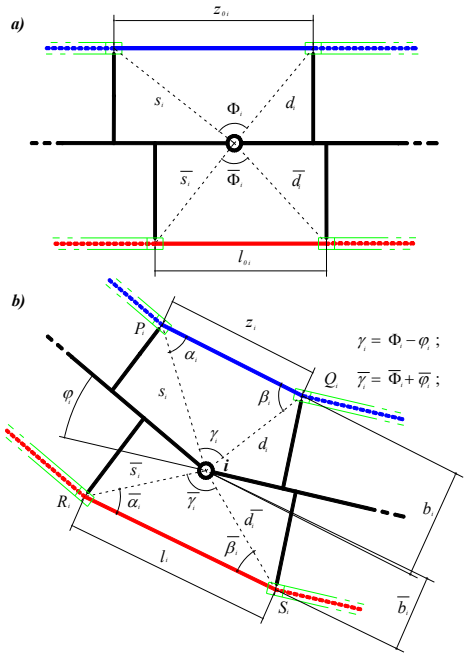

Figure 2 Initial (a) and deformed (b) configurations of the i-th joint. Adapted from [21].

As to the effects of the shape parameter ε_i on the mechanical behaviour of the finger, we observe preliminary that the function $z_i(\varphi_i)$ and its derivatives are invariant when the values of the distances s_i and d_i of fig. 2 are exchanged. This means that a joint where:

$$s_i = \bar{s} \text{ and } d_i = \varepsilon_i^* s_i, \text{ with } \varepsilon_i^* > 1, \tag{7}$$

has the same behaviour as the one with:

$$s_i = \varepsilon_i^* \bar{s} \text{ and } d_i = \bar{s} = \hat{\varepsilon}_i^* s_i \text{ with } \hat{\varepsilon}_i^* = \frac{1}{\varepsilon_i^*} < 1. \tag{8}$$

For this reason in the present study only joints with $\varepsilon_i \in [0,1]$ will be considered. Similar considerations apply for the effects of the other shape parameter $\bar{\varepsilon}_i$ and the function $\lambda_i(\varphi_i)$. Regardless of the effective shapes and sizes of the external surfaces of the phalanxes (where the contact with the objects to be grasped or with the other phalanxes takes place), we assume in the following that the range of values in which each rotation φ_i may vary has the angle Φ_i of fig. 2-a) as upper end, namely $\varphi_i \in [0, \Phi_i]$.

2.1 THE FINGER EQUILIBRIUM EQUATIONS

Under the stated hypothesis, the finger under the action of the horizontal load f applied to the flexural tendon is a conservative system. Hence, its equilibrium configuration $\boldsymbol{\varphi}$ has to satisfy the stationary condition of the total potential energy E, that is:

$$\begin{aligned} dE &= d\left(\frac{1}{2}k \cdot \Delta l^2 - f \cdot u\right) \\ &= \frac{\partial}{\partial \varphi_i}\left(\frac{1}{2}k \cdot \Delta l^2 - f \cdot u\right) d\varphi_i = 0 \qquad \forall d\varphi_i. \end{aligned} \tag{9}$$

Carrying out differentiation in eq. (9) and taking account of eq.(1) – (6), the set of equilibrium conditions is derived:

$$k\Delta l \cdot \bar{b}_i = f\, b_i, \qquad i = 1, 2, 3. \tag{10}$$

By equating the expressions of the load f obtained from each of equations (10) and simplifying the common factors, then the following chain of equalities is obtained:

$$\alpha_1 \frac{\bar{\beta}_1(\varphi_1)}{\beta_1(\varphi_1)} = \alpha_2 \frac{\bar{\beta}_2(\varphi_2)}{\beta_2(\varphi_2)} = \alpha_3 \frac{\bar{\beta}_3(\varphi_3)}{\beta_3(\varphi_3)}; \tag{11}$$

According to previous result, the finger equilibrium configurations are only those for which the three arm ratios $r_i = \alpha_i \cdot \left(\bar{\beta}_i / \beta_i\right)$ are equal. In order to the finger leaves the reference or initial configuration without significant vibrations or other dynamic effects when the load f is gradually applied to the flexor tendon, it is necessary that:

$$\rho_1(0) = \rho_2(0) = \rho_3(0). \tag{12}$$

These particular conditions can be met by several choices of the geometrical parameters of the finger joints. Among them, the one offering the possibility of obtain a quite wide set of finger closure sequences consists of choosing the angles $\Phi_i = 0$, since it will result:

$$\rho_i(0) = 0 \tag{13}$$

for any value of the shape parameters ε_i and $\varepsilon_i^{(e)}$ as well of the non-dimensional parameters α_i.

2.2 A CONDITION FOR THE FINGER STABILITY

To analyse the properties of the finger equilibrium configurations, the second variation d_2E of the potential E has to be considered. This latter is given by:

$$d_2E = \frac{\partial}{\partial \varphi_j}\left(k\Delta l\, \bar{b}_i - f\, b_i\right) d\varphi_i\, d\varphi_j \tag{14}$$

Since the total differential of Δl has the following expression:

$$d\Delta l = \frac{\partial \Delta l}{\partial \varphi_k} d\varphi_k = \bar{b}_k\, d\varphi_k \tag{15}$$

and observing that

$$\begin{aligned} &\frac{\partial}{\partial \varphi_j} \bar{b}_i(\varphi_i) = \delta_{ij} \bar{b}_i'(\varphi_i) \\ &\frac{\partial}{\partial \varphi_j} b_i(\varphi_i) = \delta_{ij} b_i'(\varphi_i), \end{aligned} \tag{16}$$

the second variation d_2E can also be written in the form:

$$\begin{aligned} d_2E &= k\left(d\Delta l\right)\bar{b}_i\, d\varphi_i + \left(k\Delta l\, \bar{b}_i' - f\, b_i'\right) d\varphi_i^2 = \\ &= k\left(d\Delta l\right)^2 + k\Delta l\, \bar{b}_i \left(\frac{\bar{b}_i'}{\bar{b}_i} - \frac{b_i'}{b_i}\right) d\varphi_i^2, \end{aligned} \tag{17}$$

where the last equality is obtained by substituting the expression $f = k\Delta l\left(\bar{b}_i / b_i\right)$ derived from equilibrium equations (10).

By eq. (17) it is immediately recognized that a sufficient condition for stability of finger equilibrium is:

$$\frac{\bar{b}_i'}{\bar{b}_i}-\frac{b_i'}{b_i}=\frac{\bar{\beta}_i'}{\bar{\beta}_i}-\frac{\beta_i'}{\beta_i}>0 \quad \forall \varphi_i \in [0,\Phi_i]. \tag{18}$$

As shown by the results of fig. 3, where the quantities $\bar{\beta}_i'/\bar{\beta}_i$ and β_i'/β_i are diagrammed as function of the relative rotations φ_i for $\bar{\Phi}_i=0$ and for the two cases of particular interest for the practical applications, namely $\Phi_i=\pi/2$ and $\Phi_i=2\pi/3$, for any value of the shape ratio ε_i the condition (18) can be satisfied choosing $\bar{\varepsilon}_i$ lesser than the limit value $\bar{\varepsilon}_{\lim}$. This particular value of $\bar{\varepsilon}_i$ depends on ε_i since it makes the $\bar{\beta}_i'/\bar{\beta}_i$ curve as function of φ_i tangent to the analogous β_i'/β_i curve. In the diagram of fig. 4, the curve of $\bar{\varepsilon}_{\lim}$ as function of ε_i are traced. They were obtained numerically solving, for each value of ε_i, the following system of algebraic equations:

$$\begin{cases} \dfrac{\beta'}{\beta}=\dfrac{\bar{\beta}'}{\bar{\beta}}, \\ \dfrac{d}{d\varphi}\left(\dfrac{\beta'}{\beta}\right)=\dfrac{d}{d\varphi}\left(\dfrac{\bar{\beta}'}{\bar{\beta}}\right). \end{cases} \tag{19}$$

In the following section it will be shown that, although the condition (18) is strongly conservative against finger buckling, by means of the finger geometries verifying it (and that are stable) it is possible to realize a quite wide set of finger closure sequences.

3 ANTHROPOMORPHIC FINGER CLOSURE

For the two cases $\Phi_i=\pi/2$ and $\Phi_i=2\pi/3$ in Figure 5-a) and b) the curves of the ratio $\bar{\beta}_i/\beta_i$ as function of φ_i are reported. These curves have been obtained with values of the shape parameters belonging to the stability regions of fig 4. Inspection of diagrams of fig. 5 reveals that:

- All the curves have a vertical asymptote at $\varphi_i=\Phi_i$ because the non-dimensional arm β_i tends to zero as the angle φ_i tends to the maximum value Φ_i. This make unattainable the condition of maximum closure of the phalanxes, a property that has to be taken in account when the angle Φ_i has to be chosen based on the finger functional specifications.
- The mean slope of the curves is increasing with ε_i. The slope $\dot{\rho}_i$ of a curve is initially decreasing with φ_i until the minimum value $\dot{\rho}_{i\min}$ is reached in the characteristic point having coordinate $(\bar{\varphi}_i,\bar{\rho}_i)$. From this minimum point the slope increases monotonically until it diverges.
- Due to the presence of a minimum point for the slope, all the curves follow a quasi-linear trend in a range of φ_i values that is approximately centered on $\varphi_i=\bar{\varphi}_i$. The higher ε_i is and the smaller $\varepsilon_i^{(e)}$ is the wider this range of φ_i values is.
- Finally, the minimum slope $\dot{\rho}_{i\min}$ is a decreasing function of ε_i.

Since the curves of fig. 5 follows a sigmoidal trend, by them it is not possible to identify by a direct method the optimal geometry of the finger joints able to achieve a given closure sequence. For this reason, it is preferable to substitute the curves of fig. 5 a) and b) by the approximating straight lines that are tangent to the curves in their characteristic point $(\bar{\varphi}_i,\bar{\rho}_i)$. These straight lines are fully identified in terms of initial offsets $\hat{\rho}_i$ and slopes $\dot{\rho}_{i\min}$ listed in Tab. I and II as function of ε_i and $\varepsilon_i^{(e)}$. This approximation of the non-dimensional arm ratios $\bar{\beta}_i/\beta_i$ is equivalent to approximating the corresponding sigmoidal curves of the ratios $r_i=\alpha_i\cdot(\bar{\beta}_i/\beta_i)$ by straight lines having slope equal to $\alpha_i\,\dot{\rho}_{i\min}$ and initial offset $\hat{r}_i=\alpha_i\,\hat{\rho}_i$.

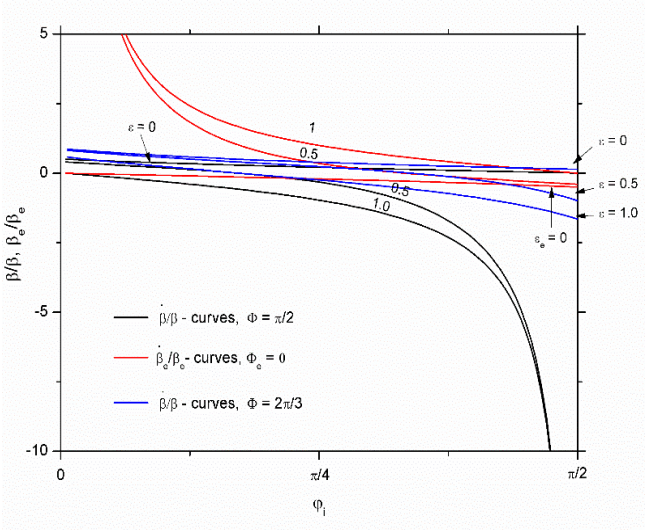

Figure 3 Diagram of logarithmic derivative $\bar{\beta}_i'/\bar{\beta}_i$ and β_i'/β_i as function of φ_i.

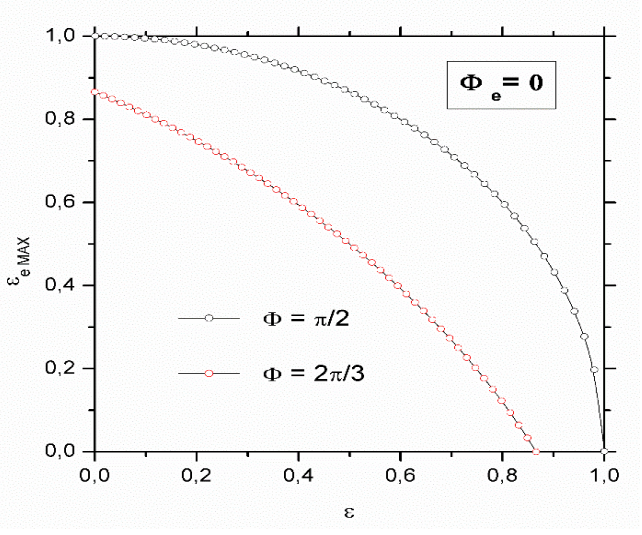

Figure 4 Diagram of the limit value $\bar{\varepsilon}_{\lim}$ as function of ε_i.

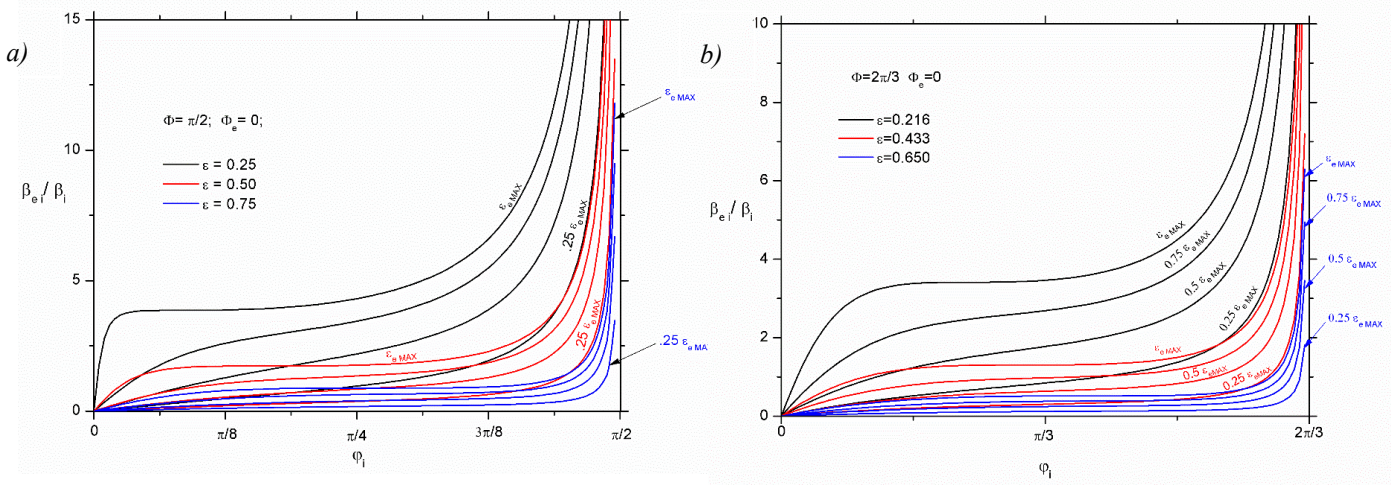

Figure 5 Diagrams of the non-dimensional arm-ratios $\rho_i = \overline{\beta}_i / \beta_i$ as function of φ_i : *a)* $\Phi = \pi/2$, *b)* $\Phi = 2\pi/3$.

By the data of Table I and II it is possible to carry out the preliminary design of a finger device having a closure sequence very similar to the one of a human finger. In other words, the closure will occurs by means of relative rotations taking place at first exclusively between the metacarpal and proximal phalanxes, then between the medial and proximal phalanxes and lastly between the medial and distal ones. To this aim, the shape ratios ε_i, $\overline{\varepsilon}_i$ and the parameters α_i have to be chosen such that the following conditions for the initial off-sets $\hat{r}_i$ and the abscissae's $r_{\Phi i}$ of fig. 6 are verified:

$$r_{\Phi 2} = \alpha_1 \left(\hat{\rho}_1 + \Phi_1 \dot{\rho}_{1\min} \right) < \alpha_2 \hat{\rho}_2 = \hat{r}_2$$
$$r_{\Phi 2} = \alpha_2 \left(\hat{\rho}_2 + \Phi_2 \dot{\rho}_{2\min} \right) < \alpha_3 \hat{\rho}_3 = \hat{r}_3. \qquad (20)$$

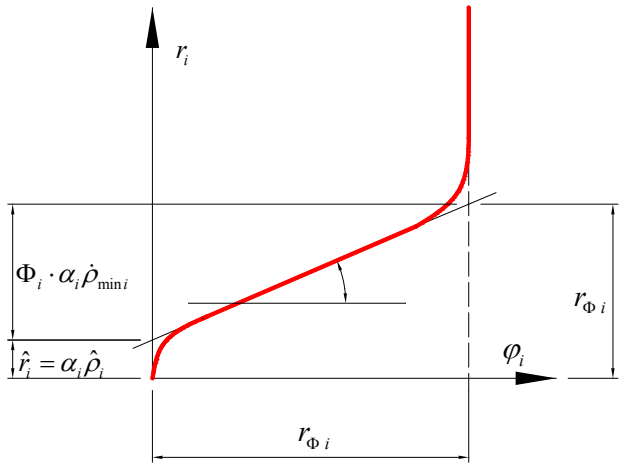

Figure 6 Diagram of the arm-ratio $r_i = \alpha_i \cdot \left(\overline{\beta}_i / \beta_i \right)$ as function of φ_i .

Table I - Initial offsets and slopes - $\Phi = \pi/2$

	$\overline{\varepsilon}$	$\dot{\rho}_{i\min}$	$\hat{\rho}_i$
ε = 0,25	0,242	1,149	0,026
$\overline{\varepsilon}_{\lim}$ = 0,968	0,484	2,210	0,441
	0,726	1,931	1,892
	0,968	0,000	3,861
ε = 0,50	0,216	0,400	0,055
$\overline{\varepsilon}_{\lim}$ = 0,866	0,433	0,674	0,310
	0,649	0,547	0,916
	0,866	0,000	1,730
ε = 0,75	0,165	0,132	0,072
$\overline{\varepsilon}_{\lim}$ = 0,661	0,331	0,197	0,236
	0,496	0,152	0,517
	0,661	0,000	0,881

Table II - Initial offsets and slopes - $\Phi = 2\pi/3$

	$\overline{\varepsilon}$	$\dot{\rho}_{i\min}$	$\hat{\rho}_i$
ε = 0,22	0,184	0,591	0,223
$\overline{\varepsilon}_{\lim}$ = 0,737	0,369	0,876	0,856
	0,553	0,677	1,973
	0,737	0,000	3,410
ε = 0,43	0,141	0,156	0,138
$\overline{\varepsilon}_{\lim}$ = 0,564	0,282	0,222	0,401
	0,423	0,169	0,799
	0,564	0,000	1,302
ε = 0,65	0,084	0,034	0,083
$\overline{\varepsilon}_{\lim}$ = 0,334	0,167	0,046	0,197
	0,251	0,034	0,342
	0,334	0,000	0,514

3.1 A FINGER CASE STUDY

In the following the results of some numerical simulations carried out for a finger whose joints verify the conditions (12), (18) and (20) are presented; this in order to give evidence to the design criteria proposed in the previous sections. Geometrical details of the analyzed device are listed in fig. 7. In the same figure the deformed configurations of the finger for several values of the displacement u imposed to the free end of the flexural tendon are shown. In the diagrams of fig. 8 a) and b) the relative rotations φ_i and the traction force of the flexor tendon, respectively, are reported as function of u.

Figures 7 and 8 show that:

- the geometry adopted for the joints is able to generate an anthropomorphic closure sequence;
- in the finger equilibrium path, buckling phenomena are absent.

In the diagram of fig. 8 a) sudden slope changes are observable. This is because the non-dimensional arm ratios ρ_i have a vertical asymptote at $\varphi_i = \Phi_i$. As far as this aspect is concerned, it must be remembered that during the closure for the finger equilibrium, (see eq. (11)), the arm ratios r_i of the three finger joints have to be equal. When at the joint i the arm ratio r_i reaches the asymptotic branch of the its curve $r_i - \varphi_i$, only very small increments of the relative rotation φ_i can occur for a given increment of r_i. Starting from this situation, further increments of the displacement u are essentially due to changes of the shortening Δz_j that occur at the other joints where the corresponding relative rotations φ_j start to increase more rapidly. The asymptotic branches of the $r_i - \varphi_i$ curves have an analogous effect also on the elongation Δl of the spring and, as a consequence, on the tendon traction $f = k\Delta l\left(\bar{b}_i / b_i\right)$. When the r_i asymptote is approached at the joint i, the corresponding local elongation Δl_i practically stops increasing while the local elongations at the other finger joints start increase more quickly for further fixed increments of the displacement applied to the flexural tendon end. This generates the sudden stiffness changes that are observable in the diagram of fig. 8 b).

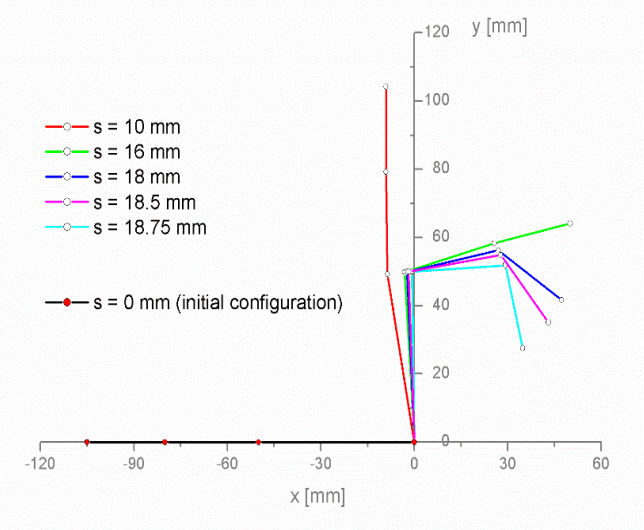

Figure 7 Deformed configurations of the examined finger device.

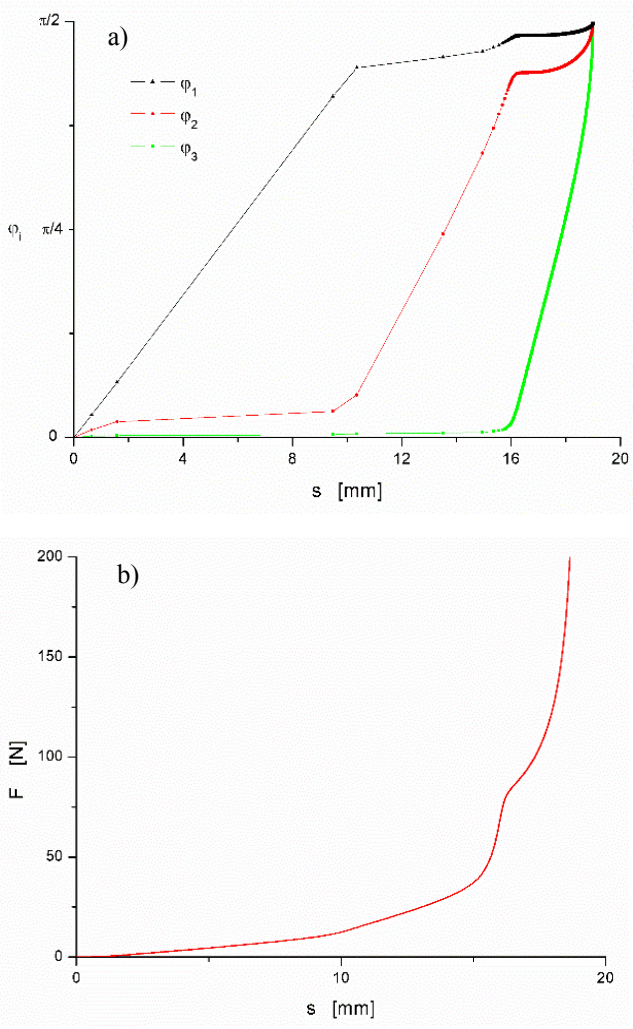

Figure 8 Diagrams of the relative rotations (a) and of the flexural tendon traction (b).

4 CONCLUSIONS

The analysis of the equilibrium of an under-actuated finger was carried out following an energetic approach and has allowed identifying some preliminary design criteria for the regularity of the finger motion and for achieving an anthropomorphic closure sequence. Furthermore, a sufficient condition for the stability of the finger equilibrium has been also derived. A validation study has been carried out analyzing numerically the behavior of a finger designed according to the proposed criteria.

The obtained results are encouraging and justify further experimental analysis to be carried out on finger prototypes. Further investigations will consist in:

- analyzing experimentally and by numerical simulations the grasping capability of fingers designed according to the proposed criteria;
- studying the effect of this kind of fingers on the adaptive properties of an under-actuated mechanical hand;
- checking the finger closing sequence by adopting tendon laws of motion computed by means of the techniques proposed in [17, 18].

REFERENCES

[1] Hirose S., Umetani Y., The development of soft gripper for versatile robot hand. *Mechanism and Machine Theory*, Vol. 13, pp. 351-359, 1978.

[2] Townsend W., The Barret Hand grasper - programmably flexible part handling and assembly. *Industrial Robot: An International Journal*, Vol. 27, No. 3, pp. 181-188, 2000.

[3] Birglen L., Kragten G.A., Herder J.L., EDs., Underactuated Grasping. *Special issue in the Journal of Mechanical Sciences*, 2010.

[4] Kaneko M., Higashimori M., Takenaka R., Namiki A., Ishikawa M., The 100G capturing robot - too fast to see. *IEEE/ASME Transaction on Mechantronics*, Vol. 8, pp. 37-44, 2003.

[5] Laliberté T., Birglen L., Gosselin C., Underactuation in robotic grasping hands. *Machine Intelligence & Robotic Control*, Vol. 4, No. 3, pp. 1-11, 2002.

[6] Doria M., Birglen L., Design of an underactuated compliant gripper for surgery using nitinol. *Journal of Medical Devices*, Vol. 3, No. 1, 2009.

[7] Penta F., Rossi C., Savino S., An underactuated finger for a robotic hand. *International Journal of Mech. and Control*, Vol. 15, No. 2, pp. 63-68, 2014.

[8] Zottola M., Ceccarelli M., Underactuated finger mechanism for LARM hand. *Advances on Theory and Practice of Robots and Manipulators*, Springer International Publishing, pp. 283-291, 2014.

[9] Nelson C.A., Dessauw E., Saiter J.M., Benzohra, M., Design of a compliant underactuated robotic finger with coordinated stiffness. *Proc. of ASME 2013 International Design Engineering Technical Conf. and Computers and Information in Engineering Conf.*, American Society of Mechanical Engineers, 2013.

[10] Groenewegen M.W., Aguirre M.E., Herder J.L., Design of a partially compliant, three-phalanx underactuated prosthetic finger. *Proc. of ASME 2015 International Design Engineering Technical Conf. and Computers and Information in Engineering Conf.*, American Society of Mechanical Engineers, 2015.

[11] Rossi C., Savino S., An underactuated multi-finger grasping device. *International Journal of Advanced Robotic Systems*, Vol. 11, No. 1, 2014.

[12] Rossi C., Savino S., Niola V., Troncone S., A study of a robotic hand with tendon driven fingers. *Robotica*, Vol. 33, No. 5, pp. 1034-1048, 2015.

[13] Niola V., Rossi C., Savino S., Carbone G., Gaspareto A., Quaglia G., An underactuated mechanical hand prosthesys. *Proc. of 14th IFToMM World Congress*, Taipei, Taiwan, October 25-30, 2015, doi: 10.6567/IFToMM.14TH.WC.PS13.005.

[14] Birglen L., Gosselin C.M., On the force capability of underactuated fingers. *Proc. of 2003 IEEE International Conference on Robotics & Automation* Taipei, Taiwan, September 14-19, 2003.

[15] Birglen L., Gosselin C.M., Geometric design of three-phalanx underactuated fingers. *Journal of Mechanical Design - Transactions of the ASME*, Vol. 128, pp. 356-364, 2006.

[16] Kragten G.A., Herder J.L., The ability of underactuated hands to grasp and hold objects. *Mechanism and Machine Theory*, Vol. 45, pp. 408-425, 2010.

[17] Niola V., Rossi C., Savino S., Strano S., Robot trajectory planning by points and tangents. *Proc. of 10th WSEAS Int. Conference on Robotics, Control and Manufacturing Technology*, Hangzhou, China, April 11-13, ISSN: 1790-5117 91, ISBN: 978-960-474-175-5, pp. 91-96, 2010.

[18] Rossi C., Savino S., Robot trajectory planning by assigning positions and tangential velocities. *Robotics and Computer Integrated Manufacturing*, Vol. 29, ISSN: 0736-5845, doi: 10.1016/j.rcim.2012.04.003, pp. 139-156, 2013.

[19] Carbone G., Rossi C., Savino S., Performance comparison between FEDERICA Hand and LARM Hand. *Int. Journal of Advanced Robotic Systems*, Vol. 12, 2015. ISSN: 17298806, DOI: 10.5772/60523.

[20] Penta F., Rossi C., Savino S., Gripping analysis of an underactuated finger. *Advances in intelligent systems and computing: Proc. of 24th Internation Workshop on Robotics in Alpe-Adria-Danube Region*, Bucharest, Romania, May 27-29, doi: 10.1007/978-3-319-21290-6, pp. 71-78, 2015.

[21] Niola V., Penta F., Rossi C., Savino, S., An underactuated mechanical hand: theoretical studies and prototyping. *International Journal of Mechanics and Control*, Vol. 16, No. 1, ISSN: 1590-8844, pp. 11-19, 2015.

[22] Niola V., Rossi C., Savino S., Carbone G., Gaspareto A., Quaglia G., An underactuated mechanical hand prosthesys. *Proc. of 14th IFToMM World Congress*, Taipei, Taiwan, October 25-30, doi: 10.6567/ IFToMM.14TH.WC.PS13.005, 2015.

ISSN 1590-8844
International Journal of Mechanics and Control, Vol. 17, No. 01, 2016

APPLICATIONS OF ADVANCED SIGNAL PROCESSING ANALYSIS

Vincenzo Niola * Giuseppe Quaremba **

* Università di Napoli Fedrico II, Dipartimento di Ingegneria Industriale

** Dipartimento di Scienze Biomediche Avanzate

ABSTRACT

Nowadays, in the industrial field, the predictive maintenance is an important methodology employed for reducing risks of machine stops. Machines are continuously monitored in order to maximize the performance, both in terms of quality and productivity. In this paper it is pointed out an advanced methodology of signal processing which allows to evaluate in advance which kind of fault can happen on a machinery. Several applications are presented in order to show the main features of the method.

Keywords: Signal processing, Industrial Diagnostic, Wavelet Transform.

1 INTRODUCTION

The Wavelet Transform (WT) [Daubechies I., Ten Lectures on Wavelets, SIAM, 1992] represents a time-scale analysis of the smoothness of a signal or, more in general, of a time series or a curve profile. The Wavelet analysis, unlike the FFT, is very useful when one analyzes and decompose signal with a not constant frequency. Qualitatively, the difference between the usual sine wave and a wavelet can be described from the localization property: the sine wave is localized in frequency domain, but not in time domain, while a wavelet is localized both in the frequency and time domain. Furthermore, the duration of its maximum oscillation is relatively small. One can regard a wavelet is a shape of wave of limited duration and zero moments of a given order. The choice of a wavelet and of signal decomposition level depends on the shape of signals and on the experience of the analyst. For its versatility, the wavelet analysis is diffused in many fields, such as Acoustics, Electrodynamics [Kaiser G., A Friendly Guide to Wavelets, Birkhäuser, 1999], Finance [Härdle W. et al. Lecture Notes in Statistics - Wavelets, Approximation, and Statistical Applications, Springer, 1998] Medicine and Statistics [Antoniadis A., Oppenheim G., Lecture notes in Statistics - Wavelets and Statistics, Springer, 1995]. In particular, the wavelets used in this paper are those proposed by Daubechies (1992).

Contact author: Vincenzo Niola

E-mail: vincenzo.niola@unina.it

She constructed a series of mather wavelets (indexed by N and denoted by db$N$) with each mother in the series having regularity proportional to N. Each Daubechies' wavelet is compactly supported in the time domain.
Typically wavelets of class m, are specifically constructed so that some properties are verified (Meyer Y., Wavelets and operators, Cambridge University Press, 2004), [1-4].
A mother wavelet ψ is a function of zero h-th moment:

$$\int_{-\infty}^{+\infty} x^h \psi(x)dx = 0\,, \quad h \in \mathbf{N}. \tag{1}$$

From this definition, it follows that, if ψ is a wavelet whose all moments are zero, also the function ψ_{ik} is a wavelet, where

$$\psi_{jk}(x) = 2^{j/2}\psi(2^j x - k)\,. \tag{2}$$

In fact, we have

$$\int_{-\infty}^{+\infty} 2^{j/2} x^h \psi(2^j x - k)dx =$$

$$= 2^{j/2} \int_{-\infty}^{+\infty} \frac{1}{2^j}\left(\frac{y+k}{2^j}\right)^h \psi(y)dy =$$

$$= \frac{2^{j/2}}{2^{j(h+1)}} \int_{-\infty}^{+\infty} (y+k)^h \psi(y)dy =$$

$$= \frac{2^{j/2}}{2^{j(h+1)}} \sum_{m=0}^{h} \binom{h}{m} k^{h-m} \int_{-\infty}^{+\infty} y^m \psi(y)dy = 0. \tag{3}$$

Moreover, consider a wavelet ψ and a function φ such that $\{\{^{\varphi_{j_0k}}\}, \{\psi_{jk}\}, k \in \mathbf{Z}, j = 0, 1, 2,\ldots\}$ is a complete orthonormal system. By Parseval theorem, for every $s \in L_2(\mathbf{R})$, it follows that

$$s(t) = \sum_k a_{j_0k}\varphi_{j_0k}(t) + \sum_{j=j_0}^{j_1}\sum_k d_{jk}\psi_{jk}(t)\,. \tag{4}$$

The decomposition of a signal $s(t)$ by wavelet is represented by the following detail function coefficients:

$$d_{jk} = \int_{-\infty}^{+\infty} s(\tau)\cdot\frac{1}{\sqrt{2^j}}\psi\left(\frac{\tau-k}{2^j}\right)d\tau \tag{5}$$

and by the approximating scaling coefficients

$$a_{j_0k} = \int_{-\infty}^{+\infty} s(\tau)\cdot\psi(\tau-k)d\tau\,. \tag{6}$$

Note that d_{jk} can be regarded, for any j, as a function of k. Consequently, it is constant if the signal $s(t)$ is a smooth function, having considered that a wavelet has zero moments. To show the above mentioned property, it is sufficient to expand the signal in Taylor's series.

2 APPLICATIONS

In this paragraph some applications of the theory and of the technique, summarized above, are presented in order to both show the technique and validate it

2.1 EXHAUST GAS RECIRCULATION EVALUATION

The first application is the reduction of emissions of NOx through the technique called Exhaust Gas Recirculation (EGR). The policy of reducing emissions in the energy sector is one of the scientific community's main research topics. There have been significant developments in automotive and business fields, particularly in diesel engines. Nowadays, the method, which is widely used in reducing emissions of a Diesel engine, is the dilution factor called EGR through which it is possible to lower NOx levels. The adoption of sophisticated signal processing method such as the one presented in the following, allows easier control of complex systems such as diesel systems Homogeneous Charge Compression Ignition (HCCI), [5–10]. The proposed method of signal processing is the verification of the following basic idea: an engine fueled with a greater amount of inert (*i.e.*, gas recirculation) should exhibit, if it is compared to a standard power supply, a more regular operating condition. The experimental set-up is presented in Fig. 1; the engine test bench has been equipped to test a 1910 cm^3 Common Rail Diesel engine. The main two methodological conditions applied are as follows: i- stationary running of the engine during all the test-run; ii- working points set at 2000rpm and 2bar regarding the mean effective pressure (MEP). The engine is set on standard running conditions (*i.e.*, amount of recirculated gas equal to that normally used by the standard mapping of the motor). These data are used to construct the so-called "reference signal" (baseline).

Subsequent acquisitions are obtained by varying the set-up of the solenoid regulating the EGR in order to gradually increase the amount of exhaust gas in the combustion chamber (performed by means of 5 very small steps, *i.e.*, with the EGR ratio starting from 2.0 and increasing of 1%, until a final value of 2.2) causes a less abrupt combustion with lower local peak of temperature and consequently less formation of nitrogen oxides (NOx).

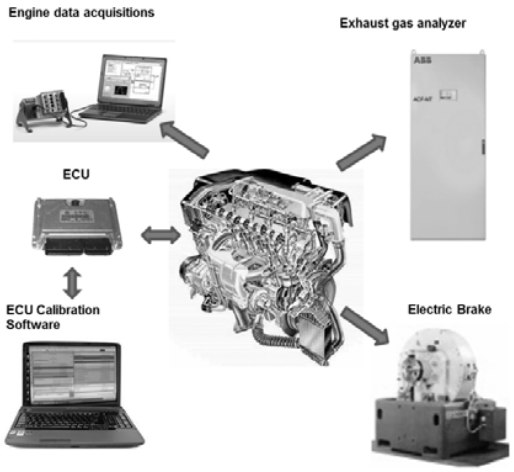

Figure 1 Engine test equipment.

Recall that the purpose of the test was to quantify the "degree of regularity" of the engine for the several set-ups of the EGR (called EGR1, EGR2, etc.) by processing only the accelerometer signals acquired during the test-run.
The measurements are referred to the morphodynamical vibration shown by the engine when it is powered with a gradual increase of the percentage of inert. To obtain this weak information from each cluster (baseline, EGR1, etc.) the accelerometer signals are "synchronized" with the tachometer signal acquired during the running-test. In order to evaluate such a phenomenon, a signal named "surrogate" has been reconstructed for each cluster. It is representative of an averaged class of frequencies and amplitudes) obtained during the test-run (baseline and EGRs). For the construction of a "surrogate" see [10].
Fig. 2 shows the comparison between the surrogates extracted from each cluster. It is quite clear that the higher the percentage of EGR, the greater its phase shift and amplitude. In particular, the change of the surrogate signals can be observed in terms of amplitude and frequency, depending on the cluster from which they were extracted.
Now the problem is to discriminate among groups in order to distinguish them. For example, if a certain "maneuver" can lead to an important and significant response of the engine, variables play a crucial role in attaining the target: to discriminate among the groups. Therefore, to achieve this goal one or more linear combinations of variables must be built in order to discriminate the clusters in the following form:

$$D_i = w_{i1}Z_1 + w_{i2}Z_2 + \ldots\ldots + w_{ip}Z_p \tag{7}$$

where D_i is the score of the i^{th} discriminant function, w are the weights given by each variable, Z are the standardized values of the p variables used in the analysis.

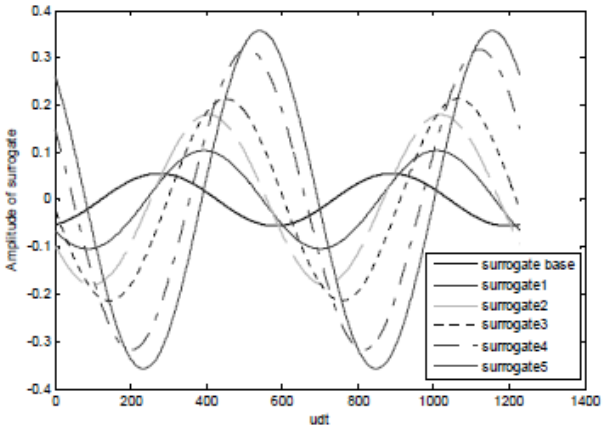

Figure 2 Comparison of 6 surrogates.

Fig. 3 shows how these parameters, defined above, help the classification of the 306 accelerometer signals. Fig. 3shows the presence of 6 well "discriminated" clusters. In particular, we observe EGR1, generated by the minimum change of the EGR ratio, (in terms of percentage from EGR ratio 2.0 of baseline to 2.02 of EGR1). The correlation coefficient (Fig. 4) shows a rather rapid increase from the baseline condition up to the set-up of EGR1, reaching the maximum under the set-up referred to as EGR4. It is clear the reduction of the correlation at EGR5 set-up, beyond which any further supply of inert gas, may affect the smooth vibrational running of the engine. The correlation coefficient confirms that an engine powered with exhaust gas recirculation produces a vibrational signature very similar to its surrogate and therefore very repetitive (about +40%). Conversely, the engine not powered by exhaust gas has a more irregular trend (about -25 %).

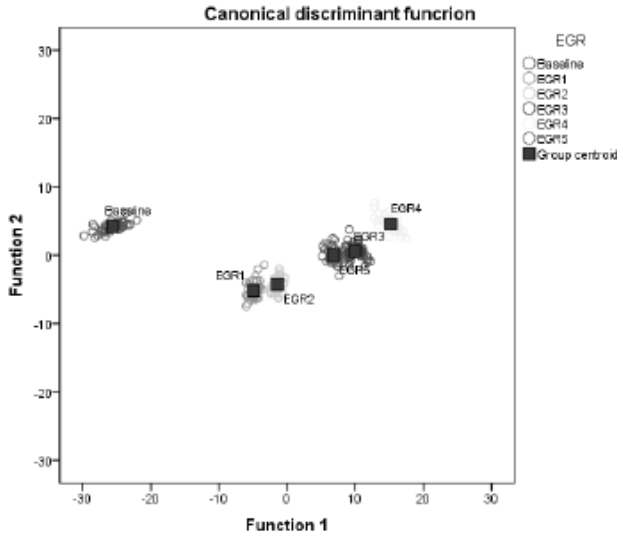

Figure 3 Classification map (306 records).

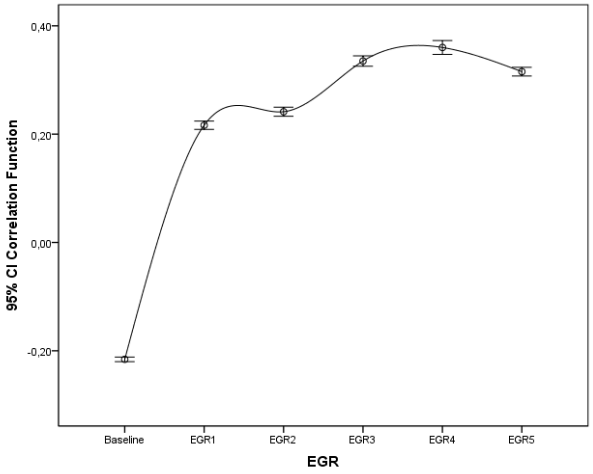

Figure 4 Correlation coefficient (306 records).

It must be remembered that correlation measure how variables are related. Before calculating a correlation coefficient, data were screened for outliers (which can cause misleading results) and evidence of a linear relationship. Pearson's correlation coefficient is a measure of linear association. Two variables can be perfectly related, but if the relationship is not linear, Pearson's correlation coefficient is not an appropriate statistic for measuring their association. However, the Pearson correlation coefficient works best when the variables are approximately normally distributed and have no outliers.
The correlation coefficient range is -1÷+1, the greater is the coefficient the greater is the relationship between the variables viz between EGR and vibrations.
Thanks to its response and sensitivity, the proposed method could be used to optimize, for example, the curve of EGR for each engine family, using the response of the mechanical system in terms of vibration.

2.2 ANALYSIS OF THE PERFORMANCE OF AN INTERNAL COMBUSTION ENGINE

The second application is a methodology for identifying and analysing the performance of an Internal Combustion (I.C.) engine and, at the same time, for the reconstruction of the morphodynamical vibration. In particular, the purpose of the method, showed in this paper, is to assess the performance of an I.C. engine trough the degree of vibrational regularity of each cylinder and, at the same time, to build a diagram characterizing the functional performance, averaged over a significant number of revolutions (namely 60 and 120). The response is processed by means of the wavelet multiresolution analysis [11].
In particular, in the following we introduce the method for the determination of the morpho-dynamical vibration performed during the combustion stage where the highest in-cylinder pressure is reached (IPv) as well as the instantaneous vibrational mean in-cylinder pressure (MIPv). The vibration monitoring was performed on the I.C. engine of a cargo ship during a commercial navigation.

The acquisition of the accelerometric signals for deriving the vibrational signatures characterizing, in particular, each cylinder, was performed by using the same unidirectional accelerometers placed on each cylinder (Fig. 5).
The synchronization was performed by means a tacho detector was placed on a toothed wheel keyed on the motor shaft. Accelerometric signals were sampled continuously at 20480 samples/s (sampling frequency) for a duration of approximately 5min, for several settings and conditions. In the following we reported the most statistically significant results: at 114 rpm, 75% cargo condition.
The measurements were performed by placing the accelerometers on the following three locations (*i.e.*, levels) of the engine: 1l - Base; 2l - Level of collector lubricating oil recovery; 3l - Level close to the motor head. With reference to the six cylinders, it does not appreciate any significant difference with the usual spectral-shape analysis.

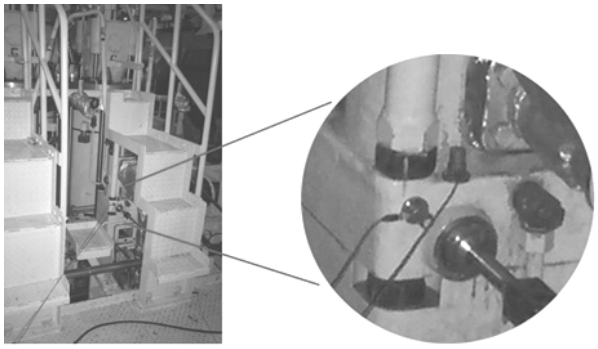

Figure 5 Accelerometer location.

The Figure 6 illustrates the spectral diagram where are highlighted the main frequencies due to several mechanical components. For instance, the 9.5Hz frequency is caused by the propeller while the 11.5Hz frequency is generated by the engine system. The 95Hz frequency is due to the chain drive wheel (50 teeth). The 45.5Hz is the frequency due to the tensioner (wheel of 25 teeth) while the 60Hz is the power generator.

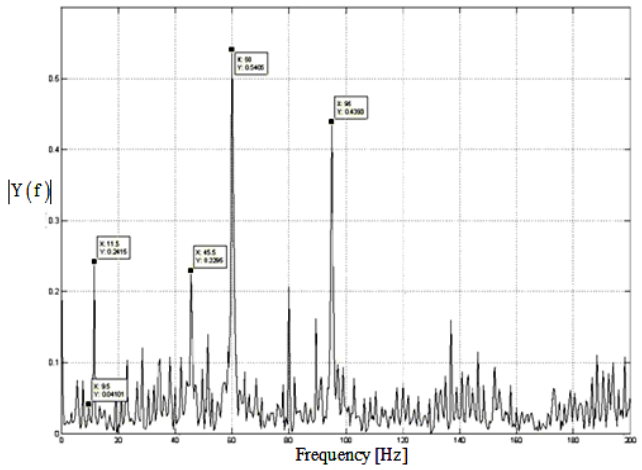

Figure 6 Working spectrum.

As *working spectrum* we mean the frequency spectrum due to typical concentrated masses. The spectrum, in the case of correct operation of the system (*i.e.*, the entire propulsion system chain), provides the basic frequencies of each component and their coupling with the ship system. A very important and critical stage of the monitoring phase was to detect the vibrational signatures as well as the performance exhibited by each cylinder during the evolution of the respective thermodynamic cycle. The Fig. 7 illustrates the importance of employing a method (based on the WT) that allows both the aimed selection of the working frequency and the reconstruction of temporal evolution of the phenomenon spectrally selected. In particular, the speed was 12 rad/s, it was used a single accelerometer placed on the head of the cylinder no. 6, with the *z* axis parallel to the main direction of the cylinder. The instantaneous vibrational sequence (*i.e.*, the wavelet coefficients), generated by the thermodynamic cycle (corresponding to the self-ignition of the fuel), is shown in Fig. 7.

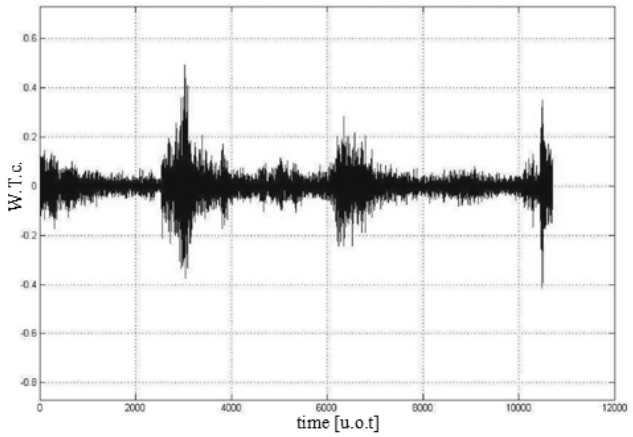

Figure 7 Wavelet coefficients at 12 rad/s.

The Fig. 8 compares the vibrational diagrams geometrically averaged of cylinder no.1, reconstructed with 20 harmonics after 13, 60 and 120 periods; the stability of the shape suggests for a good reliability of the method used for the reconstruction of the *morphodynamical* vibration. We use the word morphodynamical because the extraction of the wavelet coefficients allows the evaluation of both the morphology and the dynamic of the mechanical system vibration. Starting from the accelerometric signal, the method was applied to the other cylinders. Figure 9 shows the comparison of the aforesaid vibrational signatures due to the three cylinders: 1, 3 and 6. We note a significant difference both of the shape and of the area under the cyl no. 6. The method indirectly shows also the performance of the thermodynamic cycles of a crank-slider mechanical system. In particular, it provides important information about the ignition and the combustion phases, within 60° of crank-angle, where it depends the regularity of running and consequently the stress distribution on several mechanical components as well as the chain of cam-shaft, which is, of course, the weakest link of the mechanical arrangement.

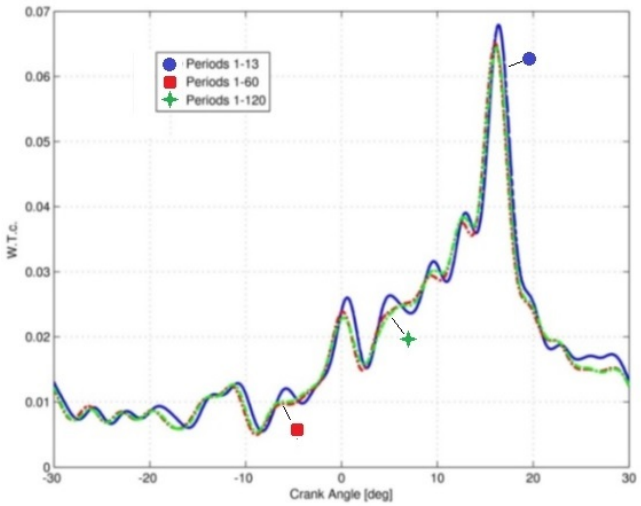

Figure 8 Comparison of MIPv at 13,60 and 120 periods (cylinder no. 1).

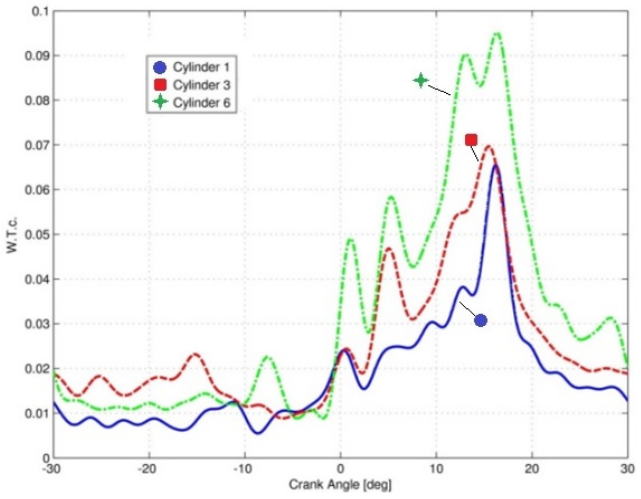

Figure 9 Comparison of MIPv of cylinders no. 1, 3 and 6.

A best performance for the analysis of thermodynamic cycles is achieved by involving also the thermal images detected trough infrared camera integrated with the technique of Wavelet Transform [12].

2.3 GRASPING ANALYSIS OF MECHANICAL HAND

A further application of the proposed technique consists in examining the signals of accelerometers fitted on the phalanxes of a mechanical hand representing a hand prosthesis prototype. This device was designed and built at the laboratory of Robotics of the D.I.I. of the University of Naples "Federico II", [13-15].

A prototype, instrumented with the accelerometers is shown in Figure 10. In the same figure it is possible to observe the hand while grasping a wooden sphere having 42 mm diameter. By examining the signals while the object is grasped, it is possible to recognize if and how instability of the grasping occurs.

Moreover two different laws of motion were adopted for the only actuator during the grasping. For both the laws of motion the maximum actuator force is 40 N, but this amount is reached in 0.2 seconds in the first case and in 0.4 in the other case. In the following we will indicate with f_1 the first law of motion and with f_2 the second one.

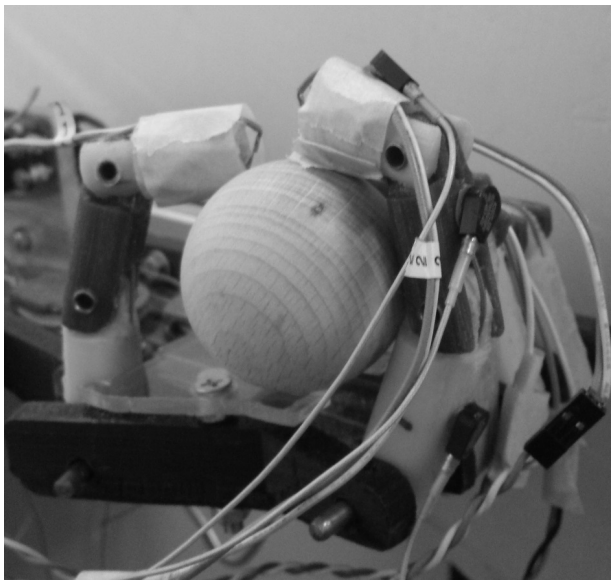

Figure 10 Hand prototype grasping a sphere.

In Figure 11 and 12 the signals by the accelerometers are reported. Figure 11 refers to the f_1 law of motion, while Figure 12 refers to f_2. How it is possible to observe, during the first 0.1 second the phalanxes of the finger approach the object and grasp it. After about 0.1 second, the phalanxes are onto contact with the object surface. During the next 0.4 seconds, the accelerometer signal doesn't show significant accelerations, thus no significant changes in the grasping occur.

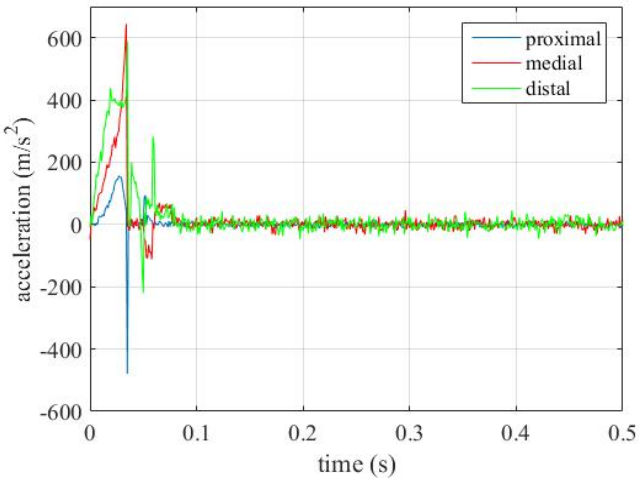

Fig. 11 Accelerometers signals with f_1 closing law of motion.

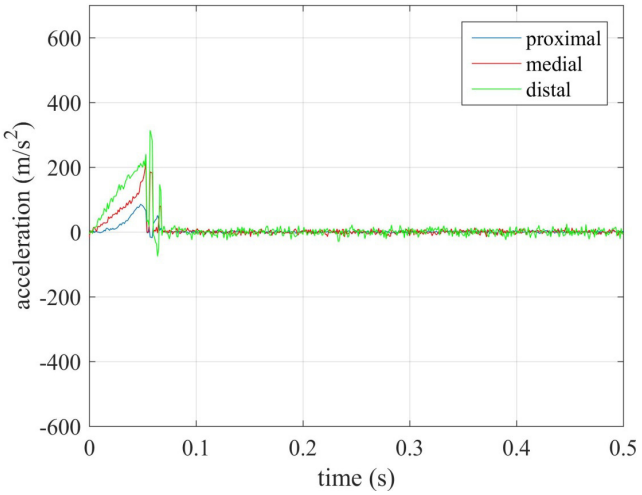

Fig. 12 Accelerometers signals with f_2 closing law of motion.

If Figure 11 and 12 are compared, it is clear that the different actuator laws of motion play a significant role both during the early phase of the grasping and also during the phase of the object holding; in fact the acceleration during the first 0.05 seconds is higher in the case of f_1 law of motion and, moreover, during the holding phase. The above suggests that suitable laws of motion of the actuator could be planned, for example by using the methods already proposed and studied in [16,17] for the motion planning of the links of a robot.

5 CONCLUSIONS

A signal processing analysis method was presented with some application examples. The main advantages of the proposed method can be summarized as follows:

1. It does not require expensive equipment;
2. it is very flexible;
3. it is fast;
4. it does not require maintenance.

Moreover, the proposed method is non-invasive, it is reliable and easy to implement. It could be performed a real-time system monitoring. The results, referred to the pressure diagrams, are of vibrational nature.
From a qualitative point of view, the comparison with the pressure trend is good; in the future a quantitative analysis will be performed in order to assess a complete monitoring of the I.C. engine system through the vibrational morphodynamics. Furthermore, the analysis of the behavior by means of this methodology can be used for analyzing how the engine changes its morphodynamics signature and for verifying how the combustion occurs. It defines a functional map of the engine vibration for each sequence of parameters such as crank angle, EGR ratio and the characteristics of combustion.

The results carried out show that little variations well define the repeatability classes of the EGR demonstrating that the morphodynamics analysis "feels" the system changing and can verify the instability conditions before they occur. Finally an application to a mechanical system represented by a mechanical hand prosthesis was also presented. Further investigations in all the presented fields were planned.

REFERENCES

[1] Gille B.A., *History of technology and invention, progress through the ages*. Maurice Daumas, New York, Vol. I, 1969.

[2] Daubechies I., Orthonormal bases of compactly supported wavelets. *Communications in Pure and Applied Mathematics*, 1988.

[3] Meyer Y., *Wavelets: algorithms and applications*. SIAM: Philadelphia, 1993.

[4] Wickerhauser M.V., *Adapted wavelet analysis from theory to software*. IEEE Press, AK Peters, Natick, Massachusetts, 1994.

[5] Jinyoung C., Junhong K., Youngjin C., Simsoo P., The effect of exhaust gas recirculation (EGR) on combustion stability, engine performance and exhaust emissions in a gasoline engine. *KSME Journal*, Vol. 15, No. 10, pp 1442-1450, 2001.

[6] Haiyong P., Yi C., Lei S., Kangyao D., Effects of EGR on combustion process of DI diesel engine during cold start. *Front. Energy Power Eng. China*, Vol. 2, No. 2, pp. 202-210, 2008.

[7] Molin J., Investigation of correlations between COV of ion integral and COV of IMEP in a port-injected natural-gas engine. *Master thesis*, Linköping, 12 December, 2008.

[8] Wasiu S.O., Sulaiman S.A., Aziz A.R.A., An experimental study of different effects of EGR rates on the performance and exhaust emissions of the stratified charge piston direct injection compressed natural gas engine. *Journal of Applied Sciences*, Vol. 11, No. 9, pp. 1479-1490, 2011.

[9] Li H., Karim G.A., Modeling the performance of turbo-charged spark ignition natural gas engine with cooled exhaust gas recirculation. *Journal of Engineering for Gas Turbine and Power*, Vol. 130, May 2008.

[10] Amoresano A., Niola V., Quaremba A., A sensitive methodology for the EGR optimization: a perspective study. *Int. Review of Mechanical Engineering (I.RE.M.E.)*, Vol. 6, No. 5, 2012. ISSN 1970 - 8734.

[11] Amoresano A., Avagliano V., Niola V., Quaremba G., The assessment of the in-cylinder pressure by means of the morpho-dynamical vibration analysis - Methodology and application. *Int. Review of Mechanical Engineering,* Vol. 7, No. 6, 2013. ISSN 1970-8734.

[12] Niola V., Quaremba G., Amoresano A., A study on infrared thermography processed trough the wavelet transform. *Proc. of 8th WSEAS International Conference on System Science and Simulation in Engineering, ICOSSSE '09*, pp. 57-62, 2009.

[13] Rossi C., Savino S., Mechanical model of a single tendon finger. *Proc. of 11th International Conference of Numerical Analysis and Applied Mathematics*, Rhodes; Greece, 21 September, Vol. 1558, pp. 1286-1292, 2013.

[14] Rossi C., Savino S., Niola V., Troncone S., A study of a robotic hand with tendon driven fingers. *Robotica*, Vol. 33, No. 5, doi: 10.1017/S0263574714001179, ISSN: 0263-5747, pp. 1034-1048, 2014.

[15] Niola V., Rossi C., Savino S., A new mechanical hand: Theoretical studies and first prototyping. *Int. Review of Mechanical Engineering*, Vol. 8, No. 5, ISSN:19708734, pp. 835-844, 2014.

[16] Rossi C., Savino S., Robot Trajectory planning by assigning positions and tangential velocities. *Robotics and Computer Integrated Manufacturing*. Vol. 29, No. 1, doi: 10.1016/j.rcim.2012.04.003, pp. 139-156, 2013.

[17] Niola V., Rossi C., Savino S., Strano S., Robot trajectory planning by points and tangents. *Proc. of 10th WSEAS Int. Conference on Robotics, Control and Manufacturing Technology*, Hangzhou, China, April 11-13, ISSN: 1790-5117 91, ISBN: 978-960-474-175-5, pp. 91-96, 2010.

ISSN 1590-8844
International Journal of Mechanics and Control, Vol. 17, No. 01, 2016

TEMPLATE FOR PREPARING PAPERS FOR PUBLISHING IN INTERNATIONAL JOURNAL OF MECHANICS AND CONTROL

Author1* Author2**

* affiliation Author1

** affiliation Author2

ABSTRACT

This is a brief guide to prepare papers in a better style for publishing in International Journal of Mechanics and Control (JoMaC). It gives details of the preferred style in a template format to ease paper presentation. The abstract must be able to indicate the principal authors' contribution to the argument containing the chosen method and the obtained results. (max 200 words)

Keywords: keywords list (max 5 words)

1 TITLE OF SECTION (E.G. INTRODUCTION)

This sample article is to show you how to prepare papers in a standard style for publishing in International Journal of Mechanics and Control.
It offers you a template for paper layout, and describes points you should notice before you submit your papers.

2 PREPARATION OF PAPERS

2.1 SUBMISSION OF PAPERS

The papers should be submitted in the form of an electronic document, either in Microsoft Word format (Word'97 version or earlier).
In addition to the electronic version a hardcopy of the complete paper including diagrams with annotations must be supplied. The final format of the papers will be A4 page size with a two column layout. The text will be Times New Roman font size 10.

Contact author: author1[1], author2[2]

[1]Address of author1.
[2]Address of author2 if different from author1's address
E-mail: author1@univ1.com , author2@univ2.com

2.2 DETAILS OF PAPER LAYOUT

2.2.1 Style of Writing

The language is English and with UK/European spelling. The papers should be written in the third person. Related work conducted elsewhere may be criticised but not the individuals conducting the work. The paper should be comprehensible both to specialists in the appropriate field and to those with a general understanding of the subject.
Company names or advertising, direct or indirect, is not permitted and product names will only be included at the discretion of the editor. Abbreviations should be spelt out in full the first time they appear and their abbreviated form included in brackets immediately after. Words used in a special context should appear in inverted single quotation mark the first time they appear. Papers are accepted also on the basis that they may be edited for style and language.

2.2.2 Paper length

Paper length is free, but should normally not exceed 10000 words and twenty illustrations.

2.2.3 Diagrams and figures

Figures and Tables will either be entered in one column or two columns and should be 80 mm or 160 mm wide respectively. A minimum line width of 1 point is required at actual size. Captions and annotations should be in 10 point with the first letter only capitalised *at actual size* (see Figure 1 and Table VII).

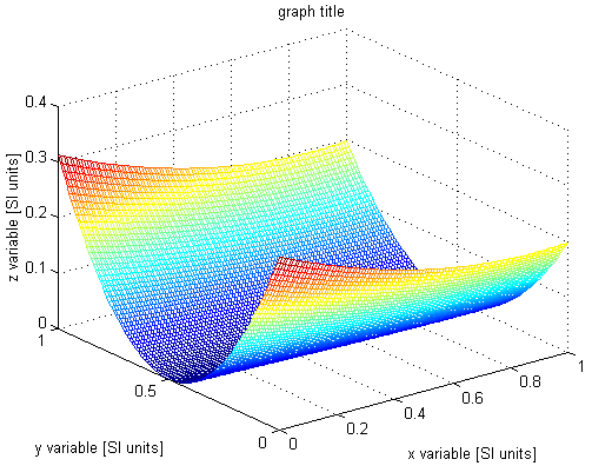

Figure 1 Simple chart.

Table VII - Experimental values

Robot Arm Velocity (rad/s)	Motor Torque (Nm)
0.123	10.123
1.456	20.234
2.789	30.345
3.012	40.456

2.2.4 Photographs and illustrations

Authors could wish to publish in full colour photographs and illustrations. Photographs and illustrations should be included in the electronic document and a copy of their original sent. Illustrations in full colour …

2.2.5 Equations

Each equation should occur on a new line with uniform spacing from adjacent text as indicated in this template. The equations, where they are referred to in the text, should be numbered sequentially and their identifier enclosed in parenthesis, right justified. The symbols, where referred to in the text, should be italicised.

- point 1
  - point 2
    - point 3

1. numbered point 1
   2. numbered point 2
      3. numbered point 3

$$W(d) = G(A_0, \sigma, d) = \frac{1}{T}\int_0^{+\infty} A_0 \cdot e^{-\frac{d^2}{2\sigma^2}} dt \qquad (1)$$

3 COPYRIGHT

Authors will be asked to sign a copyright transfer form prior to JoMaC publishing of their paper. Reproduction of any part of the publication is not allowed elsewhere without permission from JoMaC whose prior publication must be cited. The understanding is that they have been neither previously published nor submitted concurrently to any other publisher.

4 PEER REVIEW

Papers for publication in JoMaC will first undergo review by anonymous, impartial specialists in the appropriate field. Based on the comments of the referees the Editor will decide on acceptance, revision or rejection. The authors will be provided with copies of the reviewers' remarks to aid in revision and improvement where appropriate.

5 REFERENCES (DESCRIPTION)

The papers in the reference list must be cited in the text. In the text the citation should appear in square brackets [ ], as in, for example, "the red fox has been shown to jump the black cat [3] but not when...". In the Reference list the font should be Times New Roman with 10 point size. Author's first names should be terminated by a 'full stop'. The reference number should be enclosed in brackets.

The book titles should be in *italics*, followed by a 'full stop'. Proceedings or journal titles should be in *italics.* For instance:

REFERENCES (EXAMPLE)

[1] Smith J., Jones A.B. and Brown J., *The title of the book*. 1st edition, Publisher, 2001.

[2] Smith J., Jones A.B. and Brown J., The title of the paper. *Proc. of Conference Name*, where it took place, Vol. 1, paper number, pp. 1-11, 2001.

[3] Smith J., Jones A.B. and Brown J., The title of the paper. *Journal Name*, Vol. 1, No. 1, pp. 1-11, 2001.

[4] Smith J., Jones A.B. and Brown J., *Patent title*, U.S. Patent number, 2001.

International Journal of Mechanics and Control – JoMaC
Published by Levrotto&Bella
TRANSFER OF COPYRIGHT AGREEMENT

NOTE: Authors/copyright holders are asked to complete this form signing section A, B or C and mail it to the editor office with the manuscript or as soon afterwards as possible.	*Editor's office address:* Andrea Manuello Bertetto *Dept. of Mechanics* *Technical University – Politecnico di Torino* *C.so Duca degli Abruzzi, 24 – 10129 Torino – Italy* *e_mail: jomac@polito.it* *fax n.: +39.011.564.6999*

The article title:

By:_____

To be Published in ***International Journal of Mechanics and Control JoMaC***
Official legal Turin court registration Number 5320 (5 May 2000) - reg. Tribunale di Torino N. 5390 del 5 maggio 2000

A Copyright to the above article is hereby transferred to the JoMaC, effective upon acceptance for publication. However the following rights are reserved by the author(s)/copyright holder(s):
1. All proprietary rights other than copyright, such as patent rights;
2. The right to use, free or charge, all or part of this article in future works of their own, such as books and lectures;
3. The right to reproduce the article for their own purposes provided the copies are not offered for sale.

To be signed below by all authors or, if signed by only one author on behalf of all co-authors, the statement A2 below must be signed.

A1. All authors:

SIGNATURE_____DATE_____ SIGNATURE_____DATE_____

PRINTED NAME_____ PRINTED NAME_____

SIGNATURE_____DATE_____ SIGNATURE_____DATE_____

PRINTED NAME_____ PRINTED NAME_____

A2. One author on behalf of all co-authors:
"I represent and warrant that I am authorised to execute this transfer of copyright on behalf of all the authors of the article referred to above"

PRINTED NAME_____

SIGNATURE_____ TITLE_____ DATE_____

B. The above article was written as part of duties as an employee or otherwise as a work made for hire. As an authorised representative of the employer or other proprietor. I hereby transfer copyright to the above article to *International Journal of Mechanics and Control* effective upon publication. However, the following rights are reserved:
1. All proprietary rights other than copyright, such as patent rights;
2. The right to use, free or charge, all or part of this article in future works of their own, such as books and lectures;
3. The right to reproduce the article for their own purposes provided the copies are not offered for sale.

PRINTED NAME_____

SIGNATURE_____ TITLE_____ DATE_____

C. I certify that the above article has been written in the course of employment by the United States Government so that no copyright exists, or by the United Kingdom Government (Crown Copyright), thus there is no transfer of copyright.

PRINTED NAME_____

SIGNATURE_____ TITLE_____ DATE_____

CONTENTS – Special Issue for RAAD 2015

CONTENTS – Regular Issue